LASER COOLING AND TRAPPING OF NEUTRAL STRONTIUM FOR SPECTROSCOPIC MEASUREMENTS OF CASIMIR-POLDER POTENTIALS

by

ERYN C. COOK

A DISSERTATION

Presented to the Department of Physics
and the Graduate School of the University of Oregon
in partial fulfillment of the requirements
for the degree of
Doctor of Philosophy

December 2017

DISSERTATION APPROVAL PAGE

Student: Eryn C. Cook

Title: Laser Cooling and Trapping of Neutral Strontium for Spectroscopic Measurements of Casimir-Polder Potentials

This dissertation has been accepted and approved in partial fulfillment of the requirements for the Doctor of Philosophy degree in the Department of Physics by:

Hailin Wang	Chair
Daniel A. Steck	Advisor
Raymond E. Frey	Core Member
Andrew H. Marcus	Institutional Representative

and

Sara D. Hodges	Interim Vice Provost and Dean of the Graduate School

Original approval signatures are on file with the University of Oregon Graduate School.

Degree awarded December 2017

DISSERTATION ABSTRACT

Eryn C. Cook

Doctor of Philosophy

Department of Physics

December 2017

Title: Laser Cooling and Trapping of Neutral Strontium for Spectroscopic Measurements of Casimir-Polder Potentials

Casimir and Casimir-Polder effects are forces between electrically neutral bodies and particles in vacuum, arising entirely from quantum fluctuations. The modification to the vacuum electromagnetic-field modes imposed by the presence of any particle or surface can result in these mechanical forces, which are often the dominant interaction at small separations. These effects play an increasingly critical role in the operation of micro- and nano-mechanical systems as well as miniaturized atomic traps for precision sensors and quantum-information devices. Despite their fundamental importance, calculations present theoretical and numeric challenges, and precise atom-surface potential measurements are lacking in many geometric and distance regimes.

The spectroscopic measurement of Casimir-Polder-induced energy level shifts in optical-lattice trapped atoms offers a new experimental method to probe atom-surface interactions. Strontium, the current front-runner among optical frequency metrology systems, has demonstrated characteristics ideal for such precision measurements. An alkaline earth atom possessing ultra-narrow intercombination transitions, strontium can be loaded into an optical lattice at the “magic” wavelength where the probe transition is unperturbed by the trap light. Translation of the lattice will permit controlled transport of tightly-confined atomic samples to well-calibrated atom-surface separations, while optical transition shifts serve as a direct probe of the Casimir-Polder potential.

We have constructed a strontium magneto-optical trap (MOT) for future Casimir-Polder experiments. This thesis will describe the strontium apparatus, initial trap performance, and some details of the proposed measurement procedure.

CURRICULUM VITAE

NAME OF AUTHOR: Eryn C. Cook

GRADUATE AND UNDERGRADUATE SCHOOLS ATTENDED:

University of Oregon, Eugene, OR

University of Washington, Seattle, WA

Scripps College, Claremont, CA

DEGREES AWARDED:

Doctor of Philosophy in Physics, 2017, University of Oregon

Bachelor of Science in Physics, 2006, University of Washington

AREAS OF SPECIAL INTEREST:

Atomic, Molecular, and Optical Physics

PROFESSIONAL EXPERIENCE:

Graduate Teaching Fellow, University of Oregon, 2007–2009 and 2011–2017

Graduate STEM Fellow in K–12 Education, NSF GK–12, University of Oregon, 2009–2011

Graduate Pod Leader, NSF UCORE, University of Oregon, 2011

Interim Optical Engineer, Institute for Shock Physics, Washington State University, 2006–2007

Undergraduate Research Assistant, University of Washington, 2003–2006

Physics Tutor, WISE (Women in Science and Engineering), University of Washington, 2002–2003

GRANTS, AWARDS AND HONORS:

Weiser Senior Teaching Assistant Award, University of Oregon, 2013

NSF UCORE Fellowship, University of Oregon, 2011

NSF GK-12 Fellowship, University of Oregon, 2009-2011

First Place Student Presentation, CIOMP-OSA International Summer Session, 2011

Les Matson Graduate Fellowship, University of Oregon, 2007-2008

Washington State Scholar, University of Washington, 2001-2005

Gabrielle Jungels-Winkler Scholar, Scripps College, 1999-2001

National Merit Scholarship Finalist, 1999

PUBLICATIONS:

Chris Seck, Paul J. Martin, Eryn C. Cook, Brian Odom, and Daniel A. Steck, “Noise reduction of a Libbrecht–Hall-style current driver,” *Review of Scientific Instruments* **87**, 064703 (2016).

Eryn C. Cook, Paul J. Martin, Tobias L. Brown–Heft, Jeffrey C. Garman, and Daniel A. Steck, “High-passive-stability diode-laser design for use in atomic-physics experiments,” *Review of Scientific Instruments* **83**, 043101 (2012).

Eryn C. Cook, Paul J. Martin, and Daniel A. Steck, “Development of an ultra-stable, low-cost diode laser system,” *CIOMP-OSA International Summer Session: Lasers and Their Applications* Th-22 (2011).

Tao Hong, Claire Cramer, Eryn Cook, Warren Nagourney, and E. N. Fortson, “Observation of the ${}^1S_0$–${}^3P_1$ transition in atomic ytterbium for optical clocks and qubit arrays,” *Optics Letters* **30**, 2644 (2005).

ACKNOWLEDGEMENTS

The strontium project presented here belongs equally to my graduate student partner and good friend, Paul J. Martin. We started this project together with an empty optical table and built up much of the apparatus from scratch, and the UO strontium magneto-optical trap might not exist today without Paul's efforts. Paul's tenacity and strong problem-solving skills steered us through many experimental setbacks; his engineering sensibility and attention to detail allowed success on many sub-projects that otherwise may have floundered (and prevented our lab space from devolving into a chaotic jumble of optics and wires). His kindness and patience in the face of frustration are qualities I hope to emulate, and I can never thank him enough for his endless support, both personal and professional, throughout this journey.

Many undergraduates contributed to the strontium project over the years, and I am grateful for not only all the electronics and other projects completed but also for the lab camaraderie. In particular I must thank Tobias Brown-Heft, who worked with us for several years and brought extraordinary talent to every project he took on. The assistance of the UO TSA staff was also critical for the construction of many parts built over the years; thanks to Kris Johnson and John Boosinger for all the advice and machining assistance, and to Jeffrey Garman for design assistance and the CNC-machining of our external-cavity master diode lasers. Thanks also to Brandy Todd, Jani Levy, Jodi Myers, and all the physics department administrative staff for assistance with the endless purchase orders and other forms.

The strontium project owes a strong debt to the first generation of Steck lab graduate students, Tao Li, Libby Schoene, and Jeremy Thorn, who developed many pieces of equipment and computer control systems adopted from their Rb project

into the Sr apparatus. I am grateful also for the support and good times in and out of the lab shared with both the first generation and subsequent Steck lab comrades Jonathan Mackrory, Richard Wagner, and Wes Erickson. (Thanks also to Wes for jumping in to learn the ropes of the strontium apparatus during my final months on the project!)

I am grateful to Michael Raymer, Stephen Gregory, Dean Livelybrooks and the UCORE and GK-12 programs, Elly Vandergrift and the Science Literacy Program, and in particular my committee members Hailin Wang, Ray Frey, and Andrew Marcus for advice and insights on topics ranging from physics to teaching to navigating graduate school. From my undergraduate days, I want to thank Norval Fortson, Warren Nagourney, and all the students and postdocs I interacted with in the UW atomic physics labs, particularly Claire Cramer, Amar Andalkar, and Jeff Sherman. Their enthusiasm sparked my interest in experimental physics in general and optics and atomic physics in particular and motivated me to continue on to graduate school.

Finally, special thanks to my advisor, Dan Steck, for the opportunity to develop this project, and for all that I have learned throughout my time at the UO. Dan's expertise was critical to the undertaking of an ambitious experiment, and I am hopeful that the strontium apparatus will be used to explore interesting physics for many years into the future under his guidance. I am grateful for Dan's patience and willingness to share his remarkable breadth and depth of physics knowledge.

And of course, thanks also to all my friends and family (and Maya!) for critical moral support and encouragement over the years.

DEDICATION

To my father, for swinging a bucket of water around his head in the living room and the other science demos of my childhood, and to my mother, for her constant support and encouragement.

TABLE OF CONTENTS

Chapter Page

LIST OF FIGURES

LIST OF TABLES

Table Page

CHAPTER I

INTRODUCTION

Laser cooled and trapped neutral atoms can act as precision probes of subtle environmental effects. One such effect is the Casimir-Polder (CP) interaction [1]: the interaction between two neutral atoms or an atom and a neutral surface arising from quantum fluctuations of the vacuum electromagnetic field. The effect can be interpreted as a spatially-varying Lamb shift [2] — an ac-Stark shift resulting from the atomic interaction with the vacuum field modes. The macroscopic equivalent, the attractive force between two neutral bodies, is known as the Casimir effect [3], but arises from the same principles: the presence of surfaces modifies the the allowed vacuum field modes and hence the total vacuum field zero-point energy density relative to the energy density in the absence of the bodies. The Casimir effect thus joins superconductivity and superfluidity as one of the few macroscopic manifestations of a fundamentally quantum phenomenon [4].

In the near field the CP effect is equivalent to the van der Waals interaction: the potential between an atom and a perfect planar conductor can be found from the interaction energy of a fluctuating dipole and its surface image, but far-field retardation effects change the length-scaling of the interaction. A full quantum-electrodynamic (QED) treatment is required to calculate the functional form of the interaction over all atom-surface distances [5]. Regularization and renormalization challenges arise from the infinite electromagnetic field-mode-sums involved; the material response must be characterized over a broad frequency spectrum; and the effect is non-additive since the inclusion of additional atoms or surfaces fundamentally alters the spatial modes. As a result, analytic approximations or numeric methods are required for all but the most trivial surface geometries, as well as when including other real-surface properties such as finite conductivity, surface roughness, or birefringence.

Experimental tests of numeric predictions are essential for further development of the field, but despite the fact that the force is the dominant interaction at small length-scales, precision measurements of Casimir and CP effects have often lagged far behind theoretic developments. Although predicted in 1948, the retarded atom-surface CP effect was first definitively observed in 1993 [6], and the Casimir force between two conductive surfaces in 1997 [7]. These experiments sparked renewed interest in the phenomenon, but several open questions remain, and many predicted effects are yet to be detected. A thorough understanding of Casimir and CP forces is essential in the future development and operation of micro- and nano-electromechanical systems (MEMS and NEMS) and the continued miniaturization of neutral atom and ion traps (atom-chip devices) for quantum information and atomic sensor applications. Cavity quantum-electrodynamics (cavity QED) experiments and searches for predicted novel short-range forces (non-Newtonian gravitational forces) also require careful CP-interaction characterization. New experiments probing CP effects via as-yet-unexplored methods will support future theory developments and experiments in both basic and applied physics.

Strontium, a two-valence-electron alkaline earth atom with extremely narrow intercombination transitions (dipole-forbidden $\Delta S = 1$ singlet-triplet lines), is a strong candidate for a precision CP sensor. With a strong dipole-allowed cycling transition, strontium is amenable to laser cooling and trapping in a magneto-optical trap (MOT), and the narrow intercombination $^1\mathrm{S}_0 - {}^3\mathrm{P}_1$ transition allows further cooling in a second-stage MOT. Subsequent loading into an optical lattice allows tight spatial confinement, and the the trap potential leaves the frequency of an intercombination transition nearly unperturbed when the lattice beams are tuned to the transition's "magic wavelength" where the first-order ac-Stark shifts of the ground and excited states are equal. The doubly-forbidden $^1S_0 - {}^3P_0$ transition at 698 nm in ^{87}Sr, weakly allowed by hyperfine mixing, has a 1 mHz linewidth [8, 9]; such a high-Q oscillator cycling at optical frequencies is ideal for a precision optical frequency standard, and the strontium optical lattice clock developed at the National Institute of Standards and Technology (NIST) has demonstrated a fractional frequency instability $\delta\nu/\nu_0 = 10^{-18}$ [10]. This system has become the leading optical frequency standard candidate and has been adopted by several national labs [11–14].

The demonstrated elimination of systematic frequency shifts in strontium optical lattice clocks implies that such systems are ideal for the spectroscopic measurement of subtle effects like the Casimir-Polder interaction [15]. The differential CP shift of the ground and excited states leads to a measurable shift in the intercombination-transition frequencies: atoms loaded into a one-dimensional magic-wavelength optical lattice can be translated towards a surface to measure the change in this shift relative to the unshifted frequency far from the surface. The lattice ensures tight localization, collisional shifts subtract off, and the properties of strontium are favorable for minimization of important atom-surface systematics. Discrimination against static magnetic and electric field interactions is critical for Casimir and CP experiments, but the zero-total-angular-momentum ground state of the even isotopes limits spurious shifts due to surface currents or magnetic fields. The polarizability of strontium surface adsorbates is predicted to be significantly weaker than that for alkalis [16], reducing the surface-contamination electric-field patch effects which have proven a significant systematic in alkali surface-potential experiments [17]. The atom-surface distance can be measured to the 30 nm transverse localization of the lattice wells using adiabatic transfer to a surface-reflection lattice, and the total distance uncertainty then depends only on the 50 nm repeatability of lattice translation.

The differential shift of the ground and excited states of the 7.4 kHz-linewidth $^1\mathrm{S}_0 - {}^3\mathrm{P}_1$ transition in ^{88}Sr is calculated to be 1 kHz at an atom-conductor distance of 1 μm and over 10 kHz at 200 nm, the closest approach feasible without a higher-power lattice laser. The shift is thus resolvable throughout much of the theoretically interesting intermediate region where the surface-potential length-scaling crosses over from the near-field $1/z^3$ to far-field $1/z^4$ behavior. Thus far, only one experiment (using an evanescent-wave atomic mirror) has demonstrated quantitative measurements in this distance regime [18]. Unlike evanescent-wave schemes, this approach is amenable to the use of any surface partially transparent to the optical lattice beams, which will allow exploration of surface roughness contributions and the orientation and power-scaling effects predicted for birefringent materials, diffraction gratings, and thin-film surfaces. Initial experiments detecting the shift resulting from the Pyrex science cell wall will serve as a proof-of-principle for this novel spectroscopic Casimir-Polder measurement technique, and characterization of surface adsorbate and electric field effects will benefit strontium atom-chip devices under development.

This work describes the strontium apparatus we have developed for future precision CP measurements. Chapter 2 provides more detail about the CP effect and the advantages strontium offers as a precision surface-potential probe. The strontium lattice measurement procedure and calculated CP shifts are presented, and experimental systematics are evaluated. The experiment requires sample preparation via multiple stages of laser cooling and trapping; Chapter 3 covers the background physics of laser cooling and discusses the theory of the cold-atom traps involved.

Any cold-atom experiment involves a substantial initial investment in apparatus development, particularly with respected to laser systems and the vacuum chamber. The Sr project in required four distinct home-built laser systems, three with external amplification stages and two with resonant-cavity second-harmonic-generation. These systems, and the base external-cavity diode-laser (ECDL) design developed as the master (and subsequently adopted by many external atomic physics groups), are covered in Chapter 4. Chapter 5 describes the Sr vacuum system, including the Sr oven and collimated atomic beam, a permanent-magnet Zeeman slower, and two MOT trapping regions.

We have succeeded in achieving a blue 461 nm MOT and transferring cold atoms between the top and the bottom blue MOT regions, as well as 689 nm red MOT optical molasses. Chapter 6 describes the computer control and the experimental sequences for blue MOT loading, characterization, and transfer and the loading procedure for the second-stage red MOT. The optical lattice laser system, described in Chapter 4, is complete; the next steps are outlined for the future strontium CP experiment. Although the experiment presents many challenges, the demonstration of a new purely spectroscopic technique for CP-interaction measurements in the intermediate distance regime will be of great value to practical and theoretical progress in this field. Precise measurements of Casimir and CP interactions will be critical to future technological developments of nanoscale devices and miniaturized atomic traps, as well as further tests of QED predictions.

CHAPTER II

STRONTIUM AND THE CASIMIR-POLDER INTERACTION

2.1. Background and Motivation

The advent of laser cooling and trapping of atoms opened the door to a new era of control and manipulation of quantum systems, as well as the observation of predicted but previously unobserved quantum effects. From early experiments observing “quantum jumps” of single ions [19] and the long-sought achievement of Bose-Einstein condensation [20, 21] to the exquisite state-preparation, entanglement, and individual qubit read-out capabilities demonstrated today by groups pursuing quantum computation and quantum simulation applications, cold atoms and ions have allowed exploration of quantum regimes inaccessible with other systems.

Every atom of a given isotope is identical: while this may seem like an obvious statement, it is key to the possibilities cold atoms offer in the field of precision measurement. This is perhaps best exemplified by the measurement of time itself: the power of using an atomic transition “ticking” at the same rate for every atom of that element anywhere on Earth was recognized from the early days of atomic physics, and the SI second was officially defined to be equal to the 9,192,631,770 cycles of the cesium-133 ground-state hyperfine transition in the 1960’s, long before laser cooling. Reaching a fractional frequency instability of 8×10^{-15}, the precision of the early cesium atom-beam clocks far exceeded any preceeding timekeeping device, yet limitations imposed by interatomic collisions, Doppler shifts, and finite observation times left room for improvement [22]. The use of laser-cooled atoms significantly reduces many systematics, and subsequent cold-atom atomic-fountain Cs clocks have reached instabilities of $\sim 4 \times 10^{-16}$ [23]. Frequency standards based on narrow dipole-forbidden optical transitions in continuously probed cold samples, offering long interrogation times and higher quality factors resulting from much faster cycling frequencies (100's of THz as opposed to cesium's GHz rf-transition), have reached even higher levels of precision and accuracy: the current leader is the strontium optical lattice frequency standard, with a fractional instability of 2.2×10^{-16} which averages down to 2×10^{-18} within about 15 minutes [10].[1]

Of course, elimination of systematic effects is critical for optical frequency standards reaching such absurd levels of precision and stability. The intrinsic frequency of one atom may be the same as any other of the same element, but the measured frequency will depend upon shifts imparted by the atom's environment. Such perturbations must be eliminated (e.g., first-order light shifts for optical-lattice-trapped atoms, as described in Sec. 2.2) or well-characterized and subtracted (e.g., blackbody radiation light shifts, through measurement of the background temperature). The flip side of this coin is to exploit the sensitivity of such accurate and well-characterized systems to measure extremely tiny interactions. Many modern communication and navigation systems, especially the Global Positioning System (GPS), rely upon the accuracy of cesium or rubidium radiofrequency atomic clocks and will see further enhancements with the future use of optical clocks, but fundamental physics precision measurement goals were another driving force behind the development of current state-of-the-art optical frequency standards.

Among the tiny or as-yet-unobserved effects measured or constrained by atomic clocks, one area of active research is the possibility of position- or time-

---

[1] Ytterbium optical lattice clocks reach similar levels of stability [24], and despite the lower signal-to-noise ratio offered by trapped ion systems the previous frontrunners Hg^+ and Al^+ remain close behind [25].

variation of fundamental constants [26–28]. Although non-constant “constants” would appear to violate Einstein’s equivalence principle, they are required by some unification theories [29]. Potential time-variation of the fine-structure constant $\alpha = 1/4\pi\epsilon_0(e^2/\hbar c) \approx \frac{1}{137}$, which governs the strength of electromagnetic interactions, is particularly intriguing in light of astronomical evidence indicating the value may in fact have been smaller in the distant past [30], but comparisons of optical frequency standards [31–33] have ultimately constrained the current rate of change to $\dot{\alpha}/\alpha < 10^{-17}$/yr [25]. Naturally, clocks are ideal for other tests of general and special relativity: the gravitational redshift resulting from an elevation change of just 33 cm was detected by comparing the frequency of two Al^+ clocks [34], and there are several proposals for space-based clocks to probe relativistic effects [35]. Compact strontium and ytterbium optical lattice clocks are under development for installation at the International Space Station (ISS) in 2023 for the Space Optical Clocks (SOC) project [36] (a follow-up to the 2018 Atomic Clock Ensemble in Space (ACES) project, consisting of Cs fountain and hydrogen maser frequency standards [37]). Comparisons of ISS and terrestrial atomic clocks will test Lorentz invariance and search for fine-structure-constant variations; other potential applications for space-based clocks include geophysics (precision mapping of the Earth’s gravitational potential) and astronomy (very-long-baseline interferometry).

The field of precision Casimir-Polder (CP) measurements is another area which would benefit from the exquisite sensitivity offered by atomic-clock-like systems. The CP effect, the interaction between two atoms or an atom and a surface generated by the modification of the vacuum electromagnetic field modes, becomes minuscule at large distances but can be the dominant force at distances on the order of 1 μm. Between neutral molecules, the effect is more familiar in the near-field as

London/van-der-Waals(vDW) or dispersion forces, which can be derived from the interaction of correlated fluctuating dipole moments. In fact, London's 1930 fourth-order perturbation-theory calculation of the effect [38] was "considered a major accomplishment of the new quantum mechanics" [39]: invocation of "zero-point energy" arising from the uncertainty principle was critical to explain the temperature-independent component of the dipole interaction energy, which would not be predicted by classical mechanics. London/vdW interactions are ubiquitous in chemistry and are important for the understanding of everything from the boiling points of the noble gases to the mechanism by which geckos walk up walls [40].

Despite the success of London's work, investigations of the interactions between neutral molecules separated by a distance z in colloidal suspensions later showed deviation from the expected z^{-6} scaling behavior at large separations [41]. Casimir and Polder demonstrated that the observed z^{-7} scaling is explained by including the influence of retardation effects: the finite electromagnetic field propagation time reduces the correlation of the two dipoles such that the potential energy falls off faster in the far field [1]. Similarly, the interaction potential between an atom and a perfectly conducting planar surface scales as z^{-3} in the near field ($z \ll \lambda_0$, where λ_0 is the dominant transition wavelength), which can be derived semi-classically from the interaction between a fluctuating dipole and its instantaneous image [42], but in the far field, retardation effects lead to decorrelation of the dipole and image, and the interaction scales as z^{-4} for $z \gg \lambda_0$.

While London had focused on fluctuating dipole moments, the quantized electromagnetic field was necessarily central to Casimir and Polder's approach. The two viewpoints are in a sense equivalent, since coupling to the background vacuum field generates dipole fluctuations (just as spontaneous emission can be viewed as stimulated emission resulting from coupling to the vacuum field [43]). The elegance of Casimir and Polder's approach, however, allows derivation of the interaction over all distances from near- to far-field. The calculation can be simplified further by assigning each electromagnetic-field mode the zero-point energy of a quantum harmonic oscillator and summing over field-mode interactions [44], as outlined in Sec. 2.3.

A further extension by Casimir considering the interaction of two perfectly conducting planar surfaces led to another surprising result: the two (uncharged) plates feel an attractive force, even in a perfect vacuum and at zero temperature [3]. Naturally, if an atom is attracted to a surface, the force must also come into play between two surfaces composed of atoms, but Casimir demonstrated that the force can be derived without reference to the microscopic surface components. Again, the quantized vacuum-field approach quickly explains the phenomenon: between the plates, the field modes are limited by the boundary conditions such that the only allowed wavevectors are half-integer multiples of the distance z between the plates, while outside the plates an infinite continuous spectrum of field-mode frequencies is permitted. The energy density both between the two plates and outside is infinite, since both arise from divergent sums over an infinity of vacuum field modes, but subtraction of the energy density in the absence of the plates (when the distance between them goes to infinity) leads to a finite solution, and the derivative of the resulting energy gives a force[2] $\propto z^{-4}$. Alternatively, the total radiation pressure exerted by the field modes between the two plates is less than that exerted on the outside surfaces, resulting in the attractive force [39].

---

[2] Like the CP force, for real metals there is a power scaling crossover such that the force is $\propto z^{-3}$ in the near field, when z is much less than the plasma wavelength of the metal.

The Casimir effect is intriguing as a macroscopic manifestation of quantum vacuum effects, but Casimir himself perhaps downplayed the result, concluding his analysis with the comment, "Although the effect is small, an experimental confirmation seems not unfeasable and might be of a certain interest" [3]. A quantitative "experimental confirmation" would wait nearly fifty years, but today Casimir and Casimir-Polder interactions[3] generate considerable theoretical and experimental interest. Lifshitz, Dzyaloshiinsky, and Pitaevski extended the analysis to account for finite surface conductivity and temperature effects [45, 46], but quantization of the electromagnetic field in dielectric media and broadband modeling of a material's optical response remain theoretical challenges. Calculation of Casimir and CP effects in non-trivial geometries or when accounting for real surface effects like structure, surface roughness, or birefringence presents additional analytic and numerical challenges.

A full understanding of the properties of Casimir and Casimir-Polder interactions is increasingly critical in today's era of miniaturized devices and atom traps. Micro- and nano-electromechanical systems (MEMS and NEMS) encounter Casimir forces primarily as a nuisance, playing an important role in the irreversible "stiction" that renders devices inoperable when membranes or lever arms are sucked into nearby surfaces [47–49], altering nano-oscillator behavior [50, 51], and potentially limiting the ultimate density of device features [52]. However, considering the strength of the force at small separations, many groups are intrigued by the possibilities of exploiting

---

[3] Within the field, the terminology "Casimir" is generally reserved for interactions between macroscopic objects and "Casimir-Polder" for interactions involving a microscopic particle (molecule-molecule or molecule-surface interactions). Casimir-Polder effects are assumed here to encompass London / van-der-Waals interactions, although some prefer to distinguish between the two and reference different distance regimes as the van-der-Waals (near-field), Casimir-Polder (far-field retarded regime), and Lifshitz or thermal regime (very far-field, when temperature effects must be included).

the properties of the force in system design [52–54]. The potential for repulsive Casimir forces has received considerable attention but appears realistic (and has been demonstrated [55]) only in the regime in which the permittivity of the material between the two surfaces is intermediate between the surface permittivities [46]. Geometric repulsion is ruled out for symmetric objects in vacuum [56],[4] and metamaterial engineering to generate repulsion between highly magnetic and highly dielectric materials is tantalizing but challenging due to the broadband nature of the Casimir effect [59, 60]. Reduction of the force via thin film or surface structure engineering remains a topic of great experimental and theoretical interest [61–63].

The miniaturization of atomic traps is another technological arena where Casimir-Polder effects come into play. The "atom-chip" architecture makes use of the same microfabrication techniques used for MEMS and NEMS to create surface structures with embedded current conductors which magnetically trap neutral atoms within tens of microns of the surface [64, 65]. The atom-chip is a critical component in the quest for scalable quantum information processing with neutral-atom qubits [66], but the steep trap potentials and overall miniaturization are also advantageous for portable atomic clocks [67] and atom interferometers [68]. Atom interferometers have demonstrated extreme sensitivity as inertial sensors [69], and miniaturized precision sensors [70, 71] are another driving force between the development of atom-chip and chip-scale devices. However, any time atoms are brought close to surfaces the effects of the CP interaction must be considered. The loss rate from magnetic traps increases dramatically for distances less than $\sim 5\,\mu$m, in part a result of spin-flips due to thermal noise [72] but a full explanation of the lifetime reduction (particularly near dielectric surfaces) must include the reduced effective trap potential resulting from the CP

---

[4] Repulsion has been shown to be possible, however, for an oblong particle near a hole in a plate [57], but the particle is not stably levitated [58].

attraction [73]. Quantum information applications must also consider level shifts and decoherence effects near surfaces [74–77], and the CP interaction resulting from novel microstructure geometries needs further exploration; calculations and experiments in limited regimes so far reveal interesting effects [78–81]. Analogously to MEMS and NEMS, although CP effects might normally be considered an obstacle to further miniaturization, novel microtrap designs may incorporate the CP interaction into the atom trap potential [82–84].

Casimir and Casimir-Polder interactions affect many other fundamental physics experiments. Cavity quantum electrodynamics (CQED) experiments pursue strong-coupling of atoms to cavity modes by decreasing the cavity-mode volume and bringing atoms closer to the cavity surfaces [85], but in this regime atomic trajectories and energy levels are significantly altered by the CP interaction [86–88]. Proposed short-range modifications to the gravitational force [89] are constrained in the sub-millimeter regime by Casimir experiments [4, 90]; Casimir-Polder atom-surface experiment proposals also hope to explore non-Newtonian gravitation [91, 92]. However, any search for new physics must distinguish between new effects and supposedly well-understood forces; some short-range gravitation experiments attempt to shield [93] or subtract [94] Casimir effects, but such procedures rely upon their own assumptions about the nature of the interaction.

Although some Casimir experiments have reached a measurement *precision* of $< 1\%$, some question whether it is reasonable to claim an equivalent *accuracy* or agreement with theory, given both experimental systematics and the fact that theoretical calculations can vary by 5% or more depending particularly upon the surface model used [54, 95, 96]. For the most part, CP experiments have yet to reach the level of precision where such distinctions become important, but the same numeric and theoretic challenges affect both fields. Technological developments and the search for new physics at the sub-millimeter regime motivate the need for better understanding of these interactions; probes of unexplored geometries and distance scales are important, and novel experiments reproducing previously measured results in new ways will also be critical to solidify our confidence in the numeric methods and material models behind theory calculations.

Adapting a strontium optical lattice clock experiment to CP measurements promises a new method to directly probe Casimir potentials spectroscopically with potentially high precision [15]. This method will be adaptable to a variety of surfaces, and shows promise for measurements through much of the as-yet little-explored intermediate regime where the length scaling crosses over from near- to far-field. The following sections will cover the properties of strontium that have made it a prime candidate for optical frequency standards and precision measurements (Sec. 2.2), outline the mathematical framework needed to understand the Casimir-Polder interaction (Sec. 2.3), and detail the proposed measurement scheme, with an emphasis on comparison of the systematics affecting this procedure vs. previous experimental work (Sec. 2.4.2).

2.2. Properties of Strontium

An element must meet a few key requirements to be easily laser-cooled and trapped: it must be possible to obtain a sufficient vapor pressure; it must offer a strong "cycling" transition with a high photon scattering rate (and if this transition is not closed, it must be easily "repumped" with the addition of as few extra lasers as possible); and the required laser systems must be at accessible wavelengths. Early cold-atom experiments were dominated by the alkali atoms, particularly sodium and rubidium. With a single valence electron, these elements have a hydrogen-like basic atomic-energy-level structure. While sodium initially dominated the field due to a strong cycling transition at 589 nm, easily accessed with dye lasers, rubidium has since become the workhorse of atomic physics, with simple Rb MOT's built even for undergraduate teaching lab experiments [97]. Rubidium is an attractive element due to a high vapor pressure at room temperature (allowing direct magneto-optical trapping without the need for an oven and pre-cooling [98, 99]) and due to the fact that the primary cycling transition is at 780 nm, a convenient diode-laser wavelength (in fact, near enough to the wavelength used in commercial CD-ROM drives that diodes have been particularly cheap and easy to obtain).

The alkaline earths, on the other hand, have two valence electrons; as a result, the energy-level structure is split into states in which the two electron spins are either anti-aligned (total spin $S = 0$) or aligned ($S = 1$). These "singlet" and "triplet" states are generally plotted on energy-level diagrams with a horizontal offset because single-photon transitions between the two manifolds ought to be "forbidden": the electric dipole operator cannot drive a magnetic spin-flip. However, in heavier atoms spin-orbit interactions can be significant, such that the states we derive using the $L-S$ coupling scheme and label in spectroscopic notation as ${}^{2S+1}\mathrm{L}_J$ (where L = S, P, D... for angular momentum $L = 0$, 1, 2..., and total angular momentum $J = |L-S|...|L+S|$) are not actually pure. In atoms with non-zero nuclear momentum I, hyperfine interactions can further mix the states. As a result, the so-called "intercombination" transitions between the singlet and triplet manifolds sometimes have non-zero electric-dipole matrix elements and can be accessed optically, but weak coupling leads to extremely narrow linewidths compared to dipole-allowed transitions [100, 101].

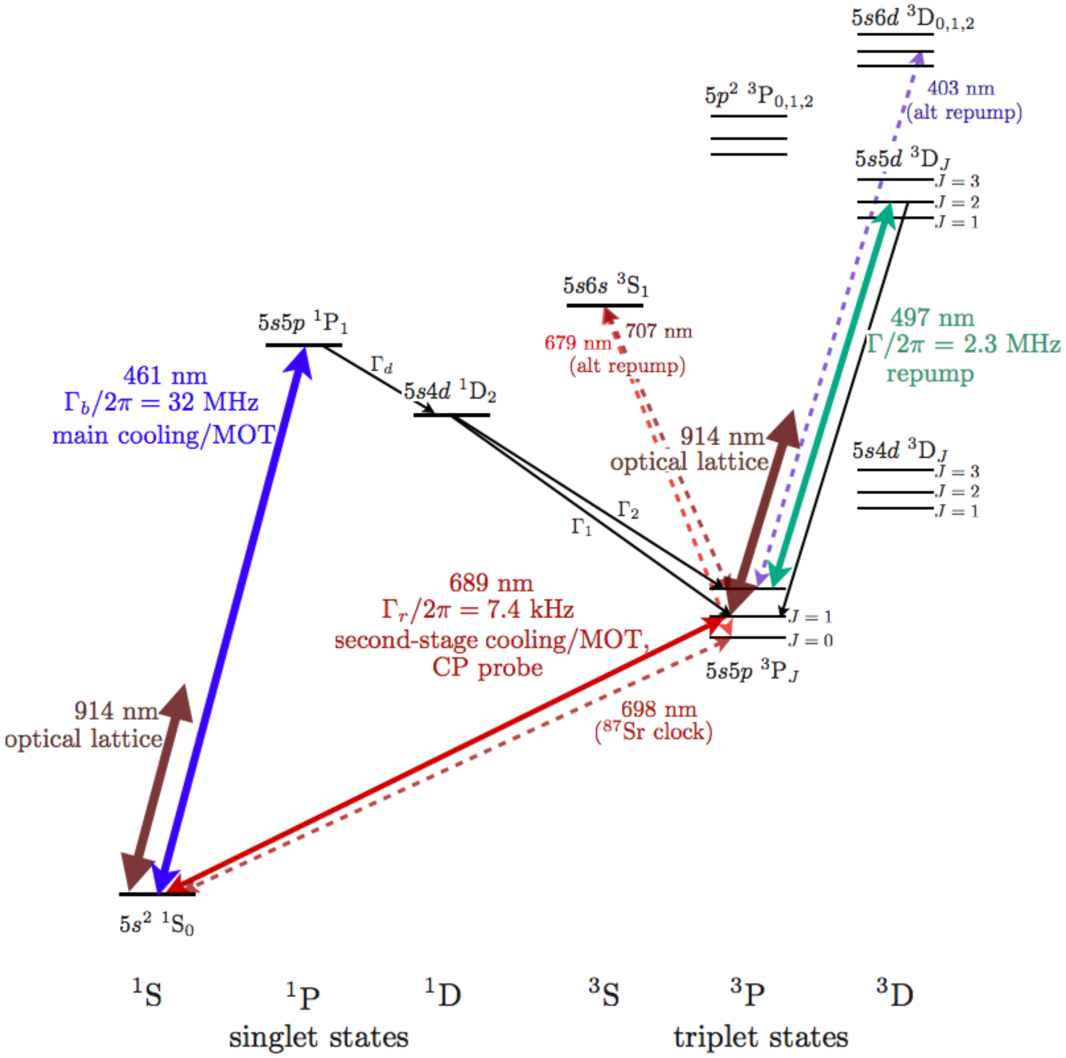

FIGURE 2.1. Strontium energy-level diagram for the low-lying states (not to scale), with electric-dipole transitions relevant to this experiment in bold and some additional transitions of interest marked with dashed lines. The optical lattice laser at 914 nm is far-detuned from any resonance but imparts an equal ac Stark shift on the ground and excited states of the CP-probe transition $^1S_0 - {}^3P_1$.

The level structure for ^{88}Sr is shown in Fig. 2.1; other alkaline earths (and related two-valence-electron atoms like Yb and Hg) show similar structures. Strontium offers a strong cycling transition between the singlet states $^1\mathrm{S}_0 - {}^1\mathrm{P}_1$ with a linewidth of 32 MHz, corresponding to a maximum scattering rate of 100 million photons/s, ideal for laser cooling. This transition is not fully closed; a small percentage of atoms (1 in 50,000) can decay from the $^1\mathrm{P}_1$ to the $^1\mathrm{D}_2$ state. Angular momentum selection rules prevent decay from this state ($L = 2$) back to the ground state ($L = 0$), so atoms in the $^1\mathrm{D}_2$ state decay into the $^3\mathrm{P}_2$ or $^3\mathrm{P}_1$ states. The $^3\mathrm{P}_1$ state has a small but nonzero coupling to $^1\mathrm{S}_0$, so these atoms eventually decay back to the ground state, but in even isotopes the $^3\mathrm{P}_2$ state is metastable: atoms which fall into this state are effectively lost from the laser-cooling process. As a result, for larger MOT populations and lifetimes a "repump" laser is required. Several repump transitions are in use or have been proposed (see Sec. 6.2.1); we use a weak 497 nm beam to cycle atoms out of the $^3\mathrm{P}_2$ state up to the $^3\mathrm{D}_2$ state, from which they will eventually find their way to $^3\mathrm{P}_1$ and then $^1\mathrm{S}_0$ to continue interacting with the trap light.

It is worth noting that the wavelengths for the main cooling beam at 461 nm and the repump beam at 497 nm are somewhat inconvenient: diode lasers at 461 nm have only just become available, and most strontium groups have historically relied upon second-harmonic-generation (SHG) to create the blue light. Since typical strontium experiments use $\sim$ 80 mW or more for laser-cooling and trapping on the $^1\mathrm{S}_0 - {}^1\mathrm{P}_1$ transition, this requires a relatively high-power 922 nm source and high-efficiency resonant-cavity frequency doubling to achieve the needed 461 nm power. (We also use resonant-cavity SHG for the 497 nm repump, but the power requirements are considerably more relaxed.) This blue laser-cooling transition, in combination with the fact that all repump schemes also require dedicated lasers at a very different wavelength from the main cooling laser, significantly complicates the laser system requirements for alkaline-earth cold-atom experiments compared to most alkalis.[5]

Another factor affecting the simplicity of a cold-atom experiment is the ease of generating sufficient atoms in the gaseous state, but the alkaline earths generally have much lower vapor pressures than the alkalis (for a given temperature typically two orders of magnitude lower than the corresponding alkali). While a heated vapor-cell MOT has been used for strontium [102, 103], most Sr experiments start with a hot oven and an additional slowing stage before the MOT capture region (see Sec. 5.2). Vacuum chamber designs must also guard against the reactivity of strontium, so the usual copper vacuum gaskets are replaced with nickel, and glass viewports with sapphire, in locations where Sr exposure is likely; these considerations also affect reference vapor-cell designs (see Sec. 4.5.1).

The popularity of the alkaline earths for cold-atom experiments was delayed relative to the alkalis in part due to these experimental challenges, but they are becoming increasingly attractive systems today, largely as a result of the narrow intercombination transitions. The decay rate of strontium's ${}^3\mathrm{P}_1$ level is $\Gamma/2\pi = 7.4$ kHz; in the even isotopes the ${}^3\mathrm{P}_{0,2}$ states are essentially metastable (they cannot decay via emission of a single photon), but hyperfine mixing allows weak optical-dipole coupling of ${}^1\mathrm{S}_0 - {}^3\mathrm{P}_0$ in the odd isotope ${}^{87}\mathrm{Sr}$. This transition has an incredible theoretical linewidth of $\sim$1 mHz [8, 9] and has been spectroscopically resolved to better than 1 Hz [104, 105]. Since the minimum temperature reached by Doppler laser cooling is proportional to the linewidth of the transition (see Sec. 3.2.1.1), the 689 nm ${}^1\mathrm{S}_0 - {}^3\mathrm{P}_1$ transition can be used for a secondary stage

---

[5] Although the alkalis also require a repump laser, it is used to depopulate optically dark hyperfine sublevels of the ground state of the cycling transition and as such is only a small frequency shift from the main trap laser.

of laser cooling to reach temperatures $\sim 1\ \mu$K, much lower than the ~ 1 mK offered by cooling on the 32 MHz ^{1}S$_0$ $-$ ^{1}P$_1$ transition. Cooling on the ultranarrow 698 nm ^{1}S$_0$ $-$ ^{3}P$_0$ transition would be impractical given the low scattering rate (even for the broader ^{1}S$_0$ $-$ ^{3}P$_1$ transition, novel cooling dynamics arise from the fact that the Doppler shift from a single photon recoil is on the order of the natural linewidth, and the scattering force is barely greater than the gravitational force [100] — see Sec. 6.5). However, the ^{1}S$_0$ $-$ ^{3}P$_0$ transition, with an achievable quality factor $Q = \nu/\Delta\nu \sim 10^{15}$ or greater, is an obvious candidate for an optical frequency standard or precision measurement probe.

The existence of ultranarrow transitions, however, is useless without a means of confining the atoms in a way that leaves the transition frequency unperturbed. The use of an optical lattice tuned to the "magic wavelength" is a critical component for the success of neutral-atom clocks. In a magneto-optical trap, magnetic-field shifts and the constant scattering of near-resonant photons prevent precision frequency metrology, but far-detuned dipole traps act as conservative potentials with minimal photon scattering. In the red-detuned optical lattice dipole trap, atoms are trapped at the antinodes of the standing-wave pattern from two counter-propagating Gaussian beams (see Sec. 3.3); when cooled to the ground vibrational state of the effectively harmonic wells, the atoms are tightly confined to a distance scale less than the clock transition wavelength, such that first-order Doppler shifts are also suppressed (the Lamb-Dicke effect [106]). However, any light field imparts an ac Stark shift to every atomic energy level, as described in Sec. 3.3. For most transitions, the ground and excited states experience opposite energy-level shifts so ac Stark cancellation is impossible. The intensity dependence of these shifts leads to spatially inhomogenous frequency shifts in the intensity gradients required for optical dipole trapping.

The realization that alkaline earth intercombination transitions possess certain wavelengths for which the first-order ground and excited level shifts are exactly the same opened the door to neutral atom confinement without intensity-dependent frequency shifts [107]. The existence of these "magic" wavelengths is again a result of the 2-electron energy level structure and the largely uncoupled singlet/triplet manifolds. Because the intercombination lines are so weak, the ac Stark shift imparted by the dipole trap laser on the ground $^1\mathrm{S}_0$ state is a result primarily of coupling to other higher-lying singlet $S = 0$ states (the dipole matrix elements of these dipole-allowed transitions are far greater than those of the intercombination transitions in the sum in Eq. 3.55). Likewise, the shift for a $^3\mathrm{P}_J$ level is determined primarily by coupling to higher-lying triplet $S = 1$ states, rather than the coupling to the lower-energy $^1\mathrm{S}_0$. As a result, the $^1\mathrm{S}_0$ and $^3\mathrm{P}_J$ states shift in the *same* direction, and because the frequency tuning of the shift is different for the two levels, there are certain special wavelengths where both shift exactly the same amount for a given light intensity.

Before the development of the magic-wavelength optical lattice clock, trapped ion optical frequency standards far exceeded the stability of neutral atom candidates, but the achievable signal-to-noise ratio of these systems may limit their ultimate performance. Optical lattice clocks, on the other hand, offer a huge improvement on the number of interrogated oscillators, and magic-wavelength trapping creates systems with extremely low sensitivity to trap or background perturbations. Many national labs have now developed optical lattice clocks, particularly using strontium [11–14], and ultra-stable transportable strontium lattice clocks are also under development [36, 108].

The alkaline earths have other properties which are appealing for various experiments. The $^1\mathrm{S}_0$ and $^3\mathrm{P}_0$ states lack electronic angular momentum and therefore offer high magnetic-field insensitivity. On the other hand, this renders the ground state unsuitable for magnetic trapping, but without a repump laser the leak from the $^1\mathrm{S}_0 - {}^1\mathrm{P}_1$ transition allows accumulation of atoms in the metastable $^3\mathrm{P}_2$ state, which can be magnetically trapped [109]. In general, the magnetic-field tuning for the cooling transitions $^1\mathrm{S}_0 - {}^1\mathrm{P}_1$ and $^1\mathrm{S}_0 - {}^3\mathrm{P}_1$ is also much smaller than that for the alkalis cooling transitions, requiring large field gradients for magneto-optical trapping, but these have proven achievable.

Many of the alkaline-earths have several isotopes; for strontium, the four that occur naturally are listed in Table 2.1. An abundance of isotopes allows experimenters to choose the atom with the most appealing properties for a given measurement. For example, strontium's even isotopes are bosonic; the pairing of nucleons leaves these isotopes with zero nuclear spin, a simplified level structure lacking hyperfine sublevels, and a completely angular-momentum-free ground state and hence a high insensitivity to magnetic field shifts. However, the ultra-narrow, doubly-forbidden $^1\mathrm{S}_0 - {}^3\mathrm{P}_0$ transition can only be accessed in $^{87}\mathrm{Sr}$, so this is the isotope used for strontium optical-lattice clocks. For our initial experiments, we are working with $^{88}\mathrm{Sr}$, but the fact that the isotope shifts are greater than the trap-transition natural linewidth means that we can easily tune our MOT lasers to trap other isotopes.

The variation in isotopic properties proved useful for experimenters pursuing a strontium Bose-Einstein condensate (BEC). The first attempts focused on the most abundant isotope, $^{88}\mathrm{Sr}$ [110], with high phase-space densities reached by second stage $^3\mathrm{P}_1$ cooling in a magic-wavelength dipole trap. (Dipole traps are conservative, and combining Doppler cooling with dipole trapping would generally not be efficient

isotope	abundance	blue MOT: 461nm $5s^2\ {}^1S_0 - 5s5p\ {}^1\mathrm{P}_1$	red MOT: 689nm $5s^2\ {}^1S_0\ -\ 5s5p\ {}^3\mathrm{P}_1$	repump: 497nm $5s5p\ {}^3\mathrm{P}_2 - 5s5d\ {}^3\mathrm{D}_2$
^{84}Sr	0.56%	-270.8	-351.49	-91.8
^{86}Sr	9.86%	-124.8	-163.81	-47.5
^{87}Sr	7.00%	-46.5	-62.15	–
^{88}Sr	82.58%	0	0	0

TABLE 2.1. Strontium isotopes: natural abundances and isotope shifts (in MHz, relative to ^{88}Sr) for transitions relevant to this experiment. (Note that the hyperfine structure for ^{87}Sr can be larger than the isotope shift; see Ref. [100].)

due to the differential ac Stark shifts of the ground and excited states; the ability to cool within the dipole trap was another important consequence of the magic-wavelength traps [107]). However, evaporative cooling was still necessary (normally this step is carried out in a magnetic trap, but lowering of an optical dipole trap potential also works); the ground-state scattering properties of the least-abundant isotope ^{84}Sr proved much more favorable to the formation of a BEC, and this became the first condensed isotope [111, 112]. (A BEC of ^{86}Sr was eventually reached by using additional forced evaporative cooling tricks in extremely low-density dipole traps [113], but the ^{88}Sr BEC was only achieved by sympathetic cooling with ^{87}Sr [114]. Fermi degeneracy of ^{87}Sr has also been demonstrated [115].) Subsequently, the first BEC generated from laser cooling alone was demonstrated in Sr, taking advantage of a nearly-degenerate ^{3}P$_1$-cooled reservoir to continuously feed into a dark-spot central condensation zone [116]; this development holds promise for the future creation of a nearly continuous-wave "atom-laser" [117].

Strontium has become an important laser-cooled atom in many other experiments. The sensitivity of optical-lattice clock-like systems have been used for precision measurements of fundamental constants [118] and gravitation [119]. Cold strontium molecules also hold promise for precision measurements [120, 121] and have been created from laser-cooled strontium atoms in two labs [122, 123]. Strontium atom-cavity QED experiments have reached the strong-coupling regime [124] and explore the prospects for inherently ultranarrow lasers based on coherent excitation of the intercombination transitions in cavity-coupled lattice-trapped strontium [125, 126]. Quantum simulation of solid-state systems using optical-lattice-trapped neutral atoms has become an exciting field [127–129], and several schemes for quantum computation using lattice-trapped strontium have also been proposed [130–133].

There have been a few proposals for Casimir-Polder measurements using lattice-trapped strontium. One envisions controlled atomic interferometry between adjacent lattice-well sites to measure the the surface-interaction-generated potential difference between adjacent wells as a phase shift [16]. This proposal has been adopted into the FORCA-G ("*Force de Casimir et Gravitation à courte distance*") experiment under development at SYRTE [134], but Rb was chosen as the probe atom for the ease of generating the needed phase-coherent splitting pulses (simpler with hyperfine transition Raman pulses as opposed to optical transitions) [16]. Other proposals hope to directly measure the change in transport behavior of atoms in vertical optical lattices brought close to surfaces. The Bloch oscillation frequency [135] should shift as a result of the added CP-potential [92, 136], but the sensitivity of initial experiments directly monitoring atomic momentum oscillations was an order of magnitude too small to detect Casimir-Polder effects [137]. Other proposals aim for better resolution by measuring the shift in the driven tunnelling resonance frequency [138–140], but to the best of our knowledge this technique has not yet been demonstrated as a CP probe. Our measurement plan, as described in Sec. 2.4.2, is more akin to that proposed by Derevianko *et al.* [15], which offers finer atom-surface distance resolution and the precision of direct optical measurement of the narrow-linewidth intercombination transition shifts resulting from the atom-surface interactions. This proposal best takes advantage of strontium's unique properties and the precise characterization and control demonstrated by strontium optical lattice clocks.

2.3. The Casimir-Polder Effect

The Casimir-Polder interaction is often described as an inherently quantum-mechanical effect, but the asymptotic behavior in the near- and far-field regimes can be calculated semi-classically from the interaction energy of a fluctuating atomic dipole and its surface image (with the inclusion of time-retardation in the far-field). However, this approach cannot accurately describe the form of the interaction in the cross-over intermediate regime. This section outlines one approach to a full QED treatment: with the interaction arising from atomic coupling to the non-zero ground-state energy of the surface-modified vacuum electromagnetic field modes, the Casimir potential is expressed as a sum over atomic dipole matrix elements and vacuum field modes. The infinite mode-sum is renormalized by subtracting off the equivalent expression for an atom far from the surface, and the sum over dipole-matrix-elements is dominated by the low-lying energy levels.

Several texts offer good introductions to QED [39, 141]; in this chapter I follow the formalism of Ref. [43]. Sec. 2.3.1 introduces the concepts and notation needed for quantized electromagnetic-field-mode expressions, Sec. 2.3.2 introduces atom-field dipole coupling in the absence of the rotating-wave-approximation, and Sec. 2.3.3 outlines the analytic calculation for the ground-state shift of a spherical atom near an infinite conducting plane. This is necessarily a simplified model; Sec. 2.3.4 briefly considers the additional complications introduced by excited level shifts, polarization effects, the inclusion of finite temperature effects, and the challenges raised by the inclusion of real-surface effects like finite conductivity, surface roughness, and non-planar geometry.

2.3.1. The Quantized Electromagnetic Field

Canonical quantization identifies the electromagnetic field modes as mathematically equivalent to the normal modes of a quantum harmonic oscillator, such that each mode of frequency $\omega_{\mathbf{k}} = c|\mathbf{k}|$ and polarization ζ ($\zeta = 1$ or 2, corresponding to two vectors normal to the propagation direction $\hat{\mathbf{k}}$) is populated/depopulated by the creation and annihilation operators $a^{\dagger}_{\mathbf{k},\zeta}(t)$ and $a_{\mathbf{k},\zeta}(t)$. Linearity allows separation of the time-dependence as $a_{\mathbf{k},\zeta}(t) = a_{\mathbf{k},\zeta}e^{-i\omega_{\mathbf{k}}t}$, and the bosonic commutation relation

$$\left[a_{\mathbf{k},\zeta}, a^{\dagger}_{\mathbf{k}',\zeta'}\right] = \delta^{3}_{\mathbf{k},\mathbf{k}'}\delta_{\zeta,\zeta'}, \tag{2.1}$$

applies. The total electromagnetic field Hamiltonian is simply the analogous harmonic oscillator Hamiltonian, summed over all field modes:

$$H_F = \sum_{\mathbf{k},\zeta} \hbar\omega_{\mathbf{k}} \left(a^{\dagger}_{\mathbf{k},\zeta} a_{\mathbf{k},\zeta} + \frac{1}{2} \right). \tag{2.2}$$

As expected, the Hamiltonian is equivalent to the total field energy (identifying $a^{\dagger}a$ — which has eigenvalues $0, 1, 2, ...$ — as the number of "photons" in a given mode), and, like the harmonic oscillator, the ground-state energy of every mode is offset from zero by $\hbar\omega_{\mathbf{k}}/2$: the "zero-point energy." All quantum fields possess a non-zero ground state; fluctuation is fundamental to quantum mechanics, a consequence of the Heisenberg uncertainty principle.

The electromagnetic field mode polarization $\hat{\epsilon}_{\mathbf{k},\zeta}$ and all spatial dependence are wholly contained in the spatial mode functions $\mathbf{f}_{\mathbf{k},\zeta}(\mathbf{r})$, so that the field operators become

$$\begin{aligned}
\mathbf{A}(\mathbf{r},t) &= i\sqrt{\frac{\hbar}{2\omega\epsilon_0}}\mathbf{f}_{\mathbf{k},\zeta}(\mathbf{r})a_{\mathbf{k},\zeta}(t) + h.c. \\
\mathbf{E}(\mathbf{r},t) &= -\sqrt{\frac{\hbar\omega}{2\epsilon_0}}\mathbf{f}_{\mathbf{k},\zeta}(\mathbf{r})a_{\mathbf{k},\zeta}(t) + h.c. \\
\mathbf{B}(\mathbf{r},t) &= i\sqrt{\frac{\hbar}{2\omega\epsilon_0}}[\nabla \times \mathbf{f}_{\mathbf{k},\zeta}(\mathbf{r})]a_{\mathbf{k},\zeta}(t) + h.c.,
\end{aligned} \tag{2.3}$$

where *h.c.* stands for Hermitian conjugate. The spatial mode functions do not contribute to the uncoupled field Hamiltonian, but they will come into play when considering the Hamiltonian for the interaction between the atom and the field. They are completely independent (as required by the superposition principle) and normalized (so that the field energy is dependent only on the photon occupation number $a^\dagger a$ as seen in Eq. 2.2), satisfying the orthonormality condition

$$\int_V d^3r\, \mathbf{f}_{\mathbf{k},\zeta}(\mathbf{r}) \cdot \mathbf{f}^*_{\mathbf{k},\zeta}(\mathbf{r}) = \delta^3_{\mathbf{k},\mathbf{k}'}\delta_{\zeta,\zeta'}, \tag{2.4}$$

where the integration volume V depends on the geometry of the situation under consideration, so must be taken to infinity (i.e., convert any sum over $\mathbf{k}$ to an integral; see below) for free-space.

The spatial mode functions observe the boundary conditions of the geometry such that, for example, the modes for a conducting box of wall lengths L_x, L_y, and L_z must obey the condition that the parallel component of the electric field vanishes at the planes,

$$\begin{aligned}\mathbf{f}_{\mathbf{k},\zeta}(\mathbf{r}) = \sqrt{\frac{8}{\pi}}\big[&\hat{x}(\hat{\epsilon}_{\mathbf{k},\zeta}\cdot\hat{x})\cos(k_x x)\sin(k_y y)\sin(k_z z)\\ &+\hat{y}(\hat{\epsilon}_{\mathbf{k},\zeta}\cdot\hat{y})\sin(k_x x)\cos(k_y y)\sin(k_z z)\\ &+\hat{z}(\hat{\epsilon}_{\mathbf{k},\zeta}\cdot\hat{z})\sin(k_x x)\sin(k_y y)\cos(k_z z)\big],\end{aligned} \tag{2.5}$$

with the wave-vectors k_x, k_y, and k_z quantized by nonnegative integers n_i:

$$k_x = \frac{\pi n_x}{L_x}, \qquad k_y = \frac{\pi n_y}{L_y}, \qquad k_z = \frac{\pi n_z}{L_z}. \tag{2.6}$$

The field modes in free space, on the other hand, are as expected simply

$$\mathbf{f}_{\mathbf{k},\zeta}(\mathbf{r}) = \frac{1}{\sqrt{V}}\hat{\epsilon}_{\mathbf{k},\zeta}e^{i\mathbf{k}\cdot\mathbf{r}}, \tag{2.7}$$

with $V \to \infty$ in any final calculation.

To understand this step, note that the free-space field modes can be derived from imagining a series of boxes of volume $V = L^3$ which impose periodic rather than conducting boundary conditions [the field at $\mathbf{r} = (x, y, z)$ is the same as the field at $\mathbf{r} = (x + L, y + L, z + L)$] [39]. The quantization condition is then $\mathbf{k}_i = 2\pi n_i/V^{1/3}$, and as $V \to \infty$ the spacing between the wave-vectors $\Delta k_i = 2\pi/V^{1/3}$ becomes infinitesimally small (in free space, any frequency is allowed). The sum over frequencies in the interaction Hamiltonian becomes an integral,

$$\sum_k \to \frac{V}{(2\pi)^3}\int_{-\infty}^{\infty} d^3\mathbf{k}, \tag{2.8}$$

and the factor $1/V$ in $|\mathbf{f}_{\mathbf{k},\zeta}(\mathbf{r})|^2$ will cancel out of the calculation. Another identity that will be useful in calculations involving mode-functions is

$$\sum_{\zeta}(\hat{\epsilon}_{\mathbf{k},\zeta}\cdot\hat{r}_{\alpha})(\hat{\epsilon}_{\mathbf{k},\zeta}\cdot\hat{r}_{\beta}) = \delta_{\alpha\beta} - \frac{k_{\alpha}k_{\beta}}{k^2}, \tag{2.9}$$

which exploits the fact that polarization components are related to wave-vector components to eliminate the sum over polarization.

Finally, the mode functions that will be of interest for the simplest Casimir-Polder calculation, that of an atom near an infinite conducting plane located at $z = 0$, must again obey the boundary condition that the parallel electric field component vanishes at the interface,

$$\mathbf{f}_{\mathbf{k},\zeta}(\mathbf{r}) = \sqrt{\frac{2}{V}}(\hat{\epsilon}_{\mathbf{k},\zeta,||}\sin k_z z - i\hat{\epsilon}_{\mathbf{k},\zeta,z}\cos k_z z)e^{i\mathbf{k}_{||}\cdot\mathbf{r}}, \tag{2.10}$$

where again the factor of $V^{1/2}$ will cancel as $V \to \infty$ in any calculation. The subscript $||$ is used to identify the component parallel to the surface, as opposed to the component in the z-direction perpendicular to the surface; note that these "half-space" mode-functions contain both the input wave and the reflected component, and while the wave-vector and polarization components in the parallel direction are unchanged upon reflection, k_z and $\hat{\epsilon}_{\mathbf{k},\zeta,z}$ receive a sign change.

2.3.2. Atom-Field Interaction

The Hamiltonian for a free atom (taking the energy E_0 of the ground state to be zero) is simply:

$$H_A = \sum_j \hbar\omega_{j0}|e_j\rangle\langle e_j|, \tag{2.11}$$

where the frequency for a transition from the ground $|g\rangle$ to the excited state $|e_j\rangle$ is $\omega_j = (E_j - E_0)/\hbar$. In the long-wavelength or dipole approximation (assuming variations of the optical field on the scale of the atom size can be neglected), the interaction between a two-level atom and the electromagnetic field is

$$H_{AF} = -\mathbf{d} \cdot \mathbf{E}, \tag{2.12}$$

where the dipole operator can be considered classically as the atom's induced dipole moment in response to the field, or quantum mechanically,

$$\mathbf{d} = \langle g|\mathbf{d}|e\rangle \big(|g\rangle \langle e| + |e\rangle \langle g| \big) = \mathbf{d}_{\mathrm{ge}}(\sigma + \sigma^\dagger). \tag{2.13}$$

The dipole matrix element $\mathbf{d}_{\mathrm{ge}} := \langle g|\, \mathbf{d}\, |e\rangle$ with dipole moment $\mathbf{d} = e\,\mathbf{r}$ (where e is the electron charge) is a measure of the strength of the coupling between the transition and the electromagnetic field; $\sigma^\dagger := |e\rangle \langle g|$ and $\sigma := |g\rangle \langle e|$ are the atomic raising and lowering operators. Extending to multiple transitions, and incorporating the expression for the quantized electromagnetic field (Eq. 2.3), the full atom-field Hamiltonian becomes

$$H_{AF} = -\sum_j \sum_{\mathbf{k},\zeta} \sqrt{\frac{\hbar\omega_{\mathbf{k}}}{2\epsilon_0}}\, \langle g|\, \mathbf{d}\, |e_j\rangle\, (\sigma_j + \sigma_j^\dagger) \cdot \big[\mathbf{f}_{\mathbf{k},\zeta}(\mathbf{r}) a_{\mathbf{k},\zeta} + \mathbf{f}^*_{\mathbf{k},\zeta}(\mathbf{r}) a^\dagger_{\mathbf{k},\zeta}\big]. \tag{2.14}$$

We can write the coupled atomic and field states as $|e_j, \alpha_{\mathbf{k},\zeta}\rangle$, where $\alpha_{\mathbf{k},\zeta}$ denotes the occupation number for the mode with wavevector $\mathbf{k}$ and polarization ζ. Note that the atom-field interaction will contain four terms which could act upon such a state:

$$\text{a) } \sigma_j a_{\mathbf{k},\zeta} \qquad \text{b) } \sigma_j a^\dagger_{\mathbf{k},\zeta} \qquad \text{c) } \sigma_j^\dagger a_{\mathbf{k},\zeta} \qquad \text{d) } \sigma_j^\dagger a^\dagger_{\mathbf{k},\zeta}. \tag{2.15}$$

The second and third terms correspond to familiar, energy-conserving atom-field events: emission of a photon from an atom in an excited state (adding a photon to a field mode and dropping the atom down from an excited state), and absorption of a photon plus promotion of the atom to an excited state. These interactions correspond to (in a two-level atom with resonance ω_0 interacting with a single resonant field mode, for simplicity)

$$\begin{aligned} &\text{b)} \qquad \sigma\, a^\dagger\,|e,\alpha\rangle = |g,\alpha+1\rangle \qquad \Delta E_A &= -\hbar\omega_0, \quad \Delta E_F = +\hbar\omega_0 \\ &\text{c)} \qquad \sigma^\dagger a\,|g,\alpha\rangle = |e,\alpha-1\rangle \qquad \Delta E_A &= +\hbar\omega_0, \quad \Delta E_F = -\hbar\omega_0. \end{aligned} \tag{2.16}$$

Here, ΔE_A is the energy gained or lost by the atom, which is compensated by equal energy transfer ΔE_F to or from the light field for these terms. However, terms a) and d) appear to violate energy conservation:

$$\begin{aligned} &\text{a)} \qquad \sigma\, a\,|e,\alpha\rangle = |g,\alpha-1\rangle \qquad \Delta E_A = -\hbar\omega_0, \quad \Delta E_F = -\hbar\omega_0 \\ &\text{d)} \qquad \sigma^\dagger a^\dagger\,|g,\alpha\rangle = |e,\alpha+1\rangle \qquad \Delta E_A = +\hbar\omega_0, \quad \Delta E_F = +\hbar\omega_0. \end{aligned} \tag{2.17}$$

Term a) leads to a net change in energy of $-2\hbar\omega_0$, while term d) leads to $+2\hbar\omega_0$! In most treatments of atom-field interactions, these terms are ignored with the justification of the rotating-wave approximation (RWA): recall that $a(t) = ae^{-i\omega t}$ while $a^\dagger(t) = ae^{+i\omega t}$, corresponding to the two components of the complex electromagnetic field. Similarly, the dipole operator will have positive and negatively-rotating components, such that $\sigma(t) \propto e^{-i\omega t}$ and $\sigma^\dagger(t) \propto e^{+i\omega t}$. Terms a) and d) will then oscillate rapidly in time as $e^{\pm(\omega_{0j}+\omega_{\mathbf{k}})t}$, while terms b) and c) evolve more slowly as $e^{\pm(\omega_{0j}-\omega_{\mathbf{k}})t}$. For a two-level atom interacting with a near-resonant field, applying the RWA and throwing out the rapidly changing components is justified; for the more general situation of a multi-level atom interacting with a potentially broad range of frequencies, it is not.

Preservation of non-energy-conserving terms may still seem disturbing, but one way to justify their presence is the time-energy uncertainty principle: if the time the system spends in the apparently energy-violating configuration is small, the actual spread in energy may be large enough to encompass the energy-conserving configuration; this is one justification sometimes used for "virtual states" or "virtual particles," and indeed processes a) and d) *taken together* can be considered as the emission and re-absorption of a virtual photon, as depicted in Fig. 2.2. This point is another important consideration regarding these terms: a) and d) always occur *together*, and in that context there is no energy violation at all.

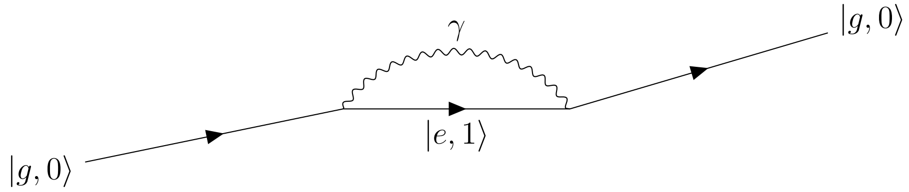

FIGURE 2.2. Feynman diagram of atom-field events usually neglected in the rotating-wave approximation.

It is the contribution from these non-energy-conserving terms that can be shown to be responsible for the quantum vacuum effects of both the Lamb shift and the Casimir-Polder interaction. For an atom in the ground state interacting with the vacuum field, in which the population of all modes is zero such that $|e_j, \alpha_{\mathbf{k},\zeta}\rangle = |g, 0_{\mathbf{k},\zeta}\rangle$ for all $\mathbf{k}, \zeta$, the interaction arises as a second-order perturbation to the ground-state energy: with the full Hamiltonian given as

$$H = H_{\mathrm{A}} + H_{\mathrm{F}} + H_{\mathrm{AF}} = H_0 + H_{\mathrm{AF}}, \tag{2.18}$$

the shift to the ground state is

$$V_{\rm CP} = \langle g, 0_{\mathbf{k},\zeta}| H_0 |g, 0_{\mathbf{k},\zeta}\rangle + \langle g, 0_{\mathbf{k},\zeta}| H_{\rm AF} |g, 0_{\mathbf{k},\zeta}\rangle + \sum_j \sum_{\mathbf{k},\zeta} \frac{|\langle g, 0_{\mathbf{k},\zeta}| H_{\rm AF} |e_j, 1_{\mathbf{k},\zeta}\rangle|^2}{E_{g,0_{\mathbf{k},\zeta}} - E_{e_j,1_{\mathbf{k},\zeta}}}. \tag{2.19}$$

It is easy to show that the first two terms go to zero, leaving

$$V_{\rm CP} = -\sum_j \sum_{\mathbf{k},\zeta} \frac{|\langle g, 0_{\mathbf{k},\zeta}| H_{\rm AF} |e_j, 1_{\mathbf{k},\zeta}\rangle|^2}{\hbar(\omega_{j0} + \omega_{\mathbf{k}})}, \tag{2.20}$$

where we have used $E_{g,0} = \hbar\omega_{\mathbf{k}}/2$ and $E_{e_j,1} = \hbar\omega_0 + 3\hbar\omega_{\mathbf{k}}/2$ in the denominator for the coupled atom-field energies. Inserting the full $H_{\rm AF}$ (Eq. 2.14), the terms normally responsible for energy-conserving absorption and emission go to zero, leaving the terms usually discarded in the RWA:

$$\begin{aligned} V_{\rm CP} = &-\sum_j \sum_{\mathbf{k},\zeta} \frac{\omega_{\mathbf{k}}}{2\epsilon_0} \frac{|\langle g| \mathbf{d} |e_j\rangle \cdot \mathbf{f}_{\mathbf{k},\zeta}(\mathbf{r})|^2}{(\omega_{j0} + \omega_{\mathbf{k}})} \\ &\times \langle g, 0_{\mathbf{k},\zeta}| \sigma_j a_{\mathbf{k},\zeta} |e_j, 1_{\mathbf{k},\zeta}\rangle \langle e_j, 1_{\mathbf{k},\zeta}| \sigma_j^\dagger a^\dagger |g, 0_{\mathbf{k},\zeta}\rangle . \end{aligned} \tag{2.21}$$

As the last two terms evaluate to 1, the end result for the ground-state Casimir-Polder shift looks deceptively simple:

$$\boxed{V_{\rm CP} = -\sum_j \sum_{\mathbf{k},\zeta} \frac{\omega_{\mathbf{k}}}{2\epsilon_0} \frac{|\langle g| \mathbf{d} |e_j\rangle \cdot \mathbf{f}_{\mathbf{k},\zeta}(\mathbf{r})|^2}{(\omega_{j0} + \omega_{\mathbf{k}})}.} \tag{2.22}$$

However, everything depends upon the mode-functions $\mathbf{f}_{\mathbf{k},\zeta}$; even for simple geometries, evaluating $V_{\rm CP}$ is non-trivial, as outlined in the next section, and for more complicated boundary conditions the mode functions themselves can become quite complex.

Without further elaboration, it is worth noting here that the simplest case would appear to be the interaction of the atom with the free-space vacuum field modes of Eq. 2.7, and in fact this is the interaction that leads to the Lamb shift. However, even in this case the result is nontrivial: the sum over frequencies in equation 2.22 (which becomes an integral — see Eq. 2.8) is divergent! Renormalization requires both subtraction of the electron's own self-energy and imposing a maximum **k**-value above which contributions to the integral are considered negligible [43, 142]; a full discussion of these issues is outside the scope of this work, as renormalization of the Casimir-Polder potential is much simpler, but the development of these techniques was an important advance in theoretical QED. It is also interesting to consider that both the intrinsic Lamb shift and the mechanical force arising from the CP interaction can be attributed to the same quantum-vacuum-fluctuation phenomenon depicted in Fig. 2.2: in the case of the Lamb shift, the emission and absorption of virtual photons imposes a sort of ac Stark shift upon the bare atomic energy levels, and in the CP case, the interaction of these virtual photons with a nearby surface (or another atom) effects a change in that ac Stark shift as a function of atom-surface (atom-atom) separation, resulting in a mechanical force [39].

2.3.3. Atom-Plane Casimir-Polder Potential

To evaluate the ground-state Casimir-Polder shift for an atom near a perfectly conducting plane at $z = 0$, we must evaluate the dot product of $\mathbf{d} = e\mathbf{r}$ in Eq. 2.22 with the half-space mode-functions (Eq. 2.10), which have transverse electric and transverse magnetic polarization components $\hat{\epsilon}_{\mathbf{k},\zeta,||}$ and $\hat{\epsilon}_{\mathbf{k},\zeta,z}$:

$$V_{\text{CP}} = -\sum_j \sum_{\mathbf{k},\zeta} \frac{\omega_{\mathbf{k}}}{\epsilon_0 V} \frac{|\langle g|\,\mathbf{d}\cdot\hat{\epsilon}_{\mathbf{k},\zeta,||}\,|e_j\rangle|^2 \sin^2 k_z z + |\langle g|\,\mathbf{d}\cdot\hat{\epsilon}_{\mathbf{k},\zeta,z}\,|e_j\rangle|^2 \cos^2 k_z z}{(\omega_{j0} + \omega_{\mathbf{k}})}. \quad (2.23)$$

The parallel and perpendicular vector components can be rewritten using $\mathbf{v}_{||} = [(\mathbf{v}\cdot\hat{x})\hat{x} + (\mathbf{v}\cdot\hat{y})\hat{y}]$ and $\mathbf{v}_z = (\mathbf{v}\cdot\hat{z})\hat{z}$, such that the numerator becomes

$$[(\hat{\epsilon}_{\mathbf{k},\zeta}\cdot\hat{x})^2 + (\hat{\epsilon}_{\mathbf{k},\zeta}\cdot\hat{y})^2]d_{j,||}^2 \sin^2 k_z z + (\hat{\epsilon}_{\mathbf{k},\zeta}\cdot\hat{z})^2 d_{j,z}^2 \cos^2 k_z z, \tag{2.24}$$

with the components of the atomic dipole operator defined as

$$\begin{aligned} d_{j,||}^2 &= d_{j,x}^2 + d_{j,y}^2 = |\langle g|\,\hat{x}\cdot\mathbf{d}\,|e_j\rangle|^2 + |\langle g|\,\hat{y}\cdot\mathbf{d}\,|e_j\rangle|^2, \\ d_{j,z}^2 &= |\langle g|\,\hat{z}\cdot\mathbf{d}\,|e_j\rangle|^2. \end{aligned} \tag{2.25}$$

The problem simplifies a bit at this point if we assume a *spherically symmetric* ground-state atom, a valid assumption for S-orbital (angular momentum $L = 0$) ground states like strontium's. In this case, $\hat{x}\cdot\mathbf{d} = \hat{y}\cdot\mathbf{d} = \hat{z}\cdot\mathbf{d}$, so that $d_{j,||} = 2d_{j,z}$. We can also eliminate the sum over polarizations in Eq. 2.23 using Eq. 2.9 and simplify to find

$$V_{CP} = -\frac{1}{\epsilon_0 V}\sum_j\sum_{\mathbf{k}}\frac{\omega_{\mathbf{k}}}{(\omega_{j0}+\omega_{\mathbf{k}})}\left[d_{j,z}^2\left(1 - \frac{k_z^2}{k^2}\cos(2k_z z)\right)\right]. \tag{2.26}$$

Note that the mode sum is currently divergent, but this is a good time to renormalize: for the Casimir-Polder effect, this amounts to simply taking the difference between this sum for finite z vs the sum for $z \to \infty$, which amounts to subtracting off the energy when the atom is infinitely far from the plane. The z-independent term then cancels, leaving

$$V_{CP} = \frac{1}{\epsilon_0 V}\sum_j\sum_{\mathbf{k}}\frac{\omega_{\mathbf{k}}}{(\omega_{j0}+\omega_{\mathbf{k}})}d_{j,z}^2\left(\frac{k_z^2}{k^2}\cos(2k_z z)\right). \tag{2.27}$$

We also need to take $V \to \infty$; as described in Sec. 2.3.1, this is equivalent to taking the sum over $\mathbf{k}$ to an integral, but in this case we would need to modify expression 2.8

slightly: for the half-space field modes, the periodic quantization conditions on k_x and k_y are the same as for the free-space field modes (so the separation $\Delta k_x = \Delta k_y = 2\pi/V^{1/3}$), but the conducting-plane limits the k_z components to $z > 0$ and the quantization condition is $\Delta k_z = \pi/V^{1/3}$, so the conversion becomes

$$\sum_k \to \frac{V}{\pi(2\pi)^2}\int_{-\infty}^{\infty} dk_x \int_{-\infty}^{\infty} dk_y \int_0^{\infty} dk_z. \tag{2.28}$$

However, the k_z integral in this case is symmetric about 0, and easier to evaluate over all k_z, so the end result is equivalent to using expression 2.8:

$$V_{CP} = \frac{1}{16\pi^3\epsilon_0}\sum_j d_{j,z}^2 \int_{-\infty}^{\infty} dk_x \int_{-\infty}^{\infty} dk_y \int_{-\infty}^{\infty} dk_z \frac{k_z^2}{(k_{j0}+k)k}\cos(2k_z z). \tag{2.29}$$

The evaluation of the integral in spherical coordinates is described in Ref. [43]; the result is

$$\boxed{V_{\text{CP}} = -\frac{1}{(4\pi\epsilon_0)4\pi}\sum_j d_{j,z}^2 \left(\partial_z^2 \frac{1}{z} f(2k_{j0}z)\right),} \tag{2.30}$$

where $f(x)$ is one of the auxiliary functions to the sine and cosine integrals,

$$\begin{aligned} f(x) &= \quad \text{Ci}(x)\sin x + \left[\frac{\pi}{2} - \text{Si}(x)\right]\cos x \\ g(x) &= -\text{Ci}(x)\cos x + \left[\frac{\pi}{2} - \text{Si}(x)\right]\sin x = -\partial_x f(x), \end{aligned} \tag{2.31}$$

with

$$\begin{aligned} \text{Si}(x) = \int_0^{\infty} \frac{\sin t}{t+x}dt \quad &= \int_0^{x} \frac{\sin t}{t}dt \quad &&= \quad \frac{\pi}{2} - f(x)\cos x - g(x)\sin(x) \\ \text{Ci}(x) = \int_0^{\infty} \frac{\cos t}{t+x}dt \quad &= \int_x^{\infty} \frac{\cos t}{t}dt \quad &&= \quad f(x)\sin(x) - g(x)\cos(x). \end{aligned} \tag{2.32}$$

These functions determine the length scaling of the Casimir-Polder potential, in particular the surprising crossover behavior from near-field to far-field scaling: $f(0) = \pi/2$, while for large $z' = 2k_{j0}z$, $f(z') \sim 1/z'$. The asymptotic behavior of the plane CP potential is then

$$\boxed{\begin{aligned} &\text{near field :} \qquad V_{\mathrm{CP}} \approx -\frac{1}{4\pi\epsilon_0}\left(\frac{1}{4z^3}\right)\sum_j d_{j,z}^2 && (2.33)\\ &\text{far field :} \qquad V_{\mathrm{CP}} \approx -\frac{1}{4\pi\epsilon_0}\left(\frac{3}{4\pi z^4}\right)\sum_j \frac{d_{j,z}^2}{k_{j0}}. && (2.34)\end{aligned}}$$

Figure 2.3 shows the full QED expression for the atom-plane CP potential (including contributions from the lowest 20 energy levels - see Refs. [143] and [144] for tabulated Sr transition data) versus the asymptotic approximations for ^{88}Sr.

The near-field Casimir-Polder result is exactly equivalent to the result for a fluctuating dipole interacting with its mirror-image dipole field, obtained semi-classically without reference to vacuum field modes [42, 145]. The interaction energy for two dipoles $\mathbf{p}_1$ and $\mathbf{p}_2$ separated by a distance $\mathbf{r}_{1,2}$ is

$$V_{\mathrm{dip}} = \frac{\mathbf{p}_1 \cdot \mathbf{p}_2 - 3(\hat{r}_{1,2} \cdot \mathbf{p}_1)(\hat{r}_{1,2} \cdot \mathbf{p}_2)}{4\pi\epsilon_0 |\mathbf{r}_{1,2}|^3}. \tag{2.35}$$

Rather than the full interaction energy, we want the energy to bring only one dipole in from ∞, which is one-half of V_{dip}. For our geometry of a "mirror" at $z = 0$, $\mathbf{r}_{1,2} = 2z\,\hat{z}$, and the dot products with the separation unit vector become the perpendicular components of the dipole moments. In the near-field, the dipoles are perfectly correlated in magnitude and direction, but as mirror images the parallel components are opposite: $|\mathbf{p}_1| = |\mathbf{p}_2| = |\mathbf{p}|$, but $\mathbf{p}_1 \cdot \mathbf{p}_2 = -p_{||}^2 + p_z^2$. Finally, assuming symmetry such that the magnitude of oscillations in the two parallel directions are

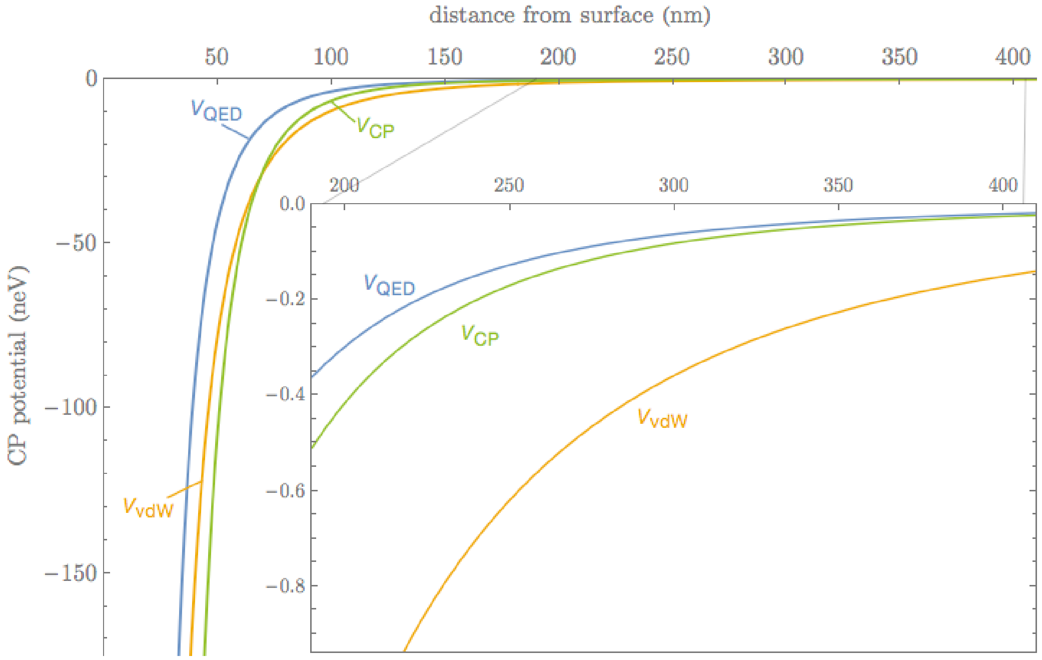

FIGURE 2.3. Casimir-Polder atom-plane potential for ^{88}Sr (ground state). V_{QED} (blue curve) is the full expression from Eq. 2.30, while V_{vdW} (orange) and V_{CP} (green) are the near- and far-field approximations, respectively, of Eq. 2.33. The inset is the potential over the atom-plane separation from 200–400 nm, a region of particular interest for the proposed experiment.

equal to that in the perpendicular z-direction, we have

$$V_{\text{dip}} = -\frac{1}{4\pi\epsilon_0}\frac{p_z^2}{4z^3}, \tag{2.36}$$

which is exactly equivalent to Eq. 2.33 if we interpret the classical dipole moment p_z as equivalent to the sum of the quantum dipole moments over all transitions. This is the classic atom-plane van der Waals result.

In the far field, the CP interaction can still be considered to be the result of the atom interacting with the field from its own fluctuating image dipole, but the atomic and image dipoles are no longer correlated. Equation 3.49 is the *instantaneous* interaction energy; in the far-field, retardation effects must be taken into account. It may seem that the problem can still be treated classically as $V = -\frac{1}{2}(\mathbf{p}_{\text{atom}} \cdot \mathbf{E}_{\text{image}})$ and indeed it can if the full expression, complete with derivatives evaluated at the retarded time $t - 2z/c$, is used for the electric field $\mathbf{E}_{\text{image}}$ due to the image dipole. However, the correct final result is only obtained if the electric field is decomposed into its positive- and negative-frequency components and "normal ordering" for operator products is obeyed [145], for which there is no classical justification; one quantum interpretation is although the total uncoupled dipole and field operators commute, their induced components do not [96]. Furthermore, the very fact that a symmetric atom whose time-averaged dipole moment $\langle \mathbf{p} \rangle = 0$ has a nonzero $\langle \mathbf{p}^2 \rangle$, even at $T = 0$ and in the absence of a light field or any other energy source, implies the quantum origin of the effect. Atomic coupling to the nonzero vacuum field explains the dipole flucuations, and the fact that the full quantum treatment leading to Eq. 2.30 reproduces both the near- and far-field behavior is further support for the quantum approach.

In the full QED expression for V_{CP} (Eq. 2.30), the change in length scaling from near-field $1/z^3$ (vdW regime) to far-field $1/z^4$ (CP regime) is governed by the behavior of the auxiliary sine integral function $f(2k_{j,0}z)$. Therefore, we might expect the argument of this function to determine the cross-over distance. Indeed, $z = 1/2k_0 = \lambda_0/4\pi$, where λ_0 is the wavelength of the dominant transition, is often taken to be the approximate transition distance. A physical argument for the transition location can be based upon a correlation criterion for dipole / image-dipole interactions: when the retarded time delay $2z/c$ is greater than the dipole oscillation period for a given frequency $1/\omega_{0j}$ the dipoles are no longer correlated [146]. This argument leads to a cross-over location of $z \sim \lambda_{0j}$. As k_{j0} increases, $f(2k_{j0}z)$ decreases for all $z \neq 0$ (and the dipole matrix element is typically smaller): as a result, the lowest-frequency transition with a large dipole matrix element $d_{j,z}$ will dominate the sum in Eq. 2.30, and this will be the "dominant" λ_0 transition that determines the cross-over distance. However, this is obviously not an abrupt change, and in fact the full expression Eq. 2.30 is not well-characterized by either the near-field or far-field expressions throughout the intermediate regime [18, 96].

Finally, it is worth noting here that both the near- and far-field expressions for the ground-state shift due to a perfect planar conductor are often written in terms of the atomic polarizability $\alpha(\omega)$ in place of the sum over dipole matrix elements (in a form more similar to that originally calculated by Casimir and Polder [1]):

$$\text{near field}: \qquad V_{\text{CP}} = -\frac{1}{4\pi\epsilon_0}\left(\frac{\hbar}{4\pi z^3}\right)\int_0^\infty \alpha(i\xi)d\xi \tag{2.37}$$

$$\text{far field}: \qquad V_{\text{CP}} = -\frac{1}{4\pi\epsilon_0}\left(\frac{3\hbar c}{8\pi z^4}\right)\alpha_0. \tag{2.38}$$

In the near-field expression, $\alpha(\omega)$ is the dynamic polarizability of the ground state (Eq. 3.57), evaluated as a contour integral over imaginary frequencies $\omega \to i\xi$ (in this form, the perfect-conductor CP potential is written in a manner analogous to the expression for the potential near a dielectric surface, which will have additional terms under the integral related to the permittivity $\epsilon(\omega)$ which characterizes the material's linear electric polarizability); in the far-field expression, α_0 is the static polarizability.

The equivalence between Eq. 2.33 and Eq. 2.37 can be seen by the relation between the atomic polarizability and the dipole matrix element: the classical polarizability times the electric field gives the classical atomic dipole moment, and from the Lorentz model of the atom (as a damped harmonic oscillator consisting of an electron bound to a charged nucleus – see Ref. [43]), $\alpha(\omega)$ can be written as

$$\alpha(\omega) = \sum_j \frac{e^2}{m} \frac{f_{0j}}{(\omega_{j0}^2 - \omega^2 - i\gamma_j\omega)}, \tag{2.39}$$

where m and e are the mass and charge of the electron, γ_j is the damping rate for the excited state (which can be shown equivalent to the decay rate Γ_j), and f_{0j} is the absorption oscillator strength, which is related to the dipole matrix element by

$$d_{jz}^2 = \frac{e^2\hbar f_{0j}}{2m\omega_0}. \tag{2.40}$$

The static polarizability $\alpha_0 = \alpha(0)$ is then

$$\alpha_0 = \sum_j \frac{2d_{jz}^2}{\hbar\,\omega_{j0}}, \tag{2.41}$$

which when inserted into Eq. 2.37 (with $\omega_{j0} = k_{j0}/c$) reproduces the far-field form of Eq. 2.33; a similar expression for the imaginary-frequency polarizability (with $\omega \to i\xi$) can be shown to reproduce the near-field result. The results of a more complex calculation for alkaline earth dynamic polarizabilities can be found in Ref. [147].

2.3.4. Further Considerations

When evaluating the ground-state CP potential, we found that only the non-energy-conserving terms proportional to σa and $\sigma^\dagger a^\dagger$ in the atom-field Hamiltonian H_{AF} gave a non-zero contribution. For an arbitrary excited state $|e_n\rangle$, however, the equivalent expression to Eq. 2.20 becomes

$$V_{\text{CP}} = -\sum_{j\neq n}\sum_{\mathbf{k},\zeta} \frac{|\langle e_n, 0_{\mathbf{k},\zeta}|\, H_{\text{AF}}\, |e_j, 1_{\mathbf{k},\zeta}\rangle|^2}{\hbar(\omega_{jn} + \omega_{\mathbf{k}})}, \tag{2.42}$$

where $\omega_{jn} = (E_{j0} - E_{n0})/\hbar$. In this case, when the state $|e_j\rangle$ is lower in energy than $|e_n\rangle$, the contribution from the usual energy-conserving H_{AF} terms $\sigma a^\dagger$ and $\sigma^\dagger a$ that drive real absorption and emission events are not zero. In general, excited states will often have non-zero angular momentum, so we cannot make the spherical-atom assumption used throughout the derivation of the ground-state shift.

The result for the excited-state potential is [43]:

$$\begin{aligned} V_{\mathrm{CP}} = -\sum_j \frac{\mathrm{sgn}(\omega_{jn})}{(4\pi\epsilon_0)8\pi} \Big[\big(d_{j,||}^2/2 - d_{j,z}^2\big)\left(\frac{1}{z}\partial_z^2\right) + \big(d_{j,||}^2/2 + d_{j,z}^2\big)\left(\partial_z^2 \frac{1}{z}\right)\Big] \\ \times \big[f(2|k_{jn}|z) - \Theta(\omega_{nj})\pi\cos(2|k_{jn}|z)\big]. \end{aligned} \tag{2.43}$$

This function may appear to be much more complicated than the ground-state shift, but the form is the same as what would be found for a*non*-spherically-symmetric ground state other than the addition of the sign function $\mathrm{sgn}(\omega_{jn})$ and the Heaviside step function $\Theta(\omega_{nj})$, both of which come into play only when the state $|e_j\rangle$ is lower in energy than $|e_n\rangle$. In this case, $\mathrm{sgn}(\omega_{jn}) = -1$ and $\Theta(\omega_{nj}) = 1$; otherwise $\mathrm{sgn}(\omega_{jn}) = 1$ and $\Theta(\omega_{nj}) = 0$ and the form is identical to the ground-state shift. These terms can thus be understood to arise from the contribution of real absorption and emission events driven by $\sigma a^\dagger$ and $\sigma^\dagger a$; their effect can decrease the shift and adds an oscillatory component to the overall expression.

Another interesting result of Eq. 2.43 applies equally to ground and excited states lacking spherical symmetry, and that is the tensor nature of the shift. The term proportional to $d_{j,||}^2/2 - d_{j,z}^2$, which disappears upon the identification of $d_{j,||}^2 = 2d_{j,z}$ for the spherical atom, represents the anisotropic response of the atom to dipole excitation. In the near-field, dominated by the $1/z^3$ terms, the contribution to the total shift from each energy level $V_j \propto \mathrm{sgn}(\omega_{jn})(d_{j,||}^2/2 + d_{j,z})/z^3$, such that orientation perpendicular to the surface generates twice the shift of parallel orientation, in keeping with the expectation from a classical dipole's anisotropic electric field. In the far field, however, this orientation dependence surprisingly cancels out [5]; the shift becomes $V_j \propto \mathrm{sgn}(\omega_{jn})\mathbf{d}_j^2/z^4$ where $\mathbf{d}_j^2 = d_{j,||}^2 + d_{j,z}^2$ is the total dipole moment [148]. This is particularly surprising given the fact that classically we might expect the far-field behavior to be governed by the radiation pattern of an oscillating dipole antenna, which is maximum perpendicular to the dipole axis and zero on-axis; this classical picture would lead us to expect the shift to disappear for a dipole perpendicular to the surface. This deviation from classical behavior demonstrates again that the far-field CP interaction requires a quantum treatment.

Note that we have made several simplifying assumptions in the discussion of the CP potential so far. All of the above assumed an atom interacting with the quantum vacuum, with on average a photon occupation number per mode of $n_{\mathbf{k}} = 0$. More generally we should expect the photon occupation number to scale with temperature T according to boson statistics,

$$n_{\mathbf{k}} = \frac{1}{e^{\hbar\omega_{\mathbf{k}}/k_B T} - 1}, \tag{2.44}$$

an effect which might be expected to significantly alter the Casimir-Polder force at finite temperature. Indeed, the full temperature-dependent model worked out by Lifshitz *et al.* [45, 46] finds that nonzero temperature significantly increases the far-field CP shift, amounting to another length-scaling transition from the z^{-4} CP-regime to a very-far-field regime where the length scaling returns to z^{-3} [96]. However, temperature considerations should not be important for our proposed intermediate-range CP measurements: the number of photons in the field modes contributing most to the CP potential, those for which $\omega_k \sim c/d$, only becomes significant when

$T \geq \hbar c/k_B d$ [39], or equivalently $d \geq \hbar c/k_B T = 7.6$ μm at room temperature, far outside our proposed measurement range.

An approximation made throughout the discussion so far which will impact our proposed experiments regards the perfect conductivity and infinite-plane nature of the surface with which the atom interacts. These assumptions allowed the use of the half-space mode functions (Eq. 2.10), which simplified the sum over electromagnetic field modes in Eq. 2.22. In general, very few geometries offer such a relatively clean analytic solution; definition of the mode-functions themselves can be nontrivial, since any additional surface imposes new boundary conditions affecting all field modes, and clearly the CP potential does not obey the superposition principle [149, 150].

The perfect-conductivity assumption is a major simplification: all metals become transparent for very short wavelengths, and finite conductivity corrections on the order of 10-20% are needed for CP experiments with real metallic surfaces [4, 151]. The presence of absorption considerably complicates the problem of expressing the electric field in simple mode functions; several approaches to the calculation of Casimir forces have been developed to encompass dielectric media [4, 45, 46, 96]. One method appropriate for linear dispersive materials uses the Green tensor to characterize the material's electromagnetic response, with the renormalized CP shift resulting from the atom-field interaction expressed as a contour integral over imaginary (Wick-rotated) frequencies of the trace of the dot product of the atomic polarizability (tensor, in the case of a non-spherically-symmetric atom) and the scattering part of the Green tensor [43, 152]; Eq. 2.37 is the perfect-conductor limit of such an expression for a spherically-symmetric atom interacting with an infinite plane. Modeling the material permittivity $\epsilon(\omega)$ over all frequencies remains a challenge in any formalism; on the other hand, Casimir and Casimir-Polder measurements can act as probes of material characteristics.

These theoretical challenges have led to the development of a variety of different analytic approximation methods and numeric approaches to calculate real-world Casimir and CP interactions for arbitrary geometries. The pairwise summation (PWS) approach tackles non-trivial geometries by summing over the microscopic atom-atom CP contributions of the surface particles [42, 153], but requires known solutions from very similar geometries for a special normalization procedure [154]; otherwise, this approach can lead to errors as Casimir and CP effects are non-additive and bulk material properties cannot necessarily be inferred from the atomic constituents [59, 155]. The proximity-force approximation (PFA) assumes the CP effect for near-planar geometries can be found from the average planar equivalent [156], but is valid only in regimes of limited curvature, and when applied piecewise to approximate other geometries as planar elements it can also run into the erroneous additivity assumption [155, 157, 158]. Taking advantage of established classical electromagnetic computational techniques, direct numeric evaluation of Green's functions (generally defined for imaginary frequencies, where integrands are better-behaved) is an accurate but inefficient approach [152, 159–161]. The dominant numeric method takes a path-integral boundary-element approach, using the interaction of effective material surface-current elements to handle arbitrary geometries and dielectric materials, but again this becomes computationally expensive for small-scale structures [162].

The quest for computationally efficient numeric approaches has motivated members of our group to explore the possibility of extending a scalar "worldline" method [158, 163, 164] to electromagnetic fields [165]. This approach, involving

Monte Carlo integration of the action over a swarm of closed-loop paths, potentially offers a method that would scale well with increasing geometric complexity, but currently the formalism is limited to geometries in which the transverse-electric (TE) and transverse-magnetic (TM) field polarizations decouple. Given the theoretical challenges, there is a need for experiments capable of measuring the CP interaction over a broad range of length scales, particularly the effects resulting from real surfaces with finite conductivity and surface roughness or structure, to test current predictions.

2.4. Probing Casimir-Polder Potentials

2.4.1. Prior Casimir and Casimir-Polder Experiments

Despite the challenges involved in calculation of Casimir and CP potentials, theory has often far out-paced experimental measurement of these effects. Van der Waals experiments have a long history, but the retarded atom-plane interaction predicted by Casimir and Polder in 1948 [3] was only measured in 1993 [6], and the classic plane-plane interaction [1] was not conclusively demonstrated until 1997 (and even then a sphere-plane configuration approximated the plane-plane equivalent). Far field thermal corrections, calculated by Lifshitz in 1956 [45], waited until 2007 [166] for atom-plane detection and 2011 [167] for the macroscopic analog. Precision Casimir and CP experiments must not only detect extremely tiny effects and calibrate sub-micron-scale separations, but also discriminate against competing electrostatic surface forces and rely upon careful surface characterization for comparison with theory.

An early Casimir experiment [168] demonstrated qualitative agreement (with near-100% error) with the expected parallel-plate Casimir force, but the challenge of aligning two plates with zero relative tilt has led most experiments to use the sphere-plane geometry, where the only distance factor is that of closest approach.[6] Lamoreaux's landmark 1997 Casimir force detection [7] involved a spherical lens and an optical flat mounted to a precision torsion pendulum: the Casimir force is proportional to the restoring force required to keep the pendulum angle fixed as the lens surface is translated toward the flat, and the relative sphere-plane distance is measured by the change in the lens-flat capacitance. Mohideen and Roy demonstrated the use of conventional atomic force microscopy (AFM) to measure Casimir forces, with a metallic sphere mounted to the AFM cantilever tip and the reflection of light from the top of the tip monitoring the relative tip deflection as the sphere is brought near a flat surface [170]. This arrangement has proven a useful configuration in many later experiments, including those investigating surface-structure effects [171], thin-film reduction of the Casimir force [61], and the repulsive Casimir effect [55]. Microelectromechanical devices (MEMS) have also proven a useful platform for Casimir measurements, via measurements of the plate tilt of a micro-torsional balance [172] or the frequency shift of similar structures used as micro-torsional oscillators [50, 62], both capacitively measured, in response to the presence of a microsphere brought near one side. (The MEMS torsional oscillator, in particular, has provided some of the most sensitive Casimir measurements thus far [173].) Note that in all configurations, the absolute separation distance requires calibration, generally by the application of a known voltage and characterization of the electrostatic force over the measured distance regime. However, several systematic effects must be accounted for in this procedure (particularly residual electrostatic interactions between the two surfaces), as discussed in Ref. [96].

---

[6] The flat plate configuration was finally definitely measured in 2002 [169], but with relatively low precision compared to sphere-plane experiments.

Despite the experimental challenges, Casimir experiments have achieved impressive precision, often well below the 1% error level. Atom-surface CP experiments have yet to approach this sensitivity, with only the more recent experiments reaching a precision below 10%. Progress in CP measurements initially outpaced Casimir experimental results, with near-field atom-surface interactions measured via the deflection of hot atomic beams into the geometrical shadow of cylindrical surfaces [174–176]. The results showed qualitative agreement with the predicted van der Waals potential, but lacked the precision to detect the far-field crossover. The atomic beam transmission measurements of the Boshier/Hinds group at Yale brought greater precision: the intensity of hot Rydberg atomic beams passing through a fixed planar channel of width 5.4 μm decreased as a function of principal quantum number n, in reasonably close agreement with theory [177], but again only in the vdW regime. [7] The first experimental observation of the far-field retarded CP interaction arrived with the Hinds group's landmark 1993 experiment [6], which measured the transmission of ground-state Cs atoms passing through a gold wedge-shaped cavity. The effective cavity length was tuned from 0.7 to 8 μm by changing the wedge angle, and the resultant transmission curve clearly favored the full retarded QED expression over the $1/z^3$ vdW interaction. The experiment could not, however, resolve the near-field transition to the vdW regime.

Laser-cooled atoms with well-defined kinetic energies brought new precision and several breakthroughs to the field of CP measurement. The new classes of measurement techniques which arose included classical and quantum surface reflection measurements. The first measurement of the interaction between a ground state atom

---

[7] The use of Rydberg atoms increases the interaction strength since the electric dipole moment scales as n^4, but it also pushes the vdW/CP crossover to greater distances since dominant Rydberg wavelengths are in the microwave range.

and a dielectric wall was demonstrated by Aspect *et al.* in the mid-1990's [178, 179] using a classical "atom-mirror" reflection technique, in which the combination of the repulsive dipole potential of a blue-detuned evanescent beam combines with the attractive surface interaction to create a potential barrier for cold atoms impinging upon a surface. Classically, all atoms with a velocity below the threshold where the kinetic energy is equal to the barrier maximum are reflected; measurement of this threshold as a function of evanescent-wave intensity gives insight into the underlying surface potential. As an evanescent wave decays exponentially perpendicular to the surface over a length on the order of the optical wavelength, this approach is feasible primarily for characterization of the near-to-intermediate regime; the threshold measurement of Aspect *et al.* hinted at the need to include the retarded interaction but could not distinguish between theories at the 10% measurement accuracy level (limited by the required careful characterization of the evanescent-beam properties). In 2010, Slama *et al.* used the evanescent-wave-mirror technique to map the atom-surface interaction over a $\sim$75 nm distance window in the intermediate regime using $\sim$100 nK Rb atoms launched toward the surface with controllable velocities from an accelerated magnetic trap [18]. One of the few experiments to probe this intermediate distance regime, the data clearly favor the full QED potential over either the near-field $1/z^3$ or the far-field $1/z^4$ asymptotic forms, although a slight overall deviation from the theoretical QED curve remains unexplained [96].

The step-function threshold for classical reflection is smoothed out by quantum-mechanical considerations, showing a finite probability for reflection of above-barrier atomic velocities as well as transmission (tunnelling) of atoms with velocities slightly below the threshold. Unlike classical reflection, dependent only on the maximum barrier height, quantum reflection probabilities depend upon the entire potential curve, but the ability to observe quantum signatures in evanescent-wave atom-mirror experiments is limited by averaging over the transverse Gaussian evanescent-beam profile [180, 181]. However, unlike the classical situation, quantum reflection can result from purely *attractive* potentials, when the potential varies rapidly over a length scale comparable to the atom's de Broglie wavelength [182], and except for very light particles atom-surface reflection is dominated by the retarded $1/z^4$ far-field CP potential [183]. Shimizu demonstrated the first surface reflection from the attractive CP potential using a cold beam of metastable Ne atoms grazing silicon and glass plates such that the plate angle tuned the normal incident velocity, and observed reflections as high as 40% (the specular nature of the reflection ruled out reflection from extreme-near-field Coulomb repulsion, which would result in random scatter from the relatively rough surface) [184]; despite $> 20\%$ measurement uncertainty, the results showed reasonable agreement with theory [183]. The reflectivity is increased by added surface structure [185]; normal-incident reflection has been demonstrated using a BEC, and a microstructured pillared surface significantly increased the reflection probability [186, 187]. While these experiments primarily probe the far-field regime, reflections of low-mass particles (cold excited He atoms) have also explored the $1/z^3$ vdW potential [188, 189]. Despite relatively low demonstrated precisions, quantum-reflection experiments remain interesting as possible probes of the full QED potential.

Laser-cooled atoms were also used in one of the most impressive series of CP experiments, the first to detect the very-far-field crossover to the thermal or Lifshitz regime. The Cornell group monitored the center-of-mass oscillation frequency of a magnetically-trapped Rb BEC near a dielectric, with the change in frequency resulting from the CP perturbation to the harmonic potential detectable out to almost 12 μm atom-surface separations [190, 191]. These experiments allowed verification of a nonequilibrium temperature model of the Lifshitz-CP effect (with only the surface at an elevated temperature, heated by a laser from behind) [166, 192, 193]. However, measurements were limited to the far-field regime (distances greater than $\sim 6\ \mu$m) by the challenge of magnetic confinement at shorter distances (particularly problematic over metallic surfaces). Patch effects resulting from Rb surface contamination were also a serious systematic [17].

At the other end of the distance scale, thermal atomic beams have still played a role in CP measurements: the Cronin and Vigué groups have explored separation scales on the order of 10 nm via the measurement of atomic diffraction [194, 195] and phase shifts [196, 197] imparted on thermal sodium and lithium beams by nano-structured gratings. Using an interferometric approach, these measurements have reached agreement with theoretical van-der-Waals models to an experimental accuracy of a few percent [198, 199]. Other interferometric techniques have been proposed for CP measurements, including combining interferometry with evanescent-wave atom-mirrors [200, 201] and the lattice-trapped strontium proposals mentioned at the end of Sec. 2.2. BEC interferometers have demonstrated great sensitivity to precision measurement of other (e.g. gravitational) effects and may offer a new method of probing CP potentials [91, 202], but to the best of our knowledge this technique has not yet been applied as a CP sensor.

There have been a handful of direct spectroscopic measurements of CP energy-level shifts, but only in the near-field van der Waals regime, and primarily using excited atoms. One of the most precise early experiments, again from the Hinds group at Yale, probed excited Cs atoms passing through a planar cavity; the observed spectral shifts were consistent with van der Waals theory within 10% [203]. Similar experimental setups measured radiative shifts in Rydberg energy levels, but resonant photon-cavity coupling can complicate interpretation of results when using such excited atoms [204, 205]. Vapor cell spectroscopic experiments have also played a role: the spectral dependence of the coefficient of reflection at a vapor-dielectric interface can be used to probe atomic resonances ("selective reflection spectroscopy"), revealing shifts and line-shape changes in the reflected vs transmitted beams attributed to vdW interactions [206, 207]. With careful lineshape analyses these experiments have detected the contribution of resonant surface polariton effects (resulting in a respulsive interaction for excited Cs near sapphire cell walls [208]) and have reached the 5-10% relative error level [209, 210].

Although cold atoms continue to offer great potential for increased precision in CP measurements, the challenge of trapping atoms near a surface, with a well-defined, measurable atom-surface separation, remains an obstacle. Hot-atom methods have best covered the near field, with the vapor cell reflectance measurements averaging over shifts from atoms within ~ 100 nm and diffraction grating results likewise best interpreted as an average dominated by the contribution from atom-surface distances ~ 10 nm. As found by the Cornell group, magnetic traps for BECs may be limited to distances greater than ~ 5 μm. The intermediate regime is potentially explorable by quantum-reflection measurements, but the only precision experiment we know of so far is the evanescent-wave-barrier reflection measurements of Slama *et al.* [18], which showed a slight discrepancy with theory and which might be difficult to adapt to distances much greater than the maximum ~ 225 nm separation, given the rapid decay of evanescent beams. There remains a great need for further experiments in the intermediate regime. Furthermore, most cold-atom experiments and proposals thus far have measured the CP effect indirectly, as a modification to the atomic trap potential (in the Cornell and proposed lattice oscillation experiments) or the repulsive potential (in the evanescent-wave experiments). We are optimistic that direct spectroscopic detection of CP energy-level shifts in lattice-trapped cold strontium will eliminate many of the systematics encountered in cold-atom CP experiments thus far, and will provide a high-precision measurement method applicable to a range of well-characterized separations in the intermediate regime.

2.4.2. The Strontium Casimir-Polder Experiment

Frequency can be measured more precisely than any other physical observable: in general, increased averaging leads to increased precision, and the higher the frequency the more quickly one can obtain a precise result. It is no surprise that many of the most precise Casimir and CP measurements thus far rely upon the measurement of a frequency signature: i.e. the resonance of a micromechanical torsional oscillator ($\omega_0/2\pi \sim 1$ kHz [173]), the oscillation frequency of a BEC in a magnetic trap ($\sim$ 230Hz [211]), and spectroscopic measurements in atomic vapor cells. The first two examples, however, rely upon frequencies derived from the nature of the object interrogating the shift: the materials and geometry of the MEMS device, the magnetic trap characteristics. Direct spectroscopic probes of atomic energy level shifts, on optical transitions cycling at THz frequencies, will remove many of the intermediate systematics that must be considered in the evaluation of the base frequency. The ultimate precision of the measurement will depend upon the magnitude of the change in frequency imparted by the interaction, but the high precision with which optical frequencies can now be measured implies that there is great promise for optical spectroscopy in this field.

A direct spectroscopic probe of strontium's energy level shifts will offer a straightforward test of our understanding of the CP interaction, and the demonstrated high precision of strontium optical lattice clocks implies that these systems are ideal for the precision measurement of this sensitive effect. Cold strontium atoms loaded into an optical lattice at the magic wavelength and translated towards a test surface will experience differential CP shifts of the ground and excited states, detectable by spectroscopy on the narrow intercombination transitions. The use of the magic wavelength will avoid trap shifts of the transition, and many of the systematics affecting other CP measurements are minimized by this experimental approach and the properties of strontium as the probe-atom choice, including magnetic sensitivity, interatomic interactions (density/collisional shifts), and surface contamination. The details of the proposed experimental procedure are described below, along with a discussion of these systematics and the potential for this experiment to probe novel distance regimes and atom-surface interaction effects.

The experiment requires initial generation of a laser-cooled strontium sample, produced by magneto-optical trapping on the strong cycling $^1\mathrm{S}_0 - {}^1\mathrm{P}_1$, 461 nm transition. For a large starting sample, we load a "top MOT" directly from a Zeeman-slowed atomic beam, then transfer to a "bottom" 461 nm MOT in a pyrex cell with better optical access (see Ch. 4-5). Subsequent transfer into the 689 nm red MOT will further cool the atoms, allowing greater transfer efficiencies into an optical lattice. The lattice, formed by a standing wave at the intercombination transition's "magic" wavelength λ_L, could be formed by retroreflection from a test surface, but this would fix the trap well locations at $z = \lambda_L/4 + n\lambda/2$ (n an integer). A better option to allow mapping of the atom-surface potential over a range of distances is mounting both the lattice fiber launcher and a retroreflecting mirror on an external translation stage. The test surface must then be at least partially transmissive at the lattice wavelength, but the atoms can be loaded into the lattice far from the test surface and translated toward the surface to map the atom-surface potential as a function of distance. With an initial bottom 461 nm MOT of $\sim 10^5$ atoms and a conservative 50% transfer efficiency into the 689 nm MOT, we can still expect to end with $\sim 10^3$ lattice-trapped atoms.

The first generation of experiments will explore the CP shift of the 689 nm $^1\mathrm{S}_0 - {}^3\mathrm{P}_1$ transition of the most abundant isotope, ^{88}Sr, using a probe beam derived from the same laser used to create the red MOT. The measured "magic" wavelength for this transition is 914(1) nm [212], resulting in a lattice well-spacing of 457 nm. For close atom-wall approaches, the shift between adjacent lattice sites may be resolvable, but with a reasonable trap depth of 22 μK, achievable with a 380 mW lattice with a 50 μm beam waist, the dipole potential is overwhelmed by the CP interaction for distances closer than $\sim$200 nm (see Fig. 2.4), so it may be preferable to eliminate all but one lattice site by selective heating of adjacent wells with a resonant $\mathrm{TEM}_{0,1}$ 461 nm beam. After loading into the optical lattice, the atoms can be prepared in the ground motional state by resolved sideband cooling, or (at the cost of more atom loss) simply by lowering the lattice beam power until only the atoms in the ground state remain trapped, then increasing the power again for tight confinement. The trap oscillation frequencies in the longitudinal and radial directions at a 22 μK well depth are 70 kHz and 300 Hz, respectively, resulting in "pancakes" of atoms trapped in the one-dimensional wells with a 450 nm radial extent but a width of only 30 nm in the longitudinal direction. The optical lattice technique thus provides a probe of excellent spatial resolution compared to prior CP experiments.

Precision translation of the lattice could be accomplished by phase-modulation of the opposing lattice beams [137, 213, 214], but this introduces additional experimental complexity (phase modulators also add unwanted structure to Gaussian beams). The

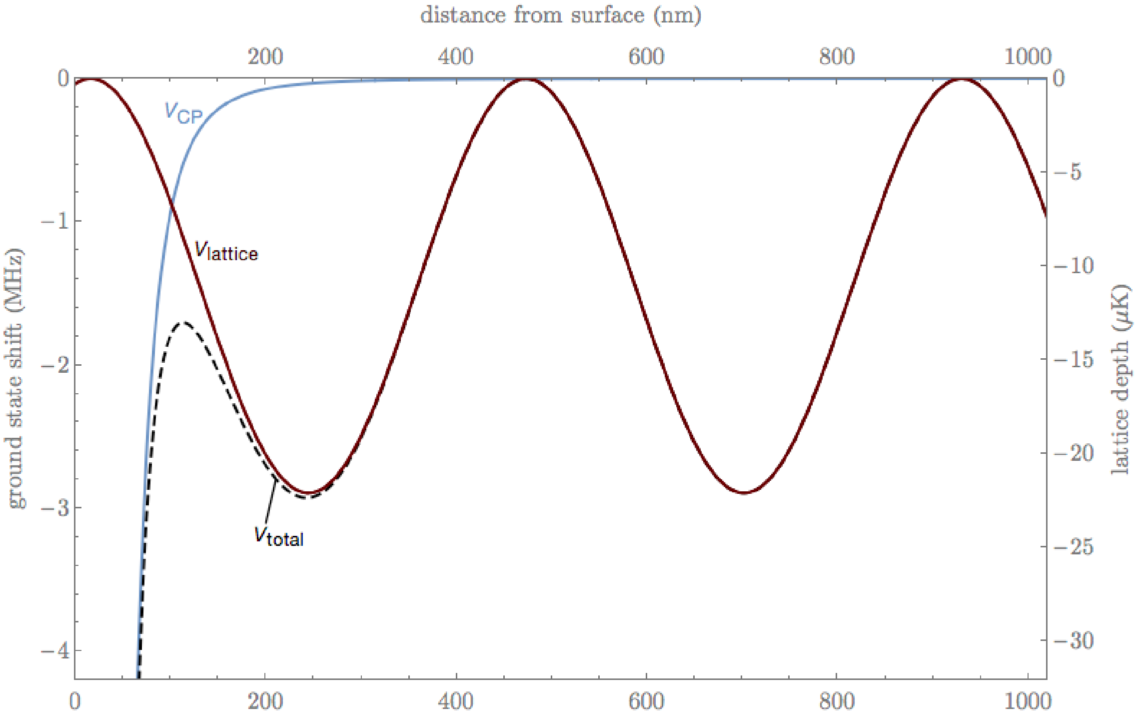

FIGURE 2.4. Optical lattice (V_{lattice}) and Casimir-Polder (V_{CP}) potentials experienced by ground-state ^{88}Sr atoms near a conductive surface, expressed as a ground-state frequency shift ($\Delta\nu = \Delta E/h$ - left axis) or temperature ($\Delta T = \Delta E/k_B$ - right axis). For atom-surface separations less than $\sim$ 200 nm, the CP potential overwhelms the lattice trap potential, as shown by the total potential curve (lattice phase arbitrarily chosen to illustrate trap distortion).

linear air-bearing translation stage planned for use in this experiment, an Aerotech ABL10100-LT used in previous Rb experiments in this lab [215, 216], offers 5 nm resolution and 50 nm repeatability, more than sufficient for initial experiments. Calibration of the atom-surface can be accomplished by direct imaging of the image and reflection at a very shallow angle ($\sim 2°$), as used for the Cornell BEC experiments [191], but this approach limits the distance resolution to $\sim$ 200 nm with our $f/3.5$ lens (numerical aperture $NA = 1.75$). For more precise distance calibration, adiabatic transfer into a lattice formed by reflection from the test surface by gradual decrease of the counter-propagating lattice beam power will fix the well sites at $\lambda/4 + n\lambda/2$, and the CP shift between adjacent well sites is resolvable, giving an absolute atom-surface distance measurement. Calibration for subsequent CP measurements is then limited only by the 50 nm repeatability of the translation stage.

As the lattice-trapped atoms are brought towards the surface, the ground and excited states of the intercombination transitions experience differential shifts as a result of the CP interaction, leading an overall spectroscopic shift of the measured transition frequency, as plotted in Fig. 2.5 for the 689 nm $^1\text{S}_0 - {}^3\text{P}_1$ transition in the perfect conductor limit. Although the shift is greater for the doubly-forbidden $\Delta J = 0, 2$ transitions, and future generations of this experiment could achieve much greater precision using these probe transitions, the $^1\text{S}_0 - {}^3\text{P}_1$ transition shift for the $m_J = \pm 1$ excited-state sublevels is easily resolvable over an accessible distance range of $\sim$200 – 1μm atom-surface separation, and that of the $m_J = 0$ sublevel for 200 – 400 nm, given the narrow 7.4 kHz natural linewidth.

The vdW/CP regime crossover length scale for strontium is set by the dominant transition, $^1\text{S}_0 - {}^1\text{P}_1$ at 461 nm, so measurements in the $\sim$50–500 nm region are

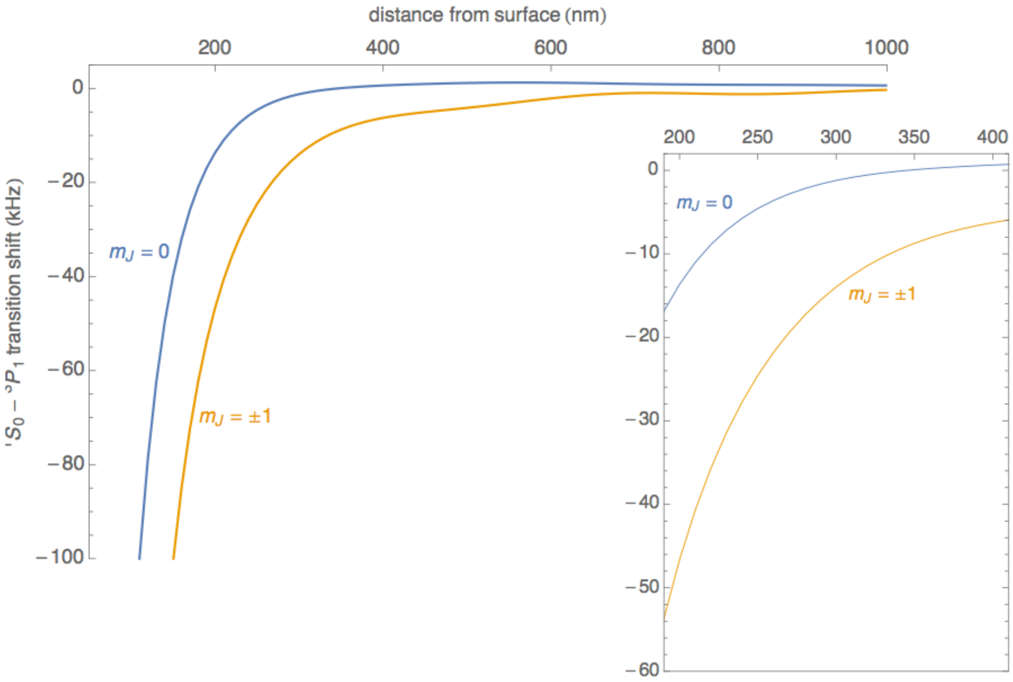

FIGURE 2.5. Casimir-Polder induced $^1\mathrm{S}_0$ − $^3\mathrm{P}_1$ transition shift vs. atom-surface separation for excited state sublevels $m_J = 0, \pm1$ in the perfect-conductor limit. The inset expands the same data over the 200–400 nm region, the region of closest approach for the current available optical lattice power.

within the theoretically interesting intermediate regime where neither the $1/z^3$ or $1/z^4$ asymptotic limits (Eq. 2.33) are good approximations to the full QED expression for the atomic energy level shifts (Eq. 2.43). To the best of our knowledge, only one experiment so far has mapped the Casimir-Polder interaction with precision in this regime: the evanescent-wave reflection experiment of Slama *et al.* [18], described in the previous section, which indirectly measured the potential between Rb and glass over $\sim 150-225$ nm separations. A direct spectroscopic probe of the $^1\mathrm{S}_0$ – $^3\mathrm{P}_1$ transition shift in the 200–400 nm region will be a useful proof-of-principle experiment in a little-explored distance regime, and future measurements on the ultranarrow $^1\mathrm{S}_0 -^3\mathrm{P}_{0,2}$ transitions will provide precision tests of theory over an even wider separation window.

However, probing even the 7.5-kHz-linewidth $^1\mathrm{S}_0 - {}^3\mathrm{P}_1$ transition is not as simple as sweeping a 689 nm beam across the atoms and watching for fluorescence. A single saturated atom will scatter on average only 23,000 photons per second (vs 10^8 photons/s on the strong cycling $^1\mathrm{S}_0 - {}^1\mathrm{P}_1$ transition); even with 10^3 atoms per lattice site, this will be far too low a count rate for detection with our CCD camera. Narrow-linewidth transitions that cannot be easily probed by fluorescence detection are often detected by shelving: we can monitor the 461 nm $^1\mathrm{S}_0 - {}^1\mathrm{P}_1$ fluorescence as a measure of the ground state population after applying a 689 nm π- pulse. When resonant, this pulse will transfer population to the relatively long-lived $^1\mathrm{P}_1$ state and cause a dip in the 461 nm signal. The current equipment is sufficient for this detection scheme: the duration of the π pulse is chosen such that the atoms complete one-half of the Rabi-flopping $|g\rangle \leftrightarrow |e\rangle$ cycle, or

$$t_\pi = \frac{\pi}{\Omega} = \frac{\pi}{\Gamma\sqrt{2}(I/I_{\mathrm{sat}})}, \tag{2.45}$$

where the Rabi frequency $\Omega^2 = 2\Gamma^2(I/I_{\text{sat}})$ can be made relatively small by choosing an intensity I on the order of the saturation intensity I_{sat} (also desirable to limit saturation broadening) so that $t_\pi \approx 50\ \mu$s, a long enough time-scale that an acousto-optic modulator (with a typical rise-time of 10-100 ns) can be used for switching. The $< 1\ \mu$s resolution of our analog output and analog input computer control system, described in Sec. 6.1, can easily control the π-pulse amplitude and duration, and record the 461 nm fluorescence decrease within the 21.5 μs $^3\text{P}_1$ excited state lifetime. The resonance would then be mapped out (so that the center frequency is resolved to an accuracy much better than either the linewidths of the 689 nm laser or atomic transition) stepwise, by repeating this cycle for many detunings of the 689 nm probe.

This experiment, although taking advantage of many of the techniques developed for strontium optical frequency standards, is much simpler than the creation of a full optical-lattice clock: we are not interested in measuring the *absolute* frequency of the $^1\text{S}_0 - {}^3\text{P}_1$ transition, but rather the *change* in frequency for atoms close to the surface vs. those far away, where the Casimir-Polder shift is negligible. This means we do not need a femtosecond frequency comb and associated electronics, merely a means of measuring the frequency *shift* of the resonant 689 nm probe. The 689 nm master laser is locked to the $^1\text{S}_0 - {}^3\text{P}_1$ transition via saturated-absorption spectroscopy in a heat-pipe vapor cell, as described in Sec. 4.5.1; subsequent frequency offsets are controlled by an AOM whose frequency is set by a direct digital synthesizer (DDS) (see Sec. 6.1) with 1-ps phase stability. The DDS frequency offset required to probe the transition near the surface vs. far away is thus a direct measure of the transition shift.

Many systematics affecting other Casimir-Polder measurements are eliminated or minimized by this proposed measurement scheme and the choice of strontium as the probe atom. The first-order Stark shift of the lattice trap light is removed by use of the "magic wavelength", and spectroscopy of ground-vibration-state lattice-trapped atoms in the Lamb-Dicke regime ensures elimination of first-order Doppler effects. Strontium offers a low susceptibility to background magnetic field shifts: unlike the alkalis, strontium's $^1\mathrm{S}_0$ ground state is completely angular momentum free, and the even isotopes also lack nuclear spin and hence hyperfine structure. (While the $m'_F = \pm 1$ sublevels of the excited state do experience a Zeeman shift of 2.1 MHz/G, the ground state CP shift dominates the overall transition shift, and this magnetic field tuning factor is much smaller than that of the alkalis due to strontium's smaller Landé g-factor g_J — see Sec. 3.2.2.) The magnetic-field insensitivity is important not only for stray background fields but also minimization of effects due to thermal surface currents when probing the CP-effect near conductive surfaces; these effects prevent magnetic confinement of BEC's near metallic surfaces [72, 73], but strontium will not only remain trapped in the optical lattice but can measure CP shifts into nearly the near-field regime with low magnetic field systematics.

The ^{88}Sr isotope also possesses a remarkably small collisional cross-section [217] (and that of fermionic ^{87}Sr is of course smaller yet). This was a challenge for groups seeking to form a strontium BEC, as efficient thermalization is required for evaporative cooling, but it is an advantage for optical frequency standards and spectroscopic measurements, where collisional broadening and shifts must be minimized. Our measurement method will be particularly insensitive to collisional shifts, as any remaining collisional shift affects the atoms both near and far from the surface and so subtracts out of the CP shift. However, a small value for the collisional shift will limit systematics due to discrepancies between shot-to-shot atom numbers during lattice loading. Even if the subtraction is incomplete, the collisional shift (see Sec. 4.5.1) for our expected number density will be trivial at our current level of precision compared to the atom-surface shift [218, 219]. Note that one might question whether results like those found in Sec. 2.3, derived for the interaction between a *single* particle and surface, even apply in measurements using a large number of atoms, given the known non-additivity of the interaction. One might assume, for example, that a BEC is a good approximation of one macroscopic probe particle in a CP experiment, but some quantum reflection experiments have found that inclusion of the mean-field energy is required to explain results [187], and the theory behind the Cornell group's experiments also included interparticle interactions [190]. The use of an ultracold, but *not* degenerate, and relatively diffuse gas of atoms with a very low collisional cross-section better approximates the situation of non-interacting particles and should simplify the comparison of measurement to theory.

Finally, a significant systematic in many CP experiments is the effect of atomic deposits on the test surfaces. Adsorbed atoms (adatoms) potentially modify the optical properties of the surface, and are known to create local electric fields ("patch" effects); the effects are particularly insidious to systematic error elimination because the adsorbed layer coverage may change with temperature, light exposure, and time [96]. Many experiments requiring close grazing angles for atom-surface interaction measurements, like the early atomic-beam and current diffraction-grating experiments, will inevitably create large atom-surface deposits, as will of course atomic beam transmission and classical- and quantum-reflection measurements. The implication of these deposits has often been ignored, but as CP experiments approach the 1% precision level they will become important considerations. The landmark 1993 detection of the retarded CP interaction by Sukenik *et al.* noted a measurable surface electric field attributed to sodium atom deposits on the gold-coated transmission cavity, and a later analysis suggested adatom patch potentials could create electric forces mimicking CP forces [6, 220]. A careful study by the Cornell group on the effect of Rb atom deposition on silicon and titanium surfaces found that the resultant electric-field-gradient forces would overwhelm the CP effect, concluding that precision CP measurements using alkali atoms would likely be limited to dielectric test surfaces [17].

The strontium optical lattice measurement technique should minimize many of the problems associated with adatom electric-field systematics. By loading the atoms into the lattice far from the surface, then translating toward the surface in a controlled manner, we can minimize surface contamination compared to CP transmission or reflection measurements. Avoiding the use of a BEC significantly decreases the atom number required for each measurement (such that fewer atoms can potentially deposit onto the surface) and could lessen the stringent background vacuum requirements [221], allowing heating of the test surface to remove or diffuse adatom patches (as demonstrated by Ref. [222]). Finally, the electric fields generated by adsorbed strontium atoms are predicted to be much smaller than those generated by the alkalis [16]. Adatoms create electric dipole potentials as a result of effective fractional charge transfer from the atom to the substrate, and the ionic character of the bond is a function of the ionization energy of the atom vs. the work function of the surface. Strontium's 5.7 eV ionization energy is greater than the work functions of many substrates of interest (most common metals and semiconductors have work functions in the 4-5 eV range), so the effective charge transfer should be lower and the adsorbed bond less ionic, as compared to an alkali like rubidium with a 4.2 eV ionization energy [17]. This will, however, be an important systematic to investigate in early experiments. Careful characterization of Sr adatom effects will benefit not only future Sr CP experiments, but also Sr atom-chip applications, since adatom patch potentials can also become problematic in the miniturization of these devices [223].

Initial experiments on this project will attempt to measure the CP shift to the ${}^1\mathrm{S}_0 - {}^3\mathrm{P}_1$ transition induced by the Pyrex wall of the science cell and explore the effect of strontium surface contamination, by controlled deposition of adatom layers and application of electric fields (as done for Rb by the Cornell group [211]). Future measurement of the ${}^1\mathrm{S}_0 -{}^3\mathrm{P}_{0,2}$ transition shifts will bring greater precision and expansion of the measurable separation, and the experimental technique can be adapted to measurement of CP effects from many interesting surfaces in the future. Any material that is at least partially transmissive at the 914 nm lattice-beam wavelength should be amenable to measurement (given sufficient lattice-beam power), allowing exploration of birefringence effects, surface roughness, and metallic and dielectric thin film layers. These materials would be difficult to explore using the evanescent-wave reflection technique, where the inferred CP potential depends critically upon careful characterization of the evanescent-wave barrier properties. This method also links measured CP shifts directly to measured atom-surface distances, where again the location of the barrier maximum in evanescent-wave experiments depends upon the barrier beam parameters (and hence surface characterization). Furthermore, the < 50 nm distance resolution is far finer than that offered by either the evanescent-wave or the proposed optical lattice interferometric transport experiments, which will necessarily average measured CP shifts over several wells. The optical lattice measurement technique thus has great potential to become a new method for CP measurements in the intermediate distance regime.

CHAPTER III

LASER COOLING AND TRAPPING: AN OVERVIEW

A thorough understanding of the structure and properties of individual atoms is naturally an appealing goal in physics: atoms are the fundamental constituents of the majority of the states of matter we interact with, but aspects of their nature can only be fully explained through quantum mechanics. Throughout the 20th-century, experiments probing atomic energy-level structure offered tests of quantum-mechanical predictions, and the advent of the laser as an intense, coherent, narrow-band light source led to new levels of spectroscopic precision. The ability to manipulate and interrogate isolated, non-interacting particles, however, remained a holy grail but non-trivial in practice: atoms in the gaseous state are typically moving far too rapidly, and under normal circumstances cooling a sample leads to a phase transition to the liquid or solid state.

The ability to control the motional states of neutral atoms experienced an unprecedented leap forward with the development of laser cooling and trapping techniques, opening new horizons for precision measurement and the exploration of predicted quantum-mechanical phenomena. This chapter will give a conceptual and historical introduction to the principles of laser cooling and trapping (Sec. 3.1), followed by a more mathematical description of the mechanical forces light exerts on atoms. Unlike Casimir-Polder interactions, most of the physics behind laser cooling is easily understood from a semi-classical approach, treating the atom quantum-mechanically but the light field classically. This is a valid approximation when the number of photons governing the interaction is large, which is true for the mechanical forces considered in this section. Another very useful approximation is to treat the atom as a two-level system: obviously no atom is truly two-level, and as we shall see there is only so far we can push this assumption (e.g., it is not a valid approach to the calculation of Casimir-Polder energy-level shifts as shown in Sec. 2.3.2), but it is a useful starting point. Radiative scattering forces, fundamental for slowing, cooling, and confinement at extraordinarily low temperatures in the magneto-optical trap (MOT), are covered in Sec. 3.2; Sec. 3.3 covers the induced dipole forces responsible for dipole and optical lattice traps. Useful references for thorough discussions of the interaction of atoms and light are Metcalf and van der Straten's classic *Laser Cooling and Trapping* [224] as well as Refs. [43] and [225].

3.1. Introduction

The understanding that light, which carries momentum, can exert mechanical forces on matter has a long history. As early as 1619, Johannes Kepler posited that a comet's tail points away from the sun as a result of some "solar breeze," and long before the photon theory of light Maxwell calculated the radiation pressure that results from a beam reflecting perfectly off a surface.

The scattering force, arising from the absorption and spontaneous reemission of resonant photons, can be particularly strong for fast cycling (broad-linewidth) atomic transitions. Long before the development of the laser, deflection of a beam of sodium atoms by D2-line resonant scattering was observed [226]. The effective cross-section for absorption on a strong transition is much greater than the geometric size of the atom [227], resulting in a scattering force in the propagation direction of the light beam that can be much greater than the force of gravity. The induced dipole force, associated with stimulated emission and energy level shifts from non-resonant light, can also be significant for atoms in light-wave geometries with large intensity gradients. Before the first Doppler laser-cooling proposals, dipole force velocity-distribution modification was proposed through the action of an intense standing-wave “dragging” atoms towards or away from regions of high intensity [228], and dipole-force trapping of transparent μm-diameter dielectric spheres by 1969 [227] demonstrated further potential for the technique.

However, proposed neutral atom optical traps, with potential depths on the order of $10^{-1} - 10^{-2}$ K, were far too weak for direct trapping from hot atomic vapors [229]. Ion traps, on the other hand, were becoming an established tool by the 1960’s [230–232]: taking advantage of much stronger forces, traps with depths ~ 1 V already confined electrons and clouds of ionized atoms to stable orbits inside combinations of static electric and magnetic fields (the Penning trap) or radiofrequency (RF) fields (the Paul trap). However, the drive for tighter localization and more precise spectroscopic measurements also motivated interest in colder samples among ion-trappers [233]. In 1978, independent proposals by Hänsch and Schawlow [234] and Wineland and Dehmelt [235] recognized the fact that spontaneous scattering of red-detuned (below the resonant frequency) laser light can remove energy and cool atomic samples. The latter pair, both famous ion trappers, couched their argument in the language of sideband cooling (or a Raman process: transitions from higher to lower kinetic energy states are more probable than the reverse) as relevant for tightly bound ions, while Hänsch and Schawlow approached the problem in terms of the velocity-dependent apparent frequency (and hence apparent detuning) of the light field in a moving atom’s frame of reference. The two points of view can be shown to be equivalent [236, 237], but the latter approach is more intuitive when considering free neutral atoms.

Hänsch and Schawlow's approach to laser cooling depends upon the Doppler effect (and as a result, cooling of neutral atoms using the scattering force is often referred to as "Doppler cooling"): in the rest-frame of a moving atom, the apparent frequency of a laser beam is shifted up or down depending on whether the atom is moving towards or away from the beam. For red-detuned light, this implies that the atom will absorb photons preferentially when moving towards the laser beam. With each absorption, the atom experiences a momentum kick in the direction of the light field, opposing the atom's motion. The atom will then spontaneously emit a photon as it drops from the excited back to the ground state, and get another momentum kick opposite the direction of emission, but this direction is random, such that over many scattering events the momentum change from the spontaneous-emission recoils averages to zero. The atom thus experiences a net cooling force, with the kinetic energy lost by the atom carried away by the re-emitted photons (the entropy decrease associated with the cooling of the atom is also offset by the entropy increase of the light field due to the random nature of spontaneous emission).

For ions tightly bound in electromagnetic traps, the addition of a single red-detuned laser beam can be enough to achieve Doppler cooling: preferential absorption occurs when the ions move toward the beam (alternatively, from the point of view of the tightly-bound-particle spectrum consisting of resonance plus sidebands separated by the trap harmonic frequency, photons are absorbed on the red sideband), and stable orbits and long trap lifetimes allow repeated absorptions and low temperatures to be reached quite quickly. The first, practically simultaneous, demonstrations were realized in 1978 [238, 239], and within a few years ion trappers were storing single Ba^+ and Mg^+ ions cooled to < 50 mK for hours [240–242].

For a hot atomic beam, on the other hand, the situation is more complicated. The initial velocity distribution is significantly altered by exposure to an intense counter-propagating beam with a fixed red detuning: a subset of atoms are cooled, collapsing into a peak centered at a lower velocity with a much narrower velocity width than the original distribution [243, 244]. However, the broad spread of atomic velocities in a hot beam (characterized by the Maxwell-Boltzmann distribution) implies that only a small fraction of atoms will have an initial velocity within the range for which the force is appreciable. More importantly, the atoms that are initially resonant will only decelerate until their changing Doppler shift takes them out of resonance with the counter-propagating beam.

An obvious solution to these problems is to sweep the laser frequency from the red toward resonance at a rate that matches the changing Doppler shift of the decelerating atoms [245]. The initially-resonant atoms will then remain resonant throughout the interaction, and atoms with lower initial velocities will become resonant over the course of the sweep. This method is known as "chirp cooling," and was first explored by Balykin *et al.* [246]. The Phillips group also experimented with chirp cooling [247], using a bias magnetic field to prevent the hyperfine optical-pumping effects in sodium that had complicated the Russian group's results. However, the Phillips group only succeeded in demonstrating chirped slowing from 1000 m/s to $\sim$ 600 m/s; nearly simultaneously, Ertmer *et al.* [248] demonstrated "stopping" and even reversing the velocity of an initially 620 m/s beam, using a sweep rate 3× slower. (As discussed further in Sec. 3.2.2, using the maximum possible deceleration is not always the best option for beam slowing.)

The Phillips group was also exploring a different method of beam slowing, one that would come to be known as the "Zeeman slower" [249, 250]. The principle is simple: rather than tuning the laser frequency to match the changing Doppler shift of the decelerating atoms, the Zeeman shift of the atomic sublevels can be tuned directly by the application of a changing magnetic field. Like chirp cooling, Zeeman slowing is a very effective technique to not only slow a portion of the atomic beam but in fact to compress much of the velocity distribution (achieving phase-space compression – which is the true measure of cooling [224]): at the start of the slower, the slowing-beam detuning and initial magnetic-field level set the resonant velocity class (the maximum-speed atoms that can be captured by the slower), but atoms with initially lower velocities become resonant over the length of the slower as the magnetic field changes strength. Unlike chirp cooling, this method does not require rapid and broadband laser frequency tuning, and Zeeman slowing provides a continuous flux of cold atoms rather than discrete bunches. For these reasons, it is often the preferred beam-slowing technique and the one used in our strontium apparatus; as such it will be explored in some depth in Sections 3.2.2.1 and 5.3.

By 1984, both chirp cooling and Zeeman slowing had proven that Doppler cooling could produce neutral atom samples with temperatures well below 100 mK (or even "stopped" – in the sense of velocity reversal [248, 251]), and the stage was set for testing proposed neutral atom traps. Magnetic trapping of low-field-seeking paramagnetic atoms required these extremely cold samples [252], and the first neutral atom trap relied upon both Zeeman cooling and a final Doppler-cooling pulse to load sodium atoms into a quadrupole trap with a depth of only 17 mK [253]. Magnetic traps avoid the heating pitfalls of optical traps, and can offer trap lifetimes limited only by background gas pressure. The development of magnetic-trap configurations and techniques would become an important field (and magnetic trapping plus evaporative cooling was key to the achievement of the first

Bose-Einstein condensates [20, 21]), but their use is outside the scope of the current strontium experiment and will not be considered further here.

Magnetic trapping is impossible for atoms lacking a magnetic moment, and the energy-level shifts involved make magnetic traps incompatible with precision spectroscopy, so laser trapping remained an important goal. However, scattering-force traps did not seem the most promising option: the Optical Earnshaw Theorem [254] argued that there could be no stable trapping point relying only upon the scattering force from static light fields because the force is proportional to beam intensity. In analogy to the Earnshaw Theorem of electrostatics, which proves that stable charged-particle traps cannot be created from stationary electric fields alone because the divergence of the electric field must be zero in free space (Gauss's Law), the Optical Earnshaw Theorem argues that the net flux of intensity in must equal the flux of intensity out so the divergence of the scattering force (*if* proportional to intensity alone) will always be zero: no arrangement of beams can achieve force lines all pointing inward to a stable trapping point. Ion traps circumvent the Earnshaw Theorem by the creation of a "pseudo-potential" from oscillating electric fields (the Paul trap), and proposals for scattering-force traps imagined similar periodically-reversing light-field configurations [255], but there were concerns that scattering-force damping could destroy the micromotion that such pseudo-potentials depend upon for stable trap orbits [256].

If the scattering force alone could not create an actual trap, however, it could be used to create neutral atom samples with diffusion times far longer than ever previously realized, through the Doppler-cooling action of three orthogonal pairs of red-detuned laser beams [256, 257]. This configuration, coined "optical molasses," presents the atoms with three-dimensional viscous confinement of a sort: in any direction the atom moves, the damping force opposes the atom's velocity.[1] Optical molasses is not a trap, since there is no restoring force (the atoms are free to diffuse out of the molasses region defined by the beam-overlap volume), and in the first demonstration in 1985 chirp pre-cooling was required to slow hot sodium-beam atoms to velocities less than 3 m/s before loading into optical molasses [257]. Subsequent cooling in the molasses, however, reached temperatures on the order of 240 μK, far below anything yet observed in neutral atoms or even ions and consistent with the predicted minimum Doppler-cooling temperature expected from the balance of cooling and spontaneous-emission heating effects. The ~ 0.2 cm^3 molasses volume led to visibly dense sodium samples ($\sim 10^6$ atoms/cm^3) with a lifetime of ~ 0.1 s.

With the remarkably cold atoms produced by optical molasses, the first optical atomic trap was quickly realized: a sodium dipole trap consisting of a single tightly-focused far-red-detuned laser beam [229]. The trap conception dated from a 1978 proposal [260], but the realization was challenging before optical molasses: the trap depth of only 5 mK and volume $\sim 10^{-7}$ cm^3 required dense, cold samples to load, and even then captured only about 500 atoms. The small trapping potential and trap volume demonstrate the challenge of dipole-force traps. Unlike the dissipative scattering force, the dipole force (also known as the gradient force) is conservative, and cannot be used for cooling. As such, it can be written as the negative gradient of the interaction energy of the induced atomic dipole moment and the electric field. Classically, the induced dipole moment is the atomic polarizability times the electric field [261], so the dipole force is proportional to the intensity gradient: for the single-beam trap, a fairly high power and a tight beam waist (220 mW and 10 μm in the

---

[1] This can also be achieved with just four laser beams, arranged normal to the faces of an imaginary tetrahedron [258, 259].

first demonstration) are needed to achieve reasonable trap depths even when capturing pre-cooled optical-molasses atoms.

However, the atomic polarizability has both a real and imaginary part: the real part, responsible for oscillations of the dipole in-phase with the electric field, gives rise to the dipole force, but the imaginary part is responsible for absorption and heating [262]. Early dipole trap proposals and experiments recognized the need for relatively large beam detunings to ensure that the dipole force dominated over the resonant scattering force along the axial trap direction, (such that the net force is aligned with the gradient of the intensity – for red-detuning, capturing atoms at the focus – rather than the propagation vector of the beam). However, heating effects remained problematic because *elastic* spontaneous scattering is not eliminated by large detunings: the first demonstrated dipole trap used a detuning of -650 GHz from the sodium D2 line, but without cooling trap lifetimes were limited to ~ 4 ms due to these heating effects [229]. It was apparently believed impossible to achieve true stability (trapping potential greater than the thermal energy of the atoms) in a single-beam dipole trap alone [256, 263], so the first demonstrations relied upon alternating dipole-trapping and Doppler-cooling cycles to achieve longer trap lifetimes [229, 264, 265], and avoided the use of higher-power trap beams as the increased trap depth would be offset by the increased thermal heating effects [256].

Dipole-force traps using much greater beam detunings would soon demonstrate that the heating effects were not nearly as dire as initially expected, but in the meantime, scattering-force traps, potentially $100\times$ deeper and $10^{15}\times$ larger than the first dipole trap, became a possibility once again. As Pritchard *et al.* argued in 1986 [266], the Optical Earnshaw Theorem relies upon the assumption that the scattering force is proportional to intensity. This is true for the two-level-atom (up to the saturation intensity), but real atoms possess internal degrees of freedom: even the simplest $J = 0$ to $J = 1$ transition is three-fold degenerate in the excited state, and the alkalis used for the early laser cooling experiments possess hyperfine structure in the ground state as well. Pritchard *et al.* suggested several ways to use these extra degrees of freedom to add a spatial dependence to the scattering force, for example through the addition of magnetic field gradients or changing magnetic field orientation, or through the use of optical pumping schemes.

The magneto-optical trap (MOT) followed shortly after [267]: combining optical molasses with a quadrupole magnetic field provides the required spatial tuning of the scattering force through the Zeeman shift of magnetic sublevels. The first and most common MOT arrangement uses the six red-detuned beams of optical molasses as well as two coils with opposing currents in the anti-Helmholtz (AH) configuration to create the magnetic field, which goes to zero at the intersection of the molasses beams (see Fig. 3.3 and Fig. 3.4). Each counter-propagating beam pair is orthogonally circular-polarized, such that each beam interacts with a particular non-zero m'_F excited-state sublevel. This level is spatially tuned by the Zeeman shift into resonance with the beam pointing toward the center of the trap (and further out of resonance with the beam pointing away from the center) as the atom moves outward from the center of the trap. The MOT cools to the same low temperatures as optical molasses alone, but also adds a restoring force to create a true trap. Even the first demonstration was wildly successful, capturing 10^7 atoms in a 0.4-K-deep trap (10× deeper than the magnetic trap of Migdall *et al.* [253] and nearly 100× deeper than the first optical-dipole trap [229], with many orders of magnitude more trapped atoms) and observing an incredible $1/e$ lifetime of 2 min (at the lowest 10^{-11} Torr chamber pressures) [267].

The strength of the MOT lies in the combination of true spatial confinement with simultaneous integrated cooling, which is not possible with conservative-force magnetic or optical-dipole traps. In comparison with optical molasses, which relies upon the Doppler shift alone to regulate the strength of the light-atom interaction, the magnetic-field tuning allows the MOT to capture a larger range of velocity classes which are Zeeman-tuned into resonance over a broad spatial extent. (This allows the MOT to capture atoms even without pre-cooling, trapping directly from the low-velocity tail of a thermal distribution in a "vapor cell" MOT [98, 99].) The MOT also offers a larger damping coefficient (which determines the rate of energy removal) to rapidly cool captured atoms into a cloud that can be made quite dense (up to a limit) by increasing the magnetic field. The configuration is extremely robust to small deviations (e.g. beam misalignments or imperfect circular polarization), and although there are optimal parameters the MOT can capture and cool atoms over a wide range of magnetic-field gradients, beam intensities, and beam detunings (when operating on a strong cycling transition).

The robust trapping and cooling capabilities of the MOT would quickly lead it to become a "workhorse" of atomic physics, but this did not hinder the continued development of magnetic and optical-dipole traps. (In fact, it probably helped, providing a means to rapidly collect large numbers of atoms into very cold, dense samples before loading into secondary traps.) In a MOT, the constant spontaneous scattering of photons limits the ability to achieve extremely high densities (desired for Bose-Einstein condensation) or preserve polarization or coherence (for quantum measurements); transferring atoms to conservative optical traps remained appealing.

While early dipole traps were in a sense far-detuned (100's of MHz) from the nearest atomic resonance, the next step for practical stand-alone optical-dipole trapping was the use of much greater trap-beam detunings. The key realization was the fact that although the trap depth decreases with increased detuning, the scattering rate decreases even more quickly, allowing greater beam powers to be used with minimal increased heating. Based on a proposal by the Phillips group [268], Miller *et al.* demonstrated a stable optical dipole trap with no additional cooling beams using a 67-nm-detuned dipole beam [269]. At such a large detuning, trap powers up to 0.9 W could be used while keeping the photon scattering rate near-negligible, such that the trap approached a true conservative potential with a predicted heating-limited trap lifetime of 47 s. Loading from a vapor-cell MOT, the trap collected 10^4 Rb atoms with a background-gas-limited 200 ms lifetime, demonstrating the practicality of the single-beam trap for future experiments.

In keeping with the nomenclature of the Phillips group proposal, such far-detuned single-beam dipole traps are often known as FORT's (Far Off-Resonance Traps). Later experiments would carry the detuning trend even further, using an 8 W Nd:YAG laser at 1064 nm to trap sodium (nearest resonance: 589 nm) for 0.8 s [270] and even a 25 W CO_2 laser at 10.6 μm to trap cesium (nearest resonance: 852 nm) for $\sim 150\ s$ [271] (at such long wavelengths, these traps rely on an interaction potential characterized essentially by the static polarizability of the atom, and as such are known as Quasi-Electrostatic Traps (QUESTs) [272, 273]). With long storage times, optical-dipole traps can allow creation of much colder, denser samples than possible in a MOT via evaporative cooling [271], and various trap geometries can be realized by overlapping multiple focused trap beams [270, 271].

The optical-dipole trap geometry of most interest to this experiment is of course the optical lattice. The interference pattern of a standing light wave creates multiple potential wells spaced by one-half the lattice beam wavelength. These periodic arrays of dipole traps, which can be created in one- to three-dimensions (a three-dimensional lattice "crystal" when three standing light waves intersect), can provide extremely tight confinement in individual wells, allowing localization of atoms trapped in the wells to length scales on par with those achieved in ion traps. The motional states of lattice-trapped atoms, like those of trapped ions, are characterized by quantized vibrational energy levels, such that fluorescence and absorption spectroscopy reveal elastic resonance plus Raman-sideband features [274].

Optical lattices are a realization of an early laser-cooling proposal by Letokhov [228], who predicted sub-Doppler spectroscopic features in cold atoms interacting with a standing light wave. The interaction of non-zero-ground-state atoms with periodic ac-Stark potentials resulting from optical-molasses beam interference was central to the explanations of observed sub-Doppler cooling in early alkali optical molasses experiments [275, 276], and the first observations of lattice-trapped atoms were a surprise byproduct of explorations of these effects [277], with MOT fluorescence and absorption spectroscopy revealing surprisingly narrow features [278, 279]. As predicted by Dicke in 1952 [106] and observed in trapped ions [280] and optical-lattice trapped atoms [212], Doppler broadening of the resonant peak is suppressed in particles confined to a length scale less than than the wavelength of the interrogated transition. In this "Lamb-Dicke" regime, the recoil energy that leads to Doppler broadening is absorbed instead by the confining potential, and the suppression and asymmetry of the Raman sidebands provides information about the strength of confinement and the vibrational-level occupation (with cooling to majority ground-state motional-energy-level occupation demonstrated again in both trapped ions [281] and lattice-trapped atoms [212]).

The narrow spectral features offered by Lamb-Dicke-regime localization were naturally of great interest for precision spectroscopy and optical-frequency metrology [11, 282], but optical-lattice-trapped neutral-atom ensembles soon proved an ideal platform for a wide range of experiments. Periodic arrays of particles can mimic solid-state systems, and the optical-lattice platform is flexible over a wide range of parameters (e.g., geometry, particle confinement, and even interparticle interactions), allowing exploration of many condensed matter phenomena [274, 283]. The configuration is also ideal for quantum chaos experiments [284–286], and neutral-atom quantum computation proposals also rely upon optical lattice trapping [130, 287–290].

This work cannot begin to cover the range of experiments made possible by laser cooling of neutral atoms, but hopefully this section has given an overview of the basic concepts behind the creation of laser-cooled samples and the potential such systems offer. It is worth keeping in mind the fact that many cold-atom experiments rely upon multiple stages of laser cooling and trapping: our strontium experiment begins with Zeeman slowing of a hot atomic beam to produce atoms cold enough for direct capture in a strong cycling-transition MOT, then transfers the atoms to a secondary MOT with a location offering better isolation and optical access. The experiment will proceed to a second stage of cooling in a narrow-line MOT before loading into an optical lattice for the Casimir-Polder measurement. Each stage offers its own complexities; the following sections will outline the mathematical background required for a basic understanding of the physics involved.

3.2. Scattering Force

The scattering force for a two-level atom is easily understood as the photon momentum $\hbar\mathbf{k}$ times the scattering rate $\Gamma\rho_{ee}$. Here, Γ is the excited-state lifetime, and the excited-state population ρ_{ee} can be found from the solution of the optical Bloch equations, or for low intensity simply from the rate equations of the ground and excited populations, leading to

$$R_{\text{scatt}} = \Gamma\rho_{ee} = \frac{\Gamma}{2}\left(\frac{\Omega^2/2}{\Delta^2 + \Omega^2/2 + \Gamma^2/4}\right), \tag{3.1}$$

which leads to the scattering force

$$\mathbf{F} = \hbar\mathbf{k}\, R_{\text{scatt}} = \frac{\Gamma}{2}\left(\frac{\Omega^2/2}{\Delta^2 + \Omega^2/2 + \Gamma^2/4}\right). \tag{3.2}$$

Here, $\Delta = \omega - \omega_0$ is the laser frequency detuning from the atomic resonance ω_0 and the Rabi frequency, given by the transition dipole matrix element times the electric field divided by $\hbar$, characterizes the strength of the atom-laser interaction.

It is often convenient to express the scattering force in terms of the saturation parameter, s:

$$\mathbf{F} = \hbar\mathbf{k}\,\frac{\Gamma}{2}\left(\frac{s}{1+s}\right), \tag{3.3}$$

where s is a measure of how hard the optical field drives the atomic transition for a given laser detuning (or at resonance, in the case of the resonant saturation parameter s_0):

$$s := \frac{\Omega^2/2}{\Delta^2 + \Gamma^2/4} = \frac{s_0}{1 + (2\Delta/\Gamma)^2}; \tag{3.4}$$

$$s_0 := \frac{2\Omega^2}{\Gamma^2} = \frac{I}{I_{\text{sat}}}. \tag{3.5}$$

At high intensities ($s \gg 1$, or the intensity $I \gg I_{\text{sat}}$ where I_{sat} is the resonant saturation intensity), the atomic populations in the ground and the excited states equalize, such that the maximum excited state population $\rho_{ee} = 1/2$, and the scattering force saturates at the maximum value

$$\mathbf{F}_{\text{max}} = \hbar\mathbf{k}\,\frac{\Gamma}{2}. \tag{3.6}$$

Equivalently, and again using the relation $I/I_{\text{sat}} = 2\Omega^2/\Gamma^2$, we can recast the expression for the scattering force as

$$\begin{aligned}\mathbf{F} &= \hbar\mathbf{k}\,\frac{\Gamma}{2}\,\frac{I/I_{\text{sat}}}{1 + I/I_{sat} + 4\Delta^2/\Gamma^2} \\ &= \hbar\mathbf{k}\,\frac{\Gamma}{2}\left(\frac{I}{I + I_{\text{sat}}}\right)\frac{\left(\frac{\Gamma}{2}\sqrt{1 + I/I_{\text{sat}}}\right)^2}{\Delta^2 + \left(\frac{\Gamma}{2}\sqrt{1 + I/I_{\text{sat}}}\right)^2}.\end{aligned} \tag{3.7}$$

In this form, it is clear that the scattering force as a function of laser detuning Δ is as expected a Lorentzian of width $\Gamma\sqrt{1 + I/I_{sat}} \approx \Gamma$ for low intensities ($I \ll I_{\text{sat}}$). The scattering force as a function of laser detuning for three intensities is plotted in Fig. 3.1. The increased width with increasing intensity is a result of power broadening of the transition lineshape: at high intensities, the absorption exactly on resonance cannot increase above the minimum necessary to equalize the populations in the ground and excited states, but the absorption in the detuned wings of the Lorentzian increases.

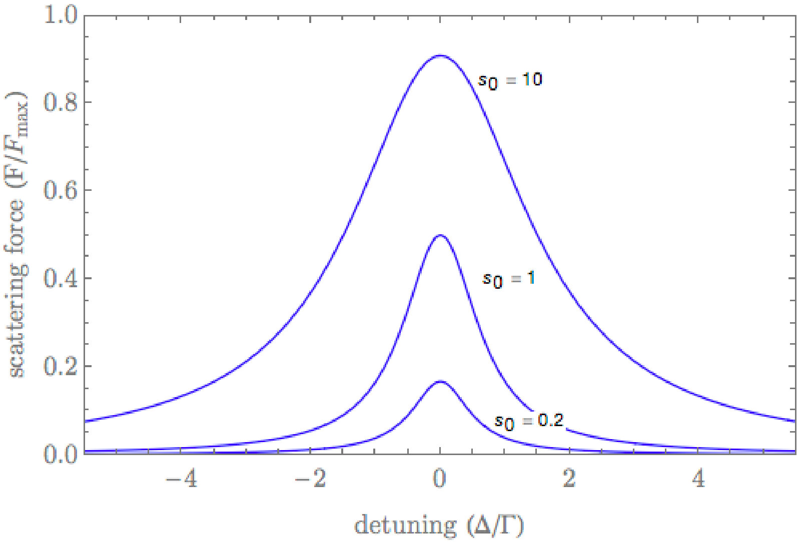

FIGURE 3.1. Scattering force (scaled by $F_{\text{max}} = \hbar k \Gamma/2$) as a function of detuning (scaled by Γ), for three resonant saturation parameters $s_0 = I/I_{\text{sat}}$, showing the effect of power broadening at high intensities.

3.2.1. Doppler Effect

Equation 3.7 gives the force experienced by a stationary atom interacting with a laser field of detuning $\Delta = \omega - \omega_0$, but an atom moving at a velocity $\mathbf{v}$ will see an additional detuning $\mathbf{k} \cdot \mathbf{v}$ due to the Doppler effect. The scattering force is then a function of the atom's velocity:

$$\mathbf{F} = \hbar \mathbf{k} \frac{\Gamma}{2} \frac{I/I_{\text{sat}}}{1 + I/I_{\text{sat}} + 4(\Delta - \mathbf{k} \cdot \mathbf{v})^2/\Gamma^2}. \tag{3.8}$$

We can again rewrite this as a Lorentzian function of velocity to show that, for a beam propagating along the same direction as the atomic motion, the force is maximized at $\mathbf{k} \cdot \mathbf{v} = \Delta$ and the range of velocities for which the force has an appreciable affect is $\Gamma/k\sqrt{1+I/I_{\text{sat}}} \approx \Gamma/k$ for $I \ll I_{\text{sat}}$:

$$F = \hbar k\,\frac{\Gamma}{2}\left(\frac{I}{I+I_{\text{sat}}}\right)\frac{\left(\frac{\Gamma}{2k}\sqrt{1+I/I_{\text{sat}}}\right)^2}{(\frac{\Delta}{k}-v)^2+\left(\frac{\Gamma}{2k}\sqrt{1+I/I_{\text{sat}}}\right)^2}. \tag{3.9}$$

When the laser field is red-detuned, $\Delta < 0$, the scattering force can be used to slow and therefore cool atoms: an atom with a Doppler shift $\mathbf{k}\cdot\mathbf{v} = \Delta$ will scatter strongly from a counter-propagating beam, with the absorption of each photon of momentum $\hbar\mathbf{k}$ decreasing the atom's velocity along the beam axis by an average $\mathbf{v}_r = \hbar\mathbf{k}/m$, the recoil velocity, until the velocity decrease brings the atom out of resonance or the transverse velocity components (un-slowed by the counter-propagating beam) take the atom outside the illumination area.

3.2.1.1. Optical Molasses

The configuration known as "optical molasses" takes advantage of the Doppler shift to decrease an atom's velocity along all three axes using three orthogonal pairs of counter-propagating, red-detuned ($\Delta < 0$) beams. Considering the problem first along one axis: the beam opposing the component of the atom's velocity along the beam axis is shifted closer to resonance, while the co-propagating beam is shifted even further to the red. As a result, the atom scatters more photons from the counter-propagating beam and experiences a greater force from this beam, a force that opposes the direction of motion. Within the range of effective velocities, it can be shown that the differential force is proportional to a constant times the atom's velocity: hence the atom experiences a frictional force along the beam axis.

To better quantify the Doppler cooling effect in one dimension, we can write the total force experienced by an atom moving with a velocity v along that axis as the sum of the two forces $\mathrm{F}_\pm$ from the two beams. This is a valid approach only when the interaction with each beam can be treated independently, which is true when each beam is far below the saturation intensity, so we can first simplify the expression for the force from each beam, Eq. 3.8, by making the assumption $I \ll I_{\mathrm{sat}}$:

$$\mathrm{F}_\pm \simeq \pm\hbar k \frac{\Gamma}{2} \frac{I/I_{\mathrm{sat}}}{1 + 4(\Delta \mp kv)^2/\Gamma^2}. \tag{3.10}$$

The net force is given by the sum of the forces from the two beams, which are two Lorentzians of opposite sign, each with a width $\sim \Gamma/k$ for $I \ll I_{\mathrm{sat}}$ and displaced from $v = 0$ by the Doppler shift kv, as shown in Fig. 3.2. We can write the total force as

$$\begin{aligned} F_{\mathrm{total}} &= F_+ + \ F_- \\ &\simeq \hbar k \frac{\Gamma}{2} \frac{I}{I_{sat}} \frac{kv}{\Gamma} \left(\frac{16\Delta/\Gamma}{1 + 8(\Delta^2 + k^2v^2)/\Gamma^2 + 16(\Delta^2 - k^2v^2)^2/\Gamma^4} \right). \end{aligned} \tag{3.11}$$

In this form, it is clear that the magnitude of the net force is given by the maximum scattering rate times an intensity factor, the ratio of the Doppler shift to the natural linewidth, and a detuning factor [291]. Further simplification arises through the assumption that the Doppler shift is small relative to both the linewidth and the detuning ($|kv| \ll \Gamma, |\Delta|$):

$$F_{\mathrm{molasses}} \simeq 4\hbar k^2 \frac{I}{I_{sat}} \frac{2\Delta/\Gamma}{\left[1 + (2\Delta/\Gamma)^2\right]^2} v. \tag{3.12}$$

Note that the force is proportional to velocity; recognizing also that $\Delta < 0$ for cooling, we can identify F_{molasses} as a frictional force with a damping coefficient α:

$$F_{\text{molasses}} = -\alpha\, v, \qquad \alpha = 4\hbar k^2 \frac{I}{I_{sat}} \frac{2|\Delta|/\Gamma}{\left[1 + (2\Delta/\Gamma)^2\right]^2}. \tag{3.13}$$

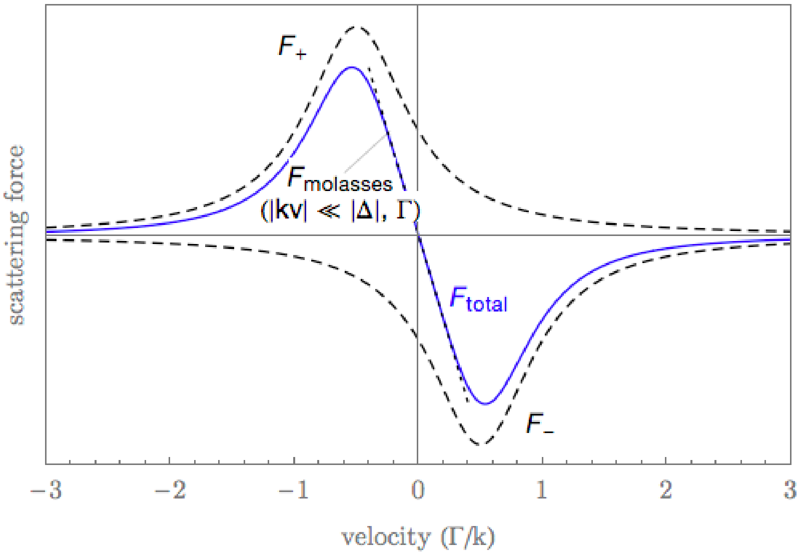

FIGURE 3.2. One-dimensional optical molasses: scattering force as a function of velocity for two counter-propagating, red-detuned beams (velocity scaled by Γ/k), for $\Delta = -\Gamma/2$ and $s_0 = I/I_{\text{sat}} = 0.1$. The dashed black curves are the scattering forces from the right- and left-propagating beams (F_+ and F_-), and the blue solid curve is the total force. The dotted black curve is the linear damping-force approximation (Eq. 3.13), valid only in the regime $|kv| \ll |\Delta|, \Gamma$.

In three dimensions, the three orthogonal pairs of counter-propagating beams lead to a frictional force in any direction of travel: the velocity will damp towards zero. The original demonstrators of the technique, Steve Chu *et al.*, likened the situation to moving through "a viscous fluid of photons"[257] and coined the phrase "optical molasses" to describe this configuration. The atom's motion is heavily overdamped for any velocity less than the molasses capture range (given by the effective width of the interaction, $v_c \approx \Gamma/k$). In fact, it appears that the velocity will damp towards zero (although of course such a result would be unphysical, as discussed in the next section) with a characteristic damping time of $\tau = \alpha/m$:

$$F_{\text{molasses}} = m\dot{v} = -\alpha v \qquad \Longrightarrow \qquad v(t) = v_0 e^{-\alpha t/m}. \tag{3.14}$$

The damping rate (for a given intensity) is maximized at $\Delta = -\Gamma/2\sqrt{3}$, which corresponds to the maximum slope of the $F_{\text{total}}(v)$ curve for $|v| \ll \Gamma/k$, but as shown in the next section this is not the detuning that gives the minimum temperature.

3.2.1.2. Temperature Limits

The treatment so far has ignored the intrinsic quantum statistical fluctuations of the scattering force, which arise from two factors: the fluctuation of the photon absorption rate, and the random direction of spontaneous photon emission. F_{molasses} as derived above is the average absorption force $\langle F_{\text{abs}} \rangle$, and the isotropic re-emission direction implies that the force resulting from spontaneous emission events will average to zero ($\langle F_{\text{spont}} \rangle = 0$), but the total force

$$\mathbf{F} = \mathbf{F}_{\text{abs}} + \delta\mathbf{F}_{\text{abs}} + \mathbf{F}_{\text{spont}} + \delta\mathbf{F}_{\text{spont}} \tag{3.15}$$

includes stochastic contributions $\delta\mathbf{F}_{\text{abs}}$ and $\delta\mathbf{F}_{\text{spont}}$ that will prevent the total energy from damping to zero [225]. There are several ultimately equivalent methods to arrive at the minimum temperature achievable through Doppler cooling alone. Analogous to Brownian motion, the time-evolution of the energy can be analyzed via a Langevin [292] or Fokker-Planck [293] equation to derive a velocity distribution which narrows with cooling until balanced by the broadening effects of the diffusive heating, settling to a steady-state Maxwellian distribution with a characteristic temperature T. Another approach recognizes that the heating effects result in a random walk in velocity or momentum space [263]: while the average momentum $\langle p \rangle$ damps to zero, the variance $\langle p^2 \rangle$ increases at a rate equal to the photon absorption rate times the momentum step size $\hbar k$, allowing the identification of a diffusion constant $2D = \langle \dot{p}^2 \rangle$. Conservation of energy and application of the equipartition theorem ultimately leads to the elegant result $k_B T = D/\alpha$ [294].

A particularly intuitive approach also relies on conservation of energy to find the steady-state energy by simply equating the heating rate to the cooling rate [224, 236]. For the one-dimensional two-beam cooling configuration, the average cooling rate is

$$\langle \dot{E}_{\mathrm{cool}} \rangle = \mathbf{F}_{\mathrm{molasses}} \cdot \mathbf{v} = -\alpha \langle v \rangle^2, \tag{3.16}$$

while each absorption/emission event corresponds to an energy gain of $2E_{\mathrm{recoil}}$, where $E_{\mathrm{recoil}} = \hbar^2 k^2 / 2m$ is the energy associated with absorbing or emitting a single photon of momentum $\hbar k$. For low intensity, these events occur at a rate $2\Gamma \rho_{ee}$ (twice the scattering rate for a single beam), so that

$$\langle \dot{E}_{\mathrm{heat}} \rangle = \frac{\hbar^2 k^2 \Gamma}{m} \frac{I}{I_{\mathrm{sat}}} \frac{1}{(2\Delta/\Gamma)^2 + 1}. \tag{3.17}$$

Setting $\langle \dot{E}_{\mathrm{heat}} \rangle = \langle \dot{E}_{\mathrm{cool}} \rangle$ leads to the steady state kinetic energy

$$\langle KE \rangle = \frac{1}{2} M \langle v \rangle^2 = \frac{\hbar \Gamma}{8} \left(\frac{\Gamma}{2\Delta} + \frac{2\Delta}{\Gamma} \right), \tag{3.18}$$

which is minimized for a detuning $\Delta = \Gamma/2$. Equating the minimum energy to $\frac{1}{2} k_{\mathrm{B}} T_D$ for this one-dimensional cooling scheme leads to an effective "Doppler temperature" along the cooling axis of

$$\boxed{k_\mathrm{B} T_D = \hbar\Gamma/2.} \tag{3.19}$$

This derivation easily generalizes to 2D- and 3D-optical molasses: for N dimensions, the scattering rate is $2N\Gamma\rho_{22}$ (assuming 2 beams per dimension, and $I \ll I_\mathrm{sat}$), so $\langle KE\rangle_\mathrm{min} \propto N$, but the dimensionality cancels out in the application of the equipartition theorem, $\langle KE\rangle_\mathrm{min} = \frac{N}{2} k_\mathrm{B} T_D$, such that the Doppler temperature remains the same. It is interesting but not surprising to note that $T_D \propto \Gamma$: the heating rate is directly proportional to the rate at which the atom experiences recoil events, so a larger cooling-transition linewidth leads to a higher Doppler temperature.

The minimum temperature achievable via Doppler cooling was assumed to be a hard limit, so early experimenters were shocked to discover samples much colder than T_D [295], [296]. Other deviations from Doppler cooling theory had also been observed, like insensitivity to beam misalignments and intensity imbalances, which would be predicted to impart large drift velocities in optical molasses [297] (the MOT is much less sensitive to these issues). These discrepancies were resolved by introducing additional cooling mechanisms, broadly known as "polarization gradient cooling," which take over at low velocities in atoms with degenerate ground-state substructure moving through a standing wave with a changing polarization profile [275, 276].

The scattering force derived above assumed a two-level atom, but early experimenters worked primarily with sodium: with nuclear spin $I = 3/2$, sodium's $^1\mathrm{S}_{1/2}$ ground state is split into two hyperfine F=1,2 sublevels, which in turn contain 3 and 5 m_F sublevels, respectively. Optical pumping is a result of angular momentum selection rules and variations in the coupling strength between each sublevel and the electromagnetic field, and results in population orientations among the ground-state sublevels (such that, for example, σ^- polarization will preferentially populate the lowest $m_F = -F$ sublevel: each σ^- photon absorption must drive a transition from $m_F \to m'_F = m_F - 1$, and while the subsequent decay can take any $\Delta m_F = -1, 0$, or $+1$ value, the net result of many scattering events will be population transfer to the lowest m_F sublevel). Optical pumping will thus redistribute the populations of the m_F sublevels of a sodium atom traveling through a field of changing polarization, but the finite time necessary to pump the atoms into the preferred state prevents the population orientation from following the field polarization adiabatically for non-zero atomic velocity. This can result in situations where the atom continuously loses potential energy as the ac-Stark shifts of the ground-state sublevels oscillate with the field polarization (as in "Sisyphus" cooling, which occurs for optical molasses formed from orthogonal linear polarizations) or where the ground-state population imbalance leads to preferential scattering of the opposing beam beyond what the Doppler shift kv alone would indicate (the form of polarization gradient cooling more relevant to the molasses in the $\sigma^\pm$ MOT). Both cooling mechanisms result in a temperature $T \propto I$ that minimizes for larger detunings Δ than expected for Doppler cooling alone, and otherwise matched the experimental observations of sub-Doppler cooling.

We work primarily with ^{88}Sr, an even isotope with no hyperfine substructure; without any ground-state degeneracy, there will be no sub-Doppler cooling in our $^1\mathrm{S}_0 - {}^1\mathrm{P}_1$ blue MOT (although we can also trap ^{87}Sr which would show such effects). However, another caveat to Doppler cooling theory will apply to the $^1\mathrm{S}_0 - {}^3\mathrm{P}_1$ red MOT: note that the derivations above assumed that the Doppler shift $|kv| \ll \Gamma$. This was a necessary assumption to derive the linearity of the damping force, but it was also implicit in the overall semi-classical treatment of the force, and hence atomic momentum, as a continuous function. For narrow-linewidth laser cooling, these assumptions are no longer valid. In fact, the change in momentum resulting from a single photon absorption, which imparts a recoil velocity $v_r = \hbar k/m$, can Doppler-shift the resonance enough to significantly effect the photon scattering rate, such that treating the momentum as a continuous function may not be valid [291].

The intricacies of narrow-linewidth laser cooling will be discussed further in Sec. 6.5, but for now it is important to note that the consideration of the recoil energy associated with the absorption of a single photon,

$$E_r = \frac{\hbar^2 k^2}{2m}, \tag{3.20}$$

sets a final fundamental limit on the temperatures attainable by any laser-cooling method relying upon resonant scattering of photons. This is known as the recoil temperature

$$\boxed{k_{\mathrm{B}} T_r = \frac{\hbar^2 k^2}{m}} \tag{3.21}$$

(assuming at minimum E_r per degree of freedom [291]). Sub-Doppler cooling of degenerate ground-state atoms results in colder samples as the laser intensity I decreases, but the recoil temperature sets the final limit even for polarization gradient cooling. For narrow-linewidth cooling, it can appear that $T_D < T_r$, but of course T_D is derived under assumptions that no longer hold true when $kv_r > \Gamma$, and the recoil temperature is the relevant parameter.

3.2.2. Zeeman Effect

With the exception of the sub-Doppler cooling discussion, so far we have treated the theory of the scattering force as if our atom were a two-level system. This is never strictly true, although for a $J = 0$ to $J' = 1$ transition it is often a good approximation. This applies to strontium's strong 461 nm cooling transition ${}^1\mathrm{S}_0 - {}^1\mathrm{P}_1$

(ignoring for now the 0.02% leak to ^{1}D$_2$), as well as the narrow-linewidth cooling transition ^{1}S$_0$ − ^{3}P$_1$. Even isotopes lack nuclear spin and hence hyperfine structure, and while the ^{1}P$_1$ and ^{3}P$_1$ levels are three-fold degenerate ($J' = 1, m'_J = -1, 0, 1$) the symmetry of the transition implies that the atom does not in a sense care about the polarization of the laser field since the dipole matrix elements of the ground to excited-state transitions are equal for all m'_J sublevels.

The introduction of a magnetic field breaks the excited state degeneracy. To review the Zeeman effect, the atomic magnetic moment $\mu = -\mu_B \mathbf{L} - g_s \mu_B \mathbf{S}$ (with Bohr magneton $\mu_B = \hbar q e / 2 m_e$ and electron-spin g-factor $g_s \simeq 2$) couples to the external magnetic field via $H_{ZE} = -\mu \cdot \mathbf{B}$ to shift the m_J sublevels by

$$E_{ZE} = g_J \mu_B B m_J = \hbar \kappa B m_J, \tag{3.22}$$

where the Landé g-factor is

$$g_J = \frac{3}{2} + \frac{S(S+1) - L(L+1)}{2J(J+1)}. \tag{3.23}$$

The result of this interaction for the $m_J \neq 0$ sublevels is a linear energy shift with magnetic field proportional to $\kappa = g_J \mu_B / \hbar$. Strontium's ground state ^{1}S$_0$ has $J = 0$ and hence no shift, but the $m'_J = \pm 1$ sublevels of the excited states of the cooling transitions experience a shift of magnitude

$$\begin{aligned} &461\text{ nm} \quad {}^1\text{S}_0 - {}^1\text{P}_1: \quad \kappa_b/2\pi &&= 1.4\text{ MHz/G} \times B \\ &689\text{ nm} \quad {}^1\text{S}_0 - {}^3\text{P}_1: \quad \kappa_r/2\pi &&= 2.1\text{ MHz/G} \times B \end{aligned} \tag{3.24}$$

for a magnetic field B measured in Gauss. The field thus acts as an additional detuning that must be considered in the scattering force,

$$F = \hbar k \frac{\Gamma}{2} \frac{I/I_{sat}}{1 + I/I_{sat} + 4(\Delta - \mathbf{k}\cdot\mathbf{v} - \kappa B)^2/\Gamma^2}, \tag{3.25}$$

(absorbing the $m_J = \pm 1$ into the sign of κ), allowing a means of spatially tuning the scattering force for transitions with a non-zero κ by the application of a spatially varying magnetic field.

The magnetic field also imposes a quantization axis, removing the cooling transition's insensitivity to laser polarization. Angular momentum selection rules require that π-polarization (linear, with polarization parallel to the external **B**-field) drives only $\Delta m_J = m_J' - m_J = 0$ transitions, while the circular polarizations $\sigma^\pm$ have angular momentum ± 1 and so drive $\Delta m_J = \pm 1$ transitions. One case to consider that will be relevant to our particular choice of Zeeman slower design (Sec. 5.3) is the situation of linear polarization, but with the electric field perpendicular to the applied magnetic field: with respect to the quantization axis, this is an equal superposition of σ^+ and σ^- and so will drive both $\Delta m_J = \pm 1$ transitions.[2]

3.2.2.1. The Zeeman Slower

In the Zeeman slower, a hot atomic beam is slowed by a strongly scattering, red-detuned, counter-propagating beam, with the changing Doppler shift of the decelerating atoms compensated by the Zeeman shift from a changing magnetic

---

[2] Note that right-hand- and left-hand-circular-polarization (RHCP and LHCP) are equivalent to σ^+ and σ^-, respectively, *only* when the light-field **k**-vector is aligned parallel to the **B**-field. The handedness of the beam is defined relative to the propagation axis **k**, while the angular momentum is relative to the quantization axis defined by **B** - so in fact, when **k** is anti-parallel to **B**, RHCP = σ^- and LHCP = σ^+.

field. In order to maximize the scattering force through the entire distance z over which the atomic beam is slowed, we need the Zeeman shift $\kappa B(z)$ to cancel both the Doppler shift $kv(z)$ and the slowing laser detuning $\Delta_\mathrm{Z} = \omega - \omega_0$ such that $\omega_0 + \kappa B(z) = \omega + kv(z)$, to give an effective detuning

$$\Delta_\mathrm{eff}(z) = \Delta_\mathrm{Z} + kv(z) - \kappa B(z) \tag{3.26}$$

equal to zero for all z. It is convenient to identify the maximum acceleration that can be imparted by the maximum force in this case ($\Delta_\mathrm{eff} = 0, I \gg I_\mathrm{sat}$) as

$$a_\mathrm{max} = \frac{F_\mathrm{max}}{m} = \frac{\hbar k \Gamma}{2m}. \tag{3.27}$$

Then from basic kinematic equations we can find an expression for the velocity as a function of distance,

$$v(z) = v_0 \left(1 - \frac{z}{L_0}\right)^{1/2}, \tag{3.28}$$

where the stopping distance L_0 is the minimum interaction length required at this maximum scattering rate to slow the atoms from v_0 to $v_f = 0$:

$$L_0 = \frac{v_0^2}{2a_\mathrm{max}}. \tag{3.29}$$

The magnetic field profile needed to cancel the Doppler shift, such that $\kappa B(z) = \Delta_\mathrm{Z} + kv(z)$, is then given by

$$\begin{aligned} B(z) &= \frac{\Delta_\mathrm{Z}}{\kappa} + \frac{kv_0}{\kappa}\sqrt{v_0^2 - 2a_\mathrm{max} z} \\ &= B_\mathrm{bias} + B_0 \left(1 - \frac{z}{L_0}\right)^{1/2}, \end{aligned} \tag{3.30}$$

where the maximum magnetic field is

$$B_0 = \frac{kv_0}{\kappa}. \tag{3.31}$$

The additional bias field

$$B_{\text{bias}} = \frac{\Delta_{\text{Z}}}{\kappa} \tag{3.32}$$

accommodates a non-zero laser detuning Δ_{Z}, which is important to ensure that the atoms cease interacting with the slowing beam as they exit the slowing region. The slowing beam also passes through the top MOT region in our configuration, so a non-zero slowing beam detuning is critical to avoid perturbing the MOT as much as possible. A useful choice for B_{bias} is to set $\Delta_{\text{Z}} \simeq kv_0/2$: this minimizes the maximum B-field, so that $B(z = 0) \simeq B_0/2 \simeq -B(z = L_0)$. This "zero-crossing" Zeeman slower configuration is not a good option for atoms with ground-state hyperfine sublevels which would be degenerate at $B = 0$, because the orientation can scramble in that location and prevent the atoms from interacting further with the slowing light, but this is not a problem for strontium.

The derivation above holds for both σ^+ and σ^- slowing, with the appropriate sign choice for κ based on which excited state sublevel is addressed by the slowing beam. Early demonstrations of Zeeman slowing exclusively used $\Delta m_F = +1$ transitions, which require a σ^+-polarized slowing beam and a magnetic field which decreases with increasing z, but it is equally effective to drive a σ^- transition with $\Delta m_F = -1$ using a magnetic field that *increases* with increasing z [298, 299]. In fact, the σ^- configuration can be preferable for creating very slow beams of atoms for which a zero-crossing Zeeman-slower is not possible: because the magnetic field must decrease in the case of a σ^+ Zeeman slower, the slowing laser detuning matches the Doppler shift of the slower exit velocity, unless an inconveniently large positive bias field is applied. The slowing laser then continues interacting with the atoms after the exit of the slower, and will in fact turn many atoms around if the chosen exit velocity is near zero. In the case of σ^- slowing, the slowing beam can be red-detuned to match the Doppler shift of the atoms at the entrance of the slower, where the magnetic field can be set to zero. The magnetic field increases throughout the slower to maintain the resonance condition then abruptly turns off at the end of the slower, such that the atoms exiting even at extremely low velocities are no longer interacting with the far-red-detuned slowing beam.

Despite the implication of the simple analysis given above, we don't actually want the atoms to come to a complete stop at the end of the Zeeman slower. The limiting width of the final velocity distribution will be set by the effective width $\Delta v = \Gamma/k\sqrt{1 + I/I_{sat}}$ of the scattering force, so if the center of the final velocity distribution is chosen to be 0, half the atoms will in fact cross $v = 0$ and begin to accelerate back towards the source of the beam just before the exit of the slower. Furthermore, the slower should be separated from the main trapping region by a distance great enough to prevent the slowing field from affecting the MOT fields, so we need the atoms to exit with a non-zero velocity and continue into the MOT region without too much gravitational droop.

The final velocity choice v_f can be taken into account by adjusting the length of the slower:

$$L = \frac{v_0^2 - v_f^2}{2a}. \tag{3.33}$$

The atomic beam divergence increases significantly in the slower so it is best to choose an exit velocity near (but not above) the capture velocity of the MOT, $v_f \simeq v_c$, to maximize the flux of trappable atoms. The increased beam divergence is the result of two effects. Decreasing the longitudinal velocity v_z from v_0 to v_f while leaving the transverse components $v_x = v_y \simeq \theta_0 v_0$ (with θ_0 as the hot atomic beam divergence angle) unchanged automatically would imply that the divergence upon exiting the slower would be

$$\theta_f \simeq \theta_0 \frac{v_0}{v_f}. \tag{3.34}$$

This angular increase can be a very significant effect (sometimes referred to as "beam explosion"), but focusing of the slowing beam to match the atomic beam divergence avoids this problem [250]. The second cause of beam divergence is the fact that even with a focused slowing beam the slowing process actually *increases* the transverse velocity distribution through the action of randomly directed recoils from spontaneously emitted photons. This effect can be estimated by assuming that the mean square of a given transverse velocity component will increase as 1/3 (assuming isotropic spontaneous emission) times the number of photons scattered times the square of the recoil velocity v_r [300]. The number of photons scattered by the fastest captured atoms during the Zeeman slowing process will be $N = (v_0 - v_f)/v_r$, so the increase in the transverse velocity will be

$$\langle v_x^2 \rangle = \langle v_y^2 \rangle \approx \frac{1}{3} N v_r^2 = \frac{1}{3}(v_0 - v_f) v_r. \tag{3.35}$$

The angular increase resulting from this effect,

$$\Delta\theta_f \approx \frac{\sqrt{(v_0 - v_f) v_r}}{\sqrt{3} v_f}, \tag{3.36}$$

is much smaller than the "beam explosion" caused by using a collimated slowing beam but remains a nontrivial contribution to beam spreading.

Another consideration which complicates the derivation of optimal Zeeman slower parameters is more subtle: for practical and effective beam slowing, one should not operate at the maximum scattering rate. Using a high saturation intensity and perfectly tuning the Zeeman field such that $\Delta_{\text{eff}} = 0$ maximizes the deceleration $a = a_{\max}$ and minimizes the length of the slower. However, stable operation requires the change in the Zeeman shift to be less than the change in the Doppler shift over the entire length of the slower, or equivalently:

$$\frac{dB}{dz} \leq \frac{k}{\kappa}\frac{dv}{dz} = \frac{ka}{\kappa v}. \tag{3.37}$$

Operating at $a_{\max}$ is equivalent to operating at the equality limit of this "adiabatic following condition," or exactly at the peak of the Lorentzian scattering force Eq. 3.25. However, any imperfection of the magnetic field profile leading to even a temporary increased gradient violating the adiabatic condition will lead to loss of atoms from the slowing process. In fact, the stochastic nature of photon absorption and emission alone will lead to occasional violations when operating at $a_{\max}$. Equivalently, consider the fact that operating at the peak of the Lorentzian scattering force leads to unstable regulation of the velocity [301]: the peak force occurs at $v_{\max} = \kappa B/k - \Delta_{\text{Z}}$, so for any $v < v_{\max}$ an acceleration leads to a greater scattering force opposing this increase in velocity, but any $v > v_{\max}$ leads to a decrease in the scattering force, and further acceleration leads to less force yet. In other words, any atom whose velocity crosses $v_{\max}$ at any point can quickly be lost from the slowing process. In this sense, it is better to operate at an acceleration less than $a_{\max}$ in order to remain on the left-hand slope of the scattering force, ideally where the slope is maximized and the force is approximately linearly proportional to velocity.

This consideration is often quantified by the Zeeman slower "design parameter" η, defined by $a = \eta\, a_{\max}$. Since it is impossible to analytically solve the equation of motion for an atom acted upon by a force that depends upon both the atom's velocity and a magnetic field which is itself an optimized function of the velocity, Bagnato *et al.* derived an equation of motion for the atom in a frame R decelerating at a constant rate $a = \eta\, a_{\max}$ relative to the lab frame, with the assumption that the Doppler shift in this frame would exactly cancel the Zeeman shift ($kv_R(z) = \kappa B(z)$) [302, 303]. The scattering force experienced by the atom in this frame then depends only on the laser detuning and the velocity of the atom $v'(z)$ *relative* to frame R, such that the evolution of the relative velocity follows the relation

$$M\frac{dv'}{dt} = -\hbar k \frac{\Gamma}{2}\frac{s'}{1+s'} + M\eta\, a_{\max} = -F_{\max}\left(\frac{s'}{1+s'} - \eta\right), \tag{3.38}$$

where the saturation parameter (Eq. 3.4) in this case includes the Doppler shift due to the atom's *relative* velocity:

$$s' = \frac{s_0}{1 + 4(\Delta_{\mathrm{Z}} + kv')^2/\Gamma^2}. \tag{3.39}$$

Stable deceleration requires $dv'/dt = 0$, so the steady-state solutions v'_{ss} are found by solving $s'/(1+s') = \eta$, or equivalently $s' = \eta/(1-\eta)$, leading to:

$$v'_{ss} = -\frac{\Delta_{\mathrm{Z}}}{k} \pm \frac{\Gamma}{2}\sqrt{\frac{1-\eta}{\eta}s_0 - 1}. \tag{3.40}$$

Only the negative root is a stable equilibrium point (one way to see this is by plotting dv'/dt vs v' [304]: at the smaller zero-crossing the slope is negative so the acceleration due to any deviation from $v' = v'_{ss}$ will push v' back towards the v'_{ss}; vice-versa is true at the larger zero-crossing), so the velocity in the lab frame is then given by

$$kv(z) = kv_R + kv'_{ss} = \kappa B(z) - \Delta_{\mathrm{Z}} - \frac{\Gamma}{2}\sqrt{\frac{1-\eta}{\eta}s_0 - 1}, \tag{3.41}$$

which is offset from the equilibrium condition that would give $a_{\max}$, $\Delta_{\mathrm{eff}} = \Delta_{\mathrm{Z}} + kv - \kappa B(z) = 0$, by the final term.

Further examination of the cooling process in the decelerating frame can be used to show that the optimal design parameter $\eta = 0.5$, and the ideal slowing beam intensity is $I = 2I_{\mathrm{sat}}$. Linear expansion of Eq. 3.38 around the stable equilibrium point v'_{ss} leads to

$$\frac{dv'}{dt} = -\frac{1}{\tau_D}(v' - v'_{ss}), \tag{3.42}$$

with

$$\frac{1}{\tau_D} = \frac{2\hbar k^2}{M s_0}\eta^2\sqrt{\frac{1-\eta}{\eta}s_0 - 1}; \tag{3.43}$$

which shows that the velocity in the decelerating frame damps toward the equilibrium condition at a rate given by τ_D^{-1}. Cooling requires compression of the velocity distribution [224], so maximizing this damping rate optimizes the cooling process. The damping rate peaks at $\eta = 0.5$ and $s_0 = 2$ to give $\tau_D^{-1} = \hbar k^2/4M$ (corresponding to a damping time $\tau_D = 30$ μs for strontium). While this results in optimal damping for a perfect magnetic field profile, it is common to choose $\eta \approx 0.4$ to account for any deviation in the actual magnetic field.

The choice of η affects both the length of the slower and the magnetic field profile, modifying equations 3.33 and 3.30 to be

$$\begin{aligned} L &= \frac{v_0^2 - v_f^2}{2\,\eta\, a_{\max}} && \text{Zeeman slower length} \\ B(z) &= \frac{\Delta}{\kappa} + \frac{k}{\kappa}\sqrt{v_0^2 - 2\eta\, a_{\max} z} && B\text{–field profile.} \end{aligned} \tag{3.44}$$

Note that the Zeeman slower can be quite effective at capturing a substantial fraction of the initial thermal velocity distribution and slowing all of these atoms to the low final velocity v_f: if the slowing beam detuning Δ and magnetic field $B(0)$ at the start of the slowing region are chosen such that atoms with a velocity v_0 are resonant, any atoms faster than v_0 are very little affected by the slower, but all atoms with a speed v such that $v_0 \leq v \leq v_f$ will come into resonance at some point along the length of the slower as the magnetic field changes (as demonstrated in Fig. 5.7 of Sec. 5.3, which simulates the velocity evolution for several velocity classes passing through the Sr experiment Zeeman slower). A Zeeman slower can thus compress a majority of the thermal distribution, with the maximum v_0 limited primarily by practical length and maximum B-field considerations.

The Zeeman slower magnetic field gradient is traditionally generated by a tapered solenoid, but permanent magnet designs can simplify construction and operation [122, 300, 305–308], as will be discussed further in Sec. 3.2.2.1. The magnetic field given in Eq. 3.30 or Eq. 3.44 is assumed to fall abruptly to zero outside the slowing region, which is of course an idealization; calculations of the optimal field configuration when taking into account inevitable fringe fields and/or shielding materials can be quite involved [304, 309, 310]. The scattering force is also dependent upon the relative intensity s_0 of the slowing beam, which we have assumed here to be a constant, but absorption (which could be significant, as the beam density becomes large near the exit of the slower) and focusing of the slowing beam (useful for limiting the increase of transverse velocity components) lead to a saturation parameter that is a function of position [306]. These subtleties will be explored further in the discussion of the Zeeman design used for our Sr experiment in Sec. 5.3

3.2.3. The Magneto-Optical Trap (MOT)

Optical molasses alone is not a trap: the random walk of an atom scattering red-detuned photons from every direction leads to a mean free path much less than width of the beams, such that many recoil events occur before the atom can wander out of the molasses region,but there is no restoring force to confine atoms inside this region. The MOT combines $\sigma^{\pm}$ optical molasses with the quadrupole field created by a set of current coils in the anti-Helmholtz (AH) configuration (equal and opposing currents, with the distance d between coils equal to the coil radius R) to create the necessary conditions for both the rapid cooling achieved by optical molasses and the restoring force required to create a confining potential.

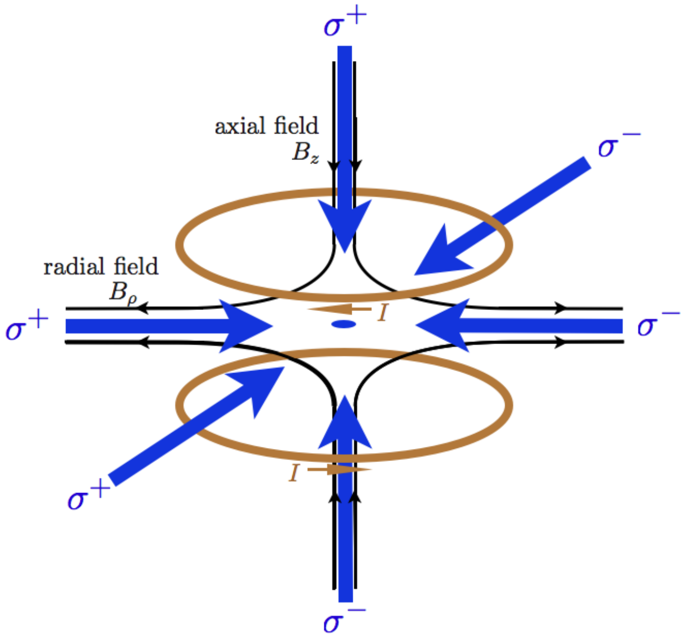

FIGURE 3.3. Magneto-optical trap (MOT) diagram: coil configuration and required trap beam polarizations for the magnetic field orientation used in both the top and bottom Sr MOTs.

Figure 3.3 depicts the traditional 6-beam MOT geometry; the optical molasses region overlaps the zero-field center of the quadrupole magnetic field. The resultant atomic energy-level shifts in one-dimension are shown in Fig. 3.4: the trap configuration requires the correct relative orientation of the $\sigma^{\pm}$ beams and the magnetic field such that each trap beam comes into resonance with atoms moving toward the beam as the atoms move away from the center. The Zeeman effect shifts the excited-state $m_J' \neq 0$ sublevels as the atoms move away from the center to bring the atoms into resonance with the opposing MOT beams, providing the spatial tuning of the scattering force.

In one dimension, we can write the total scattering force on an atom moving along the axis as the sum of the forces from the left- and right-propagating beams, as we did for optical molasses in Sec. 3.2.1.1. Again taking the assumption that $I \ll I_{sat}$, the force from each beam becomes

$$F_{\sigma^{\pm}} = \pm\hbar\mathbf{k}\,\frac{\Gamma}{2}\,\frac{I/I_{\mathrm{sat}}}{1+4(\Delta_{\mathrm{MOT}} \mp kv \mp \kappa A z)^2/\Gamma^2}, \tag{3.45}$$

where in the configuration depicted in Fig. 3.4, F_{σ^+} and F_{σ^-} arise from the rightward- and leftward-propagating beams, respectively. Here, as in Sec. 3.2.2, $\kappa = g_J \mu_B/\hbar$, and we have taken $A = dB/dz$ as the gradient of the magnetic field. The total one-dimensional MOT scattering force is then $F_{\mathrm{MOT}} = F_{\sigma^+} + F_{\sigma^-}$.

Similar to Sec. 3.2.1.1, the full expression simplifies considerably in the limit $|kv| \ll |\Delta|, \Gamma$ [224, 225]. The total force can then be written as

$$F_{\mathrm{MOT}} = -\alpha\, v - k_{\mathrm{trap}}\, z, \tag{3.46}$$

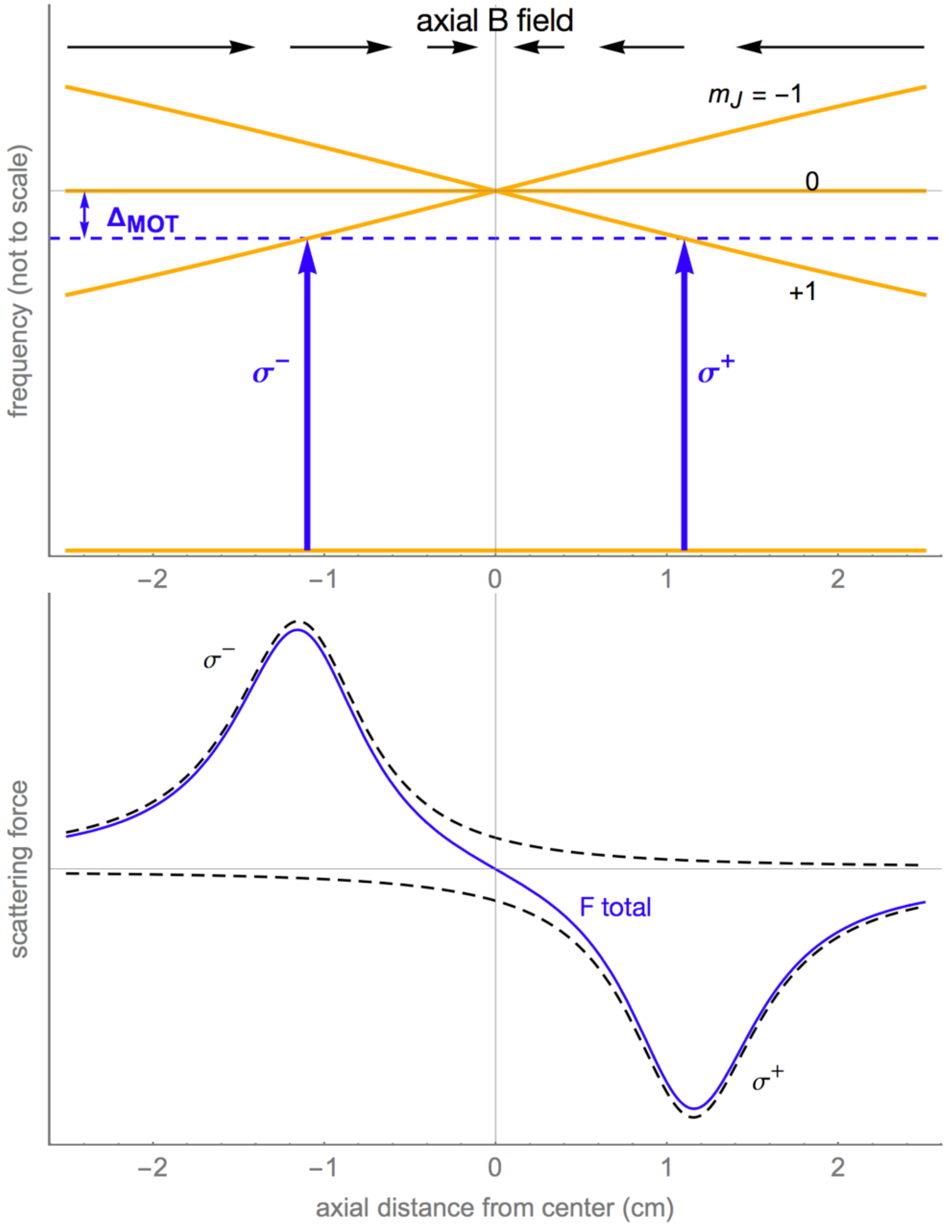

FIGURE 3.4. MOT Zeeman shift and scattering force: for the axial field of Fig. 3.3, the upward-propagating beam must have σ^- polarization, and the downward-propagating beam σ^+, for a total scattering force with the correct sign for confinement.

where the damping coefficient α is given by 3.13. The second term corresponds to a restoring force with spring-constant $k_{\text{trap}} = \alpha\,\kappa\,A/k$. The MOT thus retains the powerful cooling properties of optical molasses, rapidly damping atomic motion on the same characteristic timescale $\tau_{MOT} = \alpha/m$, and the confined motion corresponds to that of heavily overdamped harmonic oscillation at a frequency $\omega_{\text{MOT}} = \sqrt{k_{\text{trap}}/m}$.

In three dimensions, Gauss's law ($\nabla \cdot \mathbf{B} = 0$) implies that the direction of the field relative to the trap center will be opposite in the axial and radial directions (with the axial direction defined by the AH-coil-pair axis). The axial field gradient must be twice as large as the radial field gradient, so MOT confinement is typically tighter in the axial vs. radial directions: the axial k_{trap} is twice as large as the radial k_{trap}, and the oscillation frequencies will also differ by a factor of two.

The configuration depicted in Fig. 3.3 corresponds to the orientation of our coils for both the bottom and top Sr MOTs: the axial magnetic field points in towards the center of the trap, but the field points outward from the center in the radial directions. (The opposite configuration is easy to achieve by reversing the current in the AH coils, but the polarization of all beams must then switch as well.) The level shifts depicted in Fig. 3.4 are along the axial direction (vertical for our top MOT); the radial direction level shifts will be the mirror image to those shown, and the molasses beams must also be the opposite polarization from the axial beams to result in the same force diagram and achieve stable trapping in all three dimensions (although in general calculation of MOT dynamics in three dimensions is nontrivial — particularly when considering the effective lattice potentials that arise from MOT beam interference).

Note that if we keep the same magnetic field along the axial direction, but reverse the polarization of the two molasses beams, we will switch from a trapping configuration to a configuration where the two axial beams will push atoms *away* from the center of the trap. This is an important concept in the operation of the 2D top MOT that we use to load our science cell MOT, and will be discussed further in Sec. 6.2. Chapters 5 and 6 provide further discussion of practical MOT considerations like field gradient, MOT size, and MOT capture and loss dynamics, with specific reference to our top and bottom Sr MOT realizations.

3.3. Optical Dipole Force

The atomic interaction with the electromagnetic field can be treated classically as a dipole oscillating in response to the field excitation, with the strength of the response characterized by the atomic polarizability $\alpha(\omega)$. As in the quantum atom-field Hamiltonian 2.12, the energy of the interaction (with a factor of 1/2 to account for the fact that the dipole moment is *induced* by coupling to the electromagnetic field) is

$$V_{\text{dipole}} = -\frac{1}{2}\,\mathbf{d}\cdot\mathbf{E}, \tag{3.47}$$

where the atomic dipole moment is given by

$$\mathbf{d}^{\pm} = -e\,\mathbf{r}^{\pm} = \alpha(\omega)\mathbf{E}^{\pm}. \tag{3.48}$$

Here, the electron of charge e is assumed displaced by a distance $\mathbf{r}$ from the nucleus. The complex electric field positive- and negative-rotating components are denoted by E^{+} and E^{-}, which induce similar oscillating components in the electron position and hence the dipole moment.

A damped-harmonic-oscillator model for the electron equation of motion (the Lorentz model [43]) leads to a complex solution for $\alpha(\omega)$, which can be interpreted as the phase lag in the electron's response to the light field. This lag is related to the electron's radiation reaction force (and the damping term works out to be equivalent to Γ); as such the imaginary component $\mathrm{Im}[\alpha]$ is associated with the scattering force arising from absorption and spontaneous emission, while $\mathrm{Re}[\alpha]$ is associated with oscillation in phase with the driving field and the optical dipole force. The coherent, in-phase component can be interpreted as a stimulated emission response, a picture which explains the dependence of the dipole force on the existence of intensity gradients: for a plane wave, the net effect of absorption followed by stimulated emission involves no redistribution of momentum from the field to the atom, and there is no optical dipole force.

The classical picture also gives an intuitive approach to understanding the detuning dependence of the dipole force. The phase of any driven harmonic oscillator far from resonance matches that of the driving force when the drive frequency is far below resonance ($\Delta < 0$, or red-detuned), but is opposite when the drive frequency is far above resonance ($\Delta > 0$, or blue-detuned). As a result, an atom is attracted to / repelled from regions of high intensity for a dipole trap beam far detuned to the red / blue, respectively [311].

Under the approximation of one dominant resonance and large detuning, the classical approach to the dipole potential leads to

$$V_{\mathrm{dip}} = \frac{\hbar\Gamma^2}{8\Delta}\frac{I(\mathbf{r})}{I_{\mathrm{sat}}}. \tag{3.49}$$

This is equivalent to the result found semiclassically under the two-level-atom and rotating-wave approximations: when the detuning is large, the atom remains almost entirely in the ground state, so the excited-state population is eliminated from the problem, and the effective center-of-mass Hamiltonian becomes:

$$H_{\text{eff}} = \frac{p^2}{2m} + V_{\text{eff}}(\mathbf{r}), \tag{3.50}$$

where the first term is simply the kinetic energy of the atom and the second term,

$$V_{\text{eff}}(\mathbf{r}) = \frac{\hbar|\Omega(\mathbf{r})|^2}{4\Delta} = \frac{\hbar\Gamma^2}{8\Delta}\frac{I(\mathbf{r})}{I_{\text{sat}}}, \tag{3.51}$$

is equivalent to the ac-Stark shift of the ground state. An elegant approach to this result is the "dressed-atom" model introduced by Dalibard and Cohen-Tannoudji [312], which demonstrates that the eigenlevels of the atom-plus-photon Hamiltonian are shifted from the uncoupled system energy levels by the ac-Stark effect.

As a conservative potential, the dipole force is given by the negative gradient of the potential ($F_{\text{dip}} = -\nabla V_{\text{dip}}$) and so goes to zero unless $\nabla I(\mathbf{r}) \neq 0$. Note that the potential is proportional to the trap intensity and inversely proportional to detuning; this is in contrast to the scattering rate (Eq. 3.1), which in the limit of large detuning ($|\Delta| \gg \Omega, \Gamma$) becomes

$$R_{\text{scatt}} = \frac{\Gamma^2\Omega^2}{4\Delta^2}. \tag{3.52}$$

Residual photon scattering is responsible for dipole trap heating, so the fact that the scattering rate is inversely proportional to the *square* of the detuning is key to the success of the far-off-resonant dipole trap (FORT [268, 269]): with increased dipole-trap beam detuning, the scattering rate falls off more quickly than the dipole potential, such that larger beam intensities can be used to increase the trap depth with minimal photon scattering.

For accurate ac-Stark and dipole-potential calculations, the simple expression 3.51 is valid only to first order in Ω/Δ, since both the two-level-atom and rotating-wave assumptions are crude approximations when considering atomic interaction with far-detuned fields. The field couples the ground state to all higher-lying energy levels with a nontrivial dipole coupling rate, as given by the Rabi frequency $\Omega = -\mathbf{d}_{ge}E_0/\hbar$, where E_0 is the electric field amplitude and $\mathbf{d}_{ge} = \langle g|\,\hat{\epsilon}\cdot\mathbf{d}\,|e\rangle$ is the dipole matrix element which determines the strength of the ground to excited level coupling for a given electric field polarization $\hat{\epsilon}$. The full expression becomes a sum over all excited states $|e_j\rangle$ with the energy difference between $|g\rangle$ and $|e\rangle$ given by $\hbar\omega_{j0}$:

$$V_{\mathrm{dip}}(\mathbf{r}) = -\frac{\hbar}{4}|E_0(\mathbf{r})|^2 \sum_j |\,\langle g|\,\hat{\epsilon}\cdot\mathbf{d}\,|e_j\rangle\,|^2 \left(\frac{1}{\omega+\omega_{j0}} - \frac{1}{\omega-\omega_{j0}}\right). \tag{3.53}$$

For practical calculations, the sum can often be truncated after the first ~10 excited state levels as the higher-lying terms give negligible contributions, but we need the dipole matrix elements for those lower transitions.

Dipole matrix elements are related to measured transition rates through

$$\Gamma_{ik} = \frac{1}{4\pi\epsilon_0}\frac{4\omega_{ik}^3}{3\hbar c^3}|\,\langle e_i|\,\hat{\epsilon}\cdot\mathbf{d}\,|e_k\rangle\,|^2, \tag{3.54}$$

but experimentalists often report measured excited state lifetimes $1/\Gamma_T$ or the total transition rate Γ_T from the excited state to all states, in which case the branching ratios of possible decay paths must be taken into account to derive Γ_{ik}. The ratio Γ_{ik}/Γ_T is determined by a geometric factor that depends upon the laser polarization and the ground and excited state spin and angular momentum quantum numbers, as discussed (and tabulated for relevant Sr transitions) in Refs. [143] and [144].

In terms of transition rates, the ac-Stark shift of the ground state becomes

$$V_{\text{dip}}(\mathbf{r}) = -\frac{3\pi\epsilon_0 c^3}{4}|E_0(\mathbf{r})|^2 \sum_j \frac{\Gamma_{j0}}{\omega_{j0}^2}\left(\frac{1}{\omega+\omega_{j0}} - \frac{1}{\omega-\omega_{j0}}\right), \tag{3.55}$$

which with further simplification can be written as

$$V_{\text{dip}}(\mathbf{r}) = -\frac{1}{2}\alpha_g(\omega)|E_0(\mathbf{r})|^2 = -\frac{\alpha_g(\omega)I(r)}{\epsilon_0 c}, \tag{3.56}$$

where $\alpha_g(\omega)$ is the dynamic polarizability of the ground state. More generally, the dynamic polarizability for a given state $|e_i\rangle$ is

$$\alpha_i(\omega) = 6\pi\epsilon_0 c^3 \sum_k \frac{\Gamma_{ik}}{\omega_{ik}^2(\omega_{ik}^2 - \omega^2)}. \tag{3.57}$$

In the end, the quantum (semiclassical) calculation thus brings us back to the classical result for the dipole potential energy, with the quantum dependence hidden in the calculation of $\alpha_i(\omega)$.

In general, the ground and excited states of a strong optical transition will shift in opposite directions when exposed to a red-detuned dipole trap beam, such that loading into a dipole trap leads to shifts of the resonance transition with trap intensity, but at certain "magic" wavelengths the narrow intercombination transitions of the alkaline earth atoms experience no transition shift, as described in Sec. 2.2. This can be understood by considering the form of the dynamic polarizability: the dominant terms in the sum over dipole matrix elements for singlet (total spin $S = 0$) states are dipole-allowed transitions to other singlet levels, and likewise the dominant contributions to the dynamic polarizability of the triplet (S=1) states are from other triplets. As a result, the ground $^1\mathrm{S}_0$ and excited $^3\mathrm{P}_J$ states can shift in the same direction, and at certain wavelengths the shift is exactly the same. These wavelengths can be found by plotting $\alpha_{1S0}(\omega)$ and $\alpha_{3PJ}(\omega)$ to find the frequencies where the curves intersect [11], and experimentally verified by measuring the transition frequency dependence on trap beam intensity to find the wavelength at which the dependence is minimized [212].

3.3.1. Optical Dipole Trap

The simplest optical dipole trap is a single tightly focused Gaussian beam [313], with an intensity profile (for propagation along the z-axis)

$$I(r,z) = \frac{P}{\pi w^2(z)} e^{-2r^2/w^2(z)} \tag{3.58}$$

where P is the total beam power, $w(z)$ is the $1/e^2$ beam radius at a given point z as measured from the location of the tightest waist w_0,

$$w(z) = w_0 \sqrt{1 + \left(\frac{z}{z_R}\right)^2}, \tag{3.59}$$

and $z_R = \pi w_0^2/\lambda$ (the Rayleigh length) is the distance from the focus at which the beam has expanded to $\sqrt{2}w_0$. For a red-detuned beam, atoms colder than the the trap depth collect at the beam waist, with the trap depth defined as the magnitude of the maximum potential

$$U_0 = -V_{\rm dip}(0) = \alpha_g(\omega) \frac{P}{\epsilon_0\, c\, \pi w_0^2}. \tag{3.60}$$

Dipole traps cannot cool, but if the pre-cooled atomic thermal energy $k_B T \ll U_{\rm dip}$, the atoms are tightly localized at the focus, and the potential can be approximated as harmonic,

$$U_{\text{harmonic}} = \frac{1}{2} m\,\omega^2 x^2, \tag{3.61}$$

with characteristic motional frequencies ω in the radial and axial trap directions found by equating the second-order term of a Taylor expansion of U_{dip} to U_{harmonic} [215], leading to:

$$\omega_r = \sqrt{\frac{4U_0}{m w_0^2}}, \qquad \omega_z = \sqrt{\frac{2U_0}{m z_R^2}}. \tag{3.62}$$

3.3.2. Optical Lattice

Two focused counter-propagating Gaussian beams of equal intensities and beam waists produce an interference pattern with an intensity profile [313]

$$I(r, z) = \frac{4P}{\pi w^2(z)} e^{-2r^2/w^2(z)} \cos^2(kz). \tag{3.63}$$

This is identical to a single-beam dipole trap in the radial dependence but with four times the maximum intensity for the same power in each beam, and hence four times the trap depth,

$$U_0 = \alpha_g(\omega) \frac{4P}{\epsilon_0\, c\, \pi w_0^2}, \tag{3.64}$$

and the atoms are much more tightly localized in the axial direction in a periodic series of wells separated by $\lambda_L/2$, where $\lambda_L = 2\pi/k$ is the lattice wavelength. The radial trap frequency is identical to that of the dipole trap (Eq. 3.62), but the tight axial localization is evident in considering the new axial trap frequency, which can be found in the same way as above [100] to be

$$\omega_z = \sqrt{\frac{2U_0}{m \lambda_L^2}}. \tag{3.65}$$

This result is exactly parallel to the dipole trap axial frequency, with the axial localization scale z_R replaced with λ_L. The equilibrium width of an atomic cloud trapped in a single lattice well can then be found from equating the one-dimensional thermal and harmonic energies:

$$\frac{1}{2}k_{\mathrm{B}}T = \frac{1}{2}m\omega^2. \tag{3.66}$$

Alternatively, if the temperature of the atom cloud upon lattice loading is not known, lattice spectroscopy [100] can determine the mean vibrational level population.

CHAPTER IV

EXPERIMENTAL APPARATUS I: LASER SYSTEMS

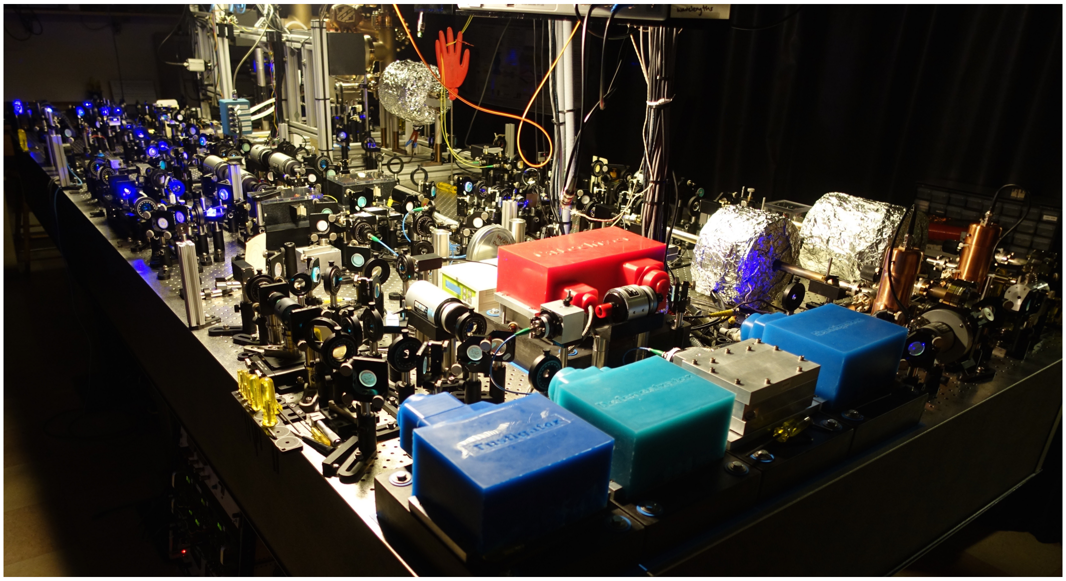

FIGURE 4.1. Strontium experiment optical table: view from master ECDL corner.

4.1. Laser Systems Overview

The strontium Casimir-Polder experiment requires four distinct laser systems, diagrammed schematically in Fig. 6.1; see Fig. 2.1 for a diagram of the relevant strontium energy levels and transition linewidths. The main cooling and blue MOT laser at 461 nm interacts with the strong cycling ${}^1\mathrm{S}_0 - {}^1\mathrm{P}_1$ transition, while the repump laser at 497 nm prevents blue MOT losses due to shelving in the metastable ${}^3\mathrm{P}_2$ state. The 689 nm system will generate even colder atomic samples in the narrow-linewdith ${}^1\mathrm{S}_0 - {}^3\mathrm{P}_1$ red MOT, and will also serve as the probe laser to monitor shifts in the energy levels of this transition due to the Casimir Polder effect. The optical lattice laser at 914 nm will be tuned to the ${}^1\mathrm{S}_0 - {}^3\mathrm{P}_1$ transition's “magic wavelength,” to hold the atoms in standing-wave dipole-potential wells without perturbing the frequency of this transition.

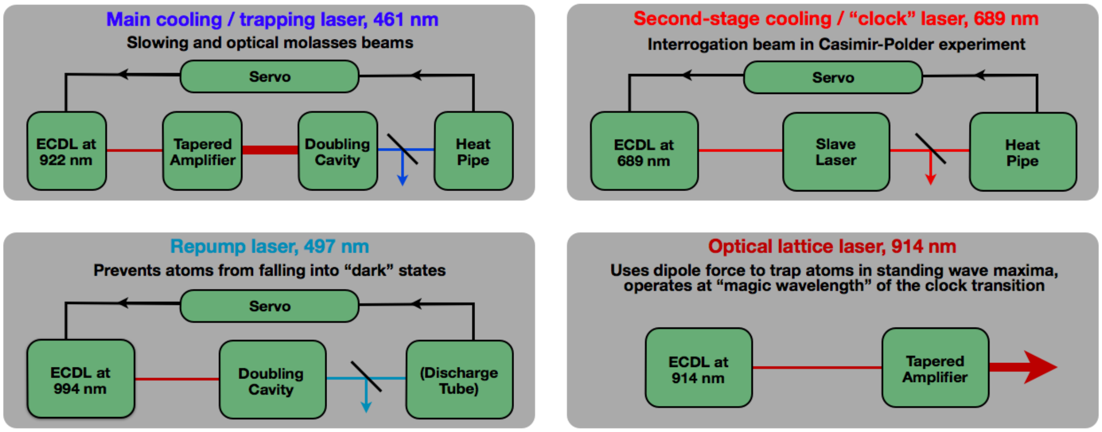

FIGURE 4.2. Strontium experiment laser systems: schematic diagram.

.

As many components are common to several laser systems, this chapter will introduce the principles of these subsystems. All four laser systems begin with a master external-cavity diode laser (ECDL), so we invested considerable effort in the development and characterization of an ultra-stable homebuilt design that was easily adaptable to all four wavelengths, described in Sec. 4.2. Three systems require external amplification to generate more power than that available directly out of the ECDL, a simple slave laser in the case of the 689 nm system and higher-powered tapered amplifiers for the 914 nm and 461 nm systems, described in Sec. 4.3. Due to the lack of reasonably-priced high-power diode lasers at the required blue and turquoise wavelengths at the time of construction, we use second-harmonic generation (SHG) in linear resonant build-up cavities for the 461 nm and 497 nm systems, as described in Sec. 4.4. Finally, the lasers interacting directly with specific atomic transitions should be stabilized to prevent slow frequency drifts off resonance. We use "heat pipe" strontium vapor-cell references for the 461 nm and 689 nm systems, and have a Sr discharge tube that could be used to lock the 497 nm system. Section 4.5 describes the strontium references and the frequency-modulation (FM) saturated-absorption spectroscopy setup used to generate the feedback signals for locking these laser systems to the heat pipe signals, and briefly discusses other laser stabilization options.

4.2. Stable External-Cavity Diode Laser (ECDL) Design

External-cavity diode lasers (ECDLs) have become an ubiquitous tool in atomic physics labs as a tunable, low-cost, energy-efficient, and compact light source available in an increasingly wide range of wavelengths [314]. Typical Fabry-Perot-style diode lasers, in which the front and back diode facets act as the lasing cavity mirrors, can offer a wide gain range (depending on operating temperature and current, often tens of nanometers). However the inherent linewidth is broad: the Schawlow-Townes-limited linewidth [315] alone would be at least 1–2 MHz, narrow enough for many cold-atom experiments, but significant contributions from other noise factors typically increase the width to several 10's of megahertz. The ECDL narrows the linewidth and allows tuning within the gain range by using a frequency-selective element as an external cavity mirror [316, 317].

A common ECDL configuration is the Littrow design, in which the rear diode facet acts as one cavity mirror and a diffraction grating acts as the second: the first-order reflection off the diffraction grating is fed back into the diode, and the zeroth-order reflection is coupled out of the cavity. The lasing frequency is thus tuned by changing the diffraction-grating angle, which changes both the length of the cavity and the frequency of the first-order beam (at the cost of a slight angle change on the output beam), and the linewidth is narrowed by both the diffraction-grating resolution and the extended length of the lasing cavity; linewidths ~ 1 MHz are easy to achieve. This simple configuration is the basis for many commercial precision diode laser systems, but for atomic-physics experiments requiring many very different wavelengths the cost of purchasing a commercial system for every source can become prohibitive; as a result there is considerable interest in the atomic-physics community in home-built ECDL designs.

We developed an ECDL design optimized for high stability, with a universal cavity block easily adapted to many wavelengths by selection of internal diode and optics and easily extended for an even-narrower-linewidth long-cavity version. The total cost for the parts and components (but excluding assembly labor) totaled ∼$6,000 (with a wide spread depending on cost of the diode itself), yet the measured linewidths and noise-susceptibility characteristics proved competitive with the published specifications of existing commercial systems (which at the time cost $20,000-$30,000). The design is freely available and has been replicated by many atomic physics groups. As this project is well-documented in our publication [318], an accompanying webpage which aids other groups in reproducing the design [319], and Ref. [144], this section is a brief summary of the project.

4.2.1. Development

Any Littrow ECDL design must incorporate both grating-angle tunability and some form of vertical cavity alignment mechanism; as such designs can be as simple as a kinematic mirror mount modified to hold the diode plus a collimation lens in one plate and the diffraction grating on the other [320]. However, any movable parts can lead to frequency instability: the tunable grating is thus the Achilles heel of the Littrow diode laser. An appealing alternative is the interference-filter-tuned "cat-

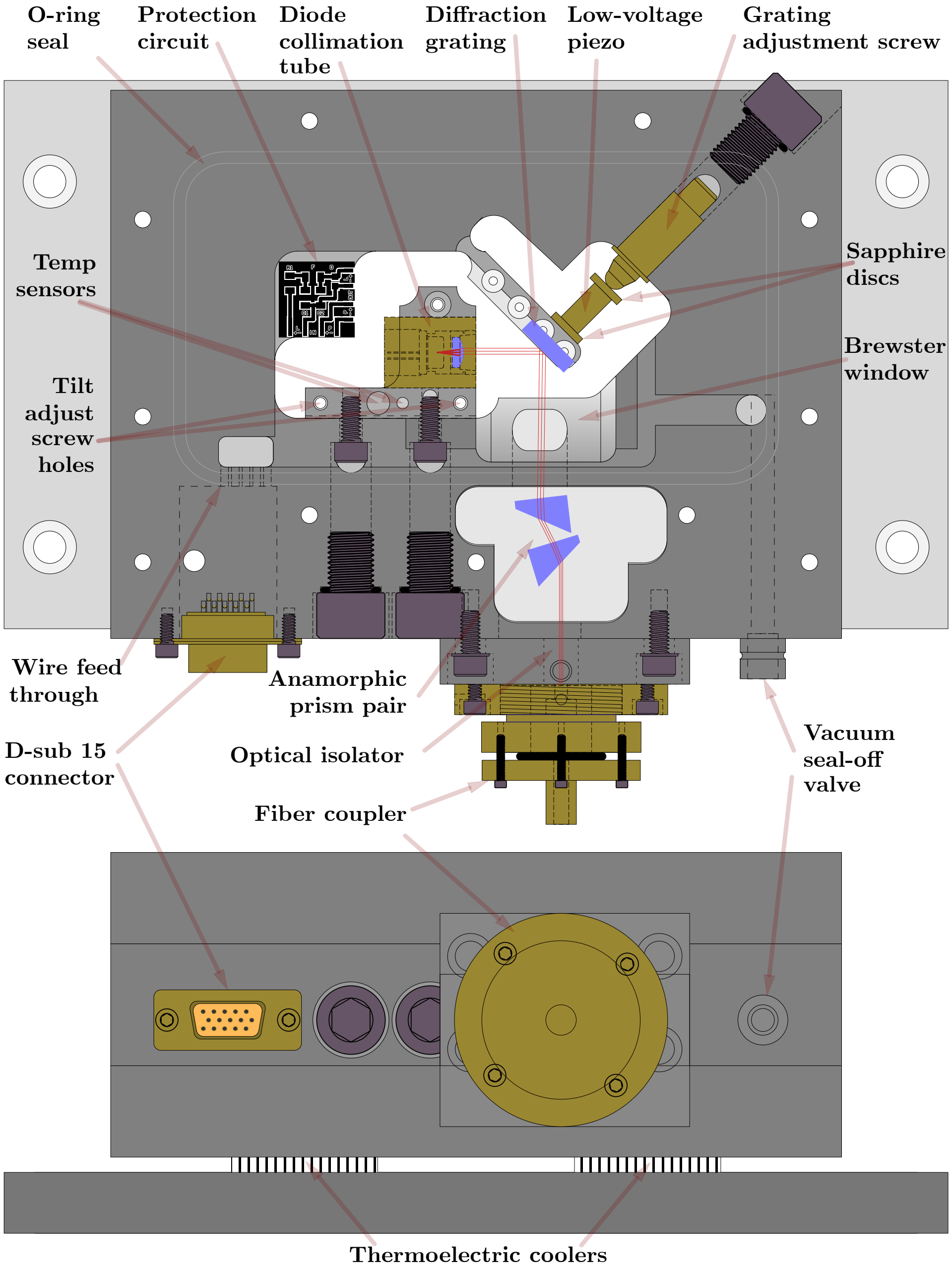

FIGURE 4.3. Stable external cavity diode laser (ECDL) design, top (lid off) and front view, with labeled peripherals.

eye" laser [321, 322], but we chose to use the Littrow configuration, optimizing our design to prevent the coupling of external noise into the cavity. The main cavity body is machined on a computer-numerical-controlled (CNC) milling machine from a single block of aluminum, and although the diffraction-grating arm is adjustable, it is machined from the same block and cut to be as stiff and light as possible to push its resonance frequency above the typical acoustic noise background. Further vibrational isolation is provided by mounting each laser on a damping baseplate and enclosing the entire body in a molded silicone cover. The design incorporates beam-shaping, optical isolation, and direct fiber-coupling, and can be vacuum/hermetically sealed to avoid long-term drifts from changes in atmospheric pressure and humidity [323].

Figure 4.3 is a diagram of the final ECDL design, for a 2.4-cm cavity-length laser. Our design utilizes a ∼45 degree angle of incidence on the diffraction grating, such that the same cavity can be used with different optics and diodes for different wavelength lasers, and the cavity body can be lengthened to narrow the linewidth. We constructed seven ECDLs with the 2.4-cm cavity-length, two prototypes at 780 nm and five of the final design, one at 780 nm and one each at the Sr experiment wavelengths. We also constructed one extra-long-cavity version of the design, stretching the entire cavity block between the diffraction grating and the diode can for a 10-cm cavity length. We use this laser as our 689 nm red MOT laser, since it has the narrowest linewidth.

4.2.2. Characterization

We characterized the short-term stability first by performing resonance spectroscopy on the diffraction-grating arm and found that the lowest resonance occurs at 12 kHz; by comparison, an older homebuilt Littrow-cavity laser (based on a modification of the popular Ricci design [324]) in use in our lab displays multiple resonances below 10 kHz, with the lowest at 1.8 kHz. We also examined the frequency-noise power-spectral-density of both new- and old-model lasers by monitoring the transmission of 780 nm versions through a rubidium vapor cell, which demonstrated both that grating-arm resonances are significant noise factors and that the new design is much less sensitive to external acoustic noise sources. Finally, we used delayed self-heterodyne spectroscopy [325] to characterize the short-term spectral widths of the old model and several new ECDL versions. While linewidths vary considerably depending on the diode used, for a 100 μs observation time we found linewidths of 32 kHz for the short-cavity 922 nm version (main Sr trapping laser, before frequency doubling) and an impressive 11.7 kHz for the long-cavity 689 nm model (red MOT laser / CP probe). These results demonstrate that our new ECDL design compares favorably with available commercial precision diode lasers.

4.3. ECDL Amplification

One limitation of external-cavity single-mode diode lasers is the low power output. For the red 689 nm MOT, we require at least 15 mW; the 689 nm extended-cavity version of our ECDL design can almost provide this much power, but taking into account losses in the beam path the situation would be borderline at best. For the blue 461 nm MOTs, we need at least 80 mW; since this light is produced by nonlinear SHG, several hundred milliwatts of 922 nm input light is required, far above the ~ 14 mW we see directly out of the 922 nm ECDL. The depth of the 994 nm optical lattice dipole trap will be proportional to lattice beam power, so again several hundred milliwatts or more would be ideal. For all of these systems, amplification of the ECDL output is required.

An amplifier is an external laser gain medium (usually of the same material as the original laser), pumped to population inversion (usually in the same way) [326]. When seeded by the original "master" laser, the stimulated photons amplify the original beam. Without seeding, the medium can appear to lase on its own due to amplified spontaneous emission (ASE), in which spontaneously emitted photons stimulate emission of identical photons. However, amplifiers lack a resonant cavity (other than undesirable partial reflections at the end facets), and ASE light is essentially amplified noise, so the spectral content of an ASE beam will generally be quite broad. On the other hand, the presence of a narrow-linewidth, stabilized seed beam above a certain power threshold leads quickly to overwhelming dominance of phase-coherent stimulated photons, such that the output amplified beam retains the spectral purity of the input seed. This configuration is sometimes referred to as a master oscillator power amplifier (MOPA).

The tapered amplifiers (TAs) used for our 922 nm and 914 nm systems are examples of diode chips designed to allow single-mode high-power amplification. The input seed is mode-matched into a narrow gain region which expands for high gain, while maintaining single-mode operation by matching the expansion angle to the diffraction angle at the design wavelength. With an input seed of typically 10 –14 mW from the master ECDLs, the TAs are capable of producing $\sim 300 - 350$ mW with 1 A drive current. Some precautions are in order when using the tapered amplifiers: they should not be pumped to saturation, corresponding to a measured seed beam intensity of $\sim$ 15 mW [144]. They also must never be operated without a seed, to prevent ASE light coupling backwards from the broad gain region into the narrow input, which could cause power damage. We use a photodiodes monitoring a small seed-beam pickoff to disable the TA current in the absence of a seed. For more details on the Sr project TAs, see Matthias Fuchs thesis [327] for the initial design and Paul Martin's thesis [144] for final design refinements and construction details.

Another method to boost the power of a spectrally pure source is not technically an amplifier but a separate oscillator entirely, a "slave" laser, injection locked to the master oscillator. The slave laser can be identical to the master, or more commonly (as in our case) a less-tunable, broader spectrum, potentially noisy laser. If the slave laser output overlaps the desired frequency range, injection of a seed beam of spectrally narrow, stabilized light pulls the stimulated emission process towards the seed beam frequency and phase until the population overwhelmingly reproduces the input light characteristics. Injection locking was first demonstrated as early as 1966 [328] in He-Ne gas lasers, and in diode lasers by 1981 [329]. Early experiments showed successful locking by proving that the heterodyne beatnote of the master and slave beams disappeared with upon injection locking, and spatial interference fringes demonstrated phase coherence as well as frequency locking. The laser spectra also remained overlapped in a Fabry-Perot analyzer as the (untuned) seed laser followed the master laser frequency tuning over a range known as the "injection bandwidth."

The external-cavity diode laser for the 689 nm system does not provide enough power for operation of the red MOT, but the extended cavity version has an impressively narrow linewidth as described in section 4.2. Injection locking of a 689 nm slave laser boosts the power while maintaining the master's spectral characteristics (as we confirmed by self-heterodyne measurements on the slave output). The slave is a simple Fabry-Perot diode laser in an acrylic housing, identical to the slave lasers constructed for the Rb experiment (see Refs. [215, 216, 311]). We seed the slave through the rejection port of an optical isolator at the slave output, again in the same manner as the Rb experiment, and the resulting output is typically ∼15 mW.

4.4. Second Harmonic Generation

Diode lasers are popular in atomic physics as a light source that is compact, low-cost, and tunable, but unfortunately there are still few diodes available at certain wavelengths. Blue diode lasers at strontium's 461 nm main trapping transition are now becoming available and are beginning to be used by Sr groups [330], but many of the commercially available systems are either low power or multimode and large bandwidth [331]; the cost of buying several low-power blue diode lasers was prohibitive at the time we were constructing our laser systems. To the best of our knowledge, there are no diodes offered at the repump transition wavelength of 497 nm. For both of these systems, we have built ECDLs at twice the required wavelength and use second harmonic generation (SHG) to reach the blue (or blue-green, in the case of 497 nm) wavelengths.

Second harmonic generation relies on the fact that a strong electric field in a crystal with a non-vanishing second-order electric susceptibility $\chi^{(2)}$ will generate a polarization field at twice the frequency of a fundamental input beam under the appropriate conditions. For the simplest case, treating both the fundamental and the second order polarization fields as plane waves and assuming negligible absorption, an expression for the expected second harmonic power P_2 can be derived from the inhomogenous Maxwell equations [332, 333]:

$$P_2 = 2\left(\frac{\mu_0}{\epsilon_0}\right)^{3/2} \frac{(2\omega)^2 d_{\mathrm{eff}}^2 L^2}{n_1 n_2^2} \, \frac{P_1^2}{A} \, \mathrm{sinc}^2(\mathit{\Delta} kL/\mathit{2}). \tag{4.1}$$

Here, ω is the frequency of the fundamental and 2ω that of the second harmonic, P_1 is the power and A is the cross-sectional beam area of the fundamental field, L is the crystal length, n_1 and n_2 are the indices of refraction for the fundamental and second harmonic, respectively, and $\Delta k = k_2 - 2k_1$ is the phase mismatch between the wave vectors $k_1 = n_1\omega/c$ of the fundamental and $k_2 = n_2 2\omega/c$ of the second harmonic. The effective nonlinear coefficient d_{eff} is a property of the material and the propagation direction of the beam. For efficient SHG, a crystal must offer a high d_{eff} and good transparency at both the fundamental and second harmonic wavelengths, as well as accessible phase-matching conditions.

The phase mismatch is a result of dispersion, and must be compensated, otherwise the fields are out of phase after propagating a distance $l_c = \Delta k/\pi$ (the "coherence length") and the instantaneously generated second-harmonic field interferes destructively with the second-harmonic field generated one coherence length earlier. Adjusting the propagation angle until the fundamental and second-harmonic beams experience the same index of refraction (taking advantage of crystal birefringence) is a common phase-matching solution. However, this technique constrains d_{eff} and has narrow temperature- and angle-tuning bandwidths. An increasingly popular alternative is "quasi-phase-matching" (QPM), in which the crystal is periodically-poled to reverse the sign of the nonlinear interaction every l_c such that the fundamental and second-harmonic beams walk out-of-phase and then back in-phase over the course of two coherence lengths [334]. Compared to birefriengent phase-matching, which achieves $\Delta k = 0$ throughout the crystal length, QPM appears to be a less efficient process since the second harmonic power grows linearly rather than quadratically with crystal length. However, QPM allows the propagation direction to be chosen to maximize the initial d_{eff}, offers broader temperature and angular bandwidths, and is intrinsically free of walk-off. For our 461 nm SHG system, we considered birefringent phase-matching in potassium niobate ($KNbO_3$) as the option offering the highest d_{eff} (16.4 pm/V), but crystals were hard to find and expensive, so we ended up choosing QPM in periodically-poled potassium titanyl phosphate ("PPKTP") as an option with a relatively high d_{eff}=14.8 pm/V at 461 nm [335].

The Sr MOT requires at least 80 mW of 461 nm light (taking into account the diffraction efficiencies of the MOT and Zeeman AOMs), but the 922 nm ECDL only puts out 15 mW, which would only give us 0.3 mW of blue light at the single-pass conversion efficiency of $\eta = P_{2\omega}/P_{\omega}^2 = 1.5$ mW/W^2 measured for our 1-cm long crystal. The 922 nm tapered amplifier provides about 300 mW at typical operating currents, but this is still not enough power to provide the necessary blue light, so a resonant build-up cavity is required. Many groups use a bow-tie ring-cavity configuration for SHG, but we opted for a standing-wave linear cavity as a compact option offering greater mechanical stability and potentially higher conversion efficiency [336].

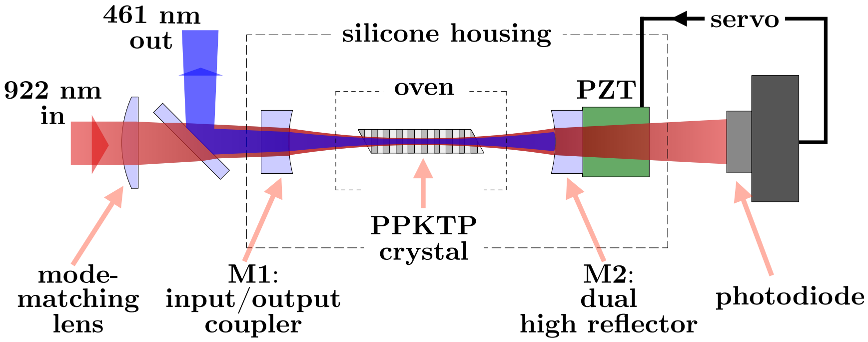

FIGURE 4.4. SHG cavity for 922 → 461 nm frequency doubling (not to scale).

Figure 4.4 depicts the cavity design for the 461 nm SHG system. The cavity consists of two 25-mm radius-of-curvature concave mirrors surrounding the crystal, the front mirror (M1) anti-reflection (AR) coated for 461 nm and partially high-reflecting (HR) for 922 nm (transmission T∼7% to impedance match other cavity losses) and the rear mirror (M2) HR-coated for both wavelengths: as such the cavity is a resonator for 922 nm and double-pass through the crystal, effectively doubling the crystal length. To achieve constructive interference of the first- and second-pass generated 461 nm beams, the crystal face is angled to allow phase correction via translation perpendicular to the cavity axis [337]. The blue light exits through the input coupler and is picked off by a dichroic in front of the cavity. The cavity is locked to the 922 nm resonance by monitoring the transmission and feeding back to a ring piezo behind M2. The crystal is mounted on a three-axis tip-tilt stage in a homebuilt oven at typically 29.7 °C.

We have seen up to 150 mW of steady-state blue light output for 300 mW of 922 nm at the input, but several factors affect cavity stability and the conversion efficiency. We opted for a relatively large beam waist inside the crystal to try to avoid thermal effects [335], but we have still observed thermal bistability [338], which manifests as a cavity resonance asymmetry with respect to the piezo sweep direction. As the piezo decreases the cavity length and and approaches the 922 nm resonance condition, the increase in circulating cavity power heats the crystal and increases the index of refraction, effectively increasing the optical path length in the crystal and working against the piezo length change, leading to a broader cavity resonance. On the opposite side of the piezo ramp, on the other hand, the peak is much narrower. When this effect is too severe, it is impossible to lock the cavity. Our original crystal oven was an aluminum copper block with a channel for crystal alignment jigs and a lid which clamped a roll of copper mesh against the top of the crystal to hold it in place; we replaced this assembly with a copper oven with a mirror-polished surface for better thermal contact with the base of the crystal. We still see slightly asymmetric peaks when ramping the cavity, and the broadening seems to be much worse in some parts of the crystal, but at "good" crystal locations the asymmetry does not prevent locking.

We also had issues with the cavity unlocking in response to loud noises and optical table vibrations (e.g., from the main MOT camera shutter — see Sec. 6.3.2.2). The cavity platform is machined from a solid $2.5'' \times 2.5''$ aluminum block, with an inset for the tip/tilt stage and separate plates for each cavity mirror (the modularity eases the cavity alignment process), which allowed us to use the shortest possible optical mounts for stability, but the kinematic mirror mounts still display ~ 1 kHz resonances which couple to other table vibrations. Rather than eliminate every source of vibration, we found that the simplest solution was the installation of a small cavity-relock circuit, adapted from a design by the Killian group [339], which uses a four-way switch to simply bypass the proportional and integral stages of the lock circuit and re-engage the cavity ramp any time the cavity power falls below a certain threshold. The lock stages are reenabled as soon as the threshold condition is met. This circuit prevents cavity unlocking events from being a serious headache, but it does not prevent all issues with cavity power fluctuations and occasional unlocking events at inconvenient times during experimental cycles.

The efficiency requirements of the 497 nm SHG system are much less stringent than the 461 nm system: the 497 nm laser repumps on the ${}^3\mathrm{P}_2 - {}^3\mathrm{D}_2$ transition, which has a saturation intensity of only 2.4 mW/cm^2. We purchased a commercial PPLN (periodically-poled $\mathrm{LiNbO_3}$) crystal from Covesion, Inc., which offers five poled tracks of different poling periods, three of which work for our wavelengths (although at relatively high temperatures — 211–240°C — but reachable with the standard crystal oven). We opted for a 2-cm long crystal, hoping that if we eventually build a 994 nm tapered amplifier or slave laser we may get enough 497 nm power out of a single-pass through the crystal, but for now a build-up cavity is still required. The conversion efficiency does not need to be very high, however, so we used the same mirrors and the same linear design as the 461 nm cavity. These mirrors are fairly lossy at 994 nm, and a bow-tie design would be preferable: since this crystal is not wedged, only temperature tuning and crystal tilt can be used to phase-match the first- and second-pass 497 nm beams. As a result of this issue (or competing etalon effects from reflections off the normal crystal facets), the cavity is extremely finicky to align well; the peak height fluctuates wildly with small adjustments, which we attribute to interference effects. However, this crude cavity still puts out as much as 5 mW at 497 nm when carefully aligned, pumped only by our standard ECDL with a high-power 994 nm diode (no external amplification), and usually gives ~ 1 mW on a day-to-day basis, so it is more than sufficient for our needs.

A disadvantage of linear resonant cavities is the problem of optical feedback destabilizing the input laser: when the cavity is not tuned to resonance, essentially all the input light is rejected and back-reflected, and even when locked on resonance any light that is not mode-matched will not couple into the cavity and likewise can back-reflect into the input laser. Diode lasers are notoriously susceptible to optical feedback, and tapered amplifiers can be damaged by small back-reflected seeds, so the 922nm system already had one 30 dB isolator installed between the master ECDL and the tapered amplifier as well as two 40 dB isolators after the tapered amplifier. However, after constructing the 461 nm SHG cavity we observed frequency and amplitude jitter on the Fabry-Perot monitoring the 922 nm TA seed, jitter that would disappear when the SHG cavity was blocked. It seemed surprising that a back-reflection from the cavity could propagate all the way through three optical isolators, the tapered amplifier chip itself, and the single-mode fiber porting the 922 nm seed light to the tapered amplifier, but installing a second isolator after the master laser fixed the problem: somehow the frequency and amplitude jitter were a result of SHG cavity feedback de-stabilizing the ECDL. We later found that Marquardt *et al.* [340] mention a similar issue in an ECDL-MOPA setup driving a sum-frequency-generation cavity; they also needed two isolators between their ECDL and the TA to prevent instabilities caused by optical feedback from the build-up cavity after the TA. Our 994 nm system also uses two optical isolators between the ECDL and the resonant build-up cavity to prevent similar issues.

4.5. Laser Stabilization

Our diode laser design demonstrates impressive passive stability: the free-running 922 nm master ECDL used to produce the 461 nm trap light will often stay within one linewidth (32 MHz) of the center of the main cooling transition for several minutes, and we are not currently actively stabilizing our repump laser. However, in atomic physics we are asking our free-running lasers, operating at frequencies of several hundred terahertz, to hit a frequency target the width of an atomic transition, typical a few to tens of megahertz: in other words we are requiring a frequency stability of one part in 10^9 from our laser systems.[1] For most applications, some form of frequency stabilization is required to lock the master laser systems to the atomic transition.

---

[1] For the 689 nm laser interrogating the 7.5 kHz transition, the requirement is even more strict at a part in 10^{11}.

A simple solution monitors the transmission of the laser through a separate atomic vapor source and feeds back to the laser frequency control to keep the laser centered on the absorption dip. However, as discussed in Section 2.2, strontium has a low vapor pressure and a hot oven is required to generate a sufficient optically-dense vapor. Hot strontium will react corrosively with glass viewports and the copper gaskets typically used in UHV flanges, however, so the vapor must be contained in a manner that avoids these problems. One solution is known as a "heat pipe" [341], [342], [343]: a long vacuum chamber with axial viewports contains solid strontium in a central region, heated to produce the optically-dense vapor. The chamber also contains an inert gas throughout the volume. As the hot strontium atoms leave the central heated region, momentum losses via collisions with this "buffer" gas prevent the atoms from reaching the chamber gaskets and windows. As long as the Sr mean-free-path in the cold buffer gas region is much shorter than the distance to the windows, the windows will not be contaminated.[2]

Our heat-pipe design is described in Sec. 4.5.1. The Doppler-broadened lineshape of a hot atomic vapor can be GHz-wide, so we use the technique of saturated absorption spectroscopy to obtain a nearly-Doppler-free absorption feature; this technique and the broadening and shifting mechanisms present in our measurements are discussed in Sec. 4.5.2. Sec. 4.5.3 describes frequency-modulation (FM) spectroscopy, a technique to obtain a dispersive, background-free "error signal" from the Lorentzian saturated-absorption lineshape.Finally, Sec. 4.5.4 describes other

---

[2] Although many atomic physics groups have adopted the nomenclature "heat pipe" to describe this apparatus, the mechanism at work is not identical to the original heat pipe design [341], in which the atomic sample is heated above the boiling point to produce a vapor that condenses to a liquid upon collisions with the buffer gas. These heat pipes are recirculating, since the liquid drops are wicked back to the center by capillary action along the thermal gradient, and produce a pure vapor in the central region. We would prefer not to operate our heat pipes above strontium's 777°C melting point.

atomic vapor references and locking techniques which we have considered and which may be useful for laser stabilization in future renovations of the Sr apparatus.

4.5.1. Heat Pipe

Our heat-pipe design contains solid strontium pellets in a 10-cm-long nickel crucible with 5-mm diameter axial holes to pass the spectroscopy beams. This crucible slides into a 0.75" OD stainless steel pipe with a viewport on one end and the other mated to a 4-way cross. A right-angle valve (MKS CV16-C1C1-MKKCV) and a thermocouple vacuum gauge (Duniway DST-531) are also mated to the cross; the final port meets a stainless steel nipple to a final viewport. On both ends, the viewports are attached to flanges welded at a 3° angle to prevent etalon effects. A 1/8" stainless-steel rod spot-welded to the inside of the long pipe section near the 4-way-cross secures the position of the Ni crucible containing the strontium midway between the two glass viewports. Ceramic clamshell heaters (Thermcraft RL106-S-L / VIP-2.5-8-0.75-2) with 4"-long non-inductively-wound resistive-heating elements and 2" thick insulation packages heat the outside of the long pipe at the location of the nickel crucible, and a J-Type thermocouple inside the insulation package near the heating element monitors the temperature.

The heat pipe does not require ultrahigh vacuum (UHV), but strontium rapidly oxidizes when exposed to air. To avoid contamination, we followed the vacuum-cleanliness precautions described in Sec. 5.5 throughout assembly and pumped down to a rough vacuum before loading the strontium. We then backfilled the chamber with argon by bringing the system back up to atmosphere with the turbopump leak valve connected to an argon canister. We enclosed the entire chamber in a glove bag (Sigma Aldrich AtmosBag) suffused with a steady flow of argon to load the nickel canister with ~3 g of solid strontium (from Sigma Aldrich, dendritic pieces ≥99.9% purity packed in argon; we found we had to cut the pieces into smaller chunks using a clean wire cutter to fit into our canister) then pumped down again. Finally, we backfilled with argon again, monitoring the thermocouple gauge to close-off the right-angle valve to the pumpdown station when we attained the desired argon pressure.

The length between the heated section containing the strontium vapor and the viewports is $L = 30$ cm. To estimate the buffer gas pressure required to prevent window contamination, we can assume that we want a maximum mean-free-path l on the order of one-tenth this distance, or

$$l \approx \frac{1}{n_{Ar}\sqrt{2}\pi d^2} = \frac{k_{\mathrm{B}}T}{P_{Ar}\sqrt{2}\pi d^2} \leq 3 \text{ cm} \tag{4.2}$$

where n_{Ar} is the argon number density, T is taken to be room temperature outside the heated region, and we assume that d is the average of the ground-state atomic radii, $d_{Sr} = 219$ pm and $d_{Ar} = 71$ pm. This estimate leads to $P_{Ar} \approx 11$ mTorr. In practice, the thermocouple gauge and manually-actuated rotary valve do not allow precise control of the argon backfill pressure. The gauge has a ~3 s response time and can only read down to 1 mTorr; our procedure was to tighten the valve nearly closed before backfill, crack it one-eighth turn open, begin backfill and shut the valve as soon as we began to see the thermocouple gauge monitor begin to rise. We aimed for ~10 mTorr but erred on the high side, reasoning that pressure-broadening effects (discussed in Sec. 4.5.2) would not affect our error-signal zero-crossing, and if they proved to be a problem at a later date we could then pump out a little more argon.[3]

---

[3] Ideally, one would begin with too much argon in the pipe and monitor the probe laser transmission, decreasing the argon pressure slowly until pressure-broadening of the saturated-absorption resonance is minimized [343]. It may be difficult to do this with our turbo station since the pumpdown rate is rapid and the valve does not allow very fine control.

The clamshell heaters are rated to 1010°C but we shouldn't need to run this hot for a sufficient strontium number density. Using the known vapor pressure curve and Beer's law, we can estimate the temperature required for a given atomic transition [343]. Beer's law states simply that the intensity of light through an atomic vapor of density n decays exponentially (assuming we are operating below saturation intensity, $I \ll I_{\text{sat}}$) with length [225]:

$$I(\omega, z) = I(\omega, 0) e^{-n\sigma(\omega) z}, \tag{4.3}$$

where the absorption cross-section as a function of laser frequency

$$\sigma(\omega) = \frac{\sigma_0}{1 + \frac{4(\omega - \omega_0 - \mathbf{k} \cdot \mathbf{v})^2}{\Gamma^2}} \tag{4.4}$$

is a Lorentzian of width Γ centered at the atomic transition frequency ω_0 minus any Doppler shift $\mathbf{k} \cdot \mathbf{v}$, weighted by the resonant cross-section $\sigma_0 = 3\lambda_0^2/(2\pi)$. The cross-section depends strongly on the velocity v of the atoms, so we can recast Beer's law as a function of temperature by considering that the number density is a function of velocity (Maxwell-Boltzmann distribution),

$$n(v) = n_0 f_{MB}(v) = \frac{n_0}{\sqrt{2\pi} v_T} e^{-v^2/2v_T^2}, \quad \text{where} \quad v_T = \sqrt{\frac{k_{\text{B}} T}{m}} \quad \text{and} \quad n_0 = P/kT, \tag{4.5}$$

and the total transmission intensity I/I_0 through a vapor of length L (assuming the number density is constant over the laser path, which is an idealization) is then found by integrating over all velocity classes:

$$I/I_0 = \exp\left[\frac{-n_0 \sigma_0 L}{\sqrt{2\pi} v_T} \int \frac{e^{-v^2/v_T^2}}{1 + \frac{4(\omega - \omega_0 - kv)^2}{\Gamma^2}} dv\right]. \tag{4.6}$$

To simplify the integral, we can show that the absorption cross-section as a function of velocity is a Lorentzian of width Γ/k, while the number density is a Gaussian of width v_T. For thermal atoms we can expect a Doppler width $kv_T/2\pi \approx 1$ GHz while the natural linewidth $\Gamma/2\pi$ is 32 MHz for the 461 nm transition and only 7.5 kHz for the 689 nm transition, so the Lorentzian absorption cross-section (properly normalized) can be approximated as a delta-function under the integral:

$$\sigma(v) = \sigma_0 \frac{\pi}{2}\frac{\Gamma}{k}\left(\frac{1}{\pi}\frac{\frac{1}{2}\frac{\Gamma}{k}}{(v - \frac{\omega-\omega_0}{k})^2 + \left(\frac{1}{2}\frac{\Gamma}{k}\right)^2}\right) \approx \sigma_0 \frac{\pi}{2}\frac{\Gamma}{k}\delta(v - \frac{\omega-\omega_0}{k}), \tag{4.7}$$

leaving

$$I/I_0 = \exp\left[- n_0\sigma_0 L\sqrt{\frac{\pi}{8}}\frac{\Gamma}{kv_T}e^{-(\omega-\omega_0)^2/2(kv_T)^2}\right]. \tag{4.8}$$

The expected transmisison as a function of T is plotted for the 461 nm ($^1\mathrm{S}_0 - {}^1\mathrm{P}_1$) and 689 nm ($^1\mathrm{S}_0 - {}^3\mathrm{P}_1$) transitions, with resonant cross-sections $\sigma_0 = 0.10$ and 0.23 $\mu\mathrm{m}^2$ respectively, in Fig. 4.5. A transmission of ∼50% might be a good goal, but anything in the range of 10%-90% should work. As expected the narrow linewidth and low scattering rate of the 689 nm transition necessitates a hotter oven but the required temperatures are still easily achievable.

In practice we find that we need to run the 689 nm heat pipe a little hotter than expected, and we also do not see nearly as much absorption of the 461 nm light as this simple model would lead us to expect. The discrepancy could be explained by the placement of the thermocouple along the outside of the pipe failing to accurately reflect the true temperature of the atoms in the center of the oven. We eventually settled on steady-state operating temperatures of 420°C for the 461 nm heatpipe and 450°C for the 689 nm heatpipe for reliable absorption dips that could be used to lock our lasers. However, over time much of the strontium has migrated away from the

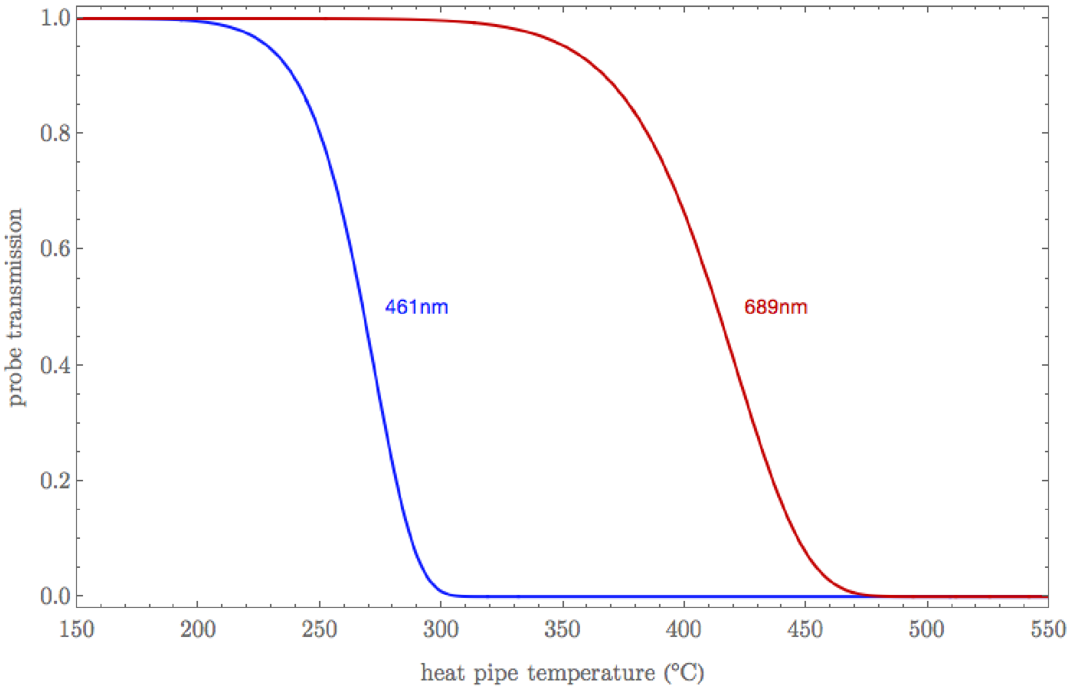

FIGURE 4.5. Heat pipe resonant probe transmission vs. temperature, as predicted by Eq. 4.5.1, for the 461 nm $^1S_0 - {}^1P_1$ and 689 nm $^1S_0 - {}^3P_1$ transitions.

center of the crucible; we now find that shifting the heaters from day to day is the best method to ensure a strong signal, and the heat pipes will need to be refilled in the near future.

The heaters were originally powered by Variacs switched by a simple on/off temperature controller (Love Controls TCS-4011), but one of the controllers failed (in the on position, allowing the temperature to rise to the maximum allowed by the Variac set point) after about a week. Some troubleshooting eventually revealed that the mechanical relays in the temperature controllers were not designed to switch high-current loads over the number of cycles required for continuous operation. The controllers now switch a 5 V signal powering a solid-state relay (Omron G3NA-220B) to switch the Variac voltage on and off; this control scheme has worked for several years.

4.5.2. Saturated Absorption Spectroscopy

The heat pipes provide an optically-dense vapor samples sufficient to monitor probe absorption, but the necessary temperature results in a severely Doppler-broadened lineshape of width

$$\Delta\omega_D = 2\sqrt{\ln 2}\frac{v_{mp}}{c}\omega_0, \quad \text{where} \quad v_{mp} = \sqrt{\frac{2k_{\mathrm{B}}T}{m}}. \tag{4.9}$$

For the 461 nm heat pipe at T = 420°C we can expect $\Delta\omega_D/2\pi = 1.3$ GHz, and for the 689 nm heat pipe at T = 450°C, $\Delta\omega_D/2\pi = 0.9$ GHz.

Saturated absorption spectroscopy [344, 345] uses two counter-propagating beams to obtain atomic spectra free from first-order Doppler broadening. The Doppler shift of an atom moving toward the pump beam is opposite the shift observed by the probe beam, such that the beams interact with different velocity classes when their detuning from resonance is nonzero. As the frequency of both beams is swept across the resonance the two beams interact simultaneously only with the atoms at zero velocity (if the two beams have zero frequency offset from one another). When the pump beam is well above the saturation intensity but the probe beam is well below, the probe transmission displays a narrow feature (the Lamb dip) at the center of a Doppler-broadened absorption lineshape, resulting from the decrease in probe absorption on the part of the zero-velocity-class atoms that are already saturated by the pump beam interaction. (If the pump and probe beams are detuned relative to one another by $\Delta_p = \Delta_{\text{pump}} - \Delta_{\text{probe}}$, this feature will shift by $\Delta_p/2$ from the center of the atomic transition.)

The Lamb dip recorded by saturation spectroscopy can have a linewidth on the order of the natural width of the transition, but a number of broadening mechanisms still come into play. Collisional broadening can come into play for dense atomic vapors, but power-broadening (see Fig. 3.1) is often the strongest effect: although the probe should be weak, maximum depopulation of the ground state and hence the strongest saturation signal will occur when the pump beam is at or above saturation intensity I_{sat}, leading to a power-broadened linewidth of

$$\Delta\omega_P = \Gamma\left(1 + \frac{I}{I_{sat}}\right)^{1/2}. \tag{4.10}$$

The extremely low saturation intensity of the red transition makes operation right at this level impractical: we use a pump beam of area ~1 mm^2 so to be below the saturation intensity of $I_{sat} = 3\ \mu\text{W/cm}^2$ would require using less than 30 nW, a beam that would be very difficult to align. A typical operating power of $I_{pump} = 0.5$ mW for the 461 nm saturated absorption system implies a power broadened linewidth of 47 MHz, which is not a huge increase over the natural $\Gamma/2\pi = 32$ MHz, but for the 689 nm system we see a linewidth of almost 1 MHz for the same pump power, a drastic increase over the 7.4 kHz natural linewidth.

Power broadening likely dominates our observed saturated absorption-linewidths, but it is worth considering other broadening mechanisms that would not normally be significant for typical ~MHz-linewidths atomic transitions but that may come into play for our narrow 689 nm error signal. One example is transit-time broadening: if an atom is moving quickly enough that it crosses the probe beam in a shorter time than the natural lifetime of the excited state, the frequency of the transition cannot be resolved to any accuracy greater than the inverse of this transit time. For a probe beam $1/e$ waist of w_0, this means that we expect a linewidth on the order of v_{mp}/w_0. A full derivation [346] finds that transit time effects lead to a lineshape of width

$$\Delta\omega_{tt} = \sqrt{2}\frac{v_{mp}}{w_0} \tag{4.11}$$

for narrow transitions. For our 2 mm probe beams, this effect is not trivial: in our heat pipe at 420°C the atoms are moving at 360 m/s and and so can cross the beam in 5.5 μs, which is far longer than the excited state lifetime $\tau = 1/\Gamma = 4.9$ ns of the 461 nm transition but shorter than the 20 μs lifetime of the 689 nm excited state, so transit time effects will be important. Indeed, the expected $\Delta\omega_{tt}/2\pi = 41$ kHz is not insignificant compared to the 7.6 kHz natural linewidth, but this effect remains insignificant compared to the power-broadened linewidth.

Collisional broadening - and potentially lineshifts - could be a more significant issue for our heat pipe saturated-absorption setup. Collisional broadening can be easily understood as a modification of the excited state lifetime as a result of collisional deexcitation, while collisional shifts – more commonly referred to as pressure shifts – can be seen as energy shifts to the ground and excited states resulting from the near-field Casimir-Polder (van-der-Waals / Lennard-Jones) interaction of two atoms in close proximity. Collisional broadening adds a homogenous decay rate $\Gamma_c = 2\sigma_b\langle v\rangle n$ to the natural transition decay rate Γ, and pressure shifts scale as $\Delta\omega_p = \sigma_p\langle v\rangle n$, where $\langle v\rangle$ is the relative collisional velocity of the two colliding species and n is the average number density. We rely upon measured collisional broadening and collisional shift cross-sections, σ_b and σ_p respectively, from Chan *et al.* [347] for the 461 nm transition and Crane *et al.* [218] for the 689 nm transition to estimate the collisional effects, which must be considered both for Sr-Sr collisions (expected to be a very small

	$\sigma_{b\ \mathrm{Sr-Sr}}$	$\sigma_{b\ \mathrm{Sr-Ar}}$	$\sigma_{p\ \mathrm{Sr-Ar}}$	Ref.
$^1\mathrm{S}_0 - {}^1\mathrm{P}_1$	–	2.97×10^{-14} cm^2	-0.96×10^{-14} cm^2	[347]
at $T = 420°\mathrm{C}$	–	$\Gamma_c/2\pi = 289$ kHz	$\Delta\omega_p/2\pi = -47$ kHz	
$^1\mathrm{S}_0 - {}^3\mathrm{P}_1$	6.55×10^{-14} cm^2	1.52×10^{-14} cm^2	–	[218]
at $T = 450°\mathrm{C}$	$\Gamma_c/2\pi = 11.4$ kHz	$\Gamma_c/2\pi = 145$ kHz	–	

TABLE 4.1. Reported ^{88}Sr collisional broadening and pressure shift cross-sections for Sr-Sr and Sr-Ar collisions, and the effective linewidth increase $\Gamma_c/2\pi$ or transition shift $\Delta\omega/2\pi$ expected at our heat pipe operating temperatures and an Ar buffer gas pressure of 30 mTorr.)

effect, given ^{88}Sr's small scattering length [217]) and Sr-Ar collisions, but reported values are not available for all cross-sections; see Table 4.1. While Sr-Ar collisional broadening is significant for the $^1\mathrm{S}_0 - {}^3\mathrm{P}_1$ transition, these effects remain well below the power-broadening systematics, and should not affect our laser servo lock points.

4.5.3. Frequency Modulation (FM) Spectroscopy

Saturated absorption spectroscopy gives us a sub-Doppler spectral feature centered at the atomic resonance (or, as in our case, one-half of the pump-probe detuning Δ_p). To lock our laser to this feature we need to convert this approximately Lorentzian lineshape into an "error signal", or an asymmetric function proportional to detuning from the line center.[4] We also need to subtract off or cancel the Doppler-broadened background absorption to prevent shifts in the error-signal zero-crossing due to amplitude fluctuations in the pump and probe beams. We use frequency-modulation spectroscopy combined with lock-in detection to generate the background-free error signal that is fed back to the laser piezo to stabilize the output frequency.

---

[4] It is possible to side-lock to a Lorentzian feature, but the side-locking technique is sensitive to long-term drifts due to changes in alignment, pump/probe beam intensities, and feature linewidth.

Frequency-modulation (FM) spectroscopy [348] uses phase-modulated light to probe spectral features, taking advantage of the high sensitivity afforded by the heterodyning of probe sidebands to generate either absorptive or dispersive signals depending upon the phase of the demodulated transmission signal. The probe beam is generally phase-modulated using an electro-optic modulator (EOM), which consists of a crystal whose dielectric tensor is rapidly modulated by the application of a strong radiofrequency (RF) drive voltage. EOM's allow near-perfect phase modulation at frequencies in the MHz-GHz range.[5] For an input field $E_0(t) = \mathrm{Re}[E_0 e^{i\omega_c t}]$ aligned with the extraordinary axis of the crystal, an RF drive at ω_m will result in a transmitted field $E_1(t) = \mathrm{Re}[E_0 e^{i(\omega_c t + M cos \omega_m t)}]$, where M is the modulation index (also known as the modulation depth, since magnitude of M sets the maximum instantaneous angular frequency deviation from the original optical frequency ω_c). Expanding in a power series and collecting frequency terms, it can be shown that the field after the EOM is given by

$$E_1(t) = \mathrm{Re}[E_0 \sum_{n=-\infty}^{\infty} J_n(M) e^{i(\omega_c + n\omega_m)t}], \tag{4.12}$$

where $J_n(M)$ are Bessel functions of the first order. The resultant field thus consists of a carrier at the input optical frequency and a series of sidebands, spaced by the RF-modulation frequency, all weighted by their respective Bessel function values at the chosen modulation depth.

In FM spectroscopy, the modulation index is kept small such that the probe spectrum after the EOM consists of a strong carrier and two relatively weak sidebands:

---

[5] Frequency modulation can also be achieved by modulation of the laser current or the radio-frequency drive of an acousto-optic modulator (AOM), but both add significant amplitude modulation that would destroy the perfect cancellation of the sideband beats and shift the error-signal zero-crossing.

$M \ll 1, J_0 = 1, J_{\pm 1} = \pm 1/2$, and all other terms of equation 4.12 become zero. Upon transmission through an atomic vapor of length L, each frequency component experiences absorption and a phase shift such that the transmitted probe field becomes

$$E_p(t) = E_0[T_0 e^{i\omega_c t} + T_1 \frac{M}{2} e^{i(\omega_c+\omega_m)t} - T_{-1}\frac{M}{2} e^{i(\omega_c-\omega_m)t}], \tag{4.13}$$

where $T_n = e^{-\delta_n - i\phi_n}$ is a function of the amplitude attenuation $\delta_n = a_n L$ and phase shift $\phi_n = \eta_n L(\omega_c + n\omega_m)/c$ induced in each field component due to the effective absorption a_n and index η_n at that frequency.

The transmitted intensity of the probe beam beam $I_p(t) = 1/2\epsilon_0 c|E_p(t)|^2$ then contains not only the slowly varying intensity envelope but heterodyne beat signals at the RF-modulation frequency due to the interaction of the carrier and the two sidebands. Discarding the higher order terms $\propto M^2$, and simplifying the result considerably by assuming that the differential attenuation and phase shift for the carrier versus the sidebands will be quite small ($|\delta_0 - \delta_{\pm 1}|, |\phi_0 - \phi_{\pm 1}| \ll 1$, easily valid for diffuse atomic vapors or small ω_m relative to the Doppler-broadened linewidth), leaves:

$$I_p(t) = \epsilon_0 c|E_p(t)|^2 e^{-2\delta_0}[1 + (\delta_{-1} - \delta_1)M\text{cos}\omega_m t + (\phi_1 + \phi_{-1} - 2\phi_0)M\text{sin}\omega_m t]. \tag{4.14}$$

Phase-sensitive detection (demodulation of the photodiode signal at the EOM's RF-drive frequency, with a variable phase-shifter between the RF local oscillator and the mixer) then allows isolation of the in-phase component, which is proportional to the difference in absorption between the upper and lower sidebands, and the quadrature component, proportional to the differential phase shift. If the phase modulation is achieved without any residual amplitude modulation, there is perfect cancellation between the upper- and lower-sideband beats when the carrier is either very far from the atomic resonance or at the center of a symmetric absorption line, but as the probe is swept across the feature the demodulated signals map out the phase or amplitude changes experienced by the sidebands with extremely high sensitivity: the original demonstration of the technique showed that extremely weak absorption lines (as low as 0.005% absorption) could be detected using FM spectroscopy [348].[6]

In the limit where the modulation frequency is larger than the linewidth of the absorption feature of interest, the feature can be probed by a single sideband and information about the absolute values of the absorption and effective index of refraction can be derived from the FM spectroscopy signals. As the carrier is swept across the spectral feature, the in-phase component reproduces the Lorentzian lineshape when either sideband is resonant, and the quadrature component displays sharp dispersive features at the resonance of the carrier and each sideband. The in-phase component is flat at the center and so would be useless as an error-signal, but the quadrature component could be used for feedback: the steep zero-crossing at the carrier resonance would provide a tight lock in this region, but the lock range is not broad. On the other hand, when $\omega_m \ll \Gamma$, it can be shown that the in-phase component approaches an exact derivative of the Lorentzian absorption lineshape, which would in theory make for a decent error signal. However, the amplitude of the beats and hence the signal-to-noise of the error signal becomes quite small.

For these reasons, we operate instead in the regime where the $\omega_m < \Gamma$, where the lineshape of the in-phase component still resembles the derivative of the absorption

---

[6] The FM spectroscopy technique is closely related to the Pound-Drever-Hall technique used to stabilize lasers to high-finesse optical cavities: the reflection of phase-modulated light incident on an optical cavity also contains beat signals due to the differential phase-shifts of the upper and lower sidebands. If the cavity linewidth is substantially narrower than the linewidth of the incident probe laser, these signals contain information about the laser's instantaneous phase noise, and can be fed back to the laser current to narrow the laser spectrum.

lineshape but the signal-to-noise ratio is reasonably large. FM spectroscopy with a phase-modulated probe and the correct demodulation phase thus gives us an error-signal at the atomic resonance, which is on the order of the natural linewidth when the resonance is the Lamb dip produced by saturated absorption spectroscopy. However, this signal is still superimposed on the Doppler-broadened probe absorption, a background that fluctuates with probe intensity. To turn the signal into a reliable lock signal with a zero-crossing that will not shift, we subtract off the background Doppler-broadened absorption dip by chopping the pump beam with an AOM. The pump modulation chops the Lamb dip recorded by the probe off and on, but does not affect the Doppler broadened background, so after lock-in detection on the probe transmission, we are left with an error signal that can be fed back to the laser piezo to keep the laser locked to the atomic resonance.

4.5.4. Alternative Laser Stabilization Techniques

The heat pipe is an effective method for containing an optically dense atomic vapor, but it does require assembling an argon-backfilled vacuum chamber with an associated vacuum gauge, and the use of hot ovens which contribute to the overall background temperature in the lab, so it is worth mentioning the benefits and pitfalls of some Sr vapor sources used by other groups. Several other vapor cell designs are in use [349, 350], but most also require vacuum components, heating elements, and often sapphire windows when a buffer gas is not used (one potentially compact option does not use heaters or sapphire windows but instead requires a 20A current source to eject strontium from a commercial dispenser, but the dispenser would need replacing on perhaps a yearly basis [351]). Another method of accessing nearly Doppler-free spectra is transverse spectroscopy on a Sr atomic beam [309]; clearly this requires an ultrahigh vacuum system but can be a good option when a beam is already available, as in our system at the small spherical octagon location. However atomic beam signals are broadened by imperfect beam collimation, and misalignments of the probe laser off perpendicular will cause Doppler shifts offset the lock center from the unshifted resonance.

A potentially attractive (if expensive) option is the see-through hollow-cathode lamp [124, 330, 352]. In a hollow-cathode lamp an electric discharge ionizes background buffer gas atoms (typically neon for Sr lamps) which then strike a Sr cathode to generate a contained Sr vapor; in the see-through version the cathode is a ring through which pump and probe lasers can pass in a saturation spectroscopy configuration. The ∼5 Torr buffer gas leads to additional pressure broadening beyond what we see in our heat pipes but the error signal is tight enough for locking the 461 nm blue MOT laser. We have not seen reports of locking the 689 nm red MOT laser using a hollow-cathode lamp, but one source stresses the importance of independently calibrating the lock point of a Ca see-through hollow-cathode feature using another source due to the large pressure shift associated with the buffer gas [353]; this would be a concern attempting to use a hollow-cathode lamp for the narrow 689 nm transition.

One of the advantages of hollow-cathode lamps is the fact that sputtered Sr atoms are collisionally excited to a variety of energy levels, unlike in the heat pipe where the population of any non-ground-state energy level is near zero even at high temperatures. This makes hollow cathode lamp spectroscopy attractive for stabilizing Sr repump lasers that interact with the metastable $^3P_2$ state. A saturated absorption/FM spectroscopy setup with a see-through hollow cathode lamp would be ideal for stabilizing our 497 nm repump system, but a much cheaper option would utilize the optogalvanic effect in a standard hollow-cathode lamp of the type used in spectrometers. These lamps are not "see-through": the cathode is a solid cup that does not permit the passage of a probe laser through excited vapor and onto a photodiode on the other side. However, shining a resonant probe laser into the cathode changes the lamp current slightly by altering the distribution of Sr atoms in excited states. Some excited energy levels have a higher probability of ionization by further electron collisions than others, so the presence of the resonant light alters the Sr^+ current at the cathode. The optogalvanic effect is weak but observable with lock-in detection. We purchased a very cheap used Sr hollow-cathode lamp and detected the signal for both the 461nm and 497nm beams, so it may be worth exploring this 497 nm stabilization technique in the future.

CHAPTER V

EXPERIMENTAL APPARATUS II: VACUUM CHAMBER, STRONTIUM BEAM, AND TRAP REGIONS

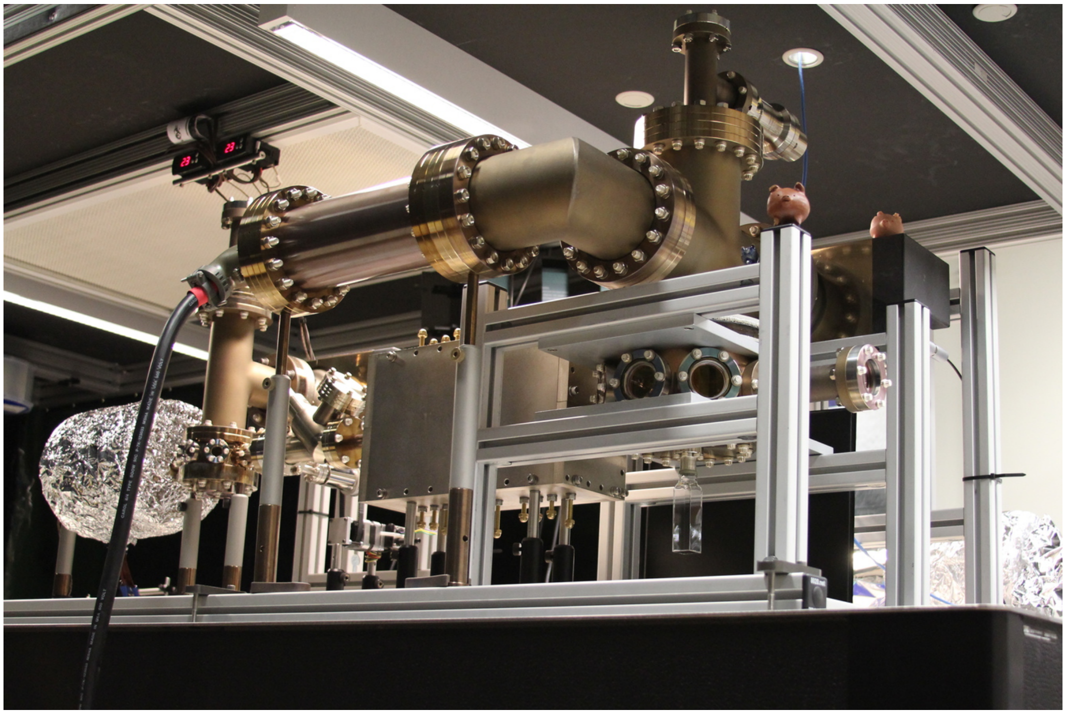

FIGURE 5.1. Strontium vacuum chamber fully assembled, before optics installation.

5.1. Overview

For MOTs of average density (and adequate repumping), background gas pressure can be a limiting factor affecting MOT lifetime [267, 354]: cold atoms are easily ejected from the MOT by any collision with room-temperature background gas molecules. For long interrogation times and good transfer rates between different traps, our MOT regions require ultra-high vacuum (UHV: $P < 10^{-8}$ torr, but for the science cell region we would prefer pressures in the 10^{-10} torr range). However, strontium's low vapor pressure means that a hot oven is required to deliver a sufficient flux of atoms to the experiment regions, and these atoms must be cooled to speeds less than the capture velocity of the blue MOT before they reach the capture zone. In effect our chamber is divided into two regions: a high-pressure side containing the strontium oven source and a low-pressure side containing the MOT capture areas, with the two areas separated by the Zeeman slowing region in a long and narrow pipe which maintains the pressure differential.[1]

A schematic of the vacuum chamber is given in Fig. 5.2. The high-pressure side contains not only the hot strontium oven, discussed in more detail in Sec. 5.2, but also the small spherical octagon (Kimball Physics MCF450-SphOct-E2A8). The atomic beam from the hot oven passes through two of the spherical octagon's eight equatorial ports; the other six have AR-coated viewports (1-1/3″ CF-flange viewports, Larson VP-075-F1). There is also a viewport on the bottom of the spherical octagon; the top is connected via a 4.5″ CF tee to a 55 L/s ion pump (Duniway RVIP-55-ST-M) and (through another tee) a right-angle valve (VAT 54032-GE02) allowing access to the turbo-pumping station during initial evacuation, but the top of the second tee also allows optical access (2-3/4″ CF viewports, Larson VP-150-F2). Many strontium groups requiring high MOT densities use transverse cooling schemes to limit the divergence of the atomic beam [355–357], and the optical access in this area gives us that option. We could also use a single probe beam perpendicular to the atomic beam at this location to lock one of our laser systems to a nearly-Doppler-free (linewidth limited by atomic beam divergence) resonance. For the current experiment we do not need a particularly dense MOT, and we have already locked the required lasers to the heat pipes discussed in 4.5.1, but the optical access in this region is still useful:

---

[1] Here, "high-pressure" simply means "high" as compared to the low-pressure side of the chamber; the vacuum in most of the high-pressure region is still $\sim 10^{-8}$ torr and so qualifies as UHV. Of course the pressure inside the strontium oven itself, however, is not UHV ($\sim$4 mTorr at 500°C).

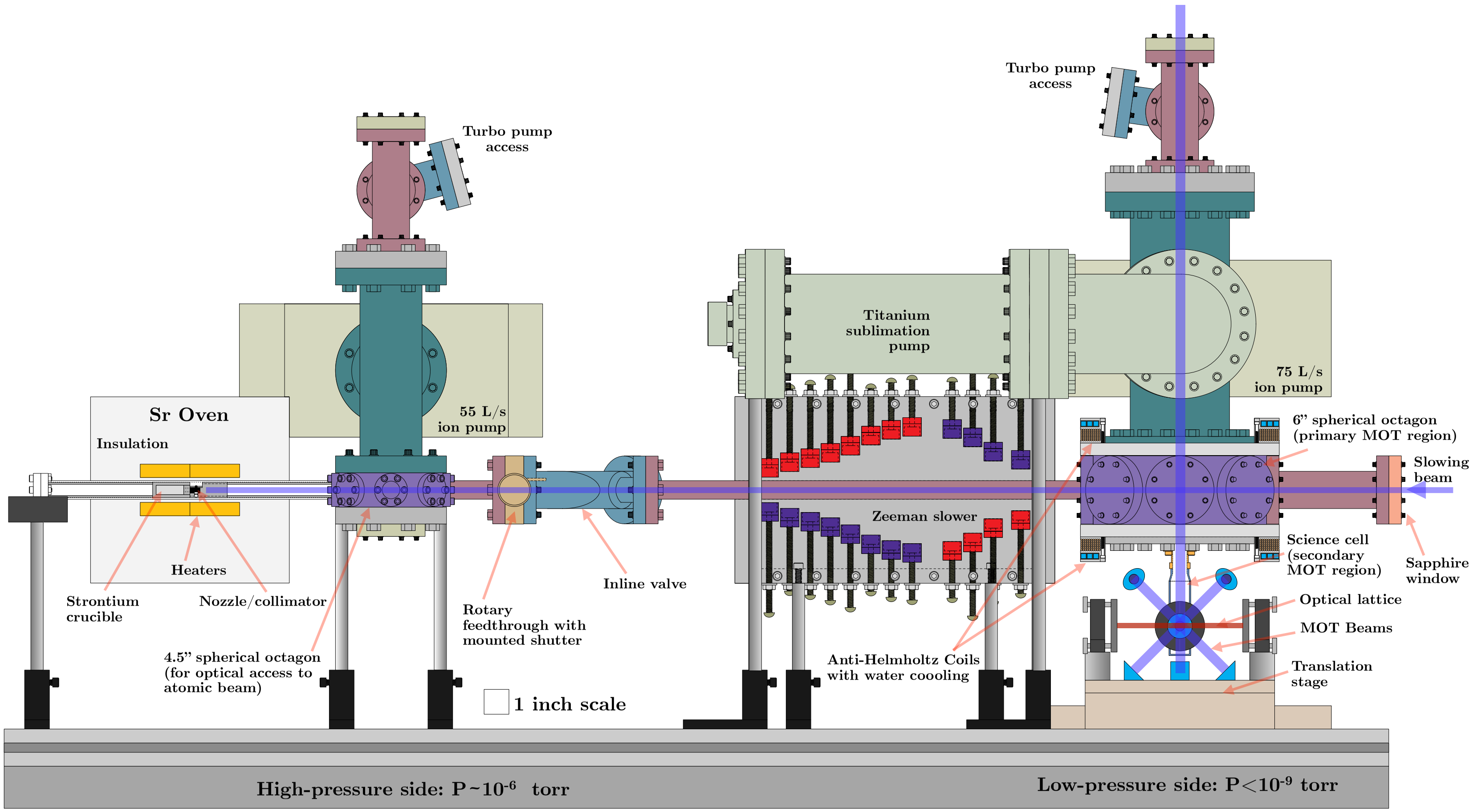

FIGURE 5.2. Sr vacuum system schematic

a CCTV camera (Marshall Electronics Video Runner 1020) positioned in one of the 45° windows aids alignment of the Zeeman-slower-beam by providing a view of the beam/oven overlap on a small LCD monitor (Pyle PLHR76) mounted to vacuum chamber frame.

The low-pressure side of the chamber contains the 6″ spherical octagon and glass cell for the top and bottom MOT regions, discussed in more detail in Sec. 5.4. Above the MOT regions, a 6″ CF 4-way cross connects on one side to a 75 L/s ion pump (Duniway RVIP-75-ST-M) and on the other to a 6″ CF elbow and a 6″ CF nipple containing a titanium sublimation pump (Duniway TSP-275-003). On top of the 4-way cross, a 2-3/4″ CF tee connects to another right-angle valve for access to the turbopump and provides vertical-MOT-beam access via an AR-coated window on top. This low-pressure region is separated from the high-pressure side by the inline valve and the Zeeman slower. The all-metal inline valve (Varian 9515052) should allow future refill of the strontium oven without the need for a complete bakeout by sealing off the low-pressure side of the chamber. The Zeeman-slower magnetic-field assembly, discussed in more detail in Sec. 5.3, was constructed separately to fit around the long nipple (CF-flange-fitted pipe) separating the inline valve and the 6″ spherical octagon containing the top MOT region. Since most designs we considered needed to be constructed directly onto the vacuum chamber we will discuss the Zeeman slower in this chapter. Likewise, optical access and magnetic-field coil positioning for MOT regions should be considered in the overall chamber design, so we also choose to discuss these aspects of the top and bottom MOT in this chapter, although more MOT experimental details will be covered in Chapter 5.

The distance between the hot strontium oven and the top MOT region is just over 1 m; this length leads to a large chamber, occupying in total (with mounting frame) a 6′ × 2.25′ rectangular area of the optical table (and at 3′ tall at the highest point, the assembly nearly reaches the optical table ceiling). However, the resulting separation of low- and high-pressure areas is quite effective. In particular, the custom 17″-long, 0.62″-ID nipple in the Zeeman slower region acts as a differential pumping tube [215]. The conductance of such a long and narrow tube is less than 1 L/s, capable of maintaining a pressure differential between the two regions of almost 2 orders of magnitude [358]. Our system does not have any dedicated vacuum gauges, but the pressure of the two regions can be monitored as a function of ion pump current. Ion pumps contain magnetically confined electron discharges; residual gas molecules are ionized by the discharge and then accelerate into a cathode made from a gettering material like titanium to be buried or chemically adsorbed. The cathode current is therefore a measure of residual gas density and hence the chamber pressure (although pressure measurements may not be exact due to the different speeds at which different gases — e.g. hydrocarbons vs. noble gases — are pumped). Typical currents on the high-pressure side are 8-11 μA, corresponding to $1 - 1.2 \times 10^{-8}$ torr (at the low end with the Sr oven off, but even with the oven at its current operating temperature of 500°C the pressure does not rise as much as might be expected in part because strontium itself is an effective gettering material.On the low pressure side, the ion pump current is nearly off-scale at 0.5-1 μA and so indicates a pressure less than 10^{-9} torr; extrapolation of the given pressure-vs-current relationship gives an expected pressure of $\sim 6 \times 10^{-10}$ torr.

The purchased ion pumps were originally chosen as overkill since the cost of an ion pump does not scale linearly with pumping speed, but a subsequent molecular-flow conductance calculation later verified their adequacy [144].[2] In particular, the

---

[2] The outgassing rate of the interior walls is reduced by the bakeout procedures described in Sec. 5.5 but cannot be brought to zero, and helium can diffuse through glass viewports and the

addition of the titanium sublimation pump (TSP) should ensure sufficient background gas removal: a TSP pumps by sputtering titanium from the filaments onto the surrounding chamber, which in our case is a $4'' - \mathrm{OD}, 10.62''$-long cylinder (the 6"CF nipple). Titanium acts as a strong getter for most gases (although less effective for the noble gases), particularly at the low pressures where ion pumps can become less effective ($< 10^{-8}$ torr) [359, 360], so the pumping speed is proportional to the coated surface area and should be on the order of 1,000 L/s for our system, much higher than the 55 and 75 L/s speeds of the ion pumps. (For their part, the ion pumps, which are rebuilt Varian StarCells, should be better at pumping inert gases.) The TSP filaments can be periodically activated ("flashed") to restore the gettering layer and bring the pressure in the MOT regions down, but we have rarely seen occassion to do so since we have not seen significant increases in system pressure.

All parts except those discussed specifically in the sections below were commercial CF-flange vacuum components made from 304 or 316 stainless-steal . Optimal UHV chamber designs [359] limit the number of joints, maximize conductance to the vacuum pumps, and minimize internal surface area.[3] We attempted to adhere to these principles, although in the end we have identified some changes that would help to minimize the overall size of the chamber while maintaining the pressure differential between the low and high regions. The ion pumps are mounted on the large four-way crosses to maximize conductance but avoid direct line-of-sight between the pump input and the atomic beam or MOT regions; the TSP is mounted on an additional elbow to prevent any sputtering of titanium into the rest of the chamber. The entire

---

stainless steel walls of the chamber itself, so UHV systems require continuous pumping sufficient to offset these effects.

[3] The "spherical octagons" are an example of the last principle: with eight external ports they provide excellent optical access, but they are machined from a hollow sphere to minimize internal surface area.

vacuum chamber was assembled on a T-slotted aluminum frame (80/20 Inc.) which supports the ion pumps, prevents stresses on chamber joints, and allows for transfer of the entire chamber from the floor (assembly and bakeout location) to the optical table.

5.2. Strontium Oven and Beam

The strontium oven must deliver a sufficient flux of atoms to the main trapping region while containing enough strontium to run for several years without requiring a refill (which would necessitate breaking vacuum in the high-pressure side of the chamber). Some oven designs allow partial recirculation of atoms lost from the main atomic beam [361, 362], but the slight reservoir lifetime increase comes at the cost of significant complication to the overall design and would require operation above strontium's 777°C melting point. Likewise, there are many methods for resistively heating a reservoir and limiting heat transfer to the rest of vacuum chamber and lab environment [363, 364] using electrical vacuum feedthroughs and thermal shields or even water-cooled housings, but these designs are also more complex than this experiment requires. For simplicity and ease of use, we chose the same external clamshell heater design used in the heat pipes(4.5.1), with a simple strontium crucible inside a stainless steel pipe serving as the oven reservoir and a bundle of capillary tubes clamped in a secondary cylinder acting as a collimation nozzle.

The overall oven design is diagrammed schematically in Figure 5.2. The strontium reservoir is a stainless-steel cylinder containing 3.21 g of solid Sr (from the same Sigma Aldrich source as the heat pipes), loaded through an end cap at the front of the cylinder. This cap has an axial 0.25″-diameter hole, which butts up against the cylinder containing the collimation assembly. The collimation nozzle itself consists of 184 capillary tubes of 203-μm-ID (Small Parts B000FN0TL2 hypodermic tubing), cut to 1-cm long and clamped in a secondary axial 0.25″ hole using a plate screwed into a flat in the cylinder top (see Fig. 5.3). Both cylinders are contained in a 0.75″-diameter, 12″-long stainless-steel pipe with 1 1/3″ CF flanges welded to either end. Two side-by-side 2″-long clamshell style heaters (Thermcraft RH-206-S-L custom part, with VIP-2.5-8-0.75-2 insulation package), controlled by the same LOVE temperature controller/solid-state-relay combinations described in Sec. 4.5.1, heat the reservoir and nozzle cylinders, with the nozzle kept 50°C hotter than the reservoir to prevent clogging.

FIGURE 5.3. Strontium oven collimation nozzle

A bundle of tubes can produce an intense atomic beam with a high degree of collimation while limiting depletion of the reservoir source. One might assume that an equally collimated atomic beam could be produced by two apertures with areas equal to the sum of the capillary tube cross-sectional areas and separated by the length of the tubes, or by a single tube with these dimensions, but while the flux of our nozzle will indeed be proportional to the total nozzle area, the collimation angle is instead a function of the length L and diameter a of an individual capillary tube. The effective conductance of the nozzle is also much lower than that of a single tube of equal total nozzle area, and the conductance of two apertures alone would be higher yet [358]: the conductance of a thin-walled aperture is proportional to the aperture area, while that of a tube is proportional to the tube diameter cubed divided by the tube length, so a tube of radius $a \ll L$ will have a lower conductance than two apertures of equal radius, and a bundle of much smaller-radius tubes will have a lower conductance yet. This low conductance allows greater oven pressures and hence an equivalent *peak* (on-axis) beam intensity with less source depletion or beam divergence.

To fully understand the expected beam intensity and angular profile, it is important to identify whether we are operating in the molecular- or continuum-flow regime [358, 363]. Molecular flow requires number densities low enough that collisions between molecules are rare compared to those between molecules and walls: the gas can be treated as non-interacting, and the flow is diffusive in nature. Continuum flow, on the other hand, implies that gas behavior is dominated by interactions between molecules and forces resulting from pressure differentials. The transition between the two regimes is characterized by the Knudsen number $K_n = l/a$, the ratio between the mean free path l and the smallest chamber dimension (in this case the tube radius a). For molecular flow, $l > a$ and so $K_n > 1$ and the oven acts as an effusive source; when it also holds that $l > L$ (the "transparent" regime) atom-atom collisions along the length L of the capillary can be ignored and the beam divergence is a function only of the aspect ratio a/L of a tube, with no dependence on the reservoir number density. Continuum flow, on the other hand, implies that $K_n \ll 1$ and atom-atom collisions are more frequent than atom-wall collisions. For atomic beam sources, continuum flow implies that interactions between atoms broaden the beam and decrease the relative peak intensity, and the angular divergence is no longer a simple function of the collimator geometry.

The mean free path for strontium-strontium collisions changes rapidly over our typical oven-temperature operating range: $l = 1/(\sqrt{2}\pi n d^2) = 12.6$ cm at 450°C, 2.5 cm at our current setpoint $T = 500°\text{C}$, but only 6.0 mm at 550°C (here, $n = P/k_{\mathrm{B}}T$ is the atomic number density and $d \approx 4.4$ Å). We are in the transparent regime for low oven temperatures but the intermediate regime ($l > a$ but $l < L$) when we run hotter, with the crossover point at $T = 530°\text{C}$. However, one advantage of the multiple-tube collimator design is the fact that the beam divergence remains small well into this intermediate regime [365]. Even when the oven pressure implies a mean free path somewhat less than the collimator length L (but still greater than a), the low conductance of a tube with $L \gg a$ implies that the number density falls, and the mean free path increases, as the atoms pass through the tube: there will still be some point along the tube where the mean free path becomes greater than the remaining tube length and the transparent condition is once again satisfied. Many atomic beam systems are in fact run in this intermediate regime to provide higher peak intensities, and measured beam divergences are indeed close to those expected for the transparent regime [366, 367].

While the divergence half-angle of the atomic beam is simplified by assuming we are in the transparent regime, it cannot be calculated directly from assuming that $\theta_{1/2} = \tan^{-1}(2a/L) \approx 2a/L$, as we might have expected if we assumed that any atom in the resultant beam must have traversed the capillary with no wall collisions. These atoms will make up the majority of the beam, and their contribution to the angular spread of the beam is weighted towards the center. On the other hand, atoms that do hit the wall can contribute as well, broadening the angular distribution. To understand the additional effect of the wall atoms, it is important to realize that atom-surface interactions are not modeled as momentum-conserving elastic collisions but are governed instead by the Knudsen Cosine Law: atomic trajectories are completely randomized by scattering events to an angular distribution proportional to $\cos\alpha$, where α is measured relative to the surface normal. Any atom that experiences a wall collision can still contribute to the atomic beam if this angle is greater than $\tan^{-1}(L'/2a)$ in the forward direction, where L' is the distance from the tube exit where the wall collision occurred; an atom could also experience several wall events and still eventually find its way into the final beam. The full calculation for even the simple transparent regime thus involves finding an expression for the beam intensity as a function of angle by adding the expected intensity distribution for atoms that pass directly through the tube to the distribution that results from integrating over the tube walls (and decreasing number density) down the length of the tube [368].

For effusion from a simple aperture the flux density $\Phi(\theta, v)$ (atoms per second per unit velocity and solid angle) is found by assuming that the probability of crossing the aperture is given by the number density per unit velocity $n(v)$ times $v\cos\theta$ (only atoms with velocity components towards the aperture exit will cross) times the area of the aperture πa^2 [358, 369]. This can be re-written in terms of the normalized Maxwell Boltzmann distribution $f(v)$ as

$$\Phi(\theta, v) = \frac{\pi a^2}{4\pi}\,\bar{v}\cos\theta\; n_0 f(v) = \frac{n_0 \bar{v}\,\pi a^2}{4\pi} j(\theta) f(v), \tag{5.1}$$

where $\bar{v} = \sqrt{8k_{\mathrm{B}}T/\pi M}$ is the mean velocity, $n_0 = P/k_{\mathrm{B}}T$ is the oven number density, and the angular distribution function $j(\theta) = \cos\theta$ for the simple aperture. For the capillary array, $j(\theta)$ becomes a complicated function dependent on a and L (but still normalized to $j(0) = 1$), but Eq. 5.1 remains valid. This implies that the peak flux or beam intensity [atoms per second per steradian, on axis ($\theta = 0$)] is exactly the same as that for an array of apertures:

$$J_{peak} = \int_0^\infty \Phi(0, v)\, dv = \frac{n_0 \bar{v}\, \pi a^2}{4\pi} N_{cap}, \tag{5.2}$$

where N_{cap} is the number of capillary tubes. The angle at which the intensity distribution falls to 1/2 this peak value is given by [368][4]

$$\theta_{1/2} = 1.68 \frac{a}{L}, \tag{5.3}$$

versus $\theta_{1/2} = \pi/3$ for the simple aperture. These results demonstrate the effective "beaming" power of the capillary tube array: the peak intensity remains equal to that of a simple aperture of the same radius, times the number of capillary tubes, but the angular width is substantially decreased. As a result the total flux is a factor of $8/3(a/L)$ smaller than that of an array of equivalent apertures [368, 369]. The low conductance of the capillary tube nozzle thus conserves the reservoir source while delivering an equally intense atomic beam.

For our capillary array, we would expect a divergence angle $\theta_{1/2} = 17$ mrad; while this is good collimation, it would still result in a 4-cm-diameter atomic beam in the MOT trapping region 1 m downstream. The beam could be even larger: other groups using capillary arrays have measured divergence angles larger than predicted [364] and attributed the discrepancy to imperfect alignment of the capillary tubes. A design which enforces hexagonal close-packing of the tube array [367] might help to mitigate

---

[4] A separate group using a Monte Carlo simulation approach also finds this equation for $\theta_{1/2}$ is a good approximation in the molecular regime for the collimation of any tube with $L/a > 10$ [366].

this problem, but our clamp design probably does allow individual tubes to have small axial misalignments which would increase the overall beam divergence angle. To further collimate the beam, we use two additional 6.35-mm diameter apertures cut from nickel gaskets on either side of the inline valve, just before the Zeeman slower tube. The second gasket, which is 46.5 cm from the exit of the oven nozzle, thus limits the beam divergence to $\theta_{ap2} = 6.8$ mrad through the majority of the vacuum chamber. The beam still clips slightly in the tube of the long 1.2cm-ID Zeeman nipple, so the tube exit acts as the final limiting aperture. The final divergence half-angle is then $\theta_f = 6.6$ mrad. We expect a hot beam diameter of 1.3 cm in the MOT region, consistent with observed unslowed atom fluorescense in this region and the size of the strontium deposits on the final sapphire window.

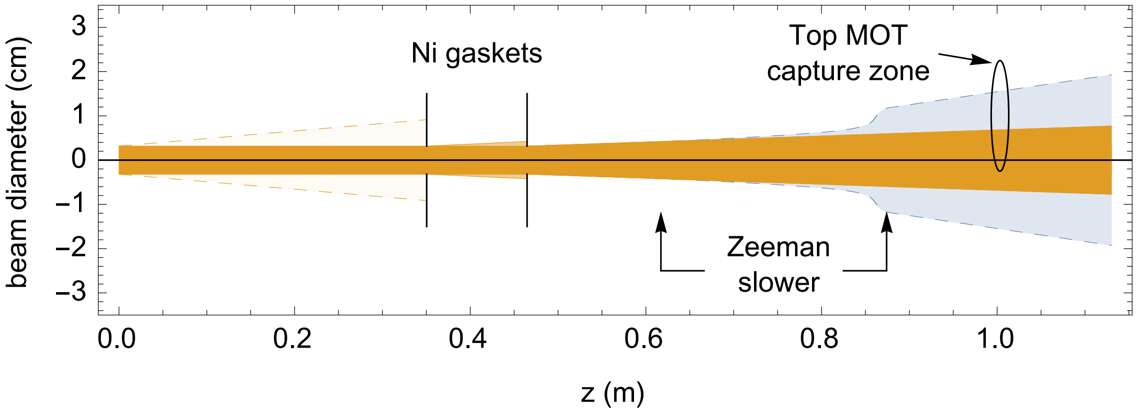

FIGURE 5.4. Atomic beam diameter as a function of distance from the collimation nozzle. The orange curves show the hot beam direct out of the nozzle (dashed) and after aperture by the first and second nickel gaskets (solid). The blue dashed curve shows worst-case calculated cooled beam expansion as a result of transverse heating in the Zeeman slower, ignoring losses to clipping in the Zeeman pipe. The MOT capture zone is determined by the extent of the MOT optical molasses, and as shown is slightly above the main beam axis: this is a result of the ∼5 mrad atomic beam-pointing misalignment relative to the main chamber axis.

The total flux of hot atoms delivered to the MOT region can be estimated from the peak axial intensity per steradian (Eq. 5.2) multiplied by the solid angle defined by the end of the Zeeman pipe, assuming that the apertured angular distribution function $j(\theta)$ is well approximated by $j(0)$:

$$\begin{aligned} Q_{\mathrm{hot}} &\approx J_{\mathrm{peak}}\Omega_{\mathrm{f}} \\ &\approx \left(9.6\times 10^{15}\ \mathrm{atoms/s\cdot sr}\right)\frac{\pi(0.006\mathrm{m})^2}{(0.96\mathrm{m})^2} \\ &\approx 1.3\times 10^{12}\ \mathrm{atoms/s} \end{aligned} \tag{5.4}$$

for a 500°C oven. The peak intensity J_{peak} may be an underestimate since it assumes a sum over capillary tube fluxes and ignores the contribution due to the gaps between the tubes; on the other hand, possible mutual misalignments of the tubes would reduce the intensity. Schioppo *et al.* [364] noted that the measured flux from a similar strontium capillary tube collimator was consistently $\sim 3.5\times$ lower than the theoretical prediction over a wide range of oven temperatures, a result consistent with a a larger initial beam divergence angle resulting from capillary tube misalignments. Without careful measurements of our atomic beam, the best we can say is the flux should be on the order of 10^{12} atoms/s.

The total flux of *cold* atoms that will be delivered to the MOT region is of course the more important parameter; this flux will be dependent on the Zeeman slower parameters and will be discussed in Sec. 5.3. However, it is worth mentioning here the fact that the Zeeman slowing process leads to a significant increase in the cooled beam divergence angle, as discussed in Sec. 3.2.2.1. Using a converging slowing beam prevents the “beam explosion” that would result from slowing the longitudinal velocity component while leaving the transverse component unchanged, but inevitable transverse heating from spontaneous recoil events still leads to beam spreading, with the angular increase given by Eq. 3.36. This effect would lead to a final beam divergence of 45 mrad exiting the slowing region, or a beam diameter of almost 4 cm in the MOT region. For the cooled atoms, the Zeeman tube itself acts as a final aperture, but the percent of cooled atoms lost to this effect is more difficult to calculate. The beam diameter as a function of distance from the oven nozzle is plotted in Fig. 5.4, showing the effect of the apertures and the Zeeman slower tube on the hot versus cooled atomic beam.

To estimate the duration between oven refills, the total flow rate through the nozzle is given by integrating the flux per steradian per unit velocity (Eq. 5.1) over the full 2π solid angle and all velocities. Equivalently, since we are in the molecular flow regime, we can use the flow rate of a single long tube of length L and radius a multiplied by the number of capillaries N_{cap} [364, 369], or

$$Q_{\text{total}} = \frac{2\pi}{3}\frac{n_0 \bar{v}\, a^3}{L} N_{cap} = 8.1 \times 10^{14} \text{ atoms/s} \tag{5.5}$$

for a 500°C operating temperature. With 3.21g loaded, we can anticipate that the source reservoir will be depleted in ∼2.5 years when the oven is in use for 8 hours a day; the lifetime may be even shorter due to the contribution from gaps between the capillaries. In retrospect, our oven pipe would accommodate a much longer reservoir cylinder containing more strontium (while we preferred to keep the heated region near the center of the pipe to avoid stressing the final CF flange, stainless steel's low coefficient of thermal conductivity means that the flange is currently almost at room temperature when the oven is running; a longer heater would probably be fine). We would also benefit from using smaller inner diameter capillary tubes: decreasing the radius by 1/2 would double the reservoir lifetime (assuming we could fit roughly $4\times N_{cap}$ in the same total nozzle area) but would leave the peak on-axis flux unchanged while increasing the total flux delivered to the MOT region by halving the divergence angle (such that fewer atoms would be lost at the first and second apertures). The overall nozzle area is also larger than necessary; decreasing this area would increase the reservoir lifetime while decreasing N_{cap} and the peak flux proportionally, but fewer atoms would be lost at the first aperture, and our planned experiments do not require large MOTs.

Two final atomic beam considerations were important in the chamber design. First, we needed a method to shutter the atomic beam when not continuously loading a top MOT. Any beam atoms not trapped by the MOT are deposited on the final sapphire window, and for MOT characterization and any future experiments in the top MOT region we prefer to have the atomic beam shuttered after loading so that the cold MOT atoms are not continuously bombarded with the atoms from the atomic beam. We installed a 2-3/4″ CF-flange-mounted viewport shutter (Kurt J. Lesker DS275VPS) before the inline valve and keep this shutter closed at all times other than when continuously loading the top MOT to prevent strontium contamination of the low pressure side of the vacuum. The shutter is actuated by a rotary magnetic feedthrough designed for manual operation, but we have attached a timing belt pulley to rotate the shaft using a stepper motor (SparkFun ROB-09238 with "Easy Driver" ROB-12779) that is computer controlled using the digital output boards to link the timing of shutter opening/closing events with other experimental sequences; see Ref. [144] for more information on atomic beam shutter control.

Finally, the atomic beam terminates on a viewport that admits the counter-propagating Zeeman-slower beam. We use Kovar-sealed borosilicate glass viewports for optical access in other locations, but this viewport is sapphire (Larson VSZ-150-F2) to prevent the semi-permanent reflective coatings that can form when hot strontium reacts with glass. Strontium deposits still build up on the window to create a slight film, so we extended the window away from the MOT spherical octagon chamber on a 6″-long nipple and heat it to 200°C using a silicone rubber heater (Omega SRFG-108/10) wrapped around the CF-flange joint with a thermocouple, controlled by an inherited temperature controller assembly (from a previous UO cold atom experiment, already equipped with a solid-state relay) switching a Variac set to 70V. We still observed substantial strontium build-up when the oven was left running without the shutter closed for an extended period, but the deposit gradually diminished over a few days. In normal operation, a very faint film is barely visible, and although this may attenuate the Zeeman-slower beam very slightly we have actually found it to be a useful diagnostic feature. Despite our alignment attempts during assembly, the deposit is about half a centimeter low and to the left of the viewport center, indicating that our atomic beam pointing angle is off by ∼5 mrad. This could be a result of nozzle clamp misalignment or a slight torque along the axis of the whole chamber causing creep after initial assembly. If perfect alignment of the atomic beam were required future designs could add flexible bellows between the oven pipe and the rest of the chamber [123] or incorporate pointing alignment into a new oven design [343], but as it is we simply use the deposit to center the input alignment of the Zeeman-slower beam and load the MOT from the cold atoms above the main hot beam axis.

5.3. Zeeman Slower

The strontium oven produces a beam of hot strontium atoms with a longitudinal speed distribution given by

$$f_{\text{beam}}(v) = \frac{v^3}{2v_T^4} e^{-v^2/2v_T^2}, \quad \text{with} \quad v_T = \sqrt{\frac{kT}{m}}. \tag{5.6}$$

This distribution is found by multiplying the usual Maxwell-Boltzmann velocity distribution (Eq. 4.5) by an extra factor of velocity v (a result of the fact that the probability of effusing through an aperture is proportional to velocity), converting to a speed distribution by integrating out the polar coordinates θ and ϕ, and renormalizing. The extra factor of v shifts the most probable, average, and root-mean-square velocities to slightly higher values than the usual:

$$\begin{array}{rcccc} & \text{gas} & & \text{beam} & & \text{Sr beam at } 500^\circ\text{C} \\ v_{mp}: & \sqrt{2}v_T & \rightarrow & \sqrt{3}v_T & = & 468 \text{ m/s} \\ \bar{v}: & \sqrt{\frac{8}{\pi}}v_T & \rightarrow & \sqrt{\frac{9\pi}{8}}v_T & = & 508 \text{ m/s} \\ v_{rms}: & \sqrt{3}v_T & \rightarrow & 2v_T & = & 541 \text{ m/s} \end{array} \tag{5.7}$$

The full beam distribution is plotted in Figure 5.5, versus the usual Maxwell-Boltzmann speed distribution (dashed), for $T = 500^\circ$C. Given the MOT capture velocity $v_c \sim 50$ m/s, only 0.14% of the beam distribution could be loaded into the MOT without further pre-cooling. The atoms can be slowed by a counter-propagating beam detuned to be resonant with the Doppler-shifted peak of the velocity distribution, but as described in Sec. 3.2.1 this beam will only be resonant with a velocity class of width $\Delta v = \Gamma/k\sqrt{1 + I/I_{\text{sat}}} \simeq 20$ m/s for $I = 2I_{\text{sat}}$. The range of affected velocities can be increased by increasing the beam intensity, but even then any atoms that interact with the cooling beam and decelerate will rapidly Doppler-shift out of resonance.

There are two methods that allow a counter-propagating beam to interact with a much larger percentage of the velocity distribution and slow the atoms to less than the MOT capture velocity: chirp cooling (sweeping the laser detuning at a rate matching the changing Doppler shift) and Zeeman slowing (using a changing magnetic field

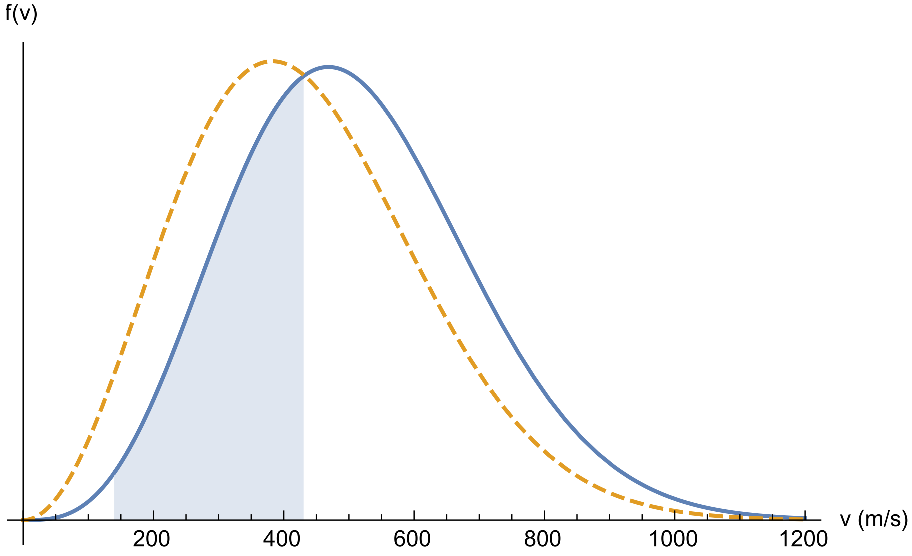

FIGURE 5.5. Normalized Maxwell-Boltzmann speed distributions at 500°C for a gas of strontium atoms (dashed) vs the atomic beam (solid). The shaded region indicates the approximate capture range of the Zeeman slower.

to equalize the Doppler shift and Zeeman shift for a fixed laser detuning). Chirp cooling requires the ability to scan the detuning of the slowing beam $\Delta = \omega - \omega_0$ from $\Delta = kv_0$, where v_0 is the speed of the fasted atoms we hope to catch, down to $\Delta \leq kv_c$. If we hoped to capture the majority of the distribution a broadband electro-optic modulator capable of rapidly sweeping over $\sim$1 GHz would be required. Furthermore, chirp cooling can only deliver one pulse of slow atoms per frequency sweep period. For a continuous source of slow atoms, Zeeman slowing is clearly the best option.

Traditionally, the magnetic field gradient required for a Zeeman slower is supplied by a tapered solenoid. However, the process of winding a bakeable solenoid is labor intensive, and coil operation requires a high power current supply and water-cooling. It is also difficult to modify the field profile after the solenoid is created (the use of multiple current supplies controlling adjacent coil sections can allow some fine-tuning [343] but at the cost of further apparatus complication). For these reasons, many groups are exploring permanent-magnet Zeeman-slower designs [122, 300, 306–308].

5.3.1. Transverse-Field Permanent-Magnet Design

We chose to duplicate the permanent-magnet transverse-magnetic-field Zeeman-slower design developed by Y. B. Ovchinnikov of the UK National Physical Laboratory [300, 306, 370]. The magnetic field in this design is created by small neodymium magnets positioned in the $x - z$ plane (atomic beam axis along $\hat{z}$) with dipole moments oriented parallel to the $\hat{x}$ axis. Ovchinnikov demonstrates that 24 such magnets provide a relatively smooth magnetic field gradient that is well-approximated by modeling each magnet as a point dipole. Each pair of magnets is positioned symmetrically about the z-axis with aligned dipole moments, such that the resultant magnetic field components B_x and B_y are zero at the beam axis, but the B_z field increases with decreasing magnet distance from the z-axis. The field profile is then easily adjusted at any time by tuning the x-position of the magnets (another adaptor of this design demonstrated real-time field optimization by connecting each magnet to a servo-motor controlled by a program monitoring the MOT fluorescence downstream [122]).

Ovchinnikov models the optimal required magnetic field by taking the analysis described in Sec. 3.2.2.1 one step further: a consideration often neglected is the fact that the slowing beam intensity is not constant throughout the slower. This can be a result of beam focusing [309], which is useful to both maximize overlap between the slowing beam profile and the diverging atomic beam and to provide a small transverse cooling effect to offset the “beam explosion” that would otherwise occur during the slowing process. However, even with no slowing beam focusing, atomic absorption may be a factor, particularly at the end of the slowing region where velocity phase-space compression results in a very dense cold beam. With a spatially-varying light field, the scattering force (Eq. 3.25) becomes

$$F(v,z) = \hbar k \frac{\Gamma}{2} \frac{s_0(z)}{1 + s_0(z) + 4\big(\Delta + kv(z) - \kappa B(z)\big)^2/\Gamma^2}, \tag{5.8}$$

where the on-resonance saturation parameter $s_0(z) = I(z)/I_{\text{sat}}$ is now a function of position along the slower. Instead of assuming that $I \gg I_{\text{sat}}$, the maximum acceleration for a given location is now defined as:

$$a_{\text{max}}(z) = \frac{\hbar k \Gamma}{2M} \frac{s_0(z)}{1 + s_0(z)} \tag{5.9}$$

which still occurs when the effective detuning $\Delta_{\text{eff}} = \Delta + kv(z) - \kappa B(z) = 0$.

As described in Sec. 3.2.2, operation at this a_{max} is in fact not optimal, since any slight increase in atomic velocity resulting from magnetic field imperfections or random scattering events will then lead to a decrease in the scattering force and loss of atoms from the slowing process, so the actual acceleration used is $a(z) = \epsilon\, a_{\text{max}}(z)$, where the coefficient ϵ is a constant related to the usual Zeeman slower design parameter $\eta = a/a_{\text{max}}$ (used when assuming constant acceleration) by

$$\epsilon = \eta \frac{1 + s_0(z)}{s_0(z)}. \tag{5.10}$$

Analogous to the stability analysis in Sec. 3.2.2, it can be shown that optimal cooling occurs for $\epsilon = 0.75$ (for a safety margin $\epsilon = 0.6$ is a reasonable parameter, which corresponds to the commonly used $\eta = .4$ for a constant $s_0 = 2$). The equilibrium velocity for the decelerating atoms will then be offset from the resonant velocity

$k v_{\text{res}} = \kappa B(z) - \Delta$,

$$k v(z) = k v_{\text{res}}(z) - \frac{\Gamma}{2}\sqrt{\big(1 + s_0(z)\big)\frac{1-\epsilon}{\epsilon}}, \tag{5.11}$$

which corresponds to the velocity for which the derivative of the scattering force is maximized.

As the deceleration rate is no longer a constant, calculation of the optimal magnetic field profile is non-trivial. Ovchinnikov develops a procedure to numerically calculate the equilibrium velocity $v(z)$ that would result from $\epsilon\, a_{max}(z)$, using an expression for the density of atoms as function of distance from the end of the slower z^* that depends in turn upon $v(z^*)$ at that location (assuming all atoms with velocities between the equilibrium velocity at that point and the Zeeman slower capture velocity v_0 have been slowed by that point) to find an expression for $s_0(z^*)$. Once $v(z)$ is known, $v_{\text{res}}(z)$ for the chosen efficiency parameter is given by Eq. 5.11, and the resonance condition $k v_{\text{res}}(z) = \kappa B(z) - \Delta$ then gives the optimal the magnetic field profile. Luckily for us, we did not have to repeat this procedure: Ovchinnikov calculates the optimal field for the same slowing parameters used in an existing high-flux Sr MOT experiment [309], which are appropriate for our experiment as well (see Table 5.1).

The slowing beam is assumed to be converging such that the diameter at the output and input of the slower are 0.3 cm and 1 cm, respectively, which sets the beam waist $\omega_0 = 10.5\ \mu$m at 10.7 cm behind the start of the slower. The absorbed power can be estimated by assuming the fastest atoms captured by the slower require $(v_0 - v_f)/v_r = 40{,}600$ scattering events, and the beam flux found in section 5.2 is 1.4×10^{12} atoms/s, so at an energy of $E \approx \hbar\omega_0$ per photon we would assume the absorbed power is $P_{\text{abs}} = 24.5$ mW. Of course, not all atoms will need this many

Zeeman shift (^{1}P$_1$, $m_F = \pm 1$)	$\kappa/2\pi = 1.4$ MHz/G
efficiency parameter	$\epsilon = 0.6$
capture velocity	$v_0 = 425$ m/s
final velocity	$v_f = 25$ m/s
slower length	$L \approx 25$ cm
Zeeman beam detuning	$\Delta =$ -500 MHz
starting B-field	$B_0 \approx$ -300 G
ending B-field	$B_f \approx +300$ G
slowing beam σ^- power	P_{σ^-}=22.5 mW
slowing beam focusing angle	$\theta = 28$ mrad

TABLE 5.1. Zeeman slower design parameters

scattering events, so Ovchinnikov's slightly lower $P_{\text{abs}} = 22.5$ mW is reasonable. This power is equivalent to a saturation parameter $s_0(25 \text{ cm}) = 0.7$ at the end of the slowing region.

The resulting optimal field, as realized by appropriate positioning of 24 magnetic dipoles, is plotted in Fig. 5.6, along with the field that would result from the constant deceleration assumption (Eq. 3.44) with design parameter $\eta = 0.4$ and a constant slowing beam intensity $s_0 = 2$. The constant acceleration field is of course idealized, as the abrupt transition from 300 G to 0 is impossible to achieve in any solenoid or permanent magnet realization, but both fields have similar same peak values (as these are determined by the starting and finishing velocity). Also shown are the measured values for the field of our completed transverse-field permanent magnet slower.

Calculated velocity profiles for atoms entering the slower at a variety of different starting longitudinal velocities are shown in Fig. 5.7, as well as the curve representing the resonant velocity that would give $\Delta_{\text{eff}} = 0$. The z-axis extends to the MOT

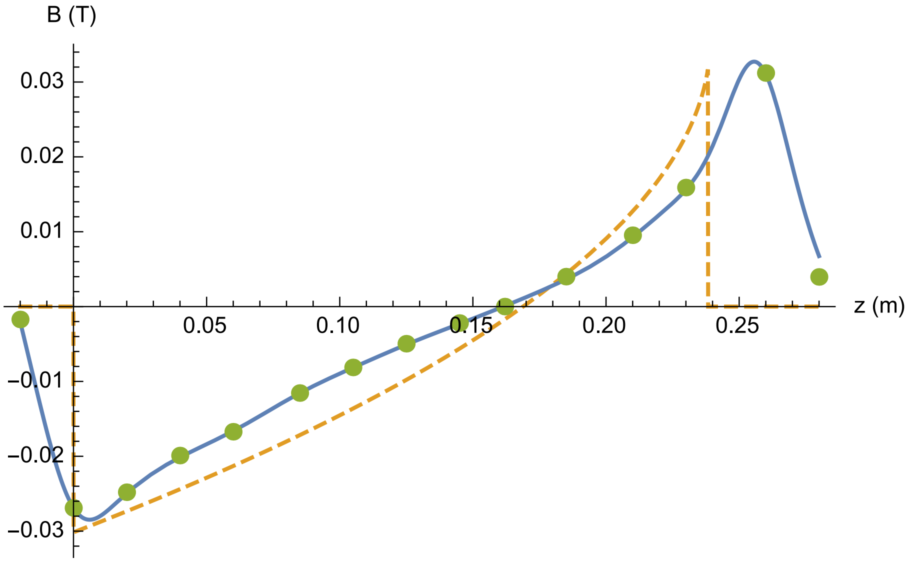

FIGURE 5.6. Zeeman slower magnetic field profiles calculated for a converging slowing beam of varying intensity (solid) and the constant acceleration, constant intensity idealization (dashed). Also shown are the magnetic field values for our completed transverse-field magnetic dipole slower, measured by a Hall probe along the slower axis with magnetic shields in place.

capture location, 32 cm beyond the start of the Zeeman slower: the resonant velocity curve demonstrates that the slowing beam is far detuned from both the slowed atoms and remaining hot atomic beam atoms in the MOT region. The velocities for the other curves are numerically evolved under the assumption that the atoms experience the scattering force given by Eq. 5.8, with $B(z)$ given by the optimal magnetic field profile of Fig. 5.6. The variable intensity parameter $s_0(z)$ corresponds to the design profile of the converging slowing beam, but the power $P = 22.5$ mW is taken to be constant, ignoring the effects of absorption. This model indicates that $v_{0\,\mathrm{max}} \simeq 425$ m/s is the indeed the approximate capture velocity (atoms with slightly greater initial speeds are affected by the scattering beam but cannot slow enough to come fully into resonance), and the final velocity is $v_f \simeq 25$ m/s. Further examination shows the average $\bar{v}_f = 25.3$ m/s, and the capture range of starting velocities is $140 - 430$ m/s (atoms with $v_0 < 140$ m/s will be turned around before the end of the slower, as indicated by the negative final velocities for the trajectories with $v_0 = 100$ and $v_0 = 50$; but since there are fewer atoms at these velocities in the initial distribution this loss is trivial).

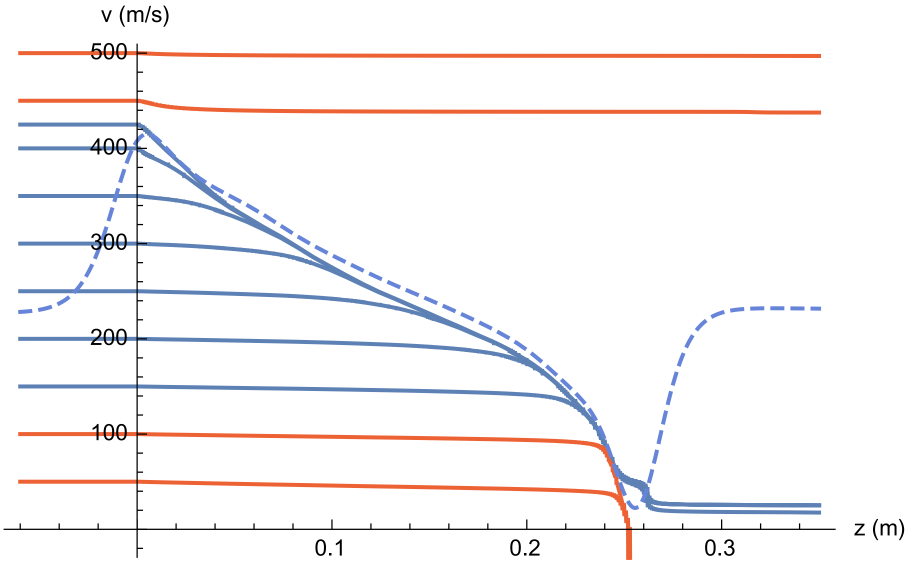

FIGURE 5.7. Atom velocity versus distance from start of Zeeman slower for varying initial velocities v_0. The blue curves show successful slowing, the red curves show the evolution for initial velocities too fast or slow for successful capture, and the dashed blue curve indicates the resonant velocity that would give a Doppler shift exactly canceling the local magnetic field for the slowing laser detuning $\Delta/2\pi = -500$ MHz.

This simple model does not include transverse velocity effects or the off-axis components of the full magnetic field distribution. While this model should be sufficient to estimate capture range dynamics, Hill *et al.* completed a full Monte-Carlo simulation of atomic trajectories in the transverse-field magnetic-dipole Zeeman slower after we had completed construction of our slower [300]. While the model of Fig. 5.7 implies that all atoms above the Zeeman slower capture velocity are relatively unaffected by the the slowing region while the majority of atoms below the capture velocity are collapsed into a final narrow distribution centered at $v_f \simeq 25$ m/s, the full simulation reveals an interesting additional feature at $v_f \simeq 200$ m/s. Hill *et al.*

attribute this additional peak to cooling of atoms lost from the slowing process in the exit region of the Zeeman slower. This may be an explanation for an interesting fluorescence phenomenon we observe in our MOT region, which will be discussed further in Sec. 6.2.

5.3.2. Calculated Cold Atom Flux

It may seem that a greater maximum capture velocity would be preferred, since the most-probable velocity of our atomic beam is $v_{\mathrm{mp}} = 468$ m/s at an oven temperature of 500°C. However, increasing $v_{0\,\mathrm{max}}$ increases both the length of the slower and the maximum magnetic field required, so many strontium groups operate in the range $400 < v_{0\,\mathrm{max}} < 450$m/s. Furthermore, the percent of atoms captured is already more than sufficient: $\sim 35\%$ of the hot beam distribution entering the Zeeman slowing region is cooled. Ignoring the aperture effect of the Zeeman tube on the transversely-spreading cooled beam, integration of the initial thermal beam distribution over the final beam solid angle and the capture velocity range of the Zeeman slower would give a cold flux of

$$\begin{aligned}
Q_{\mathrm{cold}} &= \int_{v_{0\,\mathrm{min}}}^{v_{0\,\mathrm{max}}} \int_{0}^{\theta_{\mathrm{z}}} \Phi(\theta, v)\, 2\pi \sin\theta \, d\theta \, dv \\
&\approx \pi\theta_{\mathrm{f}}^{2}\, J_{\mathrm{peak}} \int_{v_{0\,\mathrm{min}}}^{v_{0\,\mathrm{max}}} f_{\mathrm{beam}}(v)\, dv \\
&\approx 4.5 \times 10^{11}.
\end{aligned} \tag{5.12}$$

Here, as in Eq. 5.4, we have made the assumption that after several apertures the integral over the angular distribution can be approximated by the peak axial intensity J_{peak} multiplied by the cold beam solid angle.

However, a less reasonable assumption is the neglect of losses due to the fact that the cooling transition $^1\mathrm{S}_0 - {}^1\mathrm{P}_1$ is not closed [300, 343]. Most atoms that decay from the excited $^1\mathrm{P}_1$ state to $^1\mathrm{D}_2$ will be lost from the slowing process: given the $^1\mathrm{D}_2$ state lifetime $\tau = 0.3$ ms, an atom moving at 300 m/s will travel on average 9 cm during the time it is shelved in this state, experiencing no velocity reduction and falling out of step with the resonance condition. As discussed in Sec. 6.2.1, in the absence of a repump laser the probability of returning directly to the $^1\mathrm{S}_0$ ground state decreases exponentially with the number of $^1\mathrm{S}_0 - {}^1\mathrm{P}_1$ photons scattered due to these losses to the $^1\mathrm{D}_2$ state. [5] The number of photons scattered depends in turn upon the velocity, so the expression for the cold flux must be modified:

$$Q_{\mathrm{cold}} = \pi \theta_{\mathrm{f}}^2 \, J_{\mathrm{peak}} \int_{v_{0\,\mathrm{min}}}^{v_{0\,\mathrm{max}}} f_{\mathrm{beam}}(v) e^{-\frac{\Gamma_d}{\Gamma_b}\left(\frac{v-v_f}{v_r}\right)} \, dv, \tag{5.13}$$

where Γ_d and Γ_b are the transition rates for the $^1\mathrm{P}_1 -{}^1\mathrm{D}_2$ and $^1\mathrm{S}_0 - {}^1\mathrm{P}_1$ transitions, respectively, and the number of photons scattered is $(v - v_f)/v_r$, where $v_r = \hbar k/M$ is the recoil velocity. With this modification, we would ideally expect the flux of cold atoms delivered to the MOT trapping region to be $Q_{\mathrm{cold}} = 2.5 \times 10^{11}$ atoms/s for our current parameters.

Including the losses due to cooled beam clipping on the Zeeman tube as a result of the transverse-heating angular increase is more challenging: the beam spreading depicted in Fig. 5.4 is calculated from the average angular increase for atoms entering the slower at $v_{0\ \mathrm{max}}$, but atoms entering with lower velocities will scatter fewer photons and gain less transverse energy. A complete analysis of the cooled atom losses would demand integration over the initial beam velocity distribution, but as a rough estimate

---

[5] Note that the addition of our 497 nm repump laser to the slowing path would not prevent these losses: this repump depopulates the metastable $^3\mathrm{P}_2$ level, not the intermediate $^1\mathrm{D}_2$ state.

we can assume that we may lose as much as an order of magnitude due to this effect. In the end, we can expect a cold flux on the order of

$$\boxed{Q_{\text{cold}} \approx 10^{10} \text{ atoms/s.}} \qquad \textit{final cold atom flux} \tag{5.14}$$

This flux is consistent with predictions by other strontium groups and more than sufficient to achieve fast MOT loading rates.

5.3.3. Zeeman Slower Realization

Construction of the transverse-field magnetic-dipole Zeeman slower is quite simple compared to the traditional tapered-solenoid approach. A 0.5″-thick aluminum-plated cast-iron frame serves both as the magnet mounting structure and a magnetic shield.[6] The 5/8″-diameter neodynmium magnets are glued into aluminum cylinders, which are in turn attached to bronze screws threaded through the top and bottom of the iron box. The height of the magnets is thus easily adjusted, and the $\hat{z}$-axis spacing duplicates the Ovchinnikov design with 12 sections equally spaced 2.083-cm apart (with no magnets needed at the zero-crossing field location) and the spacing of the final dipole pair increased to 2.7 cm to better mimic the steep optimal field gradient at the slower exit [370].

Our aluminum cylinders are anodized red/blue to mimic traditional north/south magnetic field polarity, but the spacing from the slower axis is not a direct indicator of field strength at a given location: decreasing magnet stack thicknesses are used in the central areas in order to fit the magnets inside the frame. The magnet stacks are

---

[6] Any ferromagnetic material would serve equally well as a magnetic shield, and certain steels are easier to machine than cast iron, but we did not realize this at the time of construction and simply duplicated the original design.

well-approximated by point dipoles with magnetic moments $M = B_i V/\mu_0$ where B_i is the intrinsic induction of the material and V is the volume of the stack. The resultant total field at a given location along the slower is the sum of the individual dipole fields, plus those of the aligned image dipoles generated by the top and bottom plates of the cast iron box at $x = \pm 16.1$ cm. The inclusion of the image dipoles from the end plates of the box (2 cm from the first and last magnet pairs) is also important to meet the abrupt field gradient at the start and end of the slower; these image dipole pairs are anti-parallel to their nearest real neighbors. The optimal field on-axis was calculated using Ovchinnikov's positions and heights for 15-mm-diameter magnet stacks with $B_i = 1.1$ T surrounded by ideal magnetic shields [370]. The x-positions of our magnet stacks (composed of K&J Magnetics N42 magnets DA1, DA2, and DAH1 with thicknesses $1/16''$, $1/10''$, and $1/8''$ and residual induction $B_r = 1.3T \approx 1.1 \times B_i$) were adjusted to match the measured on-axis field to the ideal field (see Fig. 5.6).

Our Zeeman slowing beam profile differs from Ovchinnikov's parameters: to better match the divergence angle of our apertured atomic beam, we set the focus approximately 1 cm behind the oven nozzle, 63 cm behind the start of the slower. We expand the Zeeman slowing beam using a telescope with f=50.8 mm and 300 mm lenses before the periscope that brings the beam up from the optical table to the sapphire window terminating the atomic beam path. We initially adjusted the lens separation with the periscope beside the vacuum chamber, to set the waist position and check the beam size at the aperture locations (to avoid clipping), and then moved the periscope into place. The resultant beam profile gives a waist of 1.5 cm at the sapphire window, converging at an angle roughly equivalent to the apertured hot beam angle $\theta_f = 6.6$ mrad. The saturation parameter $s_0(z)$ for $P_{\sigma^-} = 22.5$ mW is then 2.2 at the start of the slower and 1.1 at the end, versus Ovchinnikov's $s_0(z) \approx 5.5$ at the start and 0.7 at the end. A simulation similar to that shown in Fig. 5.7 indicates that our beam profile may result in a higher $v_f \approx 80$ m/s and a shift of the slower capture range to lower initial velocities, $v_{0\ \mathrm{min}} - v_{0\ \mathrm{max}} \rightarrow 90 - 400$ m/s. The final velocity is apparently still less than the capture velocity of the top MOT, but the shift would limit the percent of atoms slowed to 30%. Given the uncertainty in beam-clipping losses, the estimated final cold flux is not dramatically affected.

One disadvantage of the transverse-field Zeeman slower is half of the slowing-beam power is wasted. This design is an increasing-magnetic-field σ^- slowing configuration; the relevant scattering transition is $m_F = 0$ to $m'_F = -1$. However, the quantization axis imposed by the transverse field ($\mathbf{B} \parallel \pm\hat{x}$) is perpendicular to the slowing-beam propagation vector ($\mathbf{k} \parallel -\hat{z}$), so the best we can do to match the required polarization is to use a linearly polarized slowing beam, with polarization along $\hat{y}$. Recall from Sec. 3.2.2 that this polarization is then an equal superposition of σ^+ and σ^-; the σ^+ transition $m_F = 0$ to $m'_F = +1$ is far-detuned except at the zero-crossing of the magnetic field and so half of our light has very little effect on the atomic beam. The total power of our slowing beam is typically set to $\sim$45 mW, which corresponds to the design power of 22.5 mW available for the σ^- transition.

The Zeeman slower works as advertised to load large top MOTs with the design detuning of $\Delta = -500$ MHz, and has proven robust to small slowing beam misalignments and power fluctuations. We have observed MOT loading with slowing-beam powers as low as $\sim$20 mW, and although we check the beam alignment periodically (centering on the atomic-beam deposit on the sapphire window and checking the alignment at the oven exit using the camera at the small spherical octagon), this is not critical to MOT operation. Given the observed top MOT sizes, more than sufficient for planned experiments, no effort was taken to further optimize the Zeeman slower. We have noticed that increasing the slowing beam detuning appears to lead to brighter MOTs, but because full optimization of beam detuning and alignment is not trivial in our single-pass cascaded AOM setup (Fig.) this was not further explored. If larger strontium MOTs are required for future experiments, optimization of the detuning and beam-focusing parameters would be worth investigating. Given the length of the Zeeman-slower pipe, it would also be relatively simple to redesign the field for a longer slowing region, which would allow a significantly higher $v_{0\mathrm{max}}$ and hence cooled beam flux. Finally, there are several designs for permanent-magnet longitudinal Zeeman slowers [300, 307, 371]; switching to a longitudinal-field configuration would allow us to match the σ^- polarization and save over 20 mW of currently wasted 461 nm light.

5.4. MOT Regions

Our chamber design and experimental plans require two separate MOT regions, one for direct loading and cooling from the Zeeman-slowed atomic beam, and a second region with better isolation and optical access for future cold-atom experiments. A double-MOT configuration like ours is often used to allow large collection rates in the first MOT and better control in the second, but there are clever schemes that combine the advantages of both regions in one final MOT area, for example by implementation of a cold-atom deflection stage directly after the Zeeman-slower exit (essentially a 2D-MOT, angled relative to the atomic-beam axis) [357]. However, our double-MOT setup is a robust and flexible configuration that should allow adaptation of the strontium apparatus to a variety of future cold-atom experiments.

5.4.1. Top MOT

The goal of the top MOT is to maximize the capture of cold atoms from the Zeeman-slowed beam. To maximize the capture rate, the top MOT capture radius should match the cold beam radius at the MOT location. The hot atomic beam diameter will be $\simeq 1.3$ cm, but the extent of the cold flux emerging from the slower is more difficult to predict: transverse heating effects would increase the beam diameter to as much as almost 4 cm by the MOT region, but many of these cooled atoms will clip inside of the slower pipe. Since the MOT capture radius is proportional to the MOT beam diameter, our approach is to use the largest MOT beams within reason to capture as many slow atoms as possible.

We chose the 6″ spherical octagon (Kimball Physics MCF600-SphOct-F2C8) for the top MOT chamber in part for the optical access offered by the eight 2-3/4″ CF-flange equatorial ports. One port attaches to the Zeeman slower nipple, and the opposite port meets the 6″-long nipple with the heated sapphire viewport which terminates the atomic beam and serves as the entrance for the Zeeman-slowing beam. The other 6 equatorial ports are covered by 1.4″-clear-aperture viewports (Larson VP-150-F2), AR-coated for both 461 and 689 nm. We expand the horizontal MOT beams to nearly fill the viewports using telescopes comprised of f = 50.2 mm and 500 mm lenses; periscopes bring the beams up from the optical table to a breadboard assembly mounted on the 80-20 frame around the spherical octagon. The front horizontal MOT beams intersect the atomic beam at a 135°-angle to the atomic beam axis; retro-reflecting mirrors outside the opposing spherical octagon ports create the rear horizontal MOT beams which then intersect at 45° to the atomic beam axis. Quarter-wave ($\lambda/4$) plates in front of each MOT beam port enforce the required σ^- polarization. The remaining two viewports, perpendicular to the atomic beam axis, allow real-time monitoring by camera and by eye. The σ^+ vertical MOT beam enters through the science cell located below the spherical octagon, intersects the atomic beam at 90° degrees, then travels all the way through the 6″ CF four-way cross (connecting to the TSP and ion pump) and 2-3/4″ CF tee (access to turbopump station) to another AR-coated viewport at the top of the tee, near the optical table ceiling. Another retro-reflecting mirror at this location (plus $\lambda/4$ plate) creates the opposing vertical MOT beam. (The 497 nm repump beam is overlapped with the vertical MOT beam to double-pass through the MOT.) The vertical MOT beam diameter is limited to 1 cm by the diameter (nominally 0.573″) of the science-cell glass-to-metal seal.

Given an appropriate magnetic-field gradient, the capture volume of our top MOT would be proportional to the overlap volume of the MOT beams. For our configuration, this is approximately a spheroid horizontal and vertical diameters 0.5 mm and 2.5 cm; the solid angle this volume presents to the cold atomic beam would define the captured flux. However, as described in Sec. 5.2, the strontium deposits on the final sapphire window indicate that our atomic beam is slightly misaligned off-center and low in the MOT chamber. Rather than attempting to realign the MOT beams and tweak the magnetic field to match this deviation, we align the beams to the center of each viewport pair (or the center of the vertical axis, in the case of the vertical beam) and often shift the magnetic fields to load the top MOT higher yet, so that the typical top MOT loading zone is $0.5-1$ cm above the background hot atomic beam fluorescence. This shift does not appear to affect the loading rate, confirming the prediction that the cold beam flux is substantially broadened by transverse heating effects in the Zeeman slower. Loading the MOT above the atomic-beam axis should reduce disturbances due to the effects of the Zeeman-slowing beam and constant bombardment by hot unslowed atoms, but the offset makes it difficult to estimate the cold flux delivered to the actual MOT capture region.

Of course, defining the MOT capture region to be proportional to the MOT beam overlap volume assumes that the Zeeman shift of the excited state sublevels matches the MOT beam detuning at the boundary of this volume, which is not true for our top-MOT coil configuration. The background theory of the magneto-optical trap is discussed in Sec. 3.2.3, but for the purposes of understanding the vacuum chamber design recall that the MOT magnetic-field gradient spatially tunes the scattering force to provide the required trap restoring force. The alkaline earths, with their small magnetic moments, typically need much higher magnetic field gradients than the alkalis for tight MOTs: the $\kappa/2\pi = 1.4$ MHz/G Zeeman shift of strontium's $^1\mathrm{S}_0 - {}^1\mathrm{P}_1$ transition means a field gradient of 40 G/cm would be required to match the $\Delta/2\pi = 40$ MHz MOT beam detuning over a reasonable trap radius of 0.7 cm.

The magnetic field is typically provided by a pair of coils in the anti-Helmholtz (AH) configuration (equal and opposing currents, ideally with coil separation d equal to coil radius r to maximize the gradient at the center point) which creates a quadrupole field: zero on axis at the center of the coils, increasing approximately linearly outward from the center for distances less than $\sim d/4$. The magnetic field on-axis for a pair of AH-coils with N loops carrying a current I is simply the sum of the fields generated by each loop,

$$B(z) = \frac{\mu_0 I N r^2}{2\Big(\big(r^2 + (z - d/2)^2\big)^{3/2} - \big(r^2 + (z + d/2)^2\big)^{3/2}\Big)}, \tag{5.15}$$

where z is the axial distance from the center point between the coils (more generally the field at any point can be calculated from the Biot-Savart Law). One disadvantage of the 6″-spherical octagon chosen for the top MOT region is the limitation imposed on the placement of our AH coils (assuming we want to avoid placing them inside the chamber itself): the closest possible coil separation $d = 11.25$ cm is given by placing the coils above and below the spherical octagon, which requires coils that are built into the vacuum chamber upon assembly and hence bakeable. Even with this coil separation, we require many coil turns and relatively high currents to achieve the required field gradient.

Our AH coil forms are machined from 8″-OD aluminum rings with two channels cut into the outer circumference: one (1/2″ wide x 3/4″ deep) to hold the coil wires and a separate channel (1/8″ wide x 3/4″ deep) for water cooling. A second outer ring welded around the coil circumference seals the water-cooling channel, with a Swagelok-fitted adapter for the circulation ports. We wrapped the coils with 20 AWG polyimide-insulated magnet wire (MWS 404666), using a motor to slowly spin the coil form while feeding the tensioned wire into place and painting each layer with high-temperature epoxy (Epo-Tek 353ND). The large 6″-CF 4-way cross above the spherical octagon runs through the center of the upper coil, so the coils were installed during chamber assembly, mounted to the aluminum plates that secure the 6″ spherical octagon to the 80-20 frame.

In the end, we had 308 turns per coil with an average coil radius of $r = 9.15$ cm; wired in series, the coils present a 12 Ω total resistance that rises with temperature to ~ 13.5 Ω when running at high currents, even with water cooling. Powered by a 100 V, 10 A current supply (Kepco ATE 100-10M), this resistance increase limits the maximum possible current to $I_{\max} = V_{\max}/R \simeq 7.5$ A. At this current the dissipated power is 760 W, more than enough to cause a coil meltdown without cooling, so we use two separate chillers (Neslab RTE-8 and RTE-4DD, cooling capacity $\simeq 500$ W

at 20°C) set to typically $15 - 20$°C to individually cool the coils. Current-controller operation is dependent upon the outputs of flow monitors (McMaster-Carr 2371K4) installed inline with both circulators, but the Kepco supply's automatic current-overload shutoff in response to the resistance increase with temperature is a foolproof failsafe (we originally included temperature switches as well, but the epoxy securing the temperature sensor to the coil forms failed over time; the flow switches and the current controller's own limitations are the only safeguards at this point). Vibrations from the circulators initially transmitted through the circulator tubing to the coils and chamber; potting several loops of the supply-line tubing in concrete eliminated this problem. We also observed high-frequency vibrations of the coil forms that we eventually tracked down to current-supply oscillations; operating the current supply in "slow" mode fixed the problem but we subsequently shifted back to "fast" mode for faster switching times, installing an extra 1.0 μF, 100V capacitor in parallel with the coils to prevent ringing.

The 7.5-A maximum current limits our maximum top MOT magnetic-field gradient to dB/dz = 28 G/cm at the center along the coil axis; by symmetry the gradient in the radial direction (in the plane of the optical table) is half this value. (Despite the possibility of confusion, we follow convention and designate the AH-coil axis as the top-MOT z-axis, although this is perpendicular to the atomic beam z-axis referred to in the previous section.) To avoid operating near the current controller shutdown point we typically use 6.8 A when loading the top MOT, resulting in the axial and radial field profiles plotted in Fig. 5.8. The resultant Zeeman shifts near the MOT center for the $^1P_1$ sublevels are plotted in Fig. 5.9: for small displacements from the MOT center, we are indeed operating in the region of approximately constant magnetic field gradient.

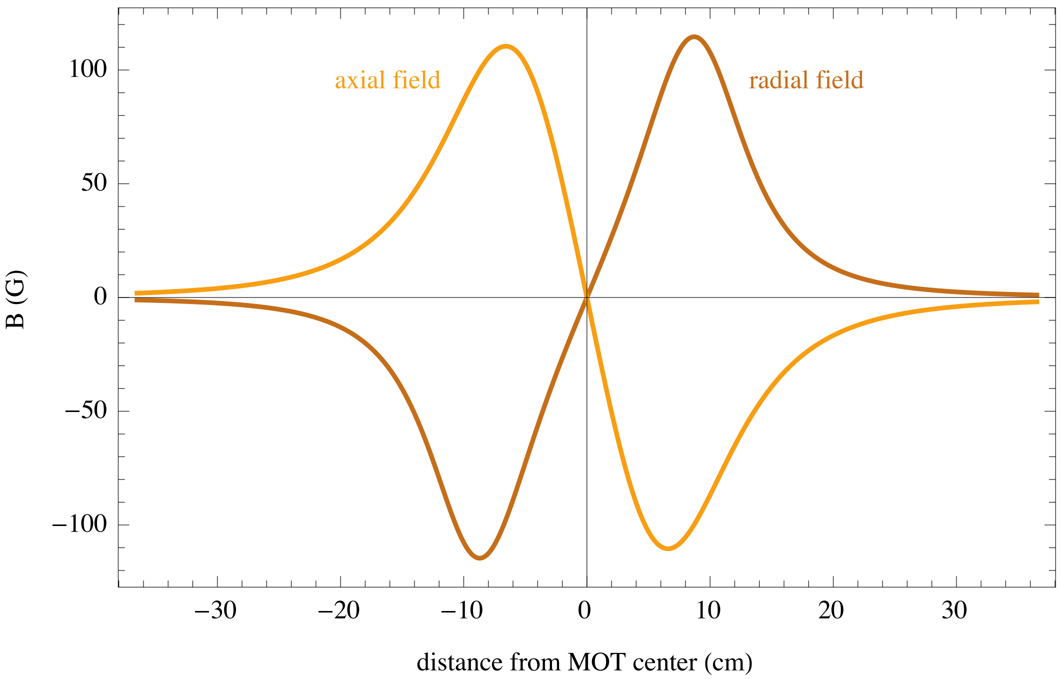

FIGURE 5.8. Top MOT axial and radial magnetic fields for anti-Helmholtz coil current $I = 6.8$ A.

In Figure 5.9, the MOT laser detuning ($\Delta_{\mathrm{MOT}}/2\pi = -40$ MHz) is marked by the dashed blue horizontal line; when the detuning is equal to the Zeeman shift, the scattering force is maximum for zero-velocity-class atoms. This location is marked by the dashed line, and would be approximately equal to the trap radius. Note that the difference in Zeeman shifts for the radial and axial fields would lead us to expect a very large, oblate MOT, $\sim$4 cm in diameter in the radial direction by $\sim$2 cm in the axial direction. The actual MOT size is much smaller, particularly in the radial direction, as a result of the beam waists used: although the scattering forces from the radial x and y MOT beams are maximized $\sim$2 cm away from the trap center, the extent of optical molasses is limited by the z-beam diameter to 1 cm in the radial direction; for our MOT, this defines the maximum possible radial trap diameter. The 2.5-cm x- and y-beam diameters do overlap with the z-beam scattering force maximum, so we

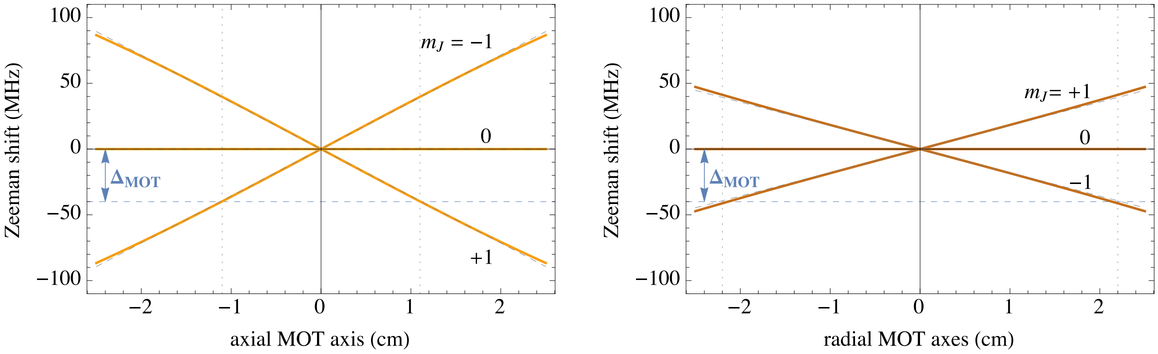

FIGURE 5.9. Top MOT $^1\mathrm{P}_1$-sublevel Zeeman shifts in the axial and radial directions. Orange curves: actual shifts due to the magnetic field of Fig. 5.8; dashed gray curves: linear approximation for axial and radial gradients $dB/dz = -26$ G/cm and $dB/dr = 13$ G/cm. Also shown is the MOT beam detuning $\Delta_{\mathrm{MOT}}/2\pi = 40$ MHz (blue, dashed): when the detuning is equal to the Zeeman shift the scattering force from the respective MOT beam is maximized for zero-velocity atoms (location marked by grey, dotted lines).

end up with a trap elongated along the z-axis, "prolate" (football-shaped) instead of oblate (pancake-shaped).

5.4.2. Bottom MOT

The bottom MOT is formed in the glass cell that extends below of the 6″ spherical octagon; this is where future strontium experiments will take place, so we often refer to it as the "science cell." This region offers the highest vacuum of our chamber, being isolated from the constant bombardment of hot and cold atoms from the main atomic beam. The glass cell offers the greatest possible optical access for the multiple MOT beams, optical lattice beams, and cameras required in future experiments, although in practice bringing all the required components into place beneath the main vacuum chamber (and working around the 80-20 frame) occasionally presents a challenge.

We opted for ColdQuanta's standard Pyrex cell (CQMC0006), a 0.879″ square by 4.5″ long cell (with no anti-reflection coatings, to save cost). The cell is mounted on a

1-1/3″ CF flange that meets the 6″ adapter CF at the spherical octagon's bottom port; the $\sim 0.5''$-diameter bore at the glass-to-metal seal location is a major disadvantage of the cell design (or our choice of cell placement), limiting the diameter of the top MOT vertical beam (which passes through the axis of the cell) as discussed above. The cell extends below the spherical octagon, offering a vertical clear aperture of almost 3.5″: we take advantage of this area and bring the retro-reflected bottom MOT radial beams in from below at 45° to the cell normal.The retro-reflected axial bottom MOT beam is normal to the opposite two cell walls, in the plane of the optical table, running through the center of the bottom MOT AH coils. The red (689nm) and blue (461nm) bottom MOT beams are collinear and expanded by telescopes comprised of f = 24.5mm and 100mm achromats to fill as much of the cell wall area as possible without clipping, to final beam diameters of ~ 1.5 cm.

Large magnetic field gradients are much easier to achieve at the bottom MOT location because the only limit on the distance between the anti-Helmholtz coils is the width of the cell itself. We repurposed coils built for a previous Rb MOT experiment in our lab [216, 311], consisting of 40mm-diameter Delrin frames wrapped with 216 turns of 23 AWG magnet wire to provide an axial field gradient of 24 G/cm per amp when separated by 50 mm. Our cell is narrower than the Rb science cell so we reoriented the Delrin coil mounts to position the coils closer to the cell walls, ending with an average coil separation $d \simeq 40$ mm. At this separation, the axial and radial field-gradient components are $dB/dz = 36$ and $dB/dr = 14$ G/cm per amp. As the bottom blue and red MOT loading sequences require various magnetic field gradients, a full discussion of the expected bottom MOT parameters will be given in Sec. 6.3 and Sec. 6.5, but for reference the magnetic field profile in Fig. 5.10 is plotted for a current of 1 A. (As indicated by Eq. 5.15, the field and gradient scale linearly with current.)

Because the coils are far from the optimal $d \approx r$ condition, the peak magnitudes of the radial and axial fields are very different and the field gradient is smaller than the maximum, but more than sufficient for our needs.

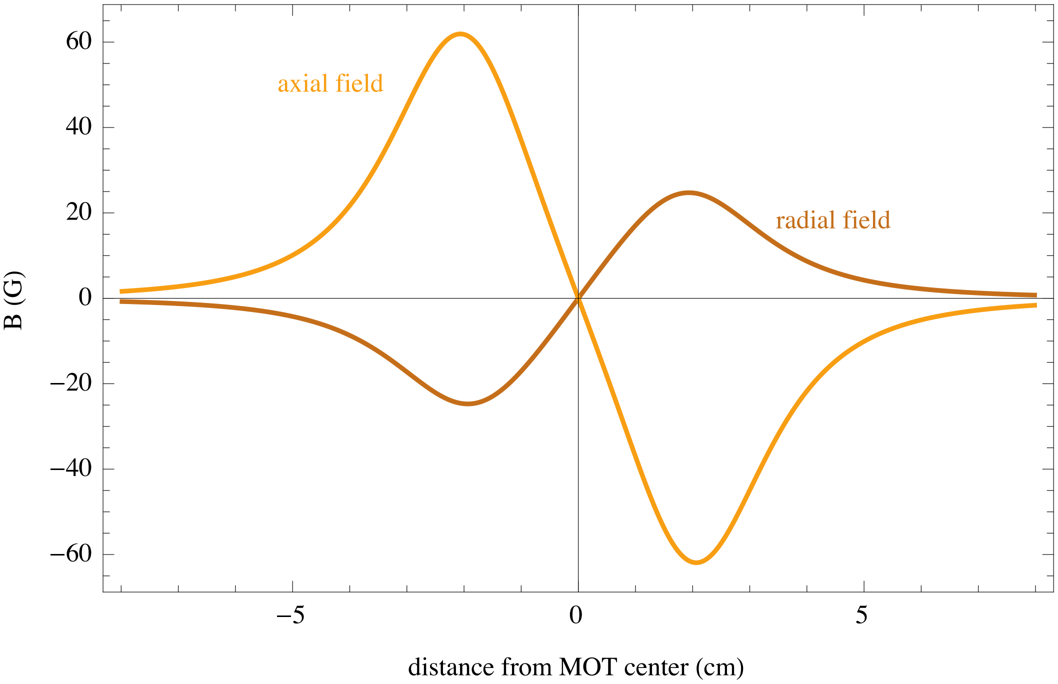

FIGURE 5.10. Bottom MOT axial and radial magnetic fields for $I = 1$ A AH-coil current: field gradients near the MOT center are $dB/dz = 36$ and $dB/dr = 14$ G/cm.

Delrin (polyoxymethylene or polyacetal) was chosen for the coil forms as an easily machinable, non-conductive material to allow fast coil-switching times by avoiding eddy currents. However, the melting point is 175°C: these coils are not bakeable, and were installed with the associated bottom MOT optics after chamber assembly and bakeout. The coils are powered by homebuilt current supplies capable of 5-A output [216]; the circuits offer the option to include over-temperature shutdowns but this section was not originally installed because we did not expect to be running the coils at high currents. However, a series of unfortunate events illustrated the importance of temperature safeguards. As described in Sec. 6.3, we occasionally run the coils briefly at 2.3 A to form a tight MOT when setting the background magnetic field offset, and on one occasion an incorrectly exited script left the coils at this high current long enough to cause melting of a portion of the coil form. The coil was salvageable but further mishaps left it in usable but ugly condition; we ultimately chose to build a replacement coil. The new coil form has an AD590 temperature sensor embedded in the form, and the current supply temperature shutdown is enabled.

5.5. Chamber Assembly and "Bakeout"

Achieving UHV is a challenge and every cold-atom group seems to follow a unique cleaning, assembly, and "bakeout" regimen with almost superstitious zeal [372]. A useful reference for detailed procedures is Appendix B of Kevin Birnbaum's thesis [359], and our practice mostly aligns with his recommendations. A key principle is of course extreme cleanliness: the enemy of ultra-high vacuum is outgassing, or the gradual emission of molecules over time from a surface under vacuum. Surface contaminants will naturally contribute a high outgassing rate, so cleaning of all parts is critical, but to reach UHV two additional slow outgassing sources must be addressed: hydrogen dissolved in the bulk material and water vapor and other atmospheric gases adsorbed to the surface. The "pre-bake" and "bakeout" procedures described below address these sources.

Vacuum parts direct from suppliers were generally considered clean enough to go straight to pre-bake[7] but we thoroughly cleaned any homebuilt or modified components by sonicating in a series of Alconox (alkaline detergent), deionized water, and isopropyl alcohol baths. Throughout the cleaning process and onwards we handled the parts only when wearing powder-free nitrile gloves and used oil-free UHV

---

[7] A few parts from Kurt J. Lesker company had visible interior deposits and required the full cleaning treatment.

aluminum foil (from All-Foils) for part storage. After cleaning, we "pre-baked" all components in air at 450°C for at least 24 hours.[8] Without baking, stainless steel outgasses at a rate of 10^{-11} torr L/cm^{2}s, and atomic hydrogen dissolved in the bulk of the material during manufacture accounts for 99% of the gas emitted [372]. A pre-bake at temperatures above 350°C speeds the process of desorption of this hydrogen, and (when done in air) promotes the formation of a layer of chromium oxide at the surface which has been claimed to act as a barrier to further hydrogen migration into the bulk. The air pre-bake can reduce hydrogen outgassing rates by a factor of 500 [373] and results in a dramatic color change of the stainless-steel pieces; as an example the two spherical octagons after pre-bake are shown in Fig. 5.12.

FIGURE 5.11. Vacuum chamber 4.5″ and 6″ spherical octagons, after air pre-bake
.

After pre-bake all parts were rinsed with acetone and then methanol, both spectroscopic grade (ultrapure), dried with compressed air, and wrapped in UHV

---

[8] Most parts were baked in an oven at the UO Technical Services Administration shop, but the 6″-CF 4-way-cross was too large to fit in this oven and was baked in a ceramics kiln at the UO Craft Center. To commemorate the experience, a tiny blue ceramic pig was constructed while the kiln temperature was monitored; this pig now guards the top of the vacuum chamber for good luck.

aluminum foil until assembly. We assembled the chamber in stages, keeping exposed ports capped with UHV aluminum foil. We rinsed the copper (or nickel) gasket for each CF joint with ultrapure methanol immediately prior to insertion and positioned them with care to avoid touching either the gasket sealing surface or the “knife-edge” flange ring that bites into the gasket; each flange was joined with silver-plated screws to avoid seizing and tightened according to the usual CF-flange procedure [359]. We assembled the chamber on the floor beside the optical table because the “bakeout” oven, which was eventually built around the chamber, would not fit in the space between the table surface and table ceiling. The 80/20 aluminum frame which allowed us in the end to lift the entire chamber onto the optical table was critical for structural support during the assembly process. It is important to avoid exerting any torque or shear stress on chamber joints during or after assembly, but the overall length of the chamber (and the top-heavy design with ion pumps, valves, and other heavy components above and often to the side of the main beam axis) would have made excessive torque difficult to avoid without the support of an adjustable frame. The frame also allowed us to assemble the front and back halves of the chamber separately, slide them together to meet at the inline valve, and then fine-tune the alignment while sighting through the final sapphire window backwards along the atomic-beam path, through the two nickel apertures and out the rear of the strontium oven pipe before the oven and nozzle were installed. (After the oven was installed we repeated this procedure with the oven on: with our eye centered in the final sapphire window we attempted to fine-tune the chamber alignment by centering the glowing oven nozzle in the nickel aperture rings.)

We initially assembled the chamber with blanks on all viewport locations and the port that would hold the science cell, and no strontium oven, for the first "bakeout." Baking an assembled vacuum chamber while continuously pumping to remove residual gases is the final step in acheiving UHV: just as the pre-bake helped to speed the process of driving adsorbed hydrogen out from the bulk of the stainless steel, the bakeout speeds outgassing of atmospheric gases (particularly water vapor) adsorbed onto the interior walls of the chamber. Glass-to-metal seals can be a point of failure, and anti-reflection coatings may have lower maximum temperature ratings than other vacuum components (although our bakeout temperature was limited by the anti-Helmholtz coil epoxy, rated to 225°C), so it is a common practice to perform one bakeout with no glass elements and a second bakeout after final assembly. The bakeout temperature should be above 180-190°C to drive off thin-film surface water[359], and typically lasts about a week. Large ovens or heater tape tented in aluminum foil are common solutions to reach the required uniform temperature. Our chamber required a combination of approaches: we constructed an oven from aluminum-foil-wrapped fire bricks and aluminum sheet metal around the low-pressure side of the chamber and wrapped the oven side of the chamber in heater tape. We also laid heater tape along the floor of the fire-brick oven; in the end we needed 13 strips of heater tape controlled by 8 Variacs (we also used the strontium oven heaters themselves). We measured the chamber temperature (particularly at sensitive locations like the anti-Helmholtz coil forms and eventually the Pyrex science cell) using 16 thermocouples read out by home-built ethernut-enabled thermocouple monitors, and individually adjusted the Variacs to avoid sudden temperature changes or temperature gradients that could stress joints and glass-to-metal seals.

We used a turbopump (BOC Edwards EXT-70H-24V) backed by a rotary-vane pump (BOC Edwards RV5) to evacuate the system during bakeout, with the ion pumps turned on and the TSP activated during cooldown. The station also contains

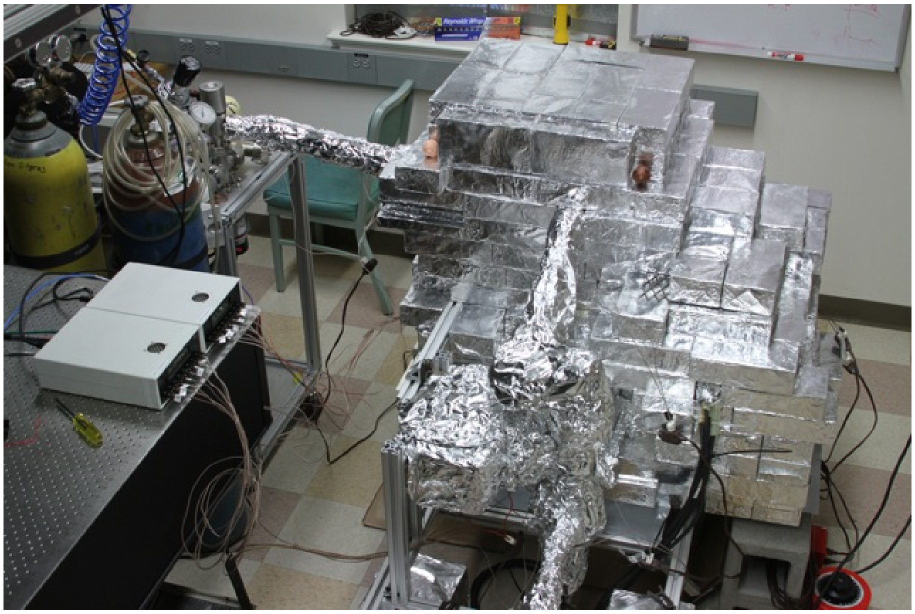

FIGURE 5.12. Vacuum chamber during bakeout: view from high-pressure side of chamber, showing fire-brick oven around low-pressure side of chamber, turbopump station upper left, foil-wrapped temporary bellows connecting both sides of chamber to turbopump station,16 thermocouples plugged into ethernut-enabled thermocouple monitor boxes, and a few of the 8 Variacs used to power the heater tape inside the oven and under the aluminum foil.

vacuum gauges and a residual gas analyzer (RGA). We attached the flexible bellows from the turbopump station to a temporary 2-3/4″ CF tee connecting on one side to the right-angle valve above the low-pressure side of the chamber and on the other (via a second flexible bellows plus 2-3/4″ CF nipple extender) to the valve above the high-pressure side of the chamber. We began each pump-down / bakeout cycle with the heat off and the valves to the chamber closed and began pumping to evacuate any contaminants from the two bellows, then slowly cracked open the two chamber valves and evacuated the entire chamber with the oven off, reaching typical pre-bakeout pressures of 10^{-8} torr. We then slowly ramped up the Variac setpoints until reaching the goal temperature of 200-225°C (limited by the coil epoxy maximum $T = 225°\text{C}$), adjusting the setpoints and often oven itself (i.e., swapping out failed heater tapes and changing the foil tenting) to avoid temperature gradients. We held at the maximum temperature for at least a week during each bakeout. During this period we also "degassed" the TSP filaments by applying a current of 40 A (just below the 45-A sputter activation current) to remove any contaminants, and then kept them hot with 32 A, rotating through each of the three filaments. The pressure measured at the turbostation wide-range gauge (WRG) naturally rises during the initial temperature increase, up to 10^{-6} torr during the first bakeout (less with each subsequent bake), then gradually falls; we began cooldown when the pressure reading more or less leveled out again in the 10^{-9} torr range. During cooldown, the ion pumps were activated at their maximum operating temperature of 150°C, with the rest of the chamber at a slightly higher temperature to prevent migration of any outgassing contaminants.

We expected our system to require two bakeouts: one with the viewports and science cell port capped by blank flanges, and no strontium oven, and a second with these parts installed. The first bakeout appeared to go smoothly, other than a malfunction on the part of the 55 L/s ion pump (sent back to Duniway for inspection),[9] and reached a final $P = 8.5\times10^{-9}$. We flushed the chamber continuously with argon (from the top of the tee above the low-pressure side of the chamber out through the oven nipple) while installing the final parts and re-installing the returned ion pump. During the second bakeout, we tested the strontium oven, which caused some pressure spikes (the walls of the collimator tubes present a large outgassing surface area, and the oven design leaves the possibility for trapped gases behind the

---

[9] The finicky behavior of this pump has continued after repair, sometimes requiring use of the overload button to force on and showing continual current fluctuations, but appears to work fine otherwise.

crucible cylinder), but otherwise all appeared well, and the final pressure at the WRG was $P = 7.1 \times 10^{-9}$ after cooldown.

However, helium leak-checking revealed problems, and slight torques applied to the chamber, particularly at the inline valve behind the Zeeman pipe, caused large pressure spikes. The initial Zeeman pipe was a 15″ long, 1-1/3″ CF nipple with a reducing nipple and reducing flange on either end to mate with the inline valve and large spherical octagon; we replaced this assembly with a 17″-long pipe with welded 2-3/4″ CF flanges to eliminate two joints.[10] However, a third bakeout still revealed insidious slow leaks, by which point it was clear that the culprits were the nickel gaskets that also serve as atomic-beam apertures on either side of the inline valve. We had used 1-1/3″ Ni gaskets (MDC 191060) in other components without issue, but the apertures were machined from apparently bead-blasted, 2-3/4″ blank gaskets from Grass Manufacturing. We eventually realized that work-hardening can reduced the ability of nickel to flow under pressure: where the knife-edge of the CF flange bit into the Ni gasket, the patterns from scratches or bead-blasting were pressed into the gasket and could form pinhole leaks. We machined new gaskets from custom cold-rolled blanks (Metal Technology, Ni-200) and then annealed the gaskets in a high-temperature oven at 1500°C; these gaskets worked fine [144]. We later discovered that another group had published an entire paper documenting similar challenges with Ni gaskets in UHV systems [374].

After the fourth and final bakeout and cooldown, the pressure reading at the turbopump station was $P = 8.1 \times 10^{-9}$ torr, and the ion pump currents were offscale and $\sim 13\ \mu$A for the 75 L/s and 55 L/s pumps at the low- and high-pressure sides of the chamber. Five people were needed to lift the evacuated chamber off the floor

---

[10] We could have used a much shorter pipe and reduced the overall length of the chamber, but we did not want to re-adjust the 80-20 frame at that point.

and onto the optical table. Over time, the 55 L/s pump current has continued to fall slightly (perhaps as a result of strontium acting as a getter), and the 75 L/s current has risen to 0.5 μA, indicating pressures at the low- and high-pressure sides of $< 10^{-9}$ and $\sim 1 \times 10^{-8}$ torr, respectively. This level of vacuum is more than sufficient for cold-atom experiments, but the TSP could be activated more frequently if lower pressures were desired.

CHAPTER VI

THE STRONTIUM MOT: COOLING AND TRAPPING ON THE $^1S_0$ – $^1P_1$ TRANSITION

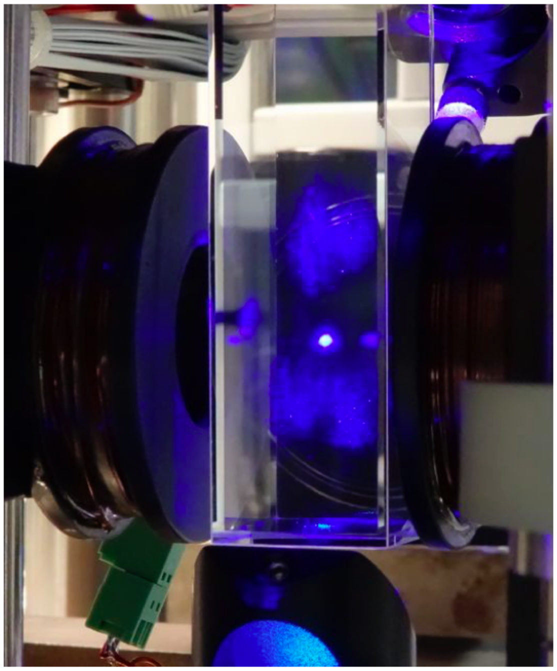

FIGURE 6.1. Science-cell 461 nm MOT.

This chapter describes our progress so far cooling and trapping strontium. We have achieved large blue magneto-optical trap (MOT) populations on the strong $^1S_0$ – $^1P_1$ cycling transition in both the top and bottom MOTs; by tuning our 461 nm and 497 nm trap and repump lasers, we have observed trapping of all three of the most abundant naturally occuring isotopes, although unless otherwise specified the work described here was carried out with ^{88}Sr. Sec. 6.1 begins by describing the computer control system, adapted from that developed for the Steck lab Rb experiment, which allows precise timing of experimental events and data acquisition.

Sections 6.2 and 6.3 describe details of the top and bottom MOTs and the 2D-MOT population transfer scheme we developed for loading the science cell bottom MOT. MOT populations are estimated from capture and loss rates (Sec. 6.2.1) and collected fluorescence intensity (Sec. 6.3.2.1); these sections also elaborate on some of the experimental issues unique to our setup, including magnetic field interactions and the limitations imposed by our imaging system. We attempted bottom MOT temperature measurements (Sec. 6.4.1) but our camera is too slow to precisely capture the 461 nm MOT-release ballistic expansion (although it should be sufficient for future red MOT and optical lattice experiments at colder trapped-atom temperatures); the size of the trapped distribution, however, indicates that our 461 nm MOT is at the expected temperature.

Finally, our current progress toward a red 689 nm MOT is covered at the end of this chapter. Narrow-line cooling on the 7.4 kHz $^1\mathrm{S}_0 - {}^3\mathrm{P}_1$ transition differs from the usual semiclassical regime of laser-atom mechanical interactions involving strong scattering transitions; we describe the experimental sequence we have been using to attempt to load a red MOT (Sec. 6.5). We have yet to observe trapped atoms in the red MOT, although we have seen evidence of 689 nm optical molasses. Some possible red MOT loading or detection complications are presented, and potential solutions are briefly explored

6.1. Computer Control, Data Acquisition, and Timing

We can load the top MOT from the Zeeman slower continuously without any special timing sequences, but most subsequent MOT transfer and data acquisition procedures require precise timing of several subsystem operations: changing the polarization of the vertical top-MOT capture/push beam, toggling or ramping magnetic field values, shuttering of various beams, and triggering the camera for data acquisition. To avoid the use of any expensive proprietary software that would limit flexibility and expansion of our computer control system, we use the “ZOINKS” architecture (“Zee Open Interface Networked Kontrol System” [375, 376]), with circuits developed by Todd Meyrath and Florian Schreck under Mark Raizen at the University of Texas [377] linked to microprocessors to synchronistically execute experimental sequences.

The basic idea of ZOINKS is to use one control computer communicating via ethernet to program the microprocessors, which load the control sequences onto interface boards (developed by Peter Gaskell of the Steck lab Rb experiment) which sync instrument-circuit execution of events to a stable external clock. The control computer sends the experimental commands in advance of the real-time sequence to the ethernet-enabled microprocessors (Ethernut 2.1 by Egnite GmbH [378]), which then load the first-in-first-out (FIFO) buffers of the interface boards. These boards are synced to a 10 MHz clock signal from an inherited commercial Rb atomic clock (shared with the Rb experiment), divided down to 250 kHz to match the data output rate of the Ethernuts, giving a timing resolution of 4 μs. When all boards are ready, a universal trigger unloads the FIFOs of each board to the instrument circuits, such that the measured timing jitter is 0.02 μs. In this way, the system takes advantage of the flexibility of ethernet communication but avoids the timing uncertainty that would arise from attempting real-time experimental control directly over ethernet links.

Each instrument box thus contains its own Ethernut and interface board in addition to the instrument circuits, and the system is easily expanded with an ethernet switch such that one computer can control many boxes. We currently use one 16-channel analog-output box, one digital-output box with two 16-channel digital output boards, and two 3-channel direct digital synthesizers (DDSs). There is also an analog-input box design, but we have fetched data directly from a digital oscilloscope (Agilent DSO6034A) or Fluke multimeter (Fluke 8845A) via telnet when needed; our primary imaging system, the Finger Lakes Instrumentation (FLI) camera (described further in Sec. 6.4.1) is also connected directly to the computer but triggered by a digital output. We ported a library of ZOINKS Perl modules and subroutines, written largely by Jeremy Thorn for the Rb experiment, to the strontium system (SrExperiment.pm). Using this library, in addition to a second module containing parameters and subroutines specific to the strontium system (SrSetup.pm), we can write fairly simple Perl scripts to execute synchronized chains of experimental events like those depicted in the timing diagrams of Fig. 6.5 and 6.7.

The analog outputs are currently used to vary the top and bottom magnetic-field coil currents, activate the bottom MOT 689 nm mechanical shutter, and adjust the pulse-analyzer set-point (as described further in Sec. 6.4.1). The analog box also acts as the "master box" for other boards: when all FIFOs are fully loaded, one channel of this box is used as a trigger to tell the other boxes to begin the experimental sequence. Digital outputs are used to inhibit the magnetic field coils, trigger the pulse analyzer, and control the stepper motors that open and close the atomic beam shutter and rotate the quarter-wave ($\lambda/4$) plate that changes the polarization of the vertical top MOT beam. We also use digital outputs to trigger the camera, mechanically shutter the Zeeman slowing beam, and to switch intensities of other beams by toggling acousto-optic modulator (AOM) radiofrequency (RF) drive signals through TTL RF switches.

A digital output is also used to control the timing of the timing of the red MOT AOM modulation through a direct digital synthesizer (DDS). The DDS sources are based on the AD9852 from Analog Devices and are capable of synthesizing a variety of analog waveforms at frequencies from DC to 135 MHz with < 25 ps jitter from the 10 MHz Rb clock input. The DDS's receive via telnet a frequency tuning "word" from the control computer in addition to the trigger from the analog box and a digital output signal for ramped frequency generation.

For many of our RF applications, direct digital synthesis is overkill: most the AOMs in this experiment are driven by RF signals produced by voltage-controlled oscillator (VCO) chips packaged into function-generator boards, which provide the option for manual or analog-input amplitude and frequency tuning. The typical stability offered by the RF function-generators, ~ 1 kHz, is much less than the linewidth of the 32 MHz $^1\mathrm{S}_0 - {}^1\mathrm{P}_1$ transition and hence more than sufficient for setting the frequency offsets of the AOMs used in the 461 nm saturated-absorption-spectroscopy (SAS) heat-pipe laser servo, Zeeman slower beam, and top and bottom MOT beams. However, the 7.4 kHz linewidth of the 689 nm $^1\mathrm{S}_0 - {}^3\mathrm{P}_1$ transition demands greater frequency stability, as well as the ability to precisely modulate the frequency during red MOT loading sequences (see Sec. 6.5), so we use DDS outputs for the 689 nm SAS and red MOT AOMs. We use two more DDS's to provide the 8.76 MHz and 3.16 MHz signals to precisely match the frequencies of the helical resonators driving the electro-optic modulators in the SAS FM-spectroscopy setups (see Sec. 4.5.1). Finally, the 914 nm optical lattice beams will require a high degree of phase-stability, and future strontium experiments may require modulation of the lattice, so we have also set up an AOM driven by a DDS signal in the 914 nm beam path.

The ZOINKS boxes are a small subset of the electronics built for this experiment (see Ref. [144] for details on some of the elements not discussed here), but they do allow automation of not only precision experimental sequences but day-to-day operations like opening and closing of the atomic beam shutter. Initial tuning and locking of the laser systems remains a manual procedure, as well as day-to-day alignment of beam paths. Besides the FLI camera, a CCTV security camera monitors the Zeeman-beam alignment as described in Sec. 5.1. The top and bottom MOTs can be observed in real-time by eye and by the use of two additional CCTV security cameras (EverFocus EQH5102 HD-SDI) mounted with close-focus 6x zoom lenses (Edmund Optics P/N 58-240 and obsolete NT52-274), which feed to generic 7" TFT-LCD dual-input monitors positioned at the vacuum chamber and the control computer.

6.2. Top 461 nm MOT

The top MOT loads directly from the Zeeman-slowed atomic beam - but slightly above the beam axis, as described in Sec. 5.2 - at the intersection of the retro-reflected 1-cm-waist ($1/e^2$ intensity radius) vertical beam and 2.2-cm-waist horizontal beams in the center of the large spherical octagon. The top MOT population is maximized by using the maximum magnetic field gradient our anti-Helmholtz (AH) coils can provide, 26(13) G/cm in the axial(radial) directions, at a current of 6.8 A. We use a MOT beam detuning of $\Delta/2\pi = -40$ MHz and typical beam powers of 2(8) mW in the axial(radial) beams. The resultant maximum MOT capture volume, discussed in Sec. 5.4.1, is a prolate spheroid with axial and radial diameters of approximately 1 cm and 2.2 cm, respectively. The repump beam, with a typical power of 0.5 mW, is co-linear with the vertical MOT beam (in order to intersect both top and bottom MOTs and take advantage of the effective power doubling gained by retroreflection). To maximize repump efficiency, we keep the beam small relative to the MOT area: this increases the intensity, and the random walk of trapped atoms takes them through the beam frequently enough to maintain the repump effectiveness.

We were initially surprised by two phenomena when first attempting to load the top MOT. The first was the amount of fluorescence in the top MOT chamber from the Zeeman slower beam. With a detuning $\Delta_Z/2\pi = -500$ MHz, we had expected this beam to be far off resonance for both the slowed atoms and the very fast atoms that were not captured by the Zeeman slower. For the slowed atoms, $v_f \simeq 25$ m/s, the Doppler shift $kv/2\pi$ for this class is only ~ 50 MHz and insufficient to bring them into resonance, while the uncaptured fast atoms, at $v \gtrsim 400$m/s leading to Doppler shifts $\gtrsim 870$ MHz, are shifted too far to the blue to be resonant. We reasoned that the fluorescence must come from the atoms that are partially slowed but then fall out of step with the resonant slowing condition — for example, we know that a significant fraction (as much as 50%, by one estimate [343]) will be lost from the slowing process due to ${}^1\mathrm{P}_1 -{}^1\mathrm{D}_2$ decays, as discussed in Sec 6.2.1.

However, we might expect the distribution of partially slowed atoms to mirror the low-velocity wing of the initial thermal distribution (since the ${}^1\mathrm{P}_1 -{}^1\mathrm{D}_2$ decay can happen at any point during the slowing process), so we were even more surprised to note that the Zeeman beam fluorescence changed dramatically when we turned on the top MOT anti-Helmholtz coils. The fluorescence increased at the edges of a sort of "hole" in the middle of the chamber, seeming to indicate some sort of magnetic-field shift causing increased or decreased fluorescence from a relatively narrow velocity class. The analysis of the transverse permanent-magnet slower performed by Hill *et al.* [300] may provide an explanation: they found (through

Monte-Carlo simulation of the slowing process) that the remaining partially-slowed thermal atoms continued to interact with the slowing beam at the exit of the slower, resulting in compression of the partially slowed atom distribution into a second peak centered at $\sim$ 200 m/s. The Doppler shift for atoms at this velocity, ~430 MHz, brings them near-enough into resonance with the Zeeman-slowing beam that some fluorescence is expected, and the additional Zeeman shift imposed by the magnetic field provided by the anti-Helmoltz coils at max current accomplishes the rest of the tuning, create a bright oval ring in the fluorescing beam centered around the zero point of the quadrupole field. As expected, we can shift the center of the ring using the top MOT Helmholtz coils; as such, the ring is a a useful diagnostic for rough-centering the MOT-beam overlap with the magnetic field zero.

The second surprise we encountered on first attempting to load the top MOT has a more straightforward explanation, but has also proven extremely useful to our subsequent experimental procedure. Our first attempts to observe a MOT were unsuccessful: we noted a bright, flickering, vertical band at the intersection of our trapping beams in the center of the large spherical octagon, but no clearly confined ball of atoms. On the contrary, the atoms appeared to jet out from the MOT region along the vertical axis; we could see weak fluorescence from ejected atoms along the vertical beam path all the way down in the science cell. Of course, as it turned out, we had the incorrect polarization for our vertical MOT beam: we had neglected to take into account a final mirror bounce after the $\lambda/4$ plate such that the polarizations of the upward/downward propagating axial beams were $\sigma^{+/-}$ instead of the required $\sigma^{-/+}$. In effect, we had made a 2D-MOT, with trapping in the radial directions, but along the third (vertical) axis, the atoms were pushed away from the MOT center instead of confined.

This problem was easily remedied with a 90° rotation of the $\lambda/4$-plate, but the mistake was fortuitous in demonstrating an efficient method for cold-atom transfer between the top and bottom MOT regions. We had planned to load the top MOT, then release and recapture the falling atoms in the bottom MOT. However, the atoms expand ballistically after release from the MOT, as described in Sec. 6.4.1, such that only a small fraction of the $\sim 1-5$ mK cloud from the 461 nm MOT would pass through the 1.4-cm-diameter glass-to-metal-seal aperture into the science cell. As a result, we had planned to follow the 461 nm MOT with a 689 nm narrow-line MOT (which would reach much lower temperatures, on the order of $T_r = 1$ μK, allowing drop-and-recapture which much less loss) in the top MOT location, but after observing the atoms in the science cell with the $\lambda/4$ plate in the 2D-MOT orientation, we realized we could load from these atoms and skip the process of loading the red MOT in the top chamber.

6.2.1. MOT Capture and Loss Dynamics

We have not made a careful measurements of the top MOT loading rate or lifetime, since the bottom 461 nm MOT or ultimately the bottom 689 nm MOT characteristics will be the critical factor in future cold-atom experiments; if the top MOT is working well enough to quickly load sufficient atom numbers into the bottom MOT, we are generally quite happy. However, it is worth noting a few estimated properties here for future reference.

The MOT capture velocity v_c defines the maximum speed of trappable atoms entering the MOT capture region. The optical molasses capture velocity is often given as $v_c \approx \Gamma/k$ where Γ is the decay rate of the cooling transition at wavelength $\lambda = 2\pi/k$, since this is the effective velocity width of the Doppler scattering force

Eq. 3.8, or the range of velocities over which the force has an appreciable effect. For the $\Gamma/2\pi = 30.5$-MHz-linewidth ${}^1\mathrm{S}_0 - {}^1\mathrm{P}_1$ transition at 461 nm, this would result in $v_c = 14$ m/s. However, the MOT capture velocity can be considerably higher: the addition of the magnetic field allows a sort of Zeeman slowing effect where the changing Doppler shift of atoms interacting with the MOT beams is compensated by the Zeeman shift. The capture velocity cannot be determined directly from the simplified expression for the 1D-MOT force equation 3.46 because this is derived in the limit where the Doppler shift and Zeeman shifts are small. It is valid for the already-captured, slow atoms near the center of the MOT but not for fast atoms approaching from the boundaries [224].

One method to estimate the MOT capture velocity is to assume the Zeeman shift exactly cancels the Doppler shift along the whole length of the trap (across the trap beam diameter), and to equate the work done by the maximum scattering force over that distance to the change in kinetic energy experienced by an atom that comes to a complete stop (and is reversed back toward the center) at the far end of the MOT [224]:

$$F_{\mathrm{scatt}} \cdot d = \frac{1}{2} m v_c^2 \quad \longrightarrow \quad v_c \approx \sqrt{\hbar k \Gamma w_0 / m}, \tag{6.1}$$

(assuming the beam intensity I is well above the saturation intensity I_{sat} to approximate $F_{\mathrm{scatt}} \sim F_{\mathrm{max}} = \hbar k \Gamma/2$), which leads to an estimate for strontium of $v_c \approx 140$ m/s for $w_0 = 1$ cm beam waists. Full calculation of the capture velocity numerically integrates the exact expression for the 1D-MOT scattering force to calculate the threshold velocity where atomic trajectories escape the MOT boundary [379]. These calculations generally find a capture velocity much higher than that estimated by $v_c \approx \Gamma/k$, and also show that although the fastest damping times are achieved by the use of a MOT beam detuning $\Delta_{\mathrm{MOT}} = \Gamma/2$, the capture velocity generally peaks at a larger detuning. Calculations by strontium groups using similar parameters to our blue MOT (chosen for that reason) find capture velocities $v_c \approx 50 - 80$ m/s.

Assuming the MOT capture velocity is indeed well above the final velocity v_f of the slowed atoms exiting the Zeeman slower, the maximum flux that can be captured can be estimated by the cold atom flux times the ratio of the MOT vs. cold-atom beam cross-sectional areas. As discussed in Sec. 5.2, the slowing process results in a substantial increase in the beam divergence angle and some atom losses to the inside of the Zeeman slower pipe; the final cold beam intensity $Q_{\text{cold}} \approx 10^{10}$ atoms/s (Sec. 5.3.2) will be distributed across an expanding beam with a diameter ~ 4 cm at the MOT location. Again, as a rough estimate, we will assume the cold flux is evenly distributed through the beam; the ellipse defined by the MOT capture zone with semi-major × semi-minor axes of $\sim 2 \times 1$ cm then allows a maximum $Q_c \approx 6 \times 10^9$ atoms/s to be captured from the Zeeman-slowed beam.

The steady-state trapped atom number will be a balance between the capture rate and inevitable losses. Several loss factors come into play: collisions with background gas molecules can be an important loss mechanism for closed-transition or adequately repumped MOTs, but several strontium groups have found that light-assisted Sr-Sr inelastic collisions contribute a significant loss rate as well. However, in the absence of a repump laser, the dominant loss channel arises from decays to untrapped states. Recall that repump lasers are useful when a cooling transition is not fully closed; in our case, the excited state of the 461 nm $^1\text{S}_0 - {}^1\text{P}_1$ transition has a small probability of decaying to $^1\text{D}_2$ rather than back to the ground state (see the level diagram in Fig. 2.1). From $^1\text{D}_2$, an electron can either decay to the $^3\text{P}_1$ state and then return to $^1\text{S}_0$ or become shelved via a decay to the metastable $^3\text{P}_2$ state.

In the first case, although both the ^{3}P$_1$ and particularly the ^{1}D$_2$ states are relatively long-lived (21.5 μs and 3 ms, respectively), the atom will usually remain trapped: at a typical maximum blue MOT temperature of 5 mK, the average atom will be moving at ~ 1 m/s and will travel only 0.3 mm and so will still be well within our MOT capture zone when it returns to the ^{1}S$_0$ state. In the latter case, the extremely long lifetime of the ^{3}P$_2$ energy level[1] implies complete loss from the MOT; if cold enough, these atoms may remain magnetically trapped in the weak quadrupole MOT field, but they will no longer interact with the MOT light over the duration of our experiments.

For the Zeeman slower, the subsequent decay paths after ^{1}D$_2$ are irrelevant: as discussed in Sec. 5.3.2, the interruption of Doppler cooling imposed by even the 3 ms lifetime of the ^{1}D$_2$ state will lead to losses from the slowing process. To further examine this effect [300, 343], the branching ratio for the two decays from ^{1}P$_1$, or the probability of a given decay path, is determined by the relative decay rates:

$$\begin{aligned} {}^1\mathrm{P}_1 - {}^1\mathrm{S}_0 : &\quad \Gamma_b = 1.9 \times 10^8 \text{ s}^{-1} \\ {}^1\mathrm{P}_1 - {}^1\mathrm{D}_2 : &\quad \Gamma_d = 3.9 \times 10^3 \text{ s}^{-1}. \end{aligned} \tag{6.2}$$

Thus the probability of a $^1\mathrm{P}_1 - {}^1\mathrm{D}_2$ decay in a single photon event is

$$P_D = \frac{\Gamma_d}{\Gamma_b + \Gamma_d} = 2 \times 10^{-5}, \tag{6.3}$$

vs. the 99.998% probability of returning directly to the ground state. While the likelihood of a decay to ^{1}D$_2$ appears minuscule, over many scattering events the effect is not trivial: after N photon exchanges, the probability of avoiding a ^{1}D$_2$ transition

---

[1] The calculated ^{3}P$_2$ total decay rate of $\sim 9 \times 10^{-4}$ s^{-1} [8, 380] leads to a state lifetime on the order of 10^3 s, or 15-20 *minutes*!

decays exponentially:

$$\begin{aligned} P_S &= \left(\frac{\Gamma_b}{\Gamma_b+\Gamma_d}\right)^N \\ &= \left(1+\frac{\Gamma_d}{\Gamma_b}\right)^{-N} \\ &\approx 1 - N\frac{\Gamma_d}{\Gamma_b} \\ &\approx e^{-\frac{\Gamma_d}{\Gamma_b}N}. \end{aligned} \tag{6.4}$$

The typical number of scattering events before a $^1\mathrm{D}_2$ decay is then $\frac{\Gamma_b}{\Gamma_d} = 5\times10^4$; while again this sounds large, recall that $(v_0 - v_f)/v_r \approx 4\times10^4$ photons are required to slow from our maximum Zeeman slower capture velocity $v_0 \sim 430$ m/s to $v_f \sim 25$ m/s (where $v_r = 9.9$ mm/s is the recoil velocity for a 461 nm photon exchange). A significant fraction of the fastest atoms initially captured by the Zeeman slower will thus be lost from the slowing process at some point due to these $^1\mathrm{D}_2$ decays, a consideration included in the final calculated cold beam flux (Eq. 5.13).

The effect on the MOT is slightly trickier to calculate, since two thirds of the atoms which decay into the $^1\mathrm{D}_2$ state will return to the ground state through the $^3\mathrm{P}_1$ decay path, given the ratio of the rates the two $^1\mathrm{D}_2$ possible decays:

$$\begin{aligned} &^1\mathrm{D}_2 -^3\mathrm{P}_1: \quad \Gamma_1 = 2.2\times10^3\ \mathrm{s}^{-1} \\ &^1\mathrm{D}_2 -^3\mathrm{P}_2: \quad \Gamma_2 = 1.1\times10^3\ \mathrm{s}^{-1}. \end{aligned} \tag{6.5}$$

The total number of trapped atoms, N_{MOT}, in steady state will be determined from the stationary solution of a rate equation of the form

$$\frac{d}{dt}N_{\mathrm{MOT}} = Q_c - \Gamma_P N_{\mathrm{MOT}} - \Gamma_C N_{\mathrm{MOT}}, \tag{6.6}$$

where Q_c is the MOT capture rate, Γ_P is the loss rate due to decays into the metastable ^{3}P$_2$ state, and Γ_C is the loss rate due to collisions ejecting atoms from the trap. Ignoring for now the effect of collisions, we can guess that the trap loss rate should be proportional to Γ_2 times the steady-state fraction of atoms in the ^{1}D$_2$ state. This can be confirmed by considering the rate equations for each level that potentially remains trapped [343]. The total MOT population can be written as the sum of the atom number in each state,

$$\begin{aligned} N_{\mathrm{MOT}} &= N_{1S0} + N_{1P1} + N_{1D2} + N_{1P1} \\ &= N_t \; + \; N_{1D2} \; + \; N_{1P1}, \end{aligned} \tag{6.7}$$

where N_i is the population in the ith level and we have taken $N_t = N_{1S0} + N_{1P1}$ as the number of the atoms participating in the cycling transition ^{1}S$_0$ − ^{1}P$_1$ driven by the MOT trapping lasers. Treating the decay to N_{1D2} as a small perturbation to the coupling dynamics of this nearly two-level system, we can assume the fraction f of N_t in the excited state ^{1}P$_1$ (such that $N_{1P1} = fN_t$) is given by the usual solution to the optical Bloch equations for the excited state population ρ_{ee},

$$f = \frac{1}{2}\frac{I/I_{sat}}{1 + I/I_{sat} + 4\Delta^2/\Gamma^2}, \tag{6.8}$$

where the laser intensity I is the sum of the six MOT beams and $I_{sat} = 40.5$ mW/cm^2. Then the rate equations for the trapped levels are

$$\begin{aligned} \frac{d}{dt}N_t \quad &= \; -\Gamma_d f N_t \; + \; \Gamma_r N_{3P1} \; + \; Q_c \\ \frac{d}{dt}N_{1D2} \quad &= \; -(\Gamma_1 + \Gamma_2)N_{1D2} \; + \; \Gamma_d f N_t \\ \frac{d}{dt}N_{3P1} \quad &= \; -\Gamma_r N_{3P1} \; + \; \Gamma_1 N_{1D2} \end{aligned} \tag{6.9}$$

(where the decay rate of the 689 nm $^1\mathrm{S}_0 - {}^3\mathrm{P}_1$ transition is $\Gamma_r/2\pi = 7.4$ kHz), and the rate equation for the total trapped MOT number becomes

$$\begin{aligned} \frac{d}{dt}N_{\mathrm{MOT}} &= \frac{d}{dt}(N_t + N_{1D2} + N_{1P1}) \\ &= Q_c - \Gamma_2 N_{1D2}. \end{aligned} \tag{6.10}$$

Comparing to Eq. 6.6, the atom loss rate due to decays into the metastable $^3\mathrm{P}_2$ state is, as expected, $\Gamma_P N_{\mathrm{MOT}} = \Gamma_2 N_{1D2}$ if collisional losses are ignored. Solving for Γ_P from the steady-state solutions of Eq. 6.9 and Eq. 6.10, we find:

$$\Gamma_P = \frac{\Gamma_2}{1 + \dfrac{\Gamma_1}{\Gamma_r} + \dfrac{\Gamma_1 + \Gamma_2}{\Gamma_d f}}. \tag{6.11}$$

The loss rate increases with increasing MOT beam power, saturating at the maximum excited-state population fraction $f = 1/2$ to $\Gamma_P = 400\ \mathrm{s}^{-1}$, corresponding to a $1/e$-lifetime when not continuously loaded with cold atoms ($Q_c \rightarrow 0$) of $\tau_{\mathrm{MOT}} = 1/\Gamma_P = 2.5$ ms. For our MOT detuning $\Delta_{\mathrm{MOT}}/2\pi = -40$ MHz and typical total beam intensity $I \approx 20\ \mathrm{mW/cm^2}$, we would still expect the MOT lifetime to be limited to 28 ms in the absence of a repump.

A repump beam coupling the $^3\mathrm{P}_2$ level to another state that can decay via an electric dipole transition back to the ground state essentially eliminates this loss channel. Several repump methods are in use or have been proposed. Many groups use two beams, at 707 and 679 nm, to couple $^3\mathrm{P}_2 -^3 \mathrm{S}_1$ (and then to pump back out of the $^3\mathrm{P}_0$ state, since decays from $^3\mathrm{S}_1$ to this state are another loss channel to a metastable state). These convenient near-IR transitions can be accessed with simple diode lasers. Our repump method uses a single 497 nm beam to couple $^3\mathrm{P}_2 - 5s5p\,^3\mathrm{D}_2$; from $^3\mathrm{D}_2$, the atoms decay to either $^3\mathrm{P}_2$ or $^3\mathrm{P}_1$ and so over many cycles are pumped back to the ground state.[2] This is an efficient repump method, but since diode lasers are not currently available at 497 nm, the construction of a second-harmonic-generation cavity to frequency-double a 994 nm diode laser adds experimental complexity. However, the 2.3 MHz linewidth has a saturation intensity of only 2.4 mW/cm^2, so very little 497 nm power is needed [382, 383]. Finally, an attractive new repump method uses a single 405 nm beam operating on the $^3\mathrm{P}_2 - 5s6p\,^3\mathrm{D}_2$ transition [381]. This is slightly less efficient than the 497 nm method, but 405 nm diodes (used in Bluray systems) are commercially available so this method avoids the need for second-harmonic-generation.

If the repump beam efficiently depopulates the metastable $^3\mathrm{P}_2$ level, MOT losses to this channel are essentially eliminated. The lifetime of the blue MOT in the absence of continuous loading is then limited by collision losses. Several potential collision channels cause MOT losses. Collisions with the room-temperature background gas atoms will eject atoms from the MOT; this loss rate is proportional to the chamber pressure, and has been measured to be only $\sim$3 s^{-1} at our $P \sim 6 \times 10^{-10}$ Torr (estimated from the low-pressure-side ion pump current - see Sec. 5.1) [343]. Elastic collisions between trapped Sr atoms cannot provide enough energy to either atom to cause trap losses, since the velocity of each is less than the trap capture velocity. Inelastic three-body Sr collisions are also negligible. Light-assisted inelastic collisions [384], on the other hand, are an important factor for Sr MOTs: this factor is dependent upon the MOT density and the trap light intensity, but we can expect a loss rate on the order of 10 s^{-1} based on measurements by strontium groups using similar MOT parameters [385].

---

[2] This discussion simplifies matters somewhat since the $5s5p\,^3\mathrm{D}_2$ state can also decay to the $5s6p\,^3\mathrm{P}_{1,2}$ states, but 99.7% of the decays are direct to $5s5p\,^3\mathrm{P}_{1,2}$ states, and the $5s6p\,^3\mathrm{P}_{1,2}$ states also decay indirectly to $5s5p\,^3\mathrm{P}_{1,2}$ through the $5s6s\,^3\mathrm{S}_1$ and $5s4d\,^3\mathrm{D}_j$ states [381].

Given the estimated capture and loss rates, we can estimate the steady-state trapped atom number from Eq. 6.6,

$$N_{\mathrm{MOT}} \approx \frac{Q_c}{\Gamma_{\mathrm{total}}}, \tag{6.12}$$

with loading rate $Q_c \approx 6 \times 10^9$ atoms/s. The loss rate Γ_{total} is the sum of the loss rates described above: $\Gamma_P \approx 35\ \mathrm{s}^{-1}$ for our MOT parameters in the absence of a repump vs. $\Gamma_P \approx 0$ with the 497 nm repump (assuming repump beam intensity well above saturation), and $\Gamma_C \approx 13\ \mathrm{s}^{-1}$ as the sum of the background gas and light-assisted inelastic collision loss rates. The approximate maximum steady-state trapped atom number without/with the repump beam is then

$$\begin{aligned} N_{\mathrm{MOT}} &\approx 1.2 \times 10^8 \text{ atoms} \qquad &&\text{(no repump)} \\ N_{\mathrm{MOT}} &\approx 4.6 \times 10^8 \text{ atoms} \qquad &&\text{(fully repumped).} \end{aligned} \tag{6.13}$$

As can be seen, the repump makes a dramatic difference, increasing the trapped atom number by nearly a factor of 4 (when using higher MOT beam intensities, the effect can be even greater).

6.3. Science Cell 461 nm MOT

We load the bottom MOT in the Pyrex science cell (described in Sec. 5.4.2) below the large spherical octagon containing the top MOT directly from the 2D-MOT-ejected cold atom beam that results from changing the polarization of the axial (vertical) top MOT beam from $\sigma^{-/+}$ to $\sigma^{+/-}$. Rotation of the input $\lambda/4$ plate before the final vertical-beam turning mirror by 90° effects the polarization change, a procedure that is computer-automated by digital outputs controlling a small stepper motor attached to laser-cut gears connecting the stepper motor shaft to the $\lambda/4$ mount [144].

The axial bottom-MOT beams, 1-cm diameter, typically ~ 2 mW, and parallel to the optical table plane, pass through the center of the two anti-Helmholtz coils mounted on either side of the Pyrex cell, which provide maximum axial(radial) magnetic-field gradients of 36(13) G/cm per amp (see Sec. 5.4.2). The radial bottom MOT beams, also 1-cm diameter but typically ~ 8 mW each, enter at 45° degrees to the science-cell walls from below to retroreflector–$\lambda/4$-waveplate assemblies near the top of the cell, with the radial beam mirrors mounted periscope-like to posts affixed to a bottom plate. This assembly allowed rough alignment external to the cell prior to maneuvering the mirrors into place. The repump beam, approximately collinear with the retroreflected vertical top MOT / push beam, passes through the bottom MOT twice. While the top MOT performance is little affected by repump beam alignment, the bottom MOT population is much more sensitive (perhaps as a result of the repump's interaction with the atoms ejected from the 2D MOT along the push-beam path), and appears to be maximized when the repump is initially aligned perfectly co-propagating with the vertical beam and then tweaked slightly while monitoring the continuously-loaded bottom-MOT fluorescence.

6.3.1. Magnetic Field Considerations

6.3.1.1. Push Beam / Bottom MOT Interactions

The vertically-propagating top MOT / push beam passes directly through the bottom MOT; while this is necessary for continuously loading, it is important the magnetic field of the bottom MOT is oriented such that this beam does *not* also act like a push beam for the atoms of the bottom MOT. This implies that the orientation of the magnetic field along the vertical axis in the two traps, *relative* to the trap center, must be opposite. Our magnetic fields satisfy this requirement: for the top MOT, the component along the vertical axis is the axial component, which points towards the center of the top MOT while for the bottom MOT it is the radial component, which points outward from the center of the bottom MOT. When the vertical beam is in the "push" polarization, σ^+ propagating upward and σ^- propagating downward, it interacts with the exited state $m'_f = +1$ passing upward and $m'_f = -1$ on the downward pass, so the downward-propagating σ^- beam is the push beam that ejects atoms from the top MOT, but both the upward-propagating and downward-propagating beams act like MOT capture beams for the bottom MOT. While this is good, since it means the push beam does not eject atoms from the bottom MOT and we can load continuously, it also implies that our bottom MOT employs 4 beam pairs rather than the usual 3 during continuous loading. For measurements and transfer procedures, we shutter all the top MOT beams to stop continuously loading the bottom MOT, which shutters the push beam as well, and we notice bottom-MOT shape and position shifts upon execution of this event.

The magnetic fields for the top and bottom MOTs are plotted along the vertical axis in Fig. 6.2, which illustrates another important point: the top MOT axial field significantly affects the vertical zero-crossing of the bottom MOT field. The orange and brown lines show the independent anti-Helmholtz fields for the top and bottom MOTs, respectively, and the black lines are the sum of the fields. With the top MOT coils set to the maximum current we use for optimal capture from the Zeeman-slowed beam, 6.8 A, the axial top-MOT field introduces a background vertical bias field at the bottom MOT location of over 30G. This offsets the bottom MOT radial-field zero-crossing from the center of the optical molasses region by over a centimeter,

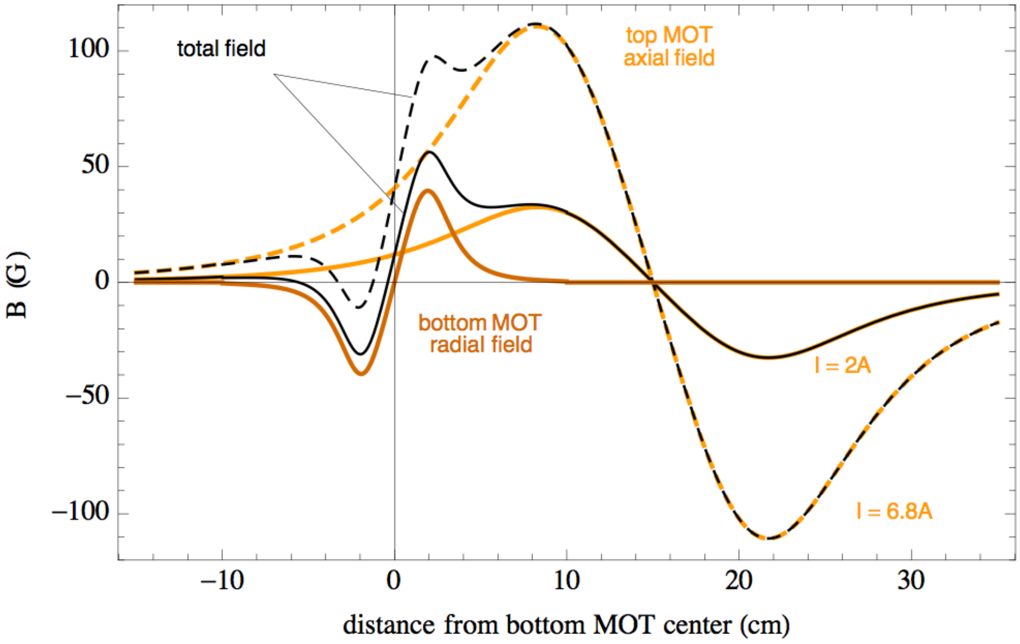

FIGURE 6.2. Interaction of the top and bottom MOT AH magnetic fields along the z−axis. The relative orientation of the two fields is critical for the 2D-MOT push-beam transfer, and the total field zero-crossing at the bottom MOT location (with a typical bottom-MOT AH-coil-current of 1.6 A) is significantly offset from the intersection of the bottom MOT beams when the top MOT AH-coils are at a high (6.8 A) current.

and the total field is far from linear near this zero-crossing point. This is a serious disadvantage of our double-MOT setup: even at 6.8 A our top MOT magnetic field gradient is much smaller than that used by many Sr groups, and to load a bottom MOT we are forced to lower the field to 2.2 A, which results in a very diffuse top MOT with a lower capture efficiency. Even then, the zero-crossing of the bottom MOT magnetic field is still offset by 3 mm from the center of the bottom MOT AH coils, so we use bias fields to make up the difference and bring the quadrupole-field-center into alignment with the optical molasses zone.

6.3.1.2. Background Magnetic Field Cancellation

Bias magnetic fields are used in most MOT experiments: while the MOT itself is quite robust, any stray background magnetic field will affect the position of the trap center, and atoms released from MOTs with insufficient background field cancellation launch in the direction of the field.Optical molasses using $\sigma^{+/-}$ beams is very sensitive to stray magnetic fields, which disturb the force balance between counter-propagating beams and effectively shift the molasses rest frame into a frame which is moving with respect to the lab (see Ref. [311] for a good discussion of this effect). Stray fields include the Earth's magnetic field, typically ~0.5 G, and any fields from nearby ion pumps or the Zeeman slower.

For full cancellation, we typically use 3 orthogonal sets of coils wound outside the main chamber. The Helmholtz (HH) coil configuration, with the same current in two coils of radius R separated by a distance $d = R$, is ideal for producing a uniform magnetic field along the coil axis; since we only anticipated the need for small magnetic-field adjustments we use rectangular coils separated by approximately the average of the two side lengths whenever possible, but we still refer to them as the $X/Y/Z$-HH coils. These coils are powered in series by homemade current supplies capable of 5 A bidirectional output, with adjustable temperature and current limit setpoints [311]. (We also use a master-slave version of this design for the bottom MOT AH-coil current.)

For the top MOT, we adapted the Steck lab Rb-MOT HH-coil solution [216] by forming coils from 6 turns of 10-conductor ribbon cable, wrapped directly at the MOT around corner axes fastened to the 80/20 support frame. We found that a fairly tight MOT formed for a range of Z-HH coil current values, allowing adjustment of the top MOT position further above the atomic beam when desired; the X/Y values appeared slightly more sensitive (probably due to the limited 1-cm-diameter vertical axial beam).[3]

For the bottom MOT, we use HH coil forms assembled from laser-cut acrylic cutouts wrapped with ∼60 turns of polyimide-insulated wire [144], but the space constraints imposed by the optics and coil mounts around the Pyrex cell led to coil parameters far from the ideal HH configuration. This was particularly true for the original bottom MOT Z-HH coils, $\sim 2.5'' \times 3.5''$ rectangles separated by $\sim 6''$. A significant non-zero Z-coil current is needed to cancel the top MOT axial field at the bottom MOT location, but the resultant magnetic field from these coils was far from uniform along the z-direction. Replacing this coil pair with a 10-conductor × 6-turn ribbon-cable pair by appropriating the lower top-MOT Z-HH coil and winding a second coil the appropriate distance below the bottom MOT results in a more uniform Z-bias field, but the maximum field available at the current our drivers can provide is barely sufficient (the ribbon cable coil pairs, with greater effective coil diameters and separation, cannot provide as strong a field as the tighter wire-wound HH pairs). A switch was eventually installed to allow use of the appropriated coil as a top- or bottom-MOT Z-coil, but we currently cannot use a Z-bias field in both MOTs at the same time. We remain concerned about imperfect magnetic-field cancellation in the science cell, as described further in Sec. 6.5.

6.3.2. MOT Imaging

Our primary imaging system is a charge-coupled device (CCD) camera from Finger Lakes Instrumentation (we refer to it as the FLI camera), inherited from a

---

[3] Despite the possibility of confusion, we have adopted the convention of referring to the $X/Y/Z$-HH coils for both the top and bottom MOTs by a laboratory $x/y/z$ frame that corresponds to vertical along the $+z$-axis, $+y$ along Zeeman-slower beam axis, and $+x$ toward the imaging cameras.

previous Steck lab Rb experiment [216, 311], with a Micro-Nikkor 55 mm f/3.5 macro lens from Nikon. While not a high-end scientific camera, the FLI does have a full-frame 512×768 pixel (px) air-cooled microlens sensor (Kodak KAF-0402ME) with a quantum-efficiency (QE) of 48% at 461 nm. We add a color filter (Schott BG40), which transmits ∼89% at 461 nm, reducing the efficiency at 461 nm to ∼43%.

6.3.2.1. MOT Size

We use fluorescence imaging, collecting the light scattered by the atoms interacting with the 461 nm MOT beams. Knowing the scattering rate per atom and the collection efficiency of our camera system thus allows conversion of integrated image pixel counts into MOT atom number N_{MOT}. Ref. [311] describes the calibration procedures used by the Rb experiment to extract this and other information from the FLI camera. We repeated the procedure to calibrate the image size with our filter [144], finding 23.75 μm per pixel, but assume the measured 6.4 photons per pixel "count" will roughly hold for our parameters as well when we operate far below saturation, if multiplied by the ratio of the total efficiencies at 461 nm vs. 780 nm (and at $\sim 43\%$ vs. $\sim 40\%$, this is a negligible correction at our level of accuracy).

We are typically most interested in imaging our atoms just after release from the MOT, as described further in Sec. 6.4.1, by pulsing the MOT beams to "freeze" the atoms in optical molasses with the MOT AH-field off. The scattering rate at our MOT beam detuning $\Delta_{\text{MOT}}/2\pi = -40$ MHz is then $\sim 10 \times 10^6$ photons/s per atom for a total MOT beam intensity $I \approx I_{\text{sat}}$ (Eq. 3.7). However, the number of photons collected per atom depends on the solid angle ratio (assuming isotropic spontaneous emission)

$$\frac{\Omega}{4\pi} \approx \frac{1}{2}\left(1 - \frac{d}{\sqrt{d^2 + R^2}}\right), \tag{6.14}$$

where d is the distance from the camera lens to the MOT and R is the radius of the effective lens aperture. At $f/3.5$, our apertured lens diameter is 55 mm/3.5, or $R = 7.85$ mm, and the camera is set at the closest possible focus, $d = 24.1$ cm. The solid angle ratio is then 0.027%, so we can expect $\sim 2,500$ photons/s per atom to reach the camera. Over a typical 2 ms exposure time, this corresponds to only ~ 5 photons/atom.

A typical false-color bottom-MOT-release image for a 2 ms exposure, 0.025 ms after release, is given in Fig. 6.3. We sum over the row and column pixel counts to examine the position distribution; imaging at a slight angle to the lab $y-z$ plane, the column-sum plot corresponds to the MOT distribution roughly along the y-axis (axial MOT-field direction) and the row-sum distribution corresponds to the z-axis (vertical - radial MOT field). Gaussian fits to the row and column sums for this image give widths of 14 and 16 pixels, respectively; given the 23.75 μm/px size conversion factor, this is a full-width-half-max (FWHM) 0.8 mm × 0.9 mm cold-atom cloud (the cloud has already begun to expand from a typical trapped MOT FWHM of ~ 0.6 mm). As expected the cloud is tighter along the axial-field direction, but we do not have a good explanation for the slight tilt, which is present in most of our bottom MOT images.

The science cell is not AR-coated, so there is considerable background MOT-beam and MOT-reflection scatter which we attempt to subtract off (still visible at the bottom and top edges of the frame), and expansion exposures also include the pre-release MOT. We subtract this off as well, and average over typically 100 cycles, but the subtraction procedure is plagued by issues described further in Sec. 6.4.1. The subtraction is probably sufficient for rough atom number estimates, however: the integrated sum of the pixel counts, minus the integrated background, is 1.3×10^5,

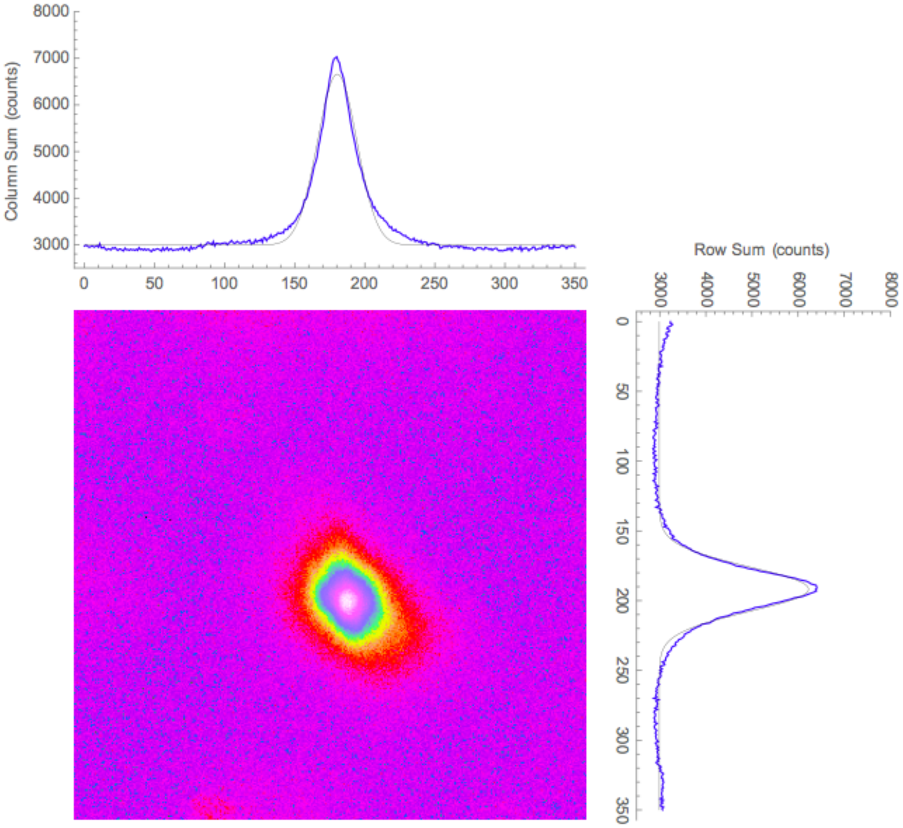

FIGURE 6.3. Example MOT image, with integrated position distributions along the axial (Column Sum) and radial (Row Sum) directions.

leading to an estimated cold-atom number of

$$\frac{1.3 \times 10^5 \text{ counts} \times (6.4 \text{ photons/count})}{5 \text{ photons/atom}} = 1.6 \times 10^5 \text{ atoms.} \tag{6.15}$$

However, this estimate can be assumed accurate to only about an order of magnitude, since we have treated the atoms as independent scatterers interacting with an un-attenuated traveling-wave light field. The scattering rate (Eq. 3.7) is only approximate for the 6-beam standing-wave light field, and as mentioned in Sec. 6.2.1

a small percentage of photons participate in light-assisted two-atom recombination events (the main contributor to collision losses). Dense MOTs may also attenuate the light field (with atoms on the outer fringes shadowing those inside), and spontaneously emitted photons likewise can be reabsorbed by adjacent MOT atoms [386, 387]. However, the most significant source of uncertainty in Eq. 6.15 is shot-to-shot variation in our attempts at background subtraction, imposed by the limitations of our camera shutter system and discussed further in the following two sections.

6.3.2.2. Camera Limitations

Although this camera is capable of the resolution and light collecting abilities required thus far, and is relatively easily programmed with the assistance of the camserver library developed by Jeremy Thorn, the biggest obstacle has proven to be the shuttering system. The mechanical shutter blades have a long history of repair and modification [311] and tend to need regular cleaning to prevent sticking (although we have only needed to replace one blade so far on the strontium experiment). The shutter is also quite noisy, and mechanical vibrations transmit through the camera mount to the rest of the optical table. This is particularly problematic for our frequency-doubling cavities, which experience amplitude fluctuations and can even come unlocked in response to these vibrations.

The camera mount inherited from the Rb experiment consists of a solid 1.5″ post attached to a 5″ × 10″ × 1″-thick cast-iron block. This block is fixed *indirectly* to an aluminum plate clamped to the optical table by screws threaded through two other cast-iron blocks (5″ × 1.5″ × 1″ thick); sandwiched between the blocks and between the lower block and the aluminum plate are layers of Sorbothane, a viscoelastic damping material. This should already be a stable and effective vibration-isolating configuration, avoiding metal-to-metal contact that would transmit mechanical vibrations directly to the optical table [359], but an informal communication from a visiting speaker (Luis Orozco) led to a significant improvement. His cavity QED group found that many small pieces of Sorbothane are much more effective for vibration isolation a than single layer, a fact known by Sorbothane manufacturers and documented in the technical literature and design guides [388]. The principle is quite simple: to prevent transmission of noise through the layer to the table, the mechanical energy must dissipate as thermal energy (deformations) through the sides of the sheet, therefore a net circumference surface area greater than or equal to the contact area is optimal. Slicing the Sorbothane layer between the plate and the plate into many pieces of $1/4''$ "confetti" had a dramatic impact on doubling-cavity stability when the camera shutter fires. We subsequently used the same technique to better isolate other mechanical beam shutters.

Another serious limitation of the FLI camera is more difficult to mitigate or work around. The camera shutter begins to open $\sim$ 10 ms after triggering, a delay which we can program into our experimental sequences. Unlike an electronic shutter system, however, the mechanical shutter requires another $\sim$ 10 ms to fully open. Equally problematic is the fact that the time to final full opening can vary by as much as a few ms shot-to-shot. This means that we cannot rely upon a programmed camera exposure time to give well-calibrated physical exposures at the millisecond precision level, which is required for certain experimental sequences.

When we require precise exposures, rather than rely upon the variable camera shutter we would ideally open the shutter "in the dark," ahead of the desired image time. We can then trigger an AOM, used as a beam shutter, to flash the MOT beams for a set duration. This procedure is still insufficient for well-calibrated intensity exposures shot-to-shot as a result of amplitude fluctuations from the 461 nm doubling cavity (particularly when the cavity is overreacting to mechanical shutter vibrations). Even without finicky SHG cavities, the Rb experiment found that although AOMs are quite reliable for fast response rise/fall times, they can drift in diffraction efficiency, particularly in response to temperature variations [311]. As a result, they developed a pulse-area analyzer to switch an AOM off after a laser pulse has reached a set integrated intensity [389]. The integrated signal from a photodiode monitoring a small pick-off from the laser beam is compared to a voltage setpoint; when the integrated signal is equal to the setpoint, the comparator output inhibits the AOM drive frequency through the RF switch. Using this method, the timing of a given laser pulse may vary by as much as 5% max (usually less) shot-to-shot, but the light exposure level is constant for each pulse. Use of this module is helpful, but the the overall system still poses serious challenges to acquiring some of the images we would like to take for full characterization of our blue MOT, as discussed further in the next section.

6.4. MOT Temperature Characterization

The minimum temperature we could hope to reach in our 461 nm ^{88}Sr MOT is the Doppler temperature (see Sec. 3.2.1.2),

$$T_D = \frac{\hbar\,\Gamma_b}{2k_{\mathrm{B}}} = 730\ \mu\mathrm{K}, \qquad \textit{Doppler limit, 461 nm MOT} \tag{6.16}$$

since the even isotopes possess no nuclear spin and hence lack the hyperfine ground-state substructure required for sub-Doppler cooling mechanisms. However, most strontium groups observe temperatures consistently higher than this minimum, $\sim 2-5$ mK, attributed to the heating effects of light-assisted collisions. Lower MOT temperatures are associated with higher transfer efficiencies from the 461 nm blue to 689 nm red MOTs, so we would like a simple method to check our MOT temperature and potentially optimize various parameters to achieve the coldest possible starting samples. However, the limitations of our experimental setup have proven challenging for characterization of the 461 nm MOT, and future parameter optimization can rely equally well upon maximizing MOT population transfers directly. We have attempted some temperature measurements, and the procedure outlined below will work well for future measurements of 689 nm MOT or lattice-trapped atoms, but in the end we rely upon a temperature estimate derived from the trapped spatial distribution for the 461 nm MOT.

6.4.1. Ballistic-Expansion Imaging

A simple method to measure trapped-atom temperatures employs direct imaging of the expanding cloud upon release of the trap over variable time delays [221, 311]. Each atom, assumed independent in the thermal cloud, experiences ballistic flight from its initial position $\mathbf{r}_0$ to final position $\mathbf{r} = \mathbf{r}_0 + \mathbf{v}\, t_{\text{delay}}$, where $\mathbf{v}$ is the initial velocity and t_{delay} is the time between trap release and imaging. Assuming a Maxwell-Boltzmann thermal distribution and isotropic expansion, imaging the entire cloud with a variable time delay maps the variance of the initial momentum distribution to that of the final position distribution as a function of t_{delay}:

$$\sigma_y^2(t_d) = \sigma_{y_0}^2 + (\sigma_p\, t_{\text{delay}}/m)^2. \tag{6.17}$$

Here σ_{y_0} is the variance of the initial position distribution (assumed Gaussian: $\mathrm{FWHM}_0 = 2\sqrt{2\ln 2}\,\sigma_0$), which has very little effect on the final distribution for long delay times.[4] The simplicity of the ballistic-expansion method is the lack of sensitivity to this initial spread, unlike release-and-recapture methods (which determine the temperature from the fraction of atoms remaining for variable trap shutoff times [257]) or time-of-flight methods that measure the percentage of atoms crossing a probe beam below the released MOT as a function of time [295].[5]

Gaussian fits to ballistic-expansion images over numerous delay times thus allow derivation of the initial velocity distribution, related to the MOT temperature T by

$$\sigma_p^2 = m^2\langle v^2\rangle = mk_{\mathrm{B}}T. \tag{6.18}$$

Of course, this description assumes instantaneous imaging, while for a sufficient signal we need a finite exposure. As described in the previous section, we use fluorescence of the MOT beams themselves for our imaging pulse, so the atoms are somewhat "frozen" in optical molasses during the exposure but still experience some diffusion; any spread during exposure would in principle act as an overall offset that wouldn't affect the slope of Eq. 6.17, but should still be avoided in case the diffusion rate increases as the cold-atom cloud fills more of the non-uniform-intensity optical molasses region. To avoid these artifacts, a short imaging time is preferred, and the derived temperature can be verified by repeating the measurement with different exposure times. Note also that we can only image the cloud over the region encompassed by our MOT beams.

---

[4] Eq. 6.17 relies upon the assumption of Gaussian initial position and momentum distributions, and uses the fact that the convolution of two Gaussians is also Gaussian [311].

[5] The ballistic-expansion technique is also often referred to as "time-of-flight" imaging, since the cloud size is in effect a function of the time the atoms fly away from their initial position.

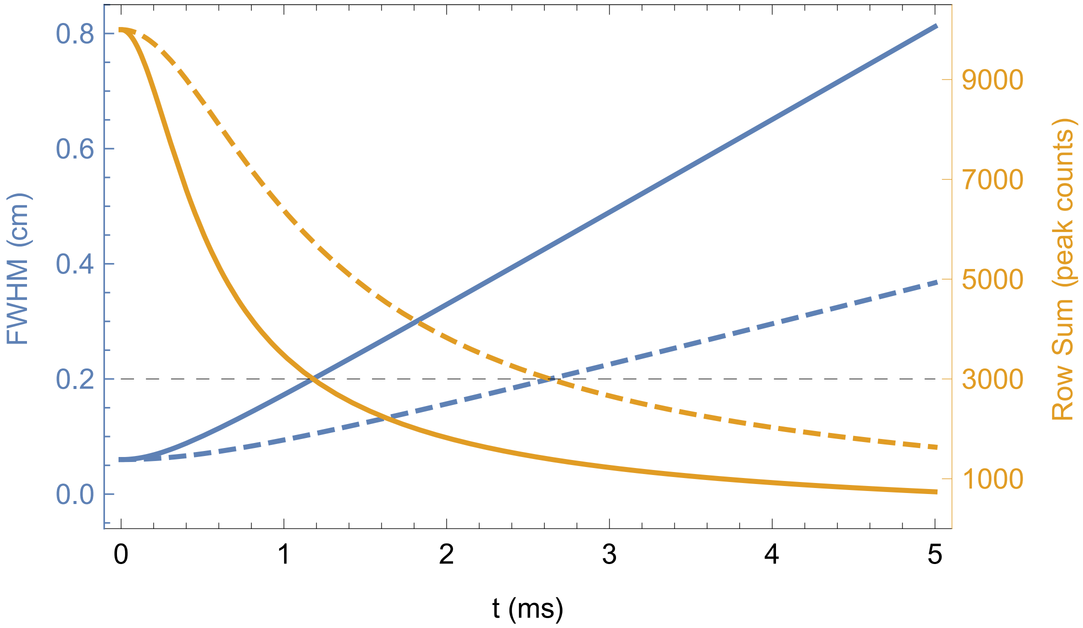

FIGURE 6.4. Simulated 461 nm MOT-release ballistic expansion over $t_d = 0$ to 5 ms from initial 5 mK and 1 mK MOTs (solid and dashed curves, respectively). The blue curves show the expected FWHM $= 2\sqrt{2\ln 2}\,\sigma_y$ from Eq. 6.18 and Eq. 6.17, and the orange curves are the peak image pixel count (1D-sum). The dashed black line is our current camera noise floor.

The challenge for ballistic-expansion imaging of the 461 nm MOT is the high initial temperature of the trapped atoms: at typical 2-5 mK ^{88}Sr MOT temperatures, the cold atoms are still moving ~ 1 m/s! The expansion upon release from an initial 0.6-mm-FWHM MOT at 5 mK is plotted in Fig. 6.4 (blue solid curve); by a delay time of 5 ms, the expanded cloud already has a FWHM of nearly 1 cm, reaching the edge of our optical molasses zone. More problematic is the decay in the peak fluorescence that would be recorded by the camera (orange solid curve). For typical 1D distributions (obtained by summing over the rows or columns) we see a maximum peak pixel count of $\sim 10,000$, and a background noise floor of ~ 3000 counts (dashed black line). The peak value decays as the cold-atom cloud expands by 1/FWHM, such that the cloud will be barely visible by the time it is ~ 2 mm in diameter, at

$t_{\text{delay}} = 1.2$ ms. The 5 mK starting temperature may be a bit of a worst-case scenario, so the ballistic expansion FWHM increase and peak count decay are also plotted for an initial 1 mK MOT (dashed blue and orange curves); the lower temperature leads to slower expansion, but even in this scenario the cold atom cloud is indistinguishable from the background by $t_{\text{delay}} = 2.6$ ms.

These time scales are challenging for our camera system: with the shutter requiring ~ 10 ms to fully open, we cannot image the expanding cloud without also capturing the initial MOT prior to release. We nevertheless attempted a ballistic-expansion temperature measurement of the blue MOT, hoping to subtract off the background initial MOT to obtain images capturing the cold-atom cloud expansion. The experimental procedure is depicted in Fig. 6.5, with the timing referenced to the sequence of events programmed through the ZOINKS computer control interface.

We begin and end each data cycle with a continuously loaded bottom MOT, with the top MOT AH-coils set to $\sim$2 A and the bottom MOT coils set to 1.6 A for a relatively large bottom MOT (useful for diagnostic purposes — checking repump frequency, etc). The first step in each sequence is to start fresh by throwing away all previously loaded atoms (shuttering all beams and switching off the AH coils), waiting 50 ms, then reloading the large bottom MOT. We wait 100 ms to ensure maximum bottom MOT capture, then we switch all top MOT coils and beams off and wait 50 ms more for the transient magnetic field to die away. (The SHIFT event: as described in Sec. 6.3.1, the equilibrium position of the bottom MOT shifts upward when the top MOT fields are switched off, and the optimal bottom MOT HH-field values — in particular along the verticle z-axis — also require adjustment.) Simultaneously, we increase the bottom-MOT AH-coil current from 1.6 (gradient 37 G/Cm) to 2.3 A (54 G/cm) for a tighter initial cold-atom cloud. We release the

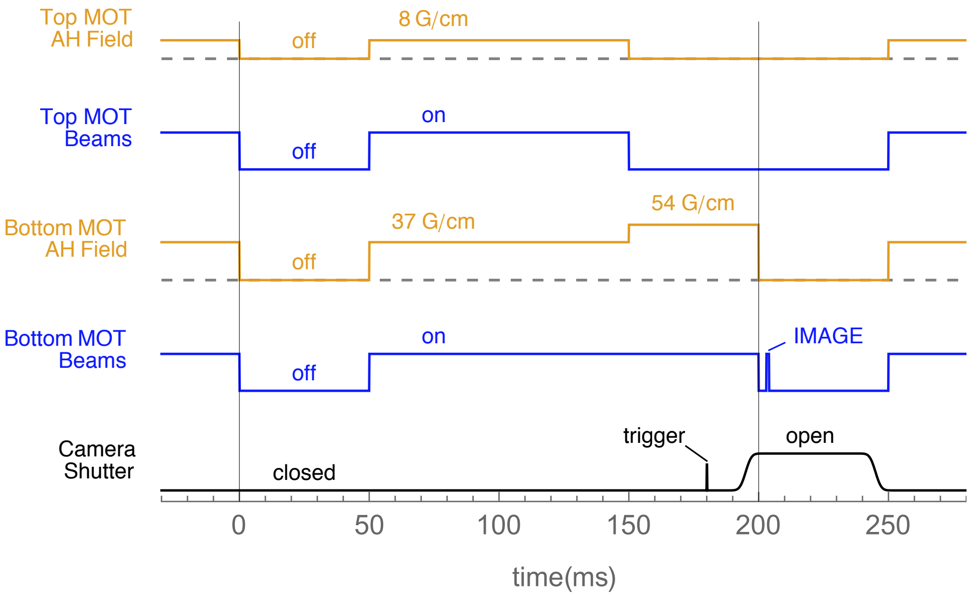

FIGURE 6.5. Ballistic-expansion-measurement timing diagram, showing the sequence of AH-field, MOT beam, and camera events per camera shot as described in the text (not shown: HH-field adjustments). The typical imaging pulse duration is 2 ms, and we vary the time delay between release and imaging from 0.25 to 2.00 ms to attempt to measure the cloud expansion as function of time. For each shot, we take a background image with the image pulse off and average 100 background and image shots per time delay.

atoms from the MOT (the DROP event) by turning off the bottom MOT AH-field and MOT beams and then image the expanding cloud by pulsing on the bottom MOT beams for ~ 2 ms after a variable time delay of 0.25 to 2.00 ms. The camera is triggered 20 ms before the DROP event to ensure that the shutter is fully open when the atoms are released, but the exposure captures the bottom MOT prior to release during the ~ 10 ms the shutter requires to open. In order to subtract off the MOT, every expansion image sequence is accompanied by a background exposure sequence in which we repeat exactly the same events but keep the image pulse off after MOT release.

For each time delay, we average 100 signal and 100 background images and subtract off the background, but background subtraction is problematic for several reasons. The shutter opening time is variable, so different exposures of pre-release-MOT can be recorded in the signal and background images. The MOT intensity itself is also variable, primarily as a result of MOT and repump beam intensity fluctuations. As described in Sec. 6.3.2.2, we can use the pulse-analyzer circuit to set controlled integrated-intensity exposures. However, we do not have a means to use this circuit more than once in the experimental sequence (the ZOINKS system cannot incorporate feedback into a single programmed timing sequence), so we use the pulse analyzer to ensure shot-to-shot consistency of the ballistic-expansion imaging pulse. To verify uniform MOT intensity during the shutter opening sequence, we could separately monitor the MOT and repump intensities and post-filter the data, discarding all runs with a variation larger than a chosen criterion, but this would not resolve the variable shutter-opening-time issue. Finally, the MOT *position* also jitters shot-to-shot, sometimes by as much as half the MOT FWHM. We do not have a satisfactory explanation for this position shift. Some jitter is expected due to interference fringes in the retro-reflected MOT beams, but not at this level, and the magnetic-field current control is accurate to better than this shift. We expect the issue is MOT beam frequency or pointing jitter due to mechanical vibrations.

The end result is often incomplete or over-compensated subtraction of the MOT itself, even with 100 background/signal averages, such that we cannot trust Gaussian fits to our expansion images to give reliable measures of the variance of the expanding cold-atom cloud. Example averaged ballistic-expansion images from a single data run are shown in Fig. 6.6, along with the 1D-integrated projections along the $y-$ and $z-$axes (row- and column-sum data). The expanding cloud is clearly visible out to at least 1.5 ms, and the widths of the 1.75 ms and 2.00 ms images also indicate the continued detection of an expanding cloud, but incomplete MOT subtraction makes it

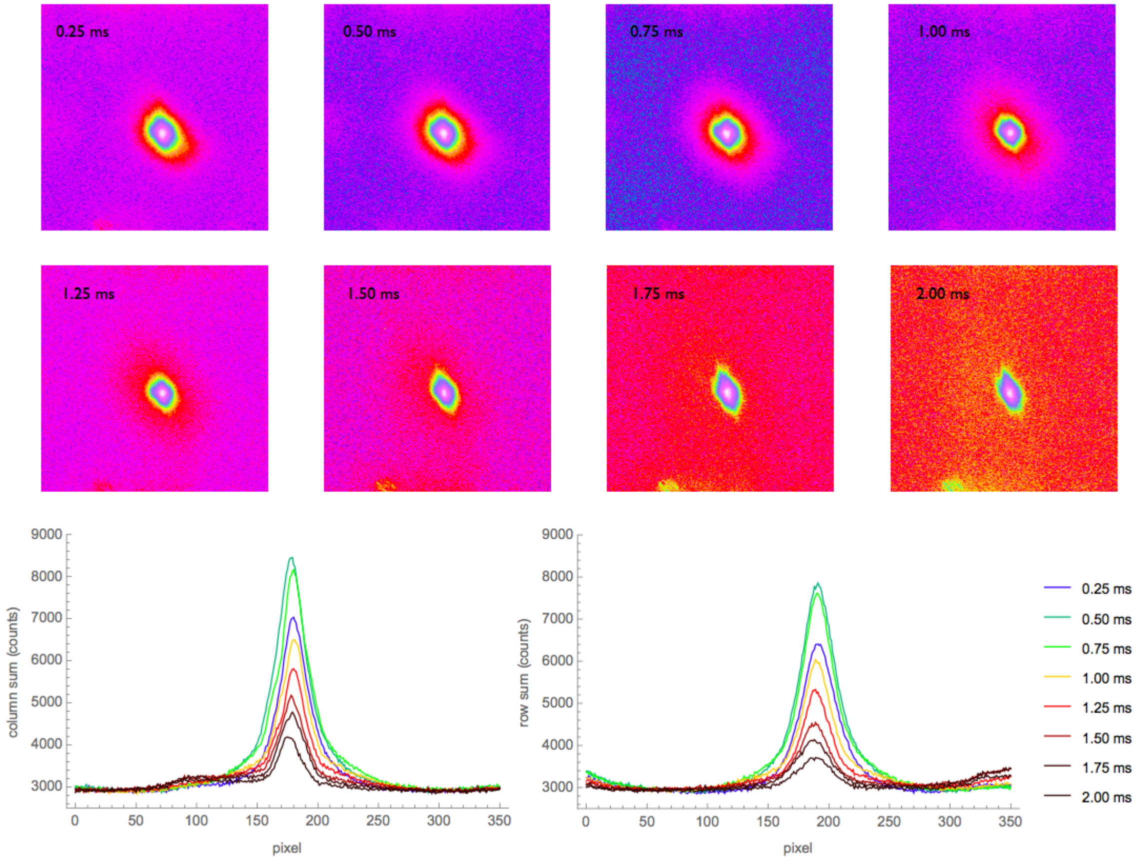

FIGURE 6.6. Ballistic-expansion images for $t_{\text{delay}} = 0.25$ to 2.00 ms, averaging 100 signal and background shots per time delay but with incomplete background subtraction. Some expansion is clearly visible, but the presence of the background MOT makes accurate characterization of the expanding cloud width challenging, and background-scatter artifacts become more problematic at longer time delays.

challenging to reliably fit the expanding wings. The incompletely subtracted scattered background light also becomes more of an issue at long time delays with low signal to noise. This was a fairly consistent data run showing the expected gradual signal decay, but the 0.25 ms delay images are noticeably weaker than the rest, likely due to sagging MOT or repump beam power, or repump frequency drifts (we currently rely upon a grad-student twiddle-lock to keep the repump on resonance by tweaking up the MOT brightness in the interims between imaging sequences).

6.4.2. MOT Temperature Estimate

We are encouraged by the fact that we can image the expanding cold-atom cloud out to nearly 2 ms when the system is working well, since this indicates that the atoms are not escaping more quickly than a reasonable ^{88}Sr blue-MOT temperature would predict. In comparison to the predicted intensity decay (Fig. 6.4), this indicates we are closer to a MOT temperature of 1 mK than 5 mK.

Another rough estimate of the MOT temperature is derived from direct imaging of the trapped atom-cloud spatial extent and equating the one-dimensional kinetic (thermal) energy to the trap potential energy at the boundary [224],

$$\frac{1}{2}k_{\mathrm{B}}T = \frac{1}{2}k_{\mathrm{trap}}z_{\mathrm{rms}}^2, \tag{6.19}$$

where the trap "spring constant" k_{trap} is a function of the trap parameters (Eq. 3.46) along the imaged axis. The typical axial beam intensity is 2 mW/cm^2, and for the tight bottom MOT obtained after the SHIFT event (top MOT fields off, no longer continuously loading), the axial magnetic field gradient is 54 G/cm, leading to $k_{\mathrm{trap}} = 8.9 \times 10^{-20}$ J/m^2. The typical MOT FWHM is $\sim 25 - 30$ pixels along the axial direction, or 0.6 – 0.7 mm; assuming a Gaussian position distribution, this corresponds to $y_{\mathrm{rms}} = \sqrt{3}(\mathrm{FWHM})/2\sqrt{2\ln 2} = 0.4{-}0.5$ mm. This leads to a reassuring estimate of T = 1 - 2 mK, with uncertainty dominated by the shot-to-shot FWHM variation. This temperature is low compared to that measured by many Sr groups, which could be a result of the fact that we are using MOT beams well below saturation (the minimum achievable Doppler cooling temperature scales with intensity, and the additional heating above the Doppler model observed in strontium is often attributed to light-assisted collision effects, which also increase with increasing intensity).

For the future 689 nm red MOT, a temperature estimate from Eq. 6.19 would not be valid, since many of the semiclassical assumptions governing the derivation of the MOT force used to define k_{trap} are not valid for narrow-line cooling, as described in the next section. However, the experimental ballistic-expansion sequences developed in our attempts to measure the blue MOT temperature will transfer well to red MOT measurements: the $\sim 1\ \mu$K red MOT temperature leads to much slower expansion, and the shutter opening time will not be a serious impediment.

6.5. Loading the Red MOT

The Doppler limit is a result of the balance between the cooling achieved by red-detuned photon absorption and the heating inherent in the random nature of these absorption and emission events, as discussed in Sec. 3.2.1.2. As such, this temperature limit is directly proportional to the linewidth of the cooling transition because the uncertainty in the emission time of the scattered photons (along with the uncertainty in the emission direction) leads to the force fluctuations. Cooling on narrow-line transitions like strontium's 7.4 kHz $^1\text{S}_0 - {}^3\text{P}_1$ transition allows much lower MOT temperatures, which will be critical for efficient transfer into an optical lattice (depth $\sim 20\ \mu$K) in future stages of this experiment.

The Doppler cooling limit generally sets the lower bound on laser-cooling temperatures achievable without sub-Doppler cooling mechanisms, while the colder recoil temperature is in a sense the fundamental quantum atom-photon limit associated with the momentum exchange of one photon. However, perhaps the first indication that semiclassical laser-cooling theory fails when it comes to strontium's $^1\text{S}_0 - {}^3\text{P}_1$ transition is the fact that the Doppler and recoil temperatures are reversed:

$$
\begin{aligned}
T_D &= \frac{\hbar \Gamma_r}{2k_\mathrm{B}} &&= 180\ \mathrm{nK}, &&\textit{Doppler limit, 689 nm MOT} \\
T_r &= \frac{\hbar^2 k_{689}^2}{m k_B} &&= 460\ \mathrm{nK}. &&\textit{Recoil limit, 689 nm MOT}
\end{aligned}
\tag{6.20}
$$

Clearly, something is wrong here: it makes no sense for the Doppler temperature to be lower than the quantum limit! Indeed, several of the approximations that led to the derivation of the Doppler temperature no longer hold for narrow-line cooling.

Semiclassical treatments of the light-atom interaction treat the atom quantum-mechanically but the light field classically. The crossover between regimes requiring a quantum treatment of the light field vs. a classical approach is generally considered dependent upon field photon number; with narrow-line cooling, we still use milliwatt beams, bombarding the atoms with over 10^{15} photons/s. While the number of photons in the field is large, however, the interaction rate is much smaller: with an excited-state lifetime $1/\Gamma_r = 21\ \mu$s, each atom can only scatter a maximum $\Gamma_r/2 = 23,000$ photons/s (the saturation intensity is only 3 μW/cm^2). This is in sharp contrast to the 461 nm transition, with a 5 ns excited-state lifetime and a maximum scattering rate of 96 million photons/s per atom. The discrete nature of photon absorption and emission on such a fast cycling transition can be largely ignored, allowing a classical treatment of the laser fields and the approximation of the scattering force as a continuous function, but this no longer holds true for narrow-linewidth transitions.

Besides the rate of scattering events, an even more fundamental consideration in narrow-line cooling is the impact of a single event. For the 689 nm transition, the recoil velocity imparted by the absorption of a single photon, $v_r = \hbar k/M = 6.6$ mm/s, implies a Doppler shift of $\Delta\nu_D = k v_r/2\pi = 9.6$ kHz, which is greater than the 7.4 kHz transition linewidth! In laser cooling it is common to use a laser linewidth on the same order as or narrower than the transition linewidth (although this is challenging when interacting with such a narrow transition), but in this case the momentum transfer from a single scattering event is enough to significantly affect the atom's coupling to the cooling field: for our ~ 11 kHz 689nm ECDL, the atom is shifted out of resonance after scattering only 2 photons if the laser is well below resonance.

As a result of these considerations, the theory of cooling on narrow-linewidth transitions requires a full quantum treatment of the atomic momentum coupling to the cooling field, via Monte Carlo simulation [291] or numerical integration of the coupled quantum equations of motion [390]. These calculations reveal interesting dynamics in narrow-line MOTs, also observed in experiments. One result that is not so surprising (and can be observed in the large intensity limit, where power broadening of the transition allows a return to the semiclassical treatment) is the fact that gravity plays a significant role. In typical MOTs, the scattering force is much greater than the gravitational force, but for Sr's $^1\mathrm{S}_0 - {}^3\mathrm{P}_1$ transition, the ratio of the maximum scattering force to the gravitational force is relatively small ($\hbar k \Gamma / 2mg = 16$), and the MOT "sags" to the bottom of the trap. Somewhat more surprising is the coldest observed temperatures, which approach the recoil limit divided by 2 at small MOT beam intensities [391], as predicted by theory [390]. Finally, momentum-space crystals are observed in MOT ballistic-expansion images when the MOT beams are slightly blue-detuned [392], fully confirming the discretized nature of the atom-photon interaction.

The first challenge of narrow-line cooling, however, is simply transferring from the relatively hot 461 nm MOT to the narrow-line MOT. For a blue MOT at 2 mK, the typical atom speed is $v_{rms} = 75$ cm/s. The Doppler shift for an atom moving towards/away from a red MOT beam is then ± 1 MHz: the vast majority of the blue MOT atoms are Doppler shifted out of resonance with the red MOT beams. Power broadening in this case is our friend: by using beams well above the saturation intensity, we increase the effective linewidth to $\Gamma_r\sqrt{1+I/I_{sat}} = 500$ kHz for a total MOT beam power of ~ 15 mW, but this still does not cover the Doppler width of the blue MOT distribution. The first trick to loading the red MOT is to broaden the interaction range by modulating the trap beams over the Doppler-broadened blue MOT distribution to capture as many atoms as possible.

The red MOT capture zone must also encompass the blue MOT volume. The MOT capture radius is roughly defined by the boundary where the Zeeman shift is equal to the MOT beam detuning ($\kappa\frac{dB}{dz}z = \Delta_{MOT}$), but not only is the red MOT beam detuning (typical final value: $\Delta_{r2} = -500$ kHz) much smaller than the blue MOT detuning ($\Delta_b = -40$ MHz), the Zeeman shift is larger ($\kappa_r/2\pi = 2.1$ MHz/G, vs. $\kappa_b/2\pi = 1.4$ MHz/G). This means a much smaller magnetic field gradient is required, along with the modulation of the red MOT detuning, to match the blue and red MOT boundaries.

The typical loading sequence, using roughly the parameters derived as optimal by Monte Carlo simulation of the capture dynamics by Katori et al. [107], is shown in the timing diagram of Fig. 6.7. The start of the sequence begins under the same conditions as those just prior to the DROP event in our ballistic-expansion imaging experiments: the top MOT beams and fields are off, and the bottom blue MOT is at the high 54 G/cm magnetic field gradient for a tight initial atom cloud. (For every red MOT loading sequence, we thus begin with the events depicted in Fig. 6.5 for 0 – 200 ms to load a large bottom MOT; these events occur before t = 0 in Fig. 6.7.) We then simultaneously switch the blue MOT beams off and the red MOT beams on, but the 689 nm light is frequency-modulated using an AOM driven by a DDS to sweep back and forth across the Doppler-broadened resonance from $\Delta_{r1} = -2$ MHz to $\Delta_{r2} = -500$ kHz. We also decrease the bottom MOT magnetic field gradient to 3 G/cm; the red MOT capture radius should then be $\sim \Delta_{r1}/(\kappa_r \frac{dB}{dz}) = 3$ mm.

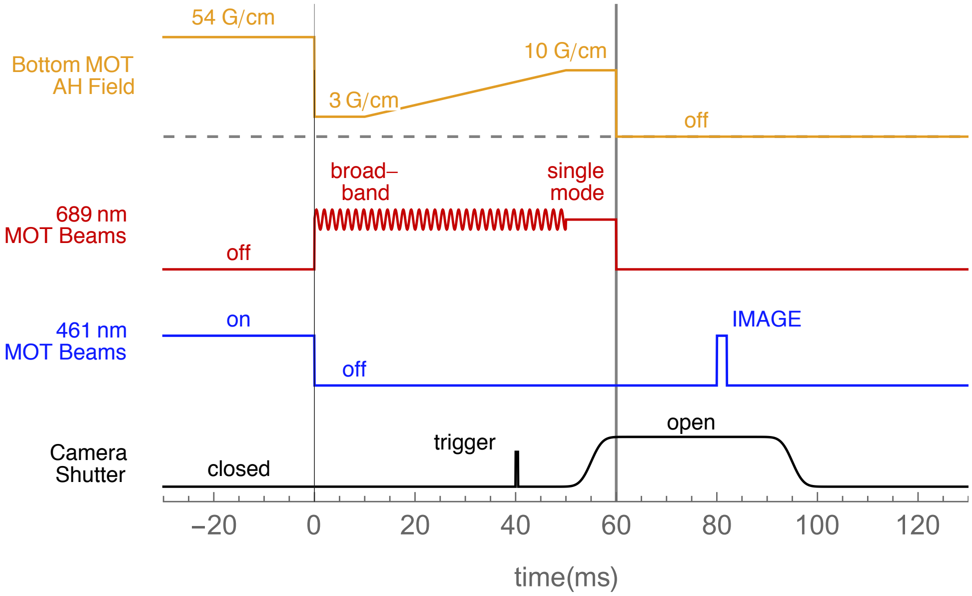

FIGURE 6.7. Timing diagram for red MOT loading and ballistic-expansion imaging.

Note that this red MOT capture range seems large, since it is more than sufficient to encompasses the initial ~ 0.6 mm blue MOT. However, it also ensures that the red MOT beams have enough *time* to interact with the atoms as they fly away from the blue MOT center. Cooling from the initial blue MOT temperature to a final temperature on the order of a typical red MOT requires scattering only $(v_0 - v_f)/v_r = 112$ photons (with $v_0 = 75$ cm/s from the 2 mK blue MOT, $v_f = 17$ mm/s for the typical speed of an atom at 1 μK, and $v_r = 6.6$ mm/s as the red MOT recoil velocity), but this takes a minimum of 5 ms even at the maximum scattering rate. In this time, a typical blue MOT atom that is not cooled could travel almost 4 mm, so the large red MOT capture volume is reasonable to ensure a sufficient distance for the cooling to occur.

For similar reasons, the red MOT field gradient is held at 3 G/cm for 10 ms, but over the next 50 ms, the field is ramped up to a final value of 10 G/cm. By this point, any atoms that would have been captured by the red MOT should be cooled, so the red MOT beam modulation is disabled and the MOT beams are set to the final detuning of Δ_{r2}, which should result in a tight red MOT of 0.2 mm FWHM. Given the low scattering rate, however, the camera will not detect the red MOT, so the final step to verify loading is to flash the atoms with the blue MOT beams for a camera image. The sequence shown in Fig. 6.7 depicts a blue MOT imaging pulse some delay after red MOT release, which would be the sequence for ballistic imaging, but actually the imaging pulse can be set to occur at any point after $t = 0$, to destructively check the red MOT loading sequence at different stages.

However, so far we have not observed any evidence of red MOT loading. We have found that we can reload a very weak blue MOT at time delays much greater than expected given the ballistic-expansion loss rate (up to 50 ms), so we believe the red beams are interacting with the atoms to create optical molasses conditions and lengthen the time scale at which the atoms remain in the bottom MOT region. We have also noticed evidence of the red MOT beams interacting with the atoms trapped in the blue MOT: exposing a continuously loaded blue MOT to chopped red MOT beams results in a slight modulation of the blue MOT fluorescence, which we attribute to temporary shelving of the atoms in the $^3\mathrm{P}_1$ state and reduction of the number of atoms interacting with the blue MOT beams.

Both of these observations seem to indicate that our 689 nm laser is set to the correct frequency, which was one of our concerns: the diminishing heat pipe absorption signal (see Sec. 4.5.1) has made locking the laser challenging on some days, but a more serious issue has been the instability of the long-cavity 689 nm

ECDL. Frequent mode-hops, we suspect due to insufficient temperature stabilization, led to many occasions when red MOT experimental runs were attempted only to eventually discover that our laser had been off-frequency or multi-mode during much of the data set. We have been using the 10-cm cavity-length design of our ECDL because we ultimately want a narrow-linewidth laser to interact with the narrow $^1\mathrm{S}_0 - {}^3\mathrm{P}_1$ transition, but for MOT transfer some degree of frequency broadening could be advantangeous (although most strontium groups we know of are actually using much *narrower* 689 nm lasers, stabilized to high-finesse external cavities). Temporarily switching to the short-cavity version of the 689 nm ECDL may be useful during this stage of the experiment, but ultimately the long-cavity instability issues must be resolved.

Other concerns are borderline red MOT beam power and the modulation parameters used during transfer (particularly our modulation rate, currently limited to 25 kHz by DDS parameters, vs. 50 kHz used by other groups, which gives a modulation period about equal to the $^3\mathrm{P}_1$ lifetime). The use of a single-pass AOM for modulation will also add red MOT beam pointing modulation, and the geometry of our setup, with no vertical MOT beam, further reduces the MOT vs. gravitational force ratio. Another serious concern has been magnetic field cancellation in the bottom MOT region. As described in Sec. 6.3.1.2, our bottom MOT Helmholtz coils are far from the ideal separation; this leads to inhomogeneities and coupling between different coil axes. We found it challenging to cancel the field sufficiently to observe the ballistic-expansion of the blue MOT out to 2 ms — in many early images, the atoms would streak to one side or the other upon release from the blue MOT, and we do not have a good way to verify that the atoms are not still streaking orthogonal to the plane imaged by the camera. Given the tiny field gradient required for the initial red MOT loading stage, any small background field would be very problematic.

The best approach in the near term may be attempting the red MOT loading sequence in the top MOT. This will require some beam realignment, and repositioning of the FLI camera, but the optics ordered for the top MOT are good for both 461 nm and 689 nm (the beam-expanding telescope lenses may need to be replaced with achromats, however). This would allow us to load in a region where the background fields can be canceled to better accuracy, and would also give us the advantage of using larger red MOT beams to provide a larger interaction region during cooling. The geometry of this setup, with the axial beam along the vertical axis, is also identical to that used by other red MOT groups: with the maximum scattering force on the same order of magnitude as the gravitational force in the red MOT, the vertical scattering force is much more important in the final cooling stages than the forces resulting from the radial beams, so our lack of a vertical beam in the bottom MOT geometry could exacerbate any other trap instabilities.

CHAPTER VII

CONCLUSION

This dissertation has summarized the development of a strontium magneto-optical trap (MOT) for future measurements of the Casimir-Polder (CP) interaction. A cold-atom spectroscopic measurement of CP-induced transition shifts will be a new experimental technique capable of probing atom-surface separation regimes little explored in other measurements thus far. Distance scales of particular interest for exploring the cross-over in length-scaling between the near-field (van der Waals) $V \propto r^{-3}$ effects and the far-field (CP) $V \propto r^{-4}$ regime will also be critical to understand for the future development of miniaturized cold-atom systems for atomic sensors and quantum information experiments.

Strontium is an ideal candidate for this future measurement: Sr offers extremely narrow, well-characterized intercombination transitions that would be ideal spectroscopic CP probes, and confinement in a "magic wavelength" optical lattice will minimize first-order ac-Stark systematics and allow a method of reliably positioning tightly-confined atomic samples a well-calibrated distance from a test surface of interest. The ground-state magnetic insensitivity and low collisional shifts of ^{88}Sr, and the anticipated low polarizability of surface adsorbates, minimize important systematic shifts. Optical lattice translation to within 200 nm of the test surface will allow measurement of CP transition shifts of over 10 kHz for the $^1S_0 - {}^3P_1$ transition, and future generations of the experiment could also utilize the ultranarrow $^1S_0 - {}^3P_0$ transition in ^{87}Sr to explore far-field effects to high precision.

The strontium CP experiment requires an ultra-high vacuum chamber and four distinct laser systems; Chapters 4 and 5 summarize the (often home-built) solutions we have developed for these systems. We have succeeded in trapping ^{88}Sr in a $^1S_0 - {}^1P_1$ "top MOT" directly from a Zeeman-slowed atomic beam, and we can reliably transfer from this region into a science-cell "bottom MOT" with an atom population $\sim 10^5$, sufficient for future experiments. The next steps require transfer into a 689 nm $^1S_0 - {}^3P_1$ science-cell MOT, and subsequently into the optical lattice at the $^1S_0 - {}^3P_1$ transition's 914 nm "magic wavelength".

The 689 and 914 nm laser systems are complete, and we have observed $^1S_0 - {}^3P_1$ optical molasses effects, but our initial attempts at transfer into the 689 nm MOT have proven unsuccessful. Further characterization of the red MOT transfer process in the top MOT region should prove helpful in overcoming this obstacle. Computer control and data acquisition systems are largely complete, and initial experiments to test atom translations in the optical lattice and the effect of Sr surface adsorbates will be useful for not only the future CP measurement, but also for the development of other Sr precision sensors and miniaturized atomic traps.

REFERENCES CITED

[1] H. B. G. Casimir, "On the attraction between two perfectly conducting plates," *Proc. K. Ned. Akad. Wet* **360**, 1–3 (1948).

[2] W. E. Lamb and R. C. Retherford, "Fine structure of the hydrogen atom by a microwave method," *Physical Review* **72**, 241–243 (1947).

[3] H. B. G. Casimir and D. Polder, "The influence of retardation on the London–van der Waals forces," *Physical Review* **73**, 360–372 (1948).

[4] M. Bordag, U. Mohideen, and V. Mostepanenko, "New developments in the Casimir effect," *Physics Reports* **353**, 1–205 (2001).

[5] G. Barton, "Frequency shifts near an interface: inadequacy of two-level atomic models," *Journal of Physics B: Atomic, Molecular, and Optical Physics* **7**, 2134–2142 (1974).

[6] C. I. Sukenik, M. G. Boshier, D. Cho, V. Sandoghdar, and E. A. Hinds, "Measurement of the Casimir-Polder force," *Physical Review Letters* **70**, 560–563 (1993).

[7] S. K. Lamoreaux, "Demonstration of the Casimir force in the 0.6 to 6 μm range," *Physical Review Letters* **78**, 5–8 (1997).

[8] R. Santra, K. V. Christ, and C. H. Greene, "Properties of metastable alkaline-earth-metal atoms calculated using an accurate effective core potential," *Physical Review A* **69**, 042510 (2004).

[9] S. G. Porsev and A. Derevianko, "Hyperfine quenching of the metastable $^3\mathrm{P}_{0,2}$ states in divalent atoms," *Physical Review A* **69**, 042506 (2004).

[10] T. Nicholson, S. Campbell, R. Hutson, G. Marti, B. Bloom, R. McNally, W. Zhang, M. Barrett, M. Safronova, G. Strouse, W. Tew, and J. Ye, "Systematic evaluation of an atomic clock at 2×10^{-18} total uncertainty," *Nature Communications* **6**, 6896 (2015).

[11] H. Katori, M. Takamoto, V. G. Pal´chikov, and V. D. Ovsiannikov, "Ultrastable optical clock with neutral atoms in an engineered light shift trap," *Physical Review Letters* **91**, 173005 (2003).

[12] X. Baillard, M. Fouché, R. Le Targat, P. G. Westergaard, A. Lecallier, F. Chapelet, M. Abgrall, G. D. Rovera, P. Laurent, P. Rosenbusch, S. Bize, G. Santarelli, A. Clairon, P. Lemonde, G. Grosche, B. Lipphardt, and H. Schnatz, "An optical lattice clock with spin-polarized ^{87}Sr atoms," *The European Physical Journal D* **48**, 11–17 (2008).

[13] B. J. Bloom, T. L. Nicholson, J. R. Williams, S. L. Campbell, M. Bishof, X. Zhang, W. Zhang, S. L. Bromley, and J. Ye, “An optical lattice clock with accuracy and stability at the 10^{-18} level,” *Nature* **506**, 71–75 (2014).

[14] S. Falke, H. Schnatz, J. S. R. V. Winfred, T. Middelmann, S. Vogt, S. Weyers, B. Lipphardt, G. Grosche, F. Riehle, U. Sterr, and C. Lisdat, “The ^{87}Sr optical frequency standard at PTB,” *Metrologia* **48**, 399–407 (2011).

[15] A. Derevianko, B. Obreshkov, and V. Dzuba, “Mapping out atom-wall interaction with atomic clocks,” *Physical Review Letters* **103**, 133201 (2009).

[16] P. Wolf, P. Lemonde, A. Lambrecht, S. Bize, A. Landragin, and A. Clairon, “From optical lattice clocks to the measurement of forces in the Casimir regime,” *Physical Review A* **75**, 063608 (2007).

[17] J. M. McGuirk, D. M. Harber, J. M. Obrecht, and E. A. Cornell, “Alkali adsorbate polarization on conducting and insulating surfaces probed with Bose-Einstein condensates,” *Physical Review A* , 062905 (2004).

[18] H. Bender, P. W. Courteille, C. Marzok, C. Zimmermann, and S. Slama, “Direct measurement of intermediate-range Casimir-Polder potentials,” *Physical Review Letters* **104**, 083201 (2010).

[19] J. C. Bergquist, R. G. Hulet, W. M. Itano, and D. J. Wineland, “Observation of quantum jumps in a single atom,” *Physical Review Letters* **57**, 1699–1702 (1986).

[20] M. H. Anderson, J. R. Ensher, M. R. Matthews, C. E. Wieman, and E. A. Cornell, “Observation of Bose-Einstein condensation in a dilute atomic vapor,” *Science* **269**, 198–201 (1995).

[21] K. B. Davis, M. O. Mewes, M. R. Andrews, N. J. van Druten, D. S. Durfee, D. M. Kurn, and W. Ketterle, “Bose-Einstein condensation in a gas of sodium atoms,” *Physical Review Letters* **75**, 3969–3973 (1995).

[22] S. A. Diddams, “Standards of time and frequency at the outset of the 21st century,” *Science* **306**, 1318–1324 (2004).

[23] M. A. Lombardi, T. P. Heavner, and S. R. Jefferts, “NIST primary frequency standards and the realization of the SI second,” *NCSLI Measure* **2**, 74–89 (2007).

[24] N. Hinkley, J. A. Sherman, N. B. Phillips, M. Schioppo, N. D. Lemke, K. Beloy, M. Pizzocaro, C. W. Oates, and A. D. Ludlow, “An Atomic Clock with 10^{-18} Instability,” *Science* **341**, 1215–1218 (2013).

[25] T. Rosenband, D. B. Hume, P. O. Schmidt, C. W. Chou, A. Brusch, L. Lorini, W. H. Oskay, R. E. Drullinger, T. M. Fortier, J. E. Stalnaker, S. A. Diddams, W. C. Swann, N. R. Newbury, W. M. Itano, D. J. Wineland, and J. C. Bergquist, "Frequency ratio of Al^+ and Hg^+ single-ion optical clocks: Metrology at the 17th decimal place," *Science* **319**, 1808–1812 (2008).

[26] J. D. Prestage, R. L. Tjoelker, and L. Maleki, "Atomic clocks and variations of the fine structure constant," *Physical Review Letters* **74**, 3511–3514 (1995).

[27] S. G. Karshenboim, "Some possibilities for laboratory searches for variations of fundamental constants," *Canadian Journal of Physics* **78**, 639–678 (2000).

[28] V. Flambaum, "Temporal and spatial variation of fundamental constants: theory and observations," in *2007 IEEE International Frequency Control Symposium Joint with the 21st European Frequency and Time Forum*, Vol. 22 (IEEE, 2007) pp. 342–349.

[29] J.-P. Uzan, "The fundamental constants and their variation: observational and theoretical status," *Reviews of Modern Physics* **75**, 403–455 (2003).

[30] J. K. Webb, M. T. Murphy, V. V. Flambaum, V. A. Dzuba, J. D. Barrow, C. W. Churchill, J. X. Prochaska, and A. M. Wolfe, "Further evidence for cosmological evolution of the fine structure constant," *Physical Review Letters* **87**, 091301 (2001).

[31] V. A. Dzuba, V. V. Flambaum, and J. K. Webb, "Calculations of the relativistic effects in many-electron atoms and space-time variation of fundamental constants," *Physical Review A* **59**, 230–237 (1999).

[32] E. J. Angstmann, V. A. Dzuba, and V. V. Flambaum, "Relativistic effects in two valence-electron atoms and ions and the search for variation of the fine-structure constant," *Physical Review A* **70**, 1–4 (2004).

[33] T. M. Fortier, N. Ashby, J. C. Bergquist, M. J. Delaney, S. A. Diddams, T. P. Heavner, L. Hollberg, W. M. Itano, S. R. Jefferts, K. Kim, W. H. Oskay, T. E. Parker, J. Shirley, J. E. Stalnaker, F. Levi, and L. Lorini, "Improved limits on variation of the fine structure constant and violation of Local Position Invariance," *Proceedings of the IEEE International Frequency Control Symposium and Exposition* **070801**, 663–665 (2007).

[34] C. W. Chou, D. B. Hume, T. Rosenband, and D. J. Wineland, "Optical clocks and relativity," *Science* **329**, 1630–1633 (2010).

[35] L. Maleki and J. Prestage, "Applications of clocks and frequency standards: from the routine to tests of fundamental models," *Metrologia* **42**, S145–S153 (2005).

[36] K. Bongs, Y. Singh, L. Smith, W. He, O. Kock, D. Świerad, J. Hughes, S. Schiller, S. Alighanbari, S. Origlia, S. Vogt, U. Sterr, C. Lisdat, R. Le Targat, J. Lodewyck, D. Holleville, B. Venon, S. Bize, G. P. Barwood, P. Gill, I. R. Hill, Y. B. Ovchinnikov, N. Poli, G. M. Tino, J. Stuhler, and W. Kaenders, "Development of a strontium optical lattice clock for the SOC mission on the ISS," *Comptes Rendus Physique* **16**, 553–564 (2015).

[37] S. G. Turyshev, N. Yu, and V. T. Toth, "General relativistic observables for the ACES experiment," *Physical Review D* **93**, 045027 (2016).

[38] F. London, "The general theory of molecular forces," *Transactions of the Faraday Society* **33**, 8b (1937).

[39] P. Milonni, *The quantum vacuum: An introduction to quantum electrodynamics* (Academic Press, 1994).

[40] K. Autumn, Y. A. Liang, S. T. Hsieh, W. Zesch, W. P. Chan, T. W. Kenny, R. Fearing, and R. J. Full, "Adhesive force of a single gecko foot-hair," *Nature* **405**, 681–685 (2000).

[41] E. J. W. Verwey, "Theory of the stability of lyophobic colloids." *The Journal of Physical and Colloid Chemistry* **51**, 631–636 (1947).

[42] J. E. Lennard-Jones, "Processes of adsorption and diffusion on solid surfaces," *Transactions of the Faraday Society* **28**, 333 (1932).

[43] D. A. Steck, "Quantum and atom optics," course notes available online at `http://steck.us/teaching` (2015).

[44] H. B. G. Casimir, "Sur les forces Van der Waals-London," *Journal de Chimie Physique* **46**, 407–410 (1949).

[45] E. Lifshitz, "The theory of molecular attractive forces between solids," *Soviet Physics* **2**, 73–83 (1956).

[46] I. E. Dzyaloshinskii, E. M. Lifshitz, and L. P. Pitaevskii, "General theory of van der Waals forces," *Physics-Uspekhi* **4**, 153–176 (1961).

[47] F. M. Serry, D. Walliser, and G. J. Maclay, "The role of the Casimir effect in the static deflection and stiction of membrane strips in microelectromechanical systems (MEMS)," *Journal of Applied Physics* **84**, 2501–2506 (1998).

[48] E. Buks and M. L. Roukes, "Metastability and the Casimir effect in micromechanical systems," *Europhysics Letters (EPL)* **54**, 220–226 (2001).

[49] F. W. DelRio, M. P. de Boer, J. A. Knapp, E. David Reedy, P. J. Clews, and M. L. Dunn, "The role of van der Waals forces in adhesion of micromachined surfaces," *Nature Materials* **4**, 629–634 (2005).

[50] H. B. Chan, V. A. Aksyuk, R. N. Kleiman, D. J. Bishop, and F. Capasso, "Quantum mechanical actuation of microelectromechanical systems by the Casimir force." *Science* **291**, 1941–4 (2001).

[51] A. A. Chumak, P. W. Milonni, and G. P. Berman, "Effects of electrostatic fields and Casimir force on cantilever vibrations," *Physical Review B* **70**, 085407 (2004).

[52] H. D. L. Santos, "Nanoelectromechanical quantum circuits and systems," *Proceedings of the IEEE* **91**, 1907–1921 (2003).

[53] H. B. Chan, V. A. Aksyuk, R. N. Kleiman, D. J. Bishop, and F. Capasso, "Nonlinear micromechanical Casimir oscillator," *Physical Review Letters* **87**, 211801 (2001).

[54] F. Capasso, J. N. Munday, D. Iannuzzi, and H. B. Chan, "Casimir forces and quantum electrodynamical torques: Physics and nanomechanics," *IEEE Journal on Selected Topics in Quantum Electronics* **13**, 400–414 (2007).

[55] J. N. Munday, F. Capasso, and V. A. Parsegian, "Measured long-range repulsive Casimir-Lifshitz forces," *Nature* **457**, 170–173 (2009).

[56] O. Kenneth and I. Klich, "Opposites attract: A theorem about the Casimir force," *Physical Review Letters* **97**, 160401 (2006).

[57] M. Levin, A. P. McCauley, A. W. Rodriguez, M. T. H. Reid, and S. G. Johnson, "Casimir repulsion between metallic objects in vacuum," *Physical Review Letters* **105**, 090403 (2010).

[58] S. J. Rahi, M. Kardar, and T. Emig, "Constraints on stable equilibria with fluctuation-induced (Casimir) forces," *Physical Review Letters* **105**, 070404 (2010).

[59] O. Kenneth, I. Klich, a. Mann, and M. Revzen, "Repulsive Casimir forces." *Physical review letters* **89**, 033001 (2002).

[60] F. S. S. Rosa, D. A. R. Dalvit, and P. W. Milonni, "Casimir interactions for anisotropic magnetodielectric metamaterials," *Physical Review A* **78**, 032117 (2008).

[61] S. de Man, K. Heeck, R. J. Wijngaarden, and D. Iannuzzi, "Halving the Casimir force with conductive oxides," *Physical Review Letters* **103**, 040402 (2009).

[62] H. B. Chan, Y. Bao, J. Zou, R. A. Cirelli, F. Klemens, W. M. Mansfield, and C. S. Pai, "Measurement of the Casimir force between a gold sphere and a silicon surface with nanoscale trench arrays," *Physical Review Letters* **101**, 030401 (2008).

[63] F. Intravaia, S. Koev, I. W. Jung, A. A. Talin, P. S. Davids, R. S. Decca, V. A. Aksyuk, D. A. R. Dalvit, and D. López, "Strong Casimir force reduction through metallic surface nanostructuring," *Nature Communications* **4**, 2515 (2013).

[64] J. Fortágh and C. Zimmermann, "Magnetic microtraps for ultracold atoms," *Reviews of Modern Physics* **79**, 235–289 (2007).

[65] M. Keil, O. Amit, S. Zhou, D. Groswasser, Y. Japha, and R. Folman, "Fifteen years of cold matter on the atom chip: Promise, realizations, and prospects," *Journal of Modern Optics* **63**, 1840–1885 (2016).

[66] J. Schmiedmayer, R. Folman, and T. Calarco, "Quantum information processing with neutral atoms on an atom chip," *Journal of Modern Optics* **49**, 1375–1388 (2002).

[67] R. Szmuk, V. Dugrain, W. Maineult, J. Reichel, and P. Rosenbusch, "Stability of a trapped-atom clock on a chip," *Physical Review A* **92**, 012106 (2015).

[68] T. Berrada, S. van Frank, R. Bücker, T. Schumm, J.-F. Schaff, and J. Schmiedmayer, "Integrated Mach-Zehnder interferometer for Bose-Einstein condensates," *Nature Communications* **4**, 1–8 (2013).

[69] Y.-J. Wang, D. Z. Anderson, V. M. Bright, E. A. Cornell, Q. Diot, T. Kishimoto, M. Prentiss, R. A. Saravanan, S. R. Segal, and S. Wu, "Atom Michelson interferometer on a chip using a Bose-Einstein condensate," *Physical Review Letters* **94**, 090405 (2005).

[70] P. D. D. Schwindt, S. Knappe, V. Shah, L. Hollberg, J. Kitching, L.-A. Liew, and J. Moreland, "Chip-scale atomic magnetometer," *Applied Physics Letters* **85**, 6409–6411 (2004).

[71] S. Abend, M. Gebbe, M. Gersemann, H. Ahlers, H. Müntinga, E. Giese, N. Gaaloul, C. Schubert, C. Lämmerzahl, W. Ertmer, W. P. Schleich, and E. M. Rasel, "Atom-chip fountain gravimeter," *Physical Review Letters* **117**, 203003 (2016).

[72] D. M. Harber, J. M. McGuirk, J. M. Obrecht, and E. A. Cornell, "Thermally induced losses in ultra-cold atoms magnetically trapped near room-temperature surfaces," *Journal of Low Temperature Physics* **133**, 229–238 (2003).

[73] Y.-J. Lin, I. Teper, C. Chin, and V. Vuletić, "Impact of the Casimir-Polder potential and Johnson noise on Bose-Einstein condensate stability near surfaces." *Physical review letters* **92**, 050404 (2004).

[74] M. Al-Amri and M. Babiker, "Quantum shifts for qubits in heterostructures," *Physical Review A* **69**, 065801 (2004).

[75] D. A. R. Dalvit and P. A. Maia Neto, "Decoherence via the dynamical Casimir effect," *Physical Review Letters* **84**, 798–801 (2000).

[76] M. Buttiker, "Decoherence from vacuum fluctuations," *arXiv.org preprint* arXiv:cond-mat/0105519 (2001).

[77] R. Folman, "Material science for quantum computing with atom chips," *arXiv.org preprint* arXiv:quant-ph/1108.3803 (2011).

[78] R. Fermani, S. Scheel, and P. Knight, "Trapping cold atoms near carbon nanotubes: Thermal spin flips and Casimir-Polder potential," *Physical Review A* **75**, 062905 (2007).

[79] C. Eberlein and R. Zietal, "Casimir-Polder interaction between a polarizable particle and a plate with a hole," *Physical Review A* **83**, 052514 (2011).

[80] K. A. Milton, P. Parashar, N. Pourtolami, and I. Brevik, "Casimir-Polder repulsion: Polarizable atoms, cylinders, spheres, and ellipsoids," *Physical Review D* **85**, 025008 (2012).

[81] P. Schneeweiss, M. Gierling, G. Visanescu, D. P. Kern, T. E. Judd, A. Günther, and J. Fortágh, "Dispersion forces between ultracold atoms and a carbon nanotube," *Nature Nanotechnology* **7**, 515–519 (2012).

[82] M. Al-Amri and M. Babiker, "Atomic reflection off conductor walls as a tool in cold atom traps," *The European Physical Journal D* **48**, 417–421 (2008).

[83] P. G. Petrov, S. MacHluf, S. Younis, R. MacAluso, T. David, B. Hadad, Y. Japha, M. Keil, E. Joselevich, and R. Folman, "Trapping cold atoms using surface-grown carbon nanotubes," *Physical Review A* **79**, 1–11 (2009).

[84] A. González-Tudela, C. L. Hung, D. E. Chang, J. I. Cirac, and H. J. Kimble, "Subwavelength vacuum lattices and atom-atom interactions in photonic crystals," *Nature Photonics* **9**, 320 (2015).

[85] H. Walther, B. T. H. Varcoe, B.-G. Englert, and T. Becker, "Cavity quantum electrodynamics," *Reports on Progress in Physics* **69**, 1325–1382 (2006).

[86] D. J. Alton, N. P. Stern, T. Aoki, H. Lee, E. Ostby, K. J. Vahala, and H. J. Kimble, "Strong interactions of single atoms and photons near a dielectric boundary," *Nature Physics* **7**, 159–165 (2011).

[87] G. Sagué, E. Vetsch, W. Alt, D. Meschede, and A. Rauschenbeutel, "Cold-atom physics using ultrathin optical fibers: Light-induced dipole forces and surface interactions," *Physical Review Letters* **99**, 163602 (2007).

[88] E. Vetsch, D. Reitz, G. Sagué, R. Schmidt, S. T. Dawkins, and A. Rauschenbeutel, "Optical interface created by laser-cooled atoms trapped in the evanescent field surrounding an optical nanofiber," *Physical Review Letters* **104**, 203603 (2010).

[89] E. Adelberger, B. Heckel, and A. Nelson, "Tests of the gravitational inverse-square law," *Annual Review of Nuclear and Particle Science* **53**, 77–121 (2003).

[90] V. Mostepanenko and I. Sokolov, "The Casimir effect leads to new restrictions on long-range force constants," *Physics Letters A* **125**, 405–408 (1987).

[91] S. Dimopoulos and A. A. Geraci, "Probing submicron forces by interferometry of Bose-Einstein condensed atoms," *Physical Review D* **68**, 124021 (2003).

[92] I. Carusotto, L. Pitaevskii, S. Stringari, G. Modugno, and M. Inguscio, "Sensitive measurement of forces at the micron scale using Bloch oscillations of ultracold atoms," *Physical Review Letters* **95**, 093202 (2005).

[93] J. Chiaverini, S. J. Smullin, A. A. Geraci, D. M. Weld, and A. Kapitulnik, "New experimental constraints on non-Newtonian forces below 10 μm," *Physical Review Letters* **90**, 151101 (2003).

[94] R. S. Decca, D. López, H. B. Chan, E. Fischbach, D. E. Krause, and C. R. Jamell, "Constraining new forces in the Casimir regime using the isoelectronic technique," *Physical Review Letters* **94**, 240401 (2005).

[95] T. Ederth, "Template-stripped gold surfaces with 0.4-nm rms roughness suitable for force measurements: Application to the Casimir force in the 20–100-nm range," *Physical Review A* **62**, 062104 (2000).

[96] D. Dalvit, P. Milonni, D. Roberts, and F. da Rosa, eds., *Casimir Physics*, Lecture Notes in Physics, Vol. 834 (Springer Berlin Heidelberg, 2011).

[97] C. Wieman, G. Flowers, and S. Gilbert, "Inexpensive laser cooling and trapping experiment for undergraduate laboratories," *American Journal of Physics* **63**, 317–330 (1995).

[98] C. Monroe, W. Swann, H. Robinson, and C. Wieman, "Very cold trapped atoms in a vapor cell," *Physical Review Letters* **65**, 1571–1574 (1990).

[99] A. Cable, M. Prentiss, and N. P. Bigelow, "Observations of sodium atoms in a magnetic molasses trap loaded by a continuous uncooled source," *Optics Letters* **15**, 507 (1990).

[100] M. Boyd, A. Ludlow, S. Blatt, S. Foreman, T. Ido, T. Zelevinsky, and J. Ye, "^{87}Sr lattice clock with inaccuracy below 10^{-15}," *Physical Review Letters* **98**, 083002 (2007).

[101] A. D. Ludlow, *The Strontium Optical Lattice Clock: Optical Spectroscopy with Sub-Hertz Accuracy*, Ph.D. thesis, University of Colorado (2008).

[102] K. Vogel, T. Dinneen, A. Gallagher, and J. Hall, "Narrow-line cooling in a strontium vapor cell magneto-optical trap," in *Technical Digest. Summaries of Papers Presented at the International Quantum Electronics Conference. Conference Edition. 1998 Technical Digest Series, Vol.7 (IEEE Cat. No.98CH36236)* (Opt. Soc. America, 1998) p. 223.

[103] T. P. Dinneen, K. R. Vogel, E. Arimondo, J. L. Hall, and A. Gallagher, "Cold collisions of Sr*-Sr in a magneto-optical trap," *Physical Review A* **59**, 1216–1222 (1999).

[104] M. D. Swallows, M. J. Martin, M. Bishof, C. Benko, Yige Lin, S. Blatt, A. M. Rey, and J. Ye, "Operating a ^{87}Sr optical lattice clock with high precision and at high density," *IEEE Transactions on Ultrasonics, Ferroelectrics and Frequency Control* **59**, 416–425 (2012).

[105] M. J. Martin, M. Bishof, M. D. Swallows, X. Zhang, C. Benko, J. Von-Stecher, A. V. Gorshkov, A. M. Rey, and J. Ye, "A quantum many-body spin system in an optical lattice clock," *Science* **341**, 632–636 (2013).

[106] R. H. Dicke, "The effect of collisions upon the Doppler width of spectral lines," *Physical Review* **89**, 472–473 (1953).

[107] H. Katori, T. Ido, and M. Kuwata-Gonokami, "Optimal design of dipole potentials for efficient loading of Sr atoms," *Journal of the Physical Society of Japan* **68**, 2479–2482 (1999).

[108] S. B. Koller, J. Grotti, S. Vogt, A. Al-Masoudi, S. Dörscher, S. Häfner, U. Sterr, and C. Lisdat, "Transportable optical lattice clock with 7×10^{-17} uncertainty," *Physical Review Letters* **118**, 073601 (2017).

[109] S. B. Nagel, C. E. Simien, S. Laha, P. Gupta, V. S. Ashoka, and T. C. Killian, "Magnetic trapping of metastable ^{3}P$_2$ atomic strontium," *Physical Review A* **67**, 011401 (2003).

[110] T. Ido, Y. Isoya, and H. Katori, "Optical-dipole trapping of Sr atoms at a high phase-space density," *Physical Review A* **61**, 061403 (2000).

[111] Y. N. M. de Escobar, P. G. Mickelson, M. Yan, B. J. DeSalvo, S. B. Nagel, and T. C. Killian, "Bose-Einstein condensation of ^{84}Sr," *Physical Review Letters* **103**, 200402 (2009).

[112] S. Stellmer, M. K. Tey, B. Huang, R. Grimm, and F. Schreck, "Bose-Einstein condensation of strontium," *Physical Review Letters* **103**, 200401 (2009).

[113] S. Stellmer, M. K. Tey, R. Grimm, and F. Schreck, "Bose-Einstein condensation of ^{86}Sr," *Physical Review A* **82**, 041602 (2010).

[114] P. G. Mickelson, Y. N. Martinez De Escobar, M. Yan, B. J. Desalvo, and T. C. Killian, "Bose-Einstein condensation of ^{88}Sr through sympathetic cooling with ^{87}Sr," *Physical Review A* **81**, 050601 (2010).

[115] B. J. DeSalvo, M. Yan, P. G. Mickelson, Y. N. Martinez de Escobar, and T. C. Killian, "Degenerate Fermi gas of ^{87}Sr," *Physical Review Letters* **105**, 030402 (2010).

[116] S. Stellmer, B. Pasquiou, R. Grimm, and F. Schreck, "Laser cooling to quantum degeneracy," *Physical Review Letters* **110**, 263003 (2013).

[117] W. Ketterle, "Nobel lecture: When atoms behave as waves: Bose-Einstein condensation and the atom laser," *Reviews of Modern Physics* **74**, 1131–1151 (2002).

[118] S. Blatt, A. D. Ludlow, G. K. Campbell, J. W. Thomsen, T. Zelevinsky, M. M. Boyd, J. Ye, X. Baillard, M. Fouché, R. Le Targat, A. Brusch, P. Lemonde, M. Takamoto, F.-L. Hong, H. Katori, and V. V. Flambaum, "New limits on coupling of fundamental constants to gravity using ^{87}Sr optical lattice clocks," *Physical Review Letters* **100**, 140801 (2008).

[119] N. Poli, F.-Y. Wang, M. G. Tarallo, A. Alberti, M. Prevedelli, and G. M. Tino, "Precision measurement of gravity with cold atoms in an optical lattice and comparison with a classical gravimeter," *Physical Review Letters* **106**, 038501 (2011).

[120] T. Zelevinsky, S. Kotochigova, and J. Ye, "Precision test of mass-ratio variations with lattice-confined ultracold molecules," *Physical Review Letters* **100**, 043201 (2008).

[121] S. Kotochigova, T. Zelevinsky, and J. Ye, "Prospects for application of ultracold Sr_2 molecules in precision measurements," *Physical Review A* **79**, 012504 (2009).

[122] G. Reinaudi, C. B. Osborn, M. McDonald, S. Kotochigova, and T. Zelevinsky, "Optical production of stable ultracold $^{88}Sr_2$ molecules," *Physical Review Letters* **109**, 115303 (2012).

[123] S. Stellmer, B. Pasquiou, R. Grimm, and F. Schreck, "Creation of ultracold Sr_2 molecules in the electronic ground state," *Physical Review Letters* **109**, 115302 (2012).

[124] M. A. Norcia and J. K. Thompson, "Simple laser stabilization to the strontium ^{88}Sr transition at 707 nm," *Review of Scientific Instruments* **87**, 023110 (2016).

[125] D. Meiser, J. Ye, D. R. Carlson, and M. J. Holland, "Prospects for a millihertz-linewidth laser," *Physical Review Letters* **102**, 163601 (2009).

[126] M. A. Norcia and J. K. Thompson, "Cold-strontium laser in the superradiant crossover regime," *Physical Review X* **6**, 011025 (2016).

[127] I. Bloch, J. Dalibard, and S. Nascimbène, "Quantum simulations with ultracold quantum gases," *Nature Physics* **8**, 267–276 (2012).

[128] A. V. Gorshkov, M. Hermele, V. Gurarie, C. Xu, P. S. Julienne, J. Ye, P. Zoller, E. Demler, M. D. Lukin, and A. M. Rey, "Two-orbital SU(N) magnetism with ultracold alkaline-earth atoms," *Nature Physics* **6**, 289–295 (2010).

[129] M. Hermele, V. Gurarie, and A. M. Rey, "Mott insulators of ultracold fermionic alkaline earth atoms: Underconstrained magnetism and chiral spin liquid," *Physical Review Letters* **103**, 135301 (2009).

[130] A. J. Daley, M. M. Boyd, J. Ye, and P. Zoller, "Quantum computing with alkaline-earth-metal atoms," *Physical Review Letters* **101**, 170504 (2008).

[131] A. J. Daley, J. Ye, and P. Zoller, "State-dependent lattices for quantum computing with alkaline-earth-metal atoms," *The European Physical Journal D* **65**, 207–217 (2011).

[132] A. V. Gorshkov, A. M. Rey, A. J. Daley, M. M. Boyd, J. Ye, P. Zoller, and M. D. Lukin, "Alkaline-earth-metal atoms as few-qubit quantum registers," *Physical Review Letters* **102**, 110503 (2009).

[133] J. Millen, G. Lochead, G. R. Corbett, R. M. Potvliege, and M. P. A. Jones, "Spectroscopy of a cold strontium Rydberg gas," *Journal of Physics B: Atomic, Molecular, and Optical Physics* **44**, 184001 (2011).

[134] A. Maury, M. Donaire, M.-P. Gorza, A. Lambrecht, and R. Guérout, "Surface-modified Wannier-Stark states in a one-dimensional optical lattice," *Physical Review A* **94**, 053602 (2016).

[135] M. Raizen, C. Salomon, and Q. Niu, "New light on quantum transport," *Physics Today* **50**, 30–34 (1997).

[136] G. Ferrari, N. Poli, F. Sorrentino, and G. M. Tino, "Long-lived Bloch oscillations with bosonic Sr atoms and application to gravity measurement at the micrometer scale," *Physical Review Letters* **97**, 060402 (2006).

[137] F. Sorrentino, A. Alberti, G. Ferrari, V. V. Ivanov, N. Poli, M. Schioppo, and G. M. Tino, "Quantum sensor for atom-surface interactions below 10 μm," *Physical Review A* **79**, 013409 (2009).

[138] V. V. Ivanov, A. Alberti, M. Schioppo, G. Ferrari, M. Artoni, M. L. Chiofalo, and G. M. Tino, "Coherent delocalization of atomic wave packets in driven lattice potentials," *Physical Review Letters* **100**, 043602 (2008).

[139] A. Alberti, G. Ferrari, V. V. Ivanov, M. L. Chiofalo, and G. M. Tino, "Atomic wave packets in amplitude-modulated vertical optical lattices," *New Journal of Physics* **12**, 065037 (2010).

[140] V. V. Ivanov, "Study of surface potentials using resonant tunnelling of cold atoms in optical lattices," *Journal of Physics B: Atomic, Molecular, and Optical Physics* **45**, 205004 (2012).

[141] R. Loudon, *The quantum theory of light* (Oxford University Press, 2000).

[142] H. A. Bethe, "The electromagnetic shift of energy levels," *Physical Review* **72**, 339–341 (1947).

[143] M. M. Boyd, *High Precision Spectroscopy of Strontium in an Optical Lattice: Towards a New Standard for Frequency and Time*, Ph.D. thesis, University of Colorado (2007).

[144] P. J. Martin, *Development of a Strontium Magneto-Optical Trap for Probing Casimir-Polder Potentials*, Ph.D. thesis, University of Oregon (2017).

[145] S. M. Barnett, A. Aspect, and P. W. Milonni, "On the quantum nature of the Casimir-Polder interaction," *Journal of Physics B: Atomic, Molecular, and Optical Physics* **33**, 143–149 (2000).

[146] L. Spruch, "Retarded, or Casimir, long-range potentials," *Physics Today* **39**, 37–45 (1986).

[147] A. Derevianko, S. G. Porsev, and J. F. Babb, "Electric dipole polarizabilities at imaginary frequencies for hydrogen, the alkali-metal, alkaline-earth, and noble gas atoms," *Atomic Data and Nuclear Data Tables* **96**, 323–331 (2010).

[148] C. Henkel, "The physics of atom-surface interactions," *arXiv.org* arXiv:quant-ph/0005038 (2004).

[149] B. M. Axilrod and E. Teller, "Interaction of the van der Waals type between three atoms," *The Journal of Chemical Physics* **11**, 299–300 (1943).

[150] M. R. Aub and S. Zienau, "Studies on the retarded interaction between neutral atoms. I. Three-body London-van der Waals interaction of neutral atoms," *Proceedings of the Royal Society A: Mathematical, Physical and Engineering Sciences* **257**, 464–476 (1960).

[151] J. Babb, G. Klimchitskaya, and V. Mostepanenko, "Casimir-Polder interaction between an atom and a cavity wall under the influence of real conditions," *Physical Review A* **70**, 042901 (2004).

[152] S. Y. Buhmann, L. Knöll, D.-G. Welsch, and H. T. Dung, "Casimir-Polder forces: A nonperturbative approach," *Physical Review A* **70**, 052117 (2004).

[153] V. Bezerra, G. Klimchitskaya, and C. Romero, "Surface roughness contribution to the Casimir interaction between an isolated atom and a cavity wall," *Physical Review A* **61**, 022115 (2000).

[154] M. Bordag, G. L. Klimchitskaya, U. Mohideen, and V. M. Mostepanenko, *Advances in the Casimir effect*, International Series of Monographs on Physics, Vol. 145 (Oxford University Press, 2009).

[155] D. A. R. Dalvit, P. A. M. Neto, A. Lambrecht, and S. Reynaud, "Probing quantum-vacuum geometrical effects with cold atoms," *Physical Review Letters* **100**, 040405 (2008).

[156] J. Błocki, J. Randrup, W. Światecki, and C. Tsang, "Proximity forces," *Annals of Physics* **105**, 427–462 (1977).

[157] R. Büscher and T. Emig, "Geometry and spectrum of Casimir forces," *Physical Review Letters* **94**, 133901 (2005).

[158] H. Gies and K. Klingmüller, "Casimir effect for curved geometries: Proximity-force-approximation validity limits," *Physical Review Letters* **96**, 220401 (2006).

[159] A. Rodriguez, M. Ibanescu, D. Iannuzzi, J. D. Joannopoulos, and S. G. Johnson, "Virtual photons in imaginary time: Computing exact Casimir forces via standard numerical electromagnetism techniques," *Physical Review A* **76**, 032106 (2007).

[160] A. Rodriguez, M. Ibanescu, D. Iannuzzi, F. Capasso, J. D. Joannopoulos, and S. G. Johnson, "Computation and visualization of Casimir forces in arbitrary geometries: Nonmonotonic lateral-wall forces and the failure of proximity-force approximations," *Physical Review Letters* **99**, 080401 (2007).

[161] S. J. Rahi, T. Emig, N. Graham, R. L. Jaffe, and M. Kardar, "Scattering theory approach to electrodynamic Casimir forces," *Physical Review D* **80**, 085021 (2009).

[162] M. T. H. Reid, A. W. Rodriguez, J. White, and S. G. Johnson, “Efficient computation of Casimir interactions between arbitrary 3D objects,” *Physical Review Letters* **103**, 040401 (2009).

[163] H. Gies, K. Langfeld, and L. Moyaerts, “Casimir effect on the worldline,” *Journal of High Energy Physics* **2003**, 018 (2003).

[164] H. Gies and K. Klingmüller, “Casimir effect for curved geometries: Proximity-force-approximation validity limits,” *Physical Review Letters* **96**, 220401 (2006).

[165] J. B. Mackrory, T. Bhattacharya, and D. A. Steck, “Worldline approach for numerical computation of electromagnetic Casimir energies: Scalar field coupled to magnetodielectric media,” *Physical Review A* **94**, 042508 (2016).

[166] J. M. Obrecht, R. J. Wild, M. Antezza, L. P. Pitaevskii, S. Stringari, and E. A. Cornell, “Measurement of the temperature dependence of the Casimir-Polder force,” *Physical Review Letters* **98**, 063201 (2007).

[167] A. O. Sushkov, W. J. Kim, D. A. R. Dalvit, and S. K. Lamoreaux, “Observation of the thermal Casimir force,” *Nature Physics* **7**, 230–233 (2011).

[168] M. Sparnaay, “Measurements of attractive forces between flat plates,” *Physica* **24**, 751–764 (1958).

[169] G. Bressi, G. Carugno, R. Onofrio, and G. Ruoso, “Measurement of the Casimir force between parallel metallic surfaces,” *Physical Review Letters* **88**, 041804 (2002).

[170] U. Mohideen and A. Roy, “Precision measurement of the Casimir force from 0.1 to 0.9 μm,” *Physical Review Letters* **81**, 4549–4552 (1998).

[171] A. Roy and U. Mohideen, “Demonstration of the nontrivial boundary dependence of the Casimir force,” *Physical Review Letters* **82**, 4380–4383 (1999).

[172] M. Lisanti, D. Iannuzzi, and F. Capasso, “Observation of the skin-depth effect on the Casimir force between metallic surfaces,” *Proceedings of the National Academy of Sciences* **102**, 11989–11992 (2005).

[173] R. S. Decca, D. López, E. Fischbach, G. L. Klimchitskaya, D. E. Krause, and V. M. Mostepanenko, “Tests of new physics from precise measurements of the Casimir pressure between two gold-coated plates,” *Physical Review D* **75**, 077101 (2007).

[174] D. Raskin and P. Kusch, “Interaction between a neutral atomic or molecular beam and a conducting surface,” *Physical Review* **179**, 712–721 (1969).

[175] A. Shih, D. Raskin, and P. Kusch, “Investigation of the interaction potential between a neutral molecule and a conducting surface,” *Physical Review A* **9**, 652–662 (1974).

[176] A. Shih and V. Parsegian, “Van der Waals forces between heavy alkali atoms and gold surfaces: Comparison of measured and predicted values,” *Physical Review A* **12**, 835–841 (1975).

[177] A. Anderson, S. Haroche, E. A. Hinds, W. Jhe, and D. Meschede, “Measuring the van der Waals forces between a Rydberg atom and a metallic surface,” *Physical Review A* **37**, 3594–3597 (1988).

[178] A. Landragin, J.-Y. Courtois, G. Labeyrie, N. Vansteenkiste, C. I. Westbrook, and A. Aspect, “Measurement of the van der Waals force in an atomic mirror,” *Physical Review Letters* **77**, 1464–1467 (1996).

[179] N. Westbrook, C. I. Westbrook, A. Landragin, G. Labeyrie, L. Cognet, V. Savalli, G. Horvath, A. Aspect, C. Hendel, K. Moelmer, J.-Y. Courtois, W. D. Phillips, R. Kaiser, and V. Bagnato, “New physics with evanescent wave atomic mirrors: The van der Waals force and atomic diffraction,” *Physica Scripta* **T78**, 7–12 (1998).

[180] B. Segev, R. Côté, and M. G. Raizen, “Quantum reflection from an atomic mirror,” *Physical Review A* **56**, R3350–R3353 (1997).

[181] R. Côté, B. Segev, and M. Raizen, “Retardation effects on quantum reflection from an evanescent-wave atomic mirror,” *Physical Review A* **58**, 3999–4013 (1998).

[182] R. Côté, H. Friedrich, and J. Trost, “Reflection above potential steps,” *Physical Review A* **56**, 1781–1787 (1997).

[183] H. Friedrich, G. Jacoby, and C. G. Meister, “Quantum reflection by Casimir – van der Waals potential tails,” *Physical Review A* **65**, 032902–032914 (2002).

[184] F. Shimizu, “Specular reflection of very slow metastable neon atoms from a solid surface,” *Physical Review Letters* **86**, 987–990 (2001).

[185] F. Shimizu and J. Fujita, “Giant quantum reflection of neon atoms from a ridged silicon surface,” *Journal of the Physical Society of Japan* **71**, 5–8 (2002).

[186] T. A. Pasquini, Y. Shin, C. Sanner, M. Saba, A. Schirotzek, D. E. Pritchard, and W. Ketterle, “Quantum reflection from a solid surface at normal incidence,” *Physical Review Letters* **93**, 223201 (2004).

[187] T. A. Pasquini, M. Saba, G. B. Jo, Y. Shin, W. Ketterle, D. E. Pritchard, T. A. Savas, and N. Mulders, "Low velocity quantum reflection of Bose-Einstein condensates," *Physical Review Letters* **97**, 093201 (2006).

[188] V. Druzhinina and M. DeKieviet, "Experimental observation of quantum reflection far from threshold," *Physical Review Letters* **91**, 193202 (2003).

[189] H. Oberst, Y. Tashiro, K. Shimizu, and F. Shimizu, "Quantum reflection of He* on silicon," *Physical Review A* **71**, 052901 (2005).

[190] M. Antezza, L. P. Pitaevskii, and S. Stringari, "Effect of the Casimir-Polder force on the collective oscillations of a trapped Bose-Einstein condensate," *Physical Review A* **70**, 053619 (2004).

[191] D. Harber, J. Obrecht, J. McGuirk, and E. Cornell, "Measurement of the Casimir-Polder force through center-of-mass oscillations of a Bose-Einstein condensate," *Physical Review A* **72**, 033610 (2005).

[192] M. Antezza, L. P. Pitaevskii, and S. Stringari, "New asymptotic behavior of the surface-atom force out of thermal equilibrium," *Physical Review Letters* **95**, 113202 (2005).

[193] M. Antezza, L. P. Pitaevskii, S. Stringari, and V. B. Svetovoy, "Casimir-Lifshitz force out of thermal equilibrium," *Physical Review A* **77**, 022901 (2008).

[194] A. D. Cronin and J. D. Perreault, "Phasor analysis of atom diffraction from a rotated material grating," *Physical Review A* **70**, 043607 (2004).

[195] J. D. Perreault, A. D. Cronin, and T. A. Savas, "Using atomic diffraction of Na from material gratings to measure atom-surface interactions," *Physical Review A* **71**, 053612 (2005).

[196] J. Perreault and A. Cronin, "Observation of atom wave phase shifts induced by van der Waals atom-surface interactions," *Physical Review Letters* **95**, 133201 (2005).

[197] J. Perreault and A. Cronin, "Measurement of atomic diffraction phases induced by material gratings," *Physical Review A* **73**, 033610 (2006).

[198] S. Lepoutre, H. Jelassi, V. P. A. Lonij, G. Trénec, M. Büchner, A. D. Cronin, and J. Vigué, "Dispersive atom interferometry phase shifts due to atom-surface interactions," *Europhysics Letters* **88**, 20002 (2009).

[199] S. Lepoutre, V. P. A. Lonij, H. Jelassi, G. Trénec, M. Büchner, A. D. Cronin, and J. Vigué, "Atom interferometry measurement of the atom-surface van der Waals interaction," *The European Physical Journal D* **62**, 309–325 (2011).

[200] M. Gorlicki, S. Feron, V. Lorent, and M. Ducloy, "Interferometric approaches to atom-surface van der Waals interactions in atomic mirrors," *Physical Review A* **61**, 013603 (1999).

[201] R. Marani, L. Cognet, V. Savalli, N. Westbrook, C. I. Westbrook, and A. Aspect, "Using atomic interference to probe atom-surface interactions," *Physical Review A* **61**, 053402 (2000).

[202] J. Chwedeńczuk, L. Pezzé, F. Piazza, and A. Smerzi, "Rabi interferometry and sensitive measurement of the Casimir-Polder force with ultracold gases," *Physical Review A* **82**, 032104 (2010).

[203] V. Sandoghdar, C. I. Sukenik, E. A. Hinds, and S. Haroche, "Direct measurement of the van der Waals interaction between an atom and its images in a micron-sized cavity," *Physical Review Letters* **68**, 3432–3435 (1992).

[204] T. Nakajima, P. Lambropoulos, and H. Walther, "Level shift and depopulation by blackbody radiation of a Rydberg atom between two metallic plates," *Physical Review A* **56**, 5100–5110 (1997).

[205] M. Marrocco, M. Weidinger, R. Sang, and H. Walther, "Quantum electrodynamic shifts of Rydberg energy levels," in *Technical Digest. 1998 EQEC. European Quantum Electronics Conference (Cat. No.98TH8326)*, Vol. 81 (IEEE, 1998) pp. 152–152.

[206] M. Oria, M. Chevrollier, D. Bloch, M. Fichet, and M. Ducloy, "Spectral observation of surface-induced van der Waals attraction on atomic vapour," *Europhysics Letters* **14**, 527–532 (1991).

[207] M. Chevrollier, M. Fichet, M. Oria, G. Rahmat, D. Bloch, and M. Ducloy, "High resolution selective reflection spectroscopy as a probe of long-range surface interaction: Measurement of the surface van der Waals attraction exerted on excited Cs atoms," *Journal de Physique II* **2**, 631–657 (1992).

[208] H. Failache, S. Saltiel, M. Fichet, D. Bloch, and M. Ducloy, "Resonant van der Waals repulsion between excited Cs atoms and sapphire surface," *Physical Review Letters* **83**, 5467–5470 (1999).

[209] M. Fichet, G. Dutier, A. Yarovitsky, P. Todorov, I. Hamdi, I. Maurin, S. Saltiel, D. Sarkisyan, M.-P. Gorza, D. Bloch, and M. Ducloy, "Exploring the van der Waals atom-surface attraction in the nanometric range," *Europhysics Letters* **77**, 54001 (2007).

[210] A. Laliotis, T. P. de Silans, I. Maurin, M. Ducloy, and D. Bloch, "Casimir-Polder interactions in the presence of thermally excited surface modes," *Nature Communications* **5**, 4364 (2014).

[211] D. M. Harber, *Experimental Investigation of Interactions Between Ultracold Atoms and Room-Temperature Surfaces*, Ph.D. thesis, University of Colorado (2005).

[212] T. Ido and H. Katori, “Recoil-free spectroscopy of neutral Sr atoms in the Lamb-Dicke regime.” *Physical Review Letters* **91**, 053001 (2003).

[213] D. Schrader, S. Kuhr, W. Alt, M. Müller, V. Gomer, and D. Meschede, “An optical conveyor belt for single neutral atoms,” *Applied Physics B: Lasers and Optics* **73**, 819–824 (2001).

[214] S. Schmid, G. Thalhammer, K. Winkler, F. Lang, and J. H. Denschlag, “Long distance transport of ultracold atoms using a 1D optical lattice,” *New Journal of Physics* **8**, 159–159 (2006).

[215] T. Li, *Manipulation of Cold Atoms Using an Optical One-Way Barrier*, Ph.D. thesis, University of Oregon (2008).

[216] E. A. Schoene, *Cold Atom Control with an Optical One-Way Barrier*, Ph.D. thesis, University of Oregon (2010).

[217] P. G. Mickelson, Y. N. Martinez, A. D. Saenz, S. B. Nagel, Y. C. Chen, T. C. Killian, P. Pellegrini, and R. Côté, “Spectroscopic determination of the s-wave scattering lengths of ^{86}Sr and ^{88}Sr,” *Physical Review Letters* **95**, 223002 (2005).

[218] J. K. Crane, M. J. Shaw, and R. W. Presta, “Measurement of the cross sections for collisional broadening of the intercombination transitions in calcium and strontium,” *Physical Review A* **49**, 1666–1674 (1994).

[219] T. Ido, T. H. Loftus, M. M. Boyd, A. D. Ludlow, K. W. Holman, and J. Ye, “Precision spectroscopy and density-dependent frequency shifts in ultracold Sr,” *Physical Review Letters* **94**, 153001 (2005).

[220] C. C. Speake and C. Trenkel, “Forces between conducting surfaces due to spatial variations of surface potential,” *Physical Review Letters* **90**, 160403 (2003).

[221] W. Ketterle, D. S. Durfee, and D. M. Stamper-Kurn, “Making, probing and understanding Bose-Einstein condensates,” *arXiv.org* arXiv:cond-mat/9904034 (1999).

[222] J. M. Obrecht, R. J. Wild, and E. A. Cornell, “Measuring electric fields from surface contaminants with neutral atoms,” *Physical Review A* **75**, 062903 (2007).

[223] K. S. Chan, M. Siercke, C. Hufnagel, and R. Dumke, “Adsorbate electric fields on a cryogenic atom chip,” *Physical Review Letters* **112**, 026101 (2014).

[224] H. J. Metcalf and P. van der Straten, *Laser Cooling and Trapping*, Graduate Texts in Contemporary Physics (Springer New York, 1999).

[225] C. J. Foot, *Atomic Physics* (Oxford University Press, 2005).

[226] R. Frisch, "Experimenteller Nachweis des Einsteinschen Strahlungsrückstoßes," *Zeitschrift Fur Physik* **86**, 42–48 (1933).

[227] A. Ashkin, "Acceleration and trapping of particles by radiation pressure," *Physical Review Letters* **24**, 156–159 (1970).

[228] V. S. Letokhov, "Narrowing of the Doppler width in a standing light wave," *JETP Letters* **7**, 272 (1968).

[229] S. Chu, J. E. Bjorkholm, A. Ashkin, and A. Cable, "Experimental observation of optically trapped atoms," *Physical Review Letters* **57**, 314–317 (1986).

[230] D. J. Wineland, "Trapped ions, laser cooling, and better clocks," *Science* **226**, 395–400 (1984).

[231] W. Paul, "Electromagnetic traps for charged and neutral particles," *Reviews of Modern Physics* **62**, 531–540 (1990).

[232] P. K. Ghosh, *Ion Traps* (Oxford University Press, 1995).

[233] D. J. Wineland, "Nobel Lecture: Superposition, entanglement, and raising Schrödinger's cat," *Reviews of Modern Physics* **85**, 1103–1114 (2013).

[234] T. Hänsch and A. Schawlow, "Cooling of gases by laser radiation," *Optics Communications* **13**, 68–69 (1975).

[235] D. Wineland and H. Dehmelt, "Proposed 10^{14} $\delta\nu < \nu$ laser fluorescence spectroscopy on Tl^+ mono-ion oscillator," *Bull. Am. Soc.* **20**, 637 (1975).

[236] D. J. Wineland and W. M. Itano, "Laser cooling of atoms," *Physical Review A* **20**, 1521–1540 (1979).

[237] W. M. Itano and D. J. Wineland, "Laser cooling of ions stored in harmonic and Penning traps," *Physical Review A* **25**, 35–54 (1982).

[238] D. J. Wineland, R. E. Drullinger, and F. L. Walls, "Radiation-pressure cooling of bound resonant absorbers," *Physical Review Letters* **40**, 1639–1642 (1978).

[239] W. Neuhauser, M. Hohenstatt, P. Toschek, and H. Dehmelt, "Optical-sideband cooling of visible atom cloud confined in parabolic well," *Physical Review Letters* **41**, 233–236 (1978).

[240] W. Neuhauser, M. Hohenstatt, P. E. Toschek, and H. Dehmelt, “Localized visible Ba$^+$ mono-ion oscillator,” *Physical Review A* **22**, 1137–1140 (1980).

[241] D. Wineland and W. M. Itano, “Spectroscopy of a single Mg$^+$ ion,” *Physics Letters A* **82**, 75–78 (1981).

[242] W. Nagourney, G. Janik, and H. Dehmelt, “Linewidth of single laser-cooled ^{24}Mg$^+$ ion in radiofrequency trap,” *Physics* **80**, 643–646 (1983).

[243] V. Minogin, “Deceleration and monochromatization of atomic beams by laser radiation pressure,” *Optics Communications* **34**, 265–268 (1980).

[244] S. V. Andreev, V. I. Balykin, V. S. Letekhov, and V. G. Minogin, “Radiative slowing and reduction of the energy spread of sodium atoms to 1.5 K in an oppositely directed laser beam,” *JETP Letters* **34**, 442–445 (1981).

[245] V. Letokhov, V. Minogin, and B. Pavlik, “Cooling and trapping of atoms and molecules by a resonant laser field,” *Optics Communications* **19**, 72–75 (1976).

[246] V. I. Balykin, V. S. Letokhov, and V. I. Mushin, “Observation of the cooling of free sodium atoms in a resonance laser field with a scanning frequency,” *JETP Letters* **29**, 560–564 (1979).

[247] J. V. Prodan and W. D. Phillips, “Chirping the light — fantastic? Recent NBS atom cooling experiments,” *Progress in Quantum Electronics* **8**, 231–235 (1984).

[248] W. Ertmer, R. Blatt, J. L. Hall, and M. Zhu, “Laser manipulation of atomic beam velocities: Demonstration of stopped atoms and velocity reversal,” *Physical Review Letters* **54**, 996–999 (1985).

[249] W. D. Phillips and H. Metcalf, “Laser deceleration of an atomic beam,” *Physical Review Letters* **48**, 596–599 (1982).

[250] J. V. Prodan, W. D. Phillips, and H. Metcalf, “Laser production of a very slow monoenergetic atomic beam,” *Physical Review Letters* **49**, 1149–1153 (1982).

[251] J. Prodan, A. Migdall, W. D. Phillips, I. So, H. Metcalf, and J. Dalibard, “Stopping atoms with laser light,” *Physical Review Letters* **54**, 992–995 (1985).

[252] D. E. Pritchard, “Cooling neutral atoms in a magnetic trap for precision spectroscopy,” *Physical Review Letters* **51**, 1336–1339 (1983).

[253] A. L. Migdall, J. V. Prodan, W. D. Phillips, T. H. Bergeman, and H. J. Metcalf, “First observation of magnetically trapped neutral atoms,” *Physical Review Letters* **54**, 2596–2599 (1985).

[254] A. Ashkin and J. P. Gordon, “Stability of radiation-pressure particle traps: An optical Earnshaw theorem,” *Optics Letters* **8**, 511 (1983).

[255] A. Ashkin, “Stable radiation-pressure particle traps using alternating light beams.” *Optics letters* **9**, 454–456 (1984).

[256] W. D. Phillips, J. V. Prodan, and H. J. Metcalf, “Laser cooling and electromagnetic trapping of neutral atoms,” *Journal of the Optical Society of America B* **2**, 1751 (1985).

[257] S. Chu, L. Hollberg, J. E. Bjorkholm, A. Cable, and A. Ashkin, “Three-dimensional viscous confinement and cooling of atoms by resonance radiation pressure,” *Physical Review Letters* **55**, 48–51 (1985).

[258] V. Minogin and J. Javanainen, “A tetrahedral light pressure trap for atoms,” *Optics Communications* **43**, 119–122 (1982).

[259] F. Shimizu, K. Shimizu, and H. Takuma, “Four-beam laser trap of neutral atoms,” *Optics Letters* **16**, 339 (1991).

[260] A. Ashkin, “Trapping of atoms by resonance radiation pressure,” *Physical Review Letters* **40**, 729–732 (1978).

[261] J. P. Gordon, “Radiation forces and momenta in dielectric media,” *Physical Review A* **8**, 14–21 (1973).

[262] R. Grimm, M. Weidemüller, and Y. B. Ovchinnikov, “Optical dipole traps for neutral atoms,” *Advances in Atomic, Molecular and Optical Physics* **42**, 95–170 (2000).

[263] J. P. Gordon and A. Ashkin, “Motion of atoms in a radiation trap,” *Physical Review A* **21**, 1606–1617 (1980).

[264] J. Dalibard, S. Reynaud, and C. Cohen-Tannoudji, “Proposals of stable optical traps for neutral atoms,” *Optics Communications* **47**, 395–399 (1983).

[265] P. L. Gould, P. D. Lett, P. S. Julienne, W. D. Phillips, H. R. Thorsheim, and J. Weiner, “Observation of associative ionization of ultracold laser-trapped sodium atoms,” *Physical Review Letters* **60**, 788–791 (1988).

[266] D. E. Pritchard, E. L. Raab, V. Bagnato, C. E. Wieman, and R. N. Watts, “Light traps using spontaneous forces,” *Physical Review Letters* **57**, 310–313 (1986).

[267] E. L. Raab, M. Prentiss, A. Cable, S. Chu, and D. E. Pritchard, “Trapping of neutral sodium atoms with radiation pressure,” *Physical Review Letters* **59**, 2631–2634 (1987).

[268] S. L. Rolston, C. Gerz, K. Helmerson, P. S. Jessen, P. D. Lett, W. D. Phillips, R. J. Spreeuw, and C. I. Westbrook, “Trapping atoms with optical potentials,” *Proceedings of SPIE* **1726**, 205 (1992).

[269] J. D. Miller, R. A. Cline, and D. J. Heinzen, "Far-off-resonance optical trapping of atoms," *Physical Review A* **47**, R4567–R4570 (1993).

[270] C. S. Adams, H. J. Lee, N. Davidson, M. Kasevich, and S. Chu, "Evaporative cooling in a crossed dipole trap," *Physical Review Letters* **74**, 3577–3580 (1995).

[271] H. Engler, T. Weber, M. Mudrich, R. Grimm, and M. Weidemüller, "Very long storage times and evaporative cooling of cesium atoms in a quasielectrostatic dipole trap," *Physical Review A* **62**, 031402 (2000).

[272] T. Takekoshi, J. R. Yeh, and R. J. Knize, "Quasi-electrostatic trap for neutral atoms," *Optics Communications* **114**, 421–424 (1995).

[273] T. Takekoshi and R. J. Knize, "CO_2 laser trap for cesium atoms," *Optics Letters* **21**, 77 (1996).

[274] P. Jessen and I. Deutsch, "Optical Lattices," in *Advances in Atomic, Molecular and Optical Physics*, edited by B. Bederson and H. Walther (Academic Press, Cambridge, 1996) pp. 95–138.

[275] J. Dalibard and C. Cohen-Tannoudji, "Laser cooling below the Doppler limit by polarization gradients: simple theoretical models," *Journal of the Optical Society of America B* **6**, 2023 (1989).

[276] P. J. Ungar, D. S. Weiss, E. Riis, and S. Chu, "Optical molasses and multilevel atoms: Theory," *Journal of the Optical Society of America B* **6**, 2058 (1989).

[277] W. D. Phillips, "Nobel Lecture: Laser cooling and trapping of neutral atoms," *Reviews of Modern Physics* **70**, 721–741 (1998).

[278] C. I. Westbrook, R. N. Watts, C. E. Tanner, S. L. Rolston, W. D. Phillips, P. D. Lett, and P. L. Gould, "Localization of atoms in a three-dimensional standing wave," *Physical Review Letters* **65**, 33–36 (1990).

[279] P. Verkerk, B. Lounis, C. Salomon, C. Cohen-Tannoudji, J.-Y. Courtois, and G. Grynberg, "Dynamics and spatial order of cold cesium atoms in a periodic optical potential," *Physical Review Letters* **68**, 3861–3864 (1992).

[280] J. C. Bergquist, W. M. Itano, and D. J. Wineland, "Recoiless optical absorption and Doppler sidebands of a single trapped ion," *Physical Review A* **36**, 428–430 (1987).

[281] F. Diedrich, J. C. Bergquist, W. M. Itano, and D. J. Wineland, "Laser cooling to the zero-point energy of motion," *Physical Review Letters* **62**, 403–406 (1989).

[282] D. J. Wineland, W. M. Itano, J. C. Bergquist, and R. G. Hulet, "Laser-cooling limits and single-ion spectroscopy," *Physical Review A* **36**, 2220–2232 (1987).

[283] I. Bloch, "Ultracold quantum gases in optical lattices," *Nature Physics* **1**, 23–30 (2005).

[284] F. L. Moore, J. C. Robinson, C. Bharucha, P. E. Williams, and M. G. Raizen, "Observation of dynamical localization in atomic momentum transfer: A new testing ground for quantum chaos," *Physical Review Letters* **73**, 2974–2977 (1994).

[285] F. L. Moore, J. C. Robinson, C. F. Bharucha, B. Sundaram, and M. G. Raizen, "Atom optics realization of the quantum δ-kicked rotor," *Physical Review Letters* **75**, 4598–4601 (1995).

[286] D. A. Steck, *Quantum Chaos, Transport, and Decoherence in Atom Optics*, Ph.D. thesis, University of Texas at Austin (2001).

[287] G. K. Brennen, C. M. Caves, P. S. Jessen, and I. H. Deutsch, "Quantum logic gates in optical lattices," *Physical Review Letters* **82**, 1060–1063 (1999).

[288] D. Jaksch, H.-J. Briegel, J. I. Cirac, C. W. Gardiner, and P. Zoller, "Entanglement of atoms via cold controlled collisions," *Physical Review Letters* **82**, 1975–1978 (1999).

[289] D. Jaksch, J. I. Cirac, P. Zoller, S. L. Rolston, R. Côté, and M. D. Lukin, "Fast quatum gates for neutral atoms," *Physical Review Letters* **85**, 2208–2211 (2000).

[290] I. Bloch, "Quantum coherence and entanglement with ultracold atoms in optical lattices," *Nature* **453**, 1016–1022 (2008).

[291] P. D. Lett, W. D. Phillips, S. L. Rolston, C. E. Tanner, R. N. Watts, and C. I. Westbrook, "Optical molasses," *Journal of the Optical Society of America B* **6**, 2084 (1989).

[292] V. S. Letokhov, V. G. Minogin, and B. D. Pavlik, "Cooling and capture of atoms and molecules by a resonant light field," *Zeitschrift Fur Physik* **45**, 698 (1977).

[293] R. J. Cook, "Quantum-mechanical fluctuations of the resonance-radiation force," *Physical Review Letters* **44**, 976–979 (1980).

[294] W. D. Phillips, "Laser cooling and trapping of neutral atoms," in *Laser Manipulation of Atoms and Ions: Proceedings of the International Schol of Physics "Enrico Fermi", Course CXVII*, edited by E. Arimondo, W. Phillips, and F. Strumia (North-Holland, Amsterdam, 1992) pp. 289–347.

[295] P. D. Lett, R. N. Watts, C. I. Westbrook, W. D. Phillips, P. L. Gould, and H. J. Metcalf, "Observation of atoms laser cooled below the Doppler limit," *Physical Review Letters* **61**, 169–172 (1988).

[296] D. S. Weiss, E. Riis, Y. Shevy, P. J. Ungar, and S. Chu, "Optical molasses and multilevel atoms: Experiment," *Journal of the Optical Society of America B* **6**, 2072 (1989).

[297] S. Chu, M. G. Prentiss, A. E. Cable, J. E. Bjorkholm, W. Pearson, and S. Svanberg, *Laser Spectroscopy VIII* (Springer-Verlag, Berlin, 1987).

[298] T. E. Barrett, S. W. Dapore-Schwartz, M. D. Ray, and G. P. Lafyatis, "Slowing atoms with σ^- polarized light," *Physical Review Letters* **67**, 3483–3486 (1991).

[299] M. A. Joffe, W. Ketterle, A. Martin, and D. E. Pritchard, "Transverse cooling and deflection of an atomic beam inside a Zeeman slower," *Journal of the Optical Society of America B* **10**, 2257 (1993).

[300] I. R. Hill, Y. B. Ovchinnikov, E. M. Bridge, E. A. Curtis, and P. Gill, "Zeeman slowers for strontium based on permanent magnets," *Journal of Physics B: Atomic, Molecular, and Optical Physics* **47**, 075006 (2014).

[301] M. Bober, J. Zachorowski, and W. Gawlik, "Designing Zeeman slower for strontium atoms - towards optical atomic clock," *Optica Applicata* **40**, 547–555 (2010).

[302] V. S. Bagnato, A. Aspect, and S. C. Zilio, "Study of laser deceleration of an atomic beam by monitoring the fluorescence along the deceleration path," *Optics Communications* **72**, 76–81 (1989).

[303] V. S. Bagnato, C. Salomon, E. Marega, and S. C. Zilio, "Influence of adiabatic following and optical pumping in the production of an intense steady flux of slow atoms," *Journal of the Optical Society of America B* **8**, 497 (1991).

[304] F. Lison, P. Schuh, D. Haubrich, and D. Meschede, "High-brilliance Zeeman-slowed cesium atomic beam," *Physical Review A* **61**, 013405 (1999).

[305] C. Adler, F. Narducci, C. Sukenik, J. Mulholland, and S. Goodale, "Design of a permanent-magnet zeeman slower," in *APS Division of Atomic, Molecular and Optical Physics Meeting Abstracts* (2006).

[306] Y. B. Ovchinnikov, "A Zeeman slower based on magnetic dipoles," *Optics Communications* **276**, 261–267 (2007).

[307] V. Lebedev and D. M. Weld, "Self-assembled Zeeman slower based on spherical permanent magnets," *Journal of Physics B: Atomic, Molecular, and Optical Physics* **47**, 155003 (2014).

[308] A. Parsagian and M. Kleinert, “Designing and building a permanent magnet Zeeman slower for calcium atoms using a 3D printer,” *American Journal of Physics* **83**, 892 (2015).

[309] I. Courtillot, A. Quessada, R. P. Kovacich, J.-J. Zondy, A. Landragin, A. Clairon, and P. Lemonde, “Efficient cooling and trapping of strontium atoms,” *Optics Letters* **28**, 468 (2003).

[310] C. J. Dedman, J. Nes, T. M. Hanna, R. G. Dall, K. G. H. Baldwin, and A. G. Truscott, “Optimum design and construction of a Zeeman slower for use with a magneto-optic trap,” *Review of Scientific Instruments* **75**, 5136–5142 (2004).

[311] J. Thorn, *Dissipative Control and Imaging of Cold Atoms*, Ph.D. thesis, University of Oregon (2012).

[312] J. Dalibard and C. Cohen-Tannoudji, “Atomic motion in laser light: Connection between semiclassical and quantum descriptions,” *Journal of Physics B: Atomic and Molecular Physics* **18**, 1661–1683 (1985).

[313] D. A. Steck, “Classical and Modern Optics,” course notes available online at `http://steck.us/teaching` (2015).

[314] C. E. Wieman and L. Hollberg, “Using diode lasers for atomic physics,” *Review of Scientific Instruments* **62**, 1–20 (1991).

[315] A. L. Schawlow and C. H. Townes, “Infrared and optical masers,” *Physical Review* **112**, 1940–1949 (1958).

[316] R. P. Salathé, “Diode lasers coupled to external resonators,” *Applied Physics* **20**, 1–18 (1979).

[317] K. B. MacAdam, A. Steinbach, and C. Wieman, “A narrowband tunable diode laser system with grating feedback, and a saturated absorption spectrometer for Cs and Rb,” *American Journal of Physics* **60**, 1098–1111 (1992).

[318] E. C. Cook, P. J. Martin, T. L. Brown-Heft, J. C. Garman, and D. A. Steck, “High passive-stability diode-laser design for use in atomic-physics experiments.” *Review of Scientific Instruments* **83**, 043101 (2012).

[319] P. J. Martin and T. L. Brown-Heft, notes available online at `http://atomoptics.uoregon.edu/~unilaser` (2012).

[320] A. S. Arnold, J. S. Wilson, and M. G. Boshier, “A simple extended-cavity diode laser,” *Review of Scientific Instruments* **69**, 1236–1239 (1998).

[321] P. Zorabedian and W. R. Trutna, “Interference-filter-tuned, alignment-stabilized, semiconductor external-cavity laser,” *Optics Letters* **13**, 826 (1988).

[322] X. Baillard, A. Gauguet, S. Bize, P. Lemonde, P. Laurent, A. Clairon, and P. Rosenbusch, “Interference-filter-stabilized external-cavity diode lasers,” *Optics Communications* **266**, 609–613 (2006).

[323] A. Takamizawa, S. Yanagimachi, T. Ikegami, and R. Kawabata, “External-cavity diode laser with frequency drift following natural variation in air pressure,” *Applied Optics* **54**, 5777–5781 (2015).

[324] L. Ricci, M. Weidemüller, T. Esslinger, A. Hemmerich, C. Zimmerman, V. Vuletic, W. Konig, and T. W. Hänsch, “A compact grating-stabilized diode laser system for atomic physics,” *Optics Communications* **117**, 541–549 (1995).

[325] L. B. Mercer, “1/f frequency noise effects on self-heterodyne linewidth measurements,” *Journal of Lightwave Technology* **9**, 485–493 (1991).

[326] P. W. Milonni and J. H. Eberly, *Lasers* (John Wiley and Sons, 1988).

[327] M. Fuchs, *Development of a High Power Stabilized Diode Laser System*, Master’s thesis, University of Oregon (2006).

[328] H. L. Stover and W. H. Steier, “Locking of laser oscillators by light injection,” *Applied Physics Letters* **8**, 91–93 (1966).

[329] S. Kobayashi and T. Kimura, “Injection locking in AlGaAs semiconductor laser,” *IEEE Journal of Quantum Electronics* **17**, 681–689 (1981).

[330] Y. Shimada, Y. Chida, N. Ohtsubo, T. Aoki, M. Takeuchi, T. Kuga, and Y. Torii, “A simplified 461-nm laser system using blue laser diodes and a hollow cathode lamp for laser cooling of Sr,” *Review of Scientific Instruments* **84** (2013), 10.1063/1.4808246.

[331] C. J. H. Pagett, P. H. Moriya, R. Celistrino Teixeira, R. F. Shiozaki, M. Hemmerling, and P. W. Courteille, “Injection locking of a low cost high power laser diode at 461 nm,” *Review of Scientific Instruments* **87**, 053105 (2016).

[332] D. A. Kleinman, “Theory of second harmonic generation of light,” *Physical Review* **128**, 1761–1775 (1962).

[333] N. Madsen, “Generation of 243 nm laser light for ATHENA,” ATHENA 2002-01 internal note (2002).

[334] D. S. Hum and M. M. Fejer, “Quasi-phasematching,” *Comptes Rendus Physique* **8**, 180–198 (2007).

[335] R. Le Targat, J.-J. Zondy, and P. Lemonde, “75%-efficiency blue generation from an intracavity PPKTP frequency doubler,” *Optics Communications* **247**, 471–481 (2005).

[336] B. G. Klappauf, Y. Bidel, D. Wilkowski, T. Chanelie, and R. Kaiser, "Detailed study of an efficient blue laser source by second-harmonic generation in a semimonolithic cavity for the cooling of strontium atoms," *Applied Optics* (2004).

[337] I. Juwiler, A. Arie, A. Skliar, and G. Rosenman, "Efficient quasi-phase-matched frequency doubling with phase compensation by a wedged crystal in a standing-wave external cavity." *Optics Letters* **24**, 1236–8 (1999).

[338] F. Torabi-Goudarzi and E. Riis, "Efficient cw high-power frequency doubling in periodically poled KTP," *Optics Communications* **227**, 389–403 (2003).

[339] A. D. Saenz, *461nm Laser for Studies In Ultracold Neutral Strontium*, Ph.D. thesis, Rice University (2005).

[340] J. H. Marquardt, "Grating-tuned semiconductor MOPA lasers for precision spectroscopy," *Proceedings of SPIE* **2834**, 34–40 (1996).

[341] C. R. Vidal and J. Cooper, "Heat-pipe oven: A new, well-defined metal vapor device for spectroscopic measurements," *Journal of Applied Physics* **40**, 3370–3374 (1969).

[342] W. H. Parkinson, E. M. Reeves, and F. S. Tomkins, "Neutral calcium, strontium and barium: Determination of f values of the principal series by the hook method," *Journal of Physics B: Atomic and Molecular Physics* **9**, 157 (1976).

[343] Y. Bidel, *Piégeage et refroidissement laser du strontium: Etude de l'effet des interférences en diffusion multiple*, Ph.D. thesis, Universite de Nice - Sophia Antipolis (2002).

[344] D. W. Preston, "Doppler-free saturated absorption: Laser spectroscopy," *American Journal of Physics* **64**, 1432–1436 (1996).

[345] T. W. Hänsch, I. S. Shahin, and A. L. Schawlow, "High-resolution saturation spectroscopy of the sodium D lines with a pulsed tunable dye laser," *Physical Review Letters* **27**, 707–710 (1971).

[346] C. J. Bordé, J. L. Hall, C. V. Kunasz, and D. G. Hummer, "Saturated absorption line shape: Calculation of the transit-time broadening by a perturbation approach," *Physical Review A* **14**, 236–263 (1976).

[347] Y. C. Chan and J. A. Gelbwachs, "Broadening, shifting and asymmetry of the strontium resonance line induced by rare gas perturbers," *Journal of Physics B: Atomic, Molecular and Optical Physics* **25**, 3601–3612 (1992).

[348] G. C. Bjorklund, "Frequency-modulation spectroscopy: a new method for measuring weak absorptions and dispersions," *Optics Letters* **5**, 15 (1980).

[349] J. A. Neuman, P. Wang, and A. Gallagher, "Robust high-temperature sapphire cell for metal vapors," *Review of Scientific Instruments* **66**, 3021–3023 (1995).

[350] Y. Li, T. Ido, T. Eichler, and H. Katori, "Narrow-line diode laser system for laser cooling of strontium atoms on the intercombination transition," *Applied Physics B* **78**, 315–320 (2004).

[351] E. M. Bridge, J. Millen, C. S. Adams, and M. P. A. Jones, "A vapor cell based on dispensers for laser spectroscopy," *Review of Scientific Instruments* **80**, 013101 (2009).

[352] T. Aoki, K. Umezawa, Y. Yamanaka, N. Takemura, Y. Sakemi, and Y. Torii, "A 461 nm laser system and hollow-cathode lamp spectroscopy for magneto-optical trapping of Sr atoms," *Journal of the Physical Society of Japan* **81**, 1–5 (2012).

[353] U. Dammalapati, I. Norris, and E. Riis, "Saturated absorption spectroscopy of calcium in a hollow-cathode lamp," *Journal of Physics B: Atomic, Molecular and Optical Physics* **42**, 165001 (2009).

[354] M. Prentiss, A. Cable, J. E. Bjorkholm, S. Chu, E. L. Raab, and D. E. Pritchard, "Atomic-density-dependent losses in an optical trap," *Optics Letters* **13**, 452 (1988).

[355] F. Sorrentino, G. Ferrari, N. Poli, R. Drullinger, and G. M. Tino, "Laser cooling and trapping of atomic strontium for ultracold atoms physics, high-precision spectroscopy and quantum sensors," *Modern Physics Letters B* **20**, 1287–1320 (2006).

[356] S. B. Nagel, *Ultracold Collisions in Atomic Strontium*, Ph.D. thesis, Rice University (2008).

[357] T. Yang, K. Pandey, M. S. Pramod, F. Leroux, C. C. Kwong, E. Hajiyev, Z. Y. Chia, B. Fang, and D. Wilkowski, "A high flux source of cold strontium atoms," *The European Physical Journal D* **69**, 226 (2015).

[358] A. Chambers, *Modern Vacuum Physics* (CRC Press, 2005).

[359] K. M. Birnbaum, *Cavity QED with Multilevel Atoms*, Ph.D. thesis, Caltech (2005).

[360] J. H. Moore, C. C. Davis, and M. A. Coplan, *Building Scientific Apparatus: A practical guide to design and construction*, 3rd ed. (Westview Press, 2003).

[361] G. M. Carter and D. E. Pritchard, "Recirculating atomic beam oven," *Review of Scientific Instruments* **49**, 120–121 (1978).

[362] J. J. McClelland, M. H. Kelley, and R. J. Celotta, "Superelastic scattering of spin-polarized electrons from sodium," *Physical Review A* **40**, 2321–2329 (1989).

[363] K. J. Ross and B. Sonntag, "High temperature metal atom beam sources," *Review of Scientific Instruments* **66**, 4409–4433 (1995).

[364] M. Schioppo, N. Poli, M. Prevedelli, S. Falke, C. Lisdat, U. Sterr, and G. M. Tino, "A compact and efficient strontium oven for laser-cooling experiments," *Review of Scientific Instruments* **83**, 1–6 (2012).

[365] G. R. Hanes, "Multiple tube collimator for gas beams," *Journal of Applied Physics* **31**, 2171–2175 (1960).

[366] H. C. W. Beijerinck and N. F. Verster, "Velocity distribution and angular distribution of molecular beams from multichannel arrays," *Journal of Applied Physics* **46**, 2083–2091 (1975).

[367] R. Senaratne, S. V. Rajagopal, Z. A. Geiger, K. M. Fujiwara, V. Lebedev, and D. M. Weld, "Effusive atomic oven nozzle design using an aligned microcapillary array," *Review of Scientific Instruments* **86**, 023105 (2015).

[368] J. A. Giordmaine and T. C. Wang, "Molecular beam formation by long parallel tubes," *Journal of Applied Physics* **31**, 463–471 (1960).

[369] N. F. Ramsey, *Molecular Beams* (Oxford University Press, 1956).

[370] Y. B. Ovchinnikov, "A permanent Zeeman slower for Sr atomic clock," *The European Physical Journal Special Topics* **163**, 95–100 (2008).

[371] Y. B. Ovchinnikov, "Longitudinal Zeeman slowers based on permanent magnetic dipoles," *Optics Communications* **285**, 1175–1180 (2012).

[372] Y. T. Sasaki, "A survey of vacuum material cleaning procedures: A subcommittee report of the American Vacuum Society Recommended Practices Committee," *Journal of Vacuum Science & Technology A: Vacuum, Surfaces, and Films* **9**, 2025 (1991).

[373] M. Bernardini, "Air bake-out to reduce hydrogen outgassing from stainless steel," *Journal of Vacuum Science & Technology A: Vacuum, Surfaces, and Films* **16**, 188 (1998).

[374] S. Kurokouchi, S. Shinoda, and S. Morita, "Properties of a newly developed concave nickel gasket for the ConFlat-type sealing system," *Journal of Vacuum Science & Technology A: Vacuum, Surfaces, and Films* **24**, 1847–1856 (2006).

[375] P. E. Gaskell, J. J. Thorn, S. Alba, and D. A. Steck, "An open-source, extensible system for laboratory timing and control," *Review of Scientific Instruments* **80**, 115103 (2009).

[376] P. E. Gaskell, notes available online at `http://atomoptics.uoregon.edu/~zoinks` (2009).

[377] T. Meyrath and F. Schreck, "A laboratory control system for cold atom experiments," available online at `http://george.ph.utexas.edu/~control` (2006).

[378] Egnite GmbH, "Ethernut platform," `http://www.ethernut.de/` (2009).

[379] K. Lindquist, M. Stephens, and C. Wieman, "Experimental and theoretical study of the vapor-cell Zeeman optical trap," *Physical Review A* **46**, 4082–4090 (1992).

[380] A. Derevianko, "Feasibility of cooling and trapping metastable alkaline-earth atoms," *Physical Review Letters* **87**, 023002 (2001).

[381] S. Stellmer and F. Schreck, "Reservoir spectroscopy of 5s5p $^3P_2$ - 5snd $^3D_{1,2,3}$ transitions in strontium," *Physical Review A* **90**, 1–14 (2014).

[382] K. R. Vogel, *Laser Cooling on a Narrow Atomic Transition and Measurement of the Two-Body Cold Collision Loss Rate in a Strontium Magneto-Optical Trap*, Ph.D. thesis, University of Colorado (1999).

[383] N. Poli, G. Ferrari, M. Prevedelli, F. Sorrentino, R. Drullinger, and G. Tino, "Laser sources for precision spectroscopy on atomic strontium," *Spectrochimica Acta Part A: Molecular and Biomolecular Spectroscopy* **63**, 981–986 (2006).

[384] J. Weiner, V. S. Bagnato, S. Zilio, and P. S. Julienne, "Experiments and theory in cold and ultracold collisions," *Reviews of Modern Physics* **71**, 1–85 (1999).

[385] K. Vogel, T. Dinneen, A. Gallagher, and J. Hall, "Near-recoil-limited temperatures obtained by laser trapping on the narrow$^1S_0$–$^3P_1$ intercombination transition of neutral strontium," in *Proceedings of the 1999 Joint Meeting of the European Frequency and Time Forum and the IEEE International Frequency Control Symposium (Cat. No.99CH36313)*, Vol. 2 (IEEE, 1999) pp. 692–695.

[386] T. Walker, D. Sesko, and C. Wieman, "Collective behavior of optically trapped neutral atoms," *Physical Review Letters* **64**, 408–411 (1990).

[387] D. W. Sesko, T. G. Walker, and C. E. Wieman, "Behavior of neutral atoms in a spontaneous force trap," *Journal of the Optical Society of America B* **8**, 946 (1991).

[388] "Engineering Design Guide," Sorbathane Inc., available online at `http://www.sorbothane.com/engineering-design-guide.aspx` (2015).

[389] D. A. Steck, "Analog and Digital Electronics," course notes available online at `http://steck.us/teaching` (2015).

[390] Y. Castin, H. Wallis, and J. Dalibard, "Limit of Doppler cooling," *Journal of the Optical Society of America B* **6**, 2046 (1989).

[391] T. H. Loftus, T. Ido, A. D. Ludlow, M. M. Boyd, and J. Ye, "Narrow line cooling: Finite photon recoil dynamics," *Physical Review Letters* **93**, 11–14 (2004).

[392] T. H. Loftus, T. Ido, M. M. Boyd, A. D. Ludlow, and J. Ye, "Narrow line cooling and momentum-space crystals," *Physical Review A* **70**, 1–14 (2004)